Non-Equilibrium Effects in Nanoparticulate Assemblies, Bond-Disordered Ferromagnets, and Collections of Two-Level Subsystems

by

Candice April Harder Viddal

A Thesis
Submitted to the Faculty of Graduate Studies of
The University of Manitoba
in Partial Fulfillment of the Requirements
for the Degree of

DOCTOR OF PHILOSOPHY

Department of Physics & Astronomy
University of Manitoba
Winnipeg, Manitoba, Canada

Abstract

The central concern of this thesis is the study of non-equilibrium behaviour in magnetic materials and its interpretation within the framework of a theoretical model based on the Preisach hypothesis, which decomposes all magnetic materials into a collection of bistable units. More specifically, we have performed comprehensive experimental characterizations of a variety of magnetic materials, including a naturally occurring mineral of nanodimensional titanomagnetite particles embedded in volcanic glass, a compressed powder of nanodimensional magnetite particles immobilized in an organic binder, a thin film of nanodimensional Fe particles embedded in alumina, and a series of sintered, bond-disordered $Ca_xSr_{1-x}RuO_3$ ferromagnets. We have measured (a) the initial magnetizing curve, the magnetizing remanence, the descending branch of the major hysteresis loop and the demagnetizing remanence as a function of applied field over a broad range of temperatures, (b) the field cooled moment, the zero field cooled moment, the thermoremanent moment and the isothermal remanent moment as a function of temperature in a broad range of applied fields, and (c) viscosity isotherms in a series of negative holding fields following recoil from positive saturation as a function of time over a wide range of temperatures. The measurements were compared with numerical simulations based on a Preisach model ensemble of thermally activated two-level subsystems, characterized individually by a double well free energy profile in a two-dimensional configuration space, an elementary moment reversal, a dissipation field and a bias field, and characterized collectively by a distribution of these characteristic fields. Our efforts were concentrated on two principal spheres of investigation. (1) By

performing detailed numerical simulations of the relaxation response of model Preisach collections of two-level subsystems under the same field and temperature protocols used to probe experimentally the relaxation dynamics of spin glasses, we have been able to show that aging, memory and rejuvenation effects are not unique to collectively ordered materials with spin glass correlations, but rather are an ubiquitous feature of materials with a broad distribution of energy barriers where relaxation proceeds as a superposition of independent overbarrier activation events, each with its own characteristic relaxation time constant. (2) The second line of inquiry pertains to probing the two principal mechanisms, thermal fluctuations and barrier growth, which are jointly responsible for shaping the measured temperature dependence of the magnetic properties of all magnetic materials which exhibit a history dependent response to an external field excitation. We have proposed a general strategy for isolating and quantifying these two mechanisms which is based on the analysis of viscosity isotherms and, in particular, on a plot of $T \ln(t_r/\tau_0)$ versus H_a , where t_r is the time at which a viscosity isotherm measured in a field H_a at temperature T reverses sign. When the magnetic response is dominated by thermal activation events, this plot will yield a universal curve from which it is possible to extract the mean elementary moment reversal and to reconstruct the distribution of metastable state excitation energies. When barrier growth dominates, the plot fractures into a family of isothermal curves from which it is, in principle, possible to reconstruct the evolution of the free energy landscape with temperature and to observe the collapse of the barriers as the material is warmed through the critical ordering temperature. The strategy is applied to the analysis of all four materials listed above.

Acknowledgements

I would like to thank my thesis advisor, Dr. Roy Roshko, for all of the tremendous support, encouragement, and guidance he has provided throughout the last ten years of my academic life. Roy, you are a truly great teacher and have been a continual source of inspiration. I can definitely say that your influence on my life has been profound.

I would also like to thank my advisory committee, Dr. Gwyn Williams and Dr. Frank Hawthorne, for all of their time, insights and criticisms throughout my entire graduate program, and for their suggestions for improving this thesis.

I also acknowledge the financial support of NSERC and the Faculty of Science at the University of Manitoba, for their provision of fellowships and grants for this research.

Gratitude is also extended to the Institute for Rock Magnetism at the University of Minnesota for allowing us to utilize their equipment for gathering data used in this thesis.

I extend sincere thanks to my parents, Walter and Emily Harder, for providing a home that nurtured my passion for learning, and encouraged me in the pursuit of all of my personal endeavours.

And last, but definitely not least, I thank my husband Jason for his patience, encouragement and complete support of all that I want to accomplish in this life. Jason, your outlook and wisdom has taught me so much, and has fundamentally changed how I perceive the world.

Table of Contents

Chapter 4: The Preisach Model

Chapter 5: Equipment and Sample Preparation

Chapter 6: Aging, Memory and Rejuvenation in Collections of Two-Level Subsystems

List of Copyrighted Material for which Permission was Obtained

Chapter 1:
Figure 1.6 on page 17 of this thesis appears as Figure 2.7 in "Hysteresis in Magnetism" by Giorgio Bertotti, Academic Press, copyright 1998.

Chapter 3:
Figure 3.4 on page 42 of this thesis appears as Figure 8.10 in "Hysteresis in Magnetism" by Giorgio Bertotti, Academic Press, copyright 1998.

Figure 3.6 on page 49 of this thesis appears as Figure 2.11 in "Hysteresis in Magnetism" by Giorgio Bertotti, Academic Press, copyright 1998.

Figure 3.7 on page 50 of this thesis appears as Figure 9.6 in "Hysteresis in Magnetism" by Giorgio Bertotti, Academic Press, copyright 1998.

Figure 3.8 on page 51 of this thesis appears as Figure 5.2.1 in "Differential Equations and Mathematical Biology" by D.S. Jones and B.D. Sleeman, George Allen & Unwin, copyright 1983.

Figures 3.9 and 3.10 on page 53 of this thesis appear as Figures 5.3.2 and 5.3.3 in "Differential Equations and Mathematical Biology" by D.S. Jones and B.D. Sleeman, George Allen & Unwin, copyright 1983.

Chapter 6:
Figure 6.5(a) on page 109 of this thesis appears as Figure 2 in Physical Review B 59, 9402 by Jonsson, Jonason and Nordblad, American Physical Society, copyright 1999*.

Figure 6.5(b) on page 109 of this appears as Figure 3 in Physical Review B 61, 1261 by Jönsson, Hansen, and Nordblad, American Physical Society, copyright 2000*.

Figure 6.5(c) on page 110 of this thesis appears as Figure 7 in Physical Review B 71, 104405-1 by Sasaki, Jönsson and Takayama, American Physical Society, copyright 2005*.

Figure 6.5(d) on page 110 of this thesis appears as Figure 1 in Physical Review B 38, 7097 by Granberg, Sandlund, Nordblad, Svedlindh, and Lundgren, American Physical Society, copyright 1988*.

Figure 6.5(e) on page 111 of this thesis appears as Figure 3 in Physical Review Letters 75, 4138 by Jonsson, Mattson, Djurberg, Khan, Nordblad, and Svedlindh, American Physical Society, copyright 1995*.

Figure 6.9(a) on page 121 of this thesis appears as Figure 3 in Physical Review B 59, 9402 by Jonsson, Jonason, and Nordblad, American Physical Society, copyright 1999*.

Figure 6.9(b) on page 121 of this thesis appears as Figure 1 in Physical Review B 59, 8770 by Jonsson, Jonason, Jönsson, and Nordblad, American Physical Society, copyright 1999*.

Figure 6.9(c) on page 122 of this thesis appears as Figure 9 in Physical Review B 71, 104405 by Sasaki, Jonsson, and Takayama, American Physical Society, copyright 2005*.

Figure 6.12(a) and 6.12(b) on page 128 of this thesis appears as Figure 8 in Physical Review B 70, 174402 by Jönsson, Mathieu, Nordblad, Yoshino, Katori, and Ito, American Physical Society, copyright 2004*.

Figure 6.12(c) on page 129 of this thesis appears as Figure 4 in Physical Review B 70, 174402 by Jönsson, Mathieu, Nordblad, Yoshino, Katori, and Ito, American Physical Society, copyright 2004*.

Figure 6.13(a) on page 130 of this thesis appears as Figure 1 in Physical Review B 71, 104404 by Jönsson, Yoshino, Mamiya, and Takayama, American Physical Society, copyright 2005*.

Figures 6.13(b) and 6.13(c) on page of this thesis appears as Figure 3 in Physical Review B 71, 104404 by Jönsson, Yoshino, Mamiya, and Takayama, American Physical Society, copyright 2005*.

Chapter 1: Basic Concepts

1.1 Introduction

Two major facets of ferromagnetic behaviour can be identified experimentally, and depending on the type of measurement that is performed, one would infer that ferromagnetism [1-6] is identified by the observance of either (a) a Curie point at a well-defined critical temperature T_C, below which the atomic moments cooperatively lock together into a parallel configuration and the material exhibits a spontaneous magnetization even in the absence of an applied magnetic field, or (b) a path-dependent response to a changing excitation field at a temperature $T < T_C$, such as a hysteresis loop similar to the one presented in Figure 1.1. The topics and experiments discussed in this thesis will be focused on the hysteretic characteristics of a diverse collection of magnetic materials measured over a wide range of temperatures (in some cases, up to or even beyond the critical temperature T_C), and a wide range of applied fields up to technical saturation.

Hysteresis loops are measured by applying a cyclical magnetic field H_a to a sample of interest, and measuring the induced magnetization M (average magnetic moment per unit volume) along the applied field direction (Figure 1.1). The presence of hysteretic behaviour is a central feature of a variety of magnetic materials including ferromagnets below their Curie temperature, superparamagnetic collections of magnetic nanoparticles below their blocking temperature [1, 7], and spin glasses below their

freezing temperature [8], and physicists are still in need of a convincing general theory to interpret this extremely rich phenomenon. From the physicists and mathematicians point of view, hysteresis represents an example of an intriguing and fundamental problem that poses significant and complex challenges. However, hysteresis is also the source of ubiquitous technological progress since it is the property that is exploited by engineers in almost all practical applications of magnetic materials, from magnetic recording to magnetic motors to hysteresis brakes in high speed automated winding machines, used, for example, in wire marking, braiding, material slitting, sheeting and weaving, to control wire tension in a precise manner for the duration of wind, hook, and cut operations [9].

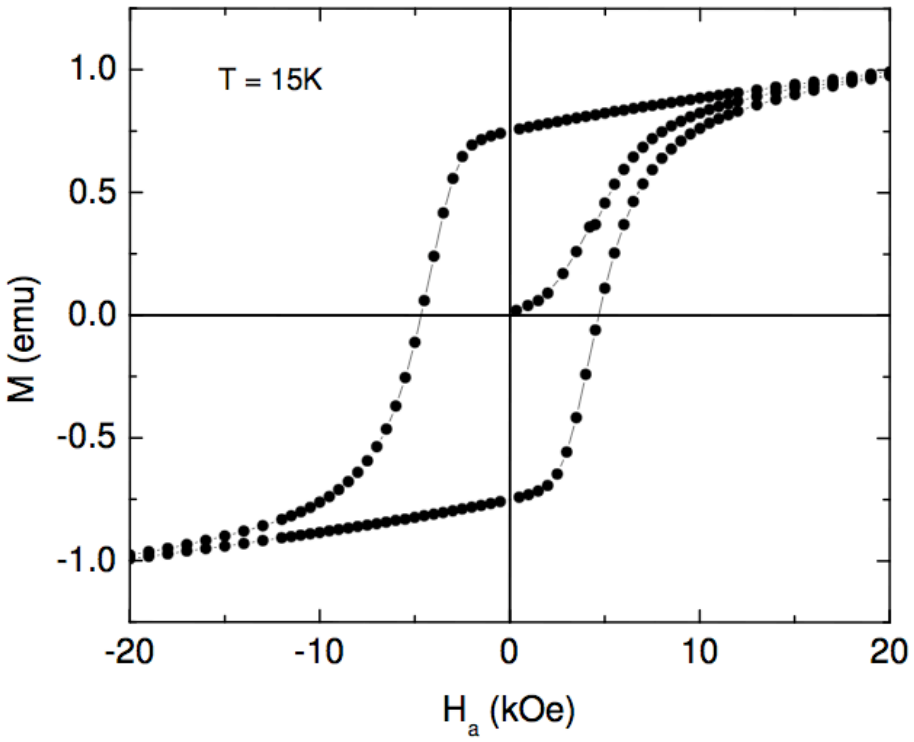

Figure 1.1 The initial magnetizing curve and the major hysteresis Loop measured at T=15K on a bond-disordered ferromagnet, $Ca_{0.2}Sr_{0.8}RuO_3$.

Hysteresis phenomena manifest themselves in various ways and in various natural, economic, and sociological spheres. In addition to the technologically pervasive role of magnetic hysteresis phenomena, hysteresis emerges in economic theories of persistent unemployment [10, 11], solutions to traffic flow problems [12-14], pulmonary tissue mechanics and its relationship to infection [15], and in environmental policy decisions where the phenomenon of hysteresis is applied in an attempt to determine the dynamics of recovery of an ecosystem succeeding the imposition of a pollution control in response to an environmental insult [17].

1.2 Hysteresis and Persistent Memory: General Considerations

The physical mechanisms underlying hysteresis phenomena lie within the sphere of nonequilibrium thermodynamics [18,19], a conceptually difficult topic with many unresolved issues. In order to elucidate the basic problem of hysteresis, we will discuss the general aspects within a framework that is independent of a particular context [20].

From a thermodynamic perspective, the macroscopic state of a material is prescribed by the values of experimentally measurable quantities called state variables. These include quantities such as energy, pressure, volume, temperature, and magnetization.

Consider a situation in which we act on a physical system via an external action, which causes the system to respond by changing its state. We wish to understand and predict the response of the system to this external action by monitoring the time dependence of a dependent output variable as a function of an independent input variable. We can designate the input variable by the symbol H, and the output variable by some quantity X. In the case of a magnetic system, the total magnetic moment M of the body is typically the output variable. In a system that exhibits hysteretic behaviour, future evolution of the output variable X depends on past history. From this perspective, stating that a system displays hysteresis is synonymous with stating that the system has memory of past input. Specifically, the output X(t) at time t not only depends on the input H(t), but also on all previous input values H(t') at earlier times $t' < t$.

In 1895, the Scottish physicist Alfred Ewing formulated a precise definition of hysteretic behaviour: *"When there are two quantities M and N, such that cyclic variations of N cause cyclic variation of M, then if the changes of M lag behind those of N, we may say that there is hysteresis in the relation of M and N."* [21] When hysteresis is strictly a consequence of a phase lag between the input and output signals, the memory effect is transient or nonpersistent. However, for systems that possess a complex internal structure, it is possible that the state of the system which has been subjected to a time-dependent input H(t) and then subsequently held at constant input H_0 for all times $t > t_0$ continues to retain memory of the past history of the input at all times $t < t_0$, even after a sufficient time has elapsed for all input transients to dissipate. For a particular value of H, there are several states that may potentially be occupied, but it is the history of the input

which selects which one of these states is *actually* occupied at the time t_0 of application of H_0. The system remains in that state indefinitely, as long as the external conditions are

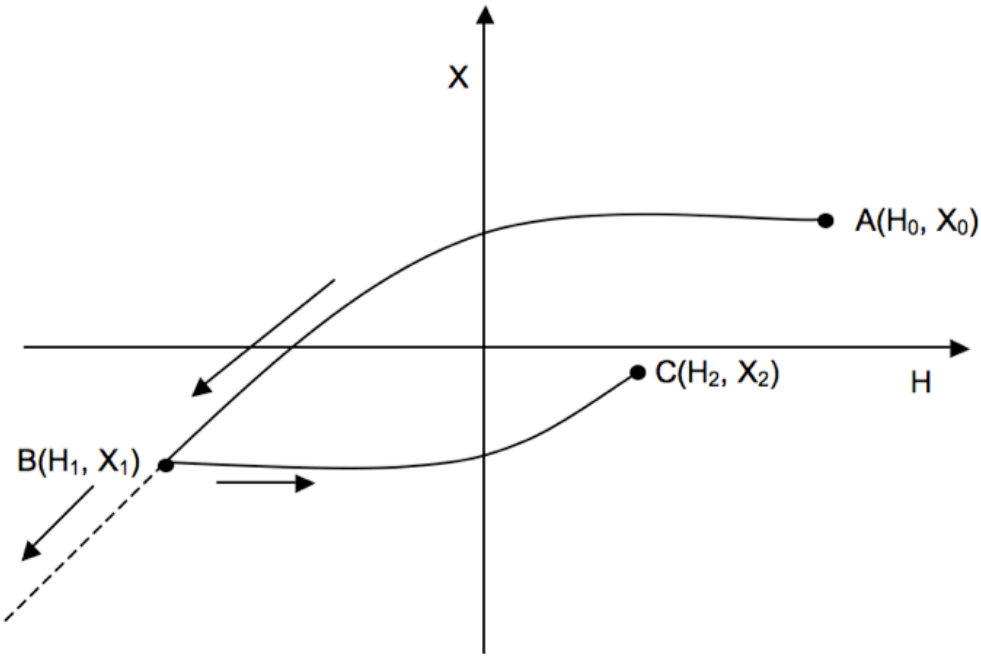

Figure 1.2 Evolutionary branching. The path that is taken by the system upon increasing the field from H_1 to $H > H_1$ depends on the sense of approach to the point $B(H_1, X_1)$ prior to increasing the field.

not modified further, and this produces the persistent memory effect. Furthermore, the equilibrium state under given conditions of field H and temperature T is unique, and thus, a system with persistent memory which is trapped in one of many states, cannot be in thermodynamic equilibrium.

Figure 1.2 shows the path traced out by a system which has been prepared in the state $A(H_0, X_0)$ and then subjected to a decreasing input H until the state $B(H_1, X_1)$ is reached. For a system that has persistent memory, future evolution depends upon past history. Thus, if the field H is subsequently increased from H_1 to H_2, the system will trace out a new evolutionary branch from $B(H_1, X_1)$ to $C(H_2, X_2)$, as opposed to retracing the

original path back to $A(H_0, X_0)$. The fact that the original path is not retraced in the reverse sense when the field direction is changed indicates that the system is not in thermodynamic equilibrium, and is a manifestation of irreversible, dissipative effects as the system exchanges energy with its surroundings.

The direction in which the path X(H) is traced out is established by macroscopic thermodynamics. The First Law of Thermodynamics is $dU = HdX + \delta Q$ [22,23] for a system where HdX is the work done on the system by external sources in the infinitesimal transformation where the output changes by an amount dX. For a closed path, $\oint dU = 0$ and

$$\oint_{\text{cycle}} HdX = -\oint_{\text{cycle}} \delta Q . \qquad (1.1)$$

From this relation it is evident that X(H) must always be traversed counterclockwise, so as to make the area of the loop (left hand side) positive and hence the heat flow (integral on right hand side) negative (corresponding to a loss). To traverse the loop clockwise would be to transform perfectly the heat absorbed from the reservoir into work, a violation of the second law of thermodynamics. For systems in thermodynamic equilibrium with their surroundings, net heat loss has ceased, and there is a one-to-one correspondence between the value of H and the resulting value of X at a temperature T. Under these circumstances, the X(H) curve is independent of the sense in which it is traversed.

When the values of H and X are sufficient to identify the state of a system, then the system is said to have **local memory** [20]. The various states associated with a given H are necessarily designated by different values of X, which is to say that a single point in the H-X plane uniquely identifies one and only one state. When H and X do not completely characterize the state of the system, then the system is said to have **nonlocal memory** [20]. Many states are associated with a single point in the H-X plane, and a whole series of X(H) curves emanating from the initial point (H_1,X_1) in Figure 1.2 may be made manifest, depending on past input history. Thus, in a system with nonlocal memory, additional internal state variables are needed to complete the characterization of the state of the system.

1.3 Metastability and Free Energy Landscapes

The observation of hysteretic behaviour in a magnetic system is a direct consequence of the complex, multi-valley structure of its intrinsic free energy landscape [20]. That is, due to the complexity and variety of the energy contributions involved in a magnetic system, as well as the presence of structural disorder, the system becomes trapped in local free energy minima known as **metastable states** and the global lowest energy state is inaccessible to the system on laboratory time scales. Thermodynamic equilibrium is forever out of reach.

As a means of exploring the relationship between hysteresis and metastability, we will consider transformations from one thermodynamic state to another. A thermodynamic transformation can occur under constraints which involve both thermal

energy and external work considerations, such as constant temperature and constant applied field. A force that is not counterbalanced by other forces may cause a 'displacement' or change in another quantity, such as position, volume, magnetic moment, etc. These force/displacement pairs are known as conjugate variables and the product of the force and 'displacement' is the energy transferred in the process. A thermodynamic potential can be introduced which controls how the ensuing transformation will unfold when the system is constrained to have one fixed variable in each of the conjugate pairs fundamental to our discussion, namely (T,S) and (H,X). Thus, there are four possible combinations for the constraint variables, and hence four thermodynamic potentials that can be defined: the Helmholtz free energy F(X,T), the Gibbs free energy G(H,T), the internal energy U(X,S) and the enthalpy E(H,S) [22, 23]. Each thermodynamic potential has the property that it never increases in any transformation which has its arguments fixed at a constant value [22,23]. When the thermodynamic potential appropriate to the constraints attains its global minimum, thermodynamic equilibrium is achieved. Of particular interest for magnetic systems are the properties of the potentials for transformations that occur under fixed temperature and fixed field.

For simplicity, we will consider a system with local memory, where the values of the field H, the state variable X, and the temperature T, completely specify the thermodynamic states. Let F(X,T) be the Helmholtz free energy of the system. If H and X are conjugate work variables, then G(H,T) = F - HX is the corresponding Gibbs free energy. The only spontaneous transformations that can occur between two states under fixed H and T are those for which the Gibbs function decreases. During transformations

of this type, the state variable X varies as the system passes sequentially from one thermodynamic state, delineated by a particular value of X, to another. Transformations proceed until G attains its global minimum value and thereby thermodynamic equilibrium is achieved. The energy of these nonequilibrium states at fixed H and T is given by $G_L(X;H,T) = F(X,T)-HX$ and is called the Landau free energy. The Landau free energy, expressed as a function of X, is the energy when the state variable X is constrained to assume a particular value; in other words, since the system has not reached equilibrium, it can only acquire a certain value of X which corresponds to one of the local energy minima that could be occupied to give that value of X, and not the sum over all possible minima for all values of X. That is, the system has not ergodically explored its options, and only 'sees' the minima which give one particular value of X. By contrast, the Gibbs energy G is a function of H and T only, with X also expressed in terms of H and T via the equation of state for the system.

When the two competing thermodynamic forces acting on the system during the approach to equilibrium balance, namely, the force $[dF/dX]_T$ describing internal mechanisms and the external applied field H, equilibrium is attained. The condition for equilibrium is thus

$$\left[\frac{\partial F}{\partial X}\right]_T = H . \qquad (1.2)$$

Combining this equilibrium requirement with the definition of the Landau free energy $G_L(X;H,T) = F(X,T)-HX$ leads to

$$\left[\frac{\partial G_L}{\partial X}\right]_{H,T} = 0 \qquad (1.3)$$

which shows that G_L is an extremum in equilibrium. However, the fact that the thermodynamic forces acting on the system balance does not imply that complete thermodynamic equilibrium has been attained, only that the system occupies one of many metastable states with a particular value of X. (See Figure 1.3.) The past input history determines which of the innumerable minima accessible to the system will actually be occupied. Persistent memory arises naturally out of the sheer number of metastable states accessible to the system.

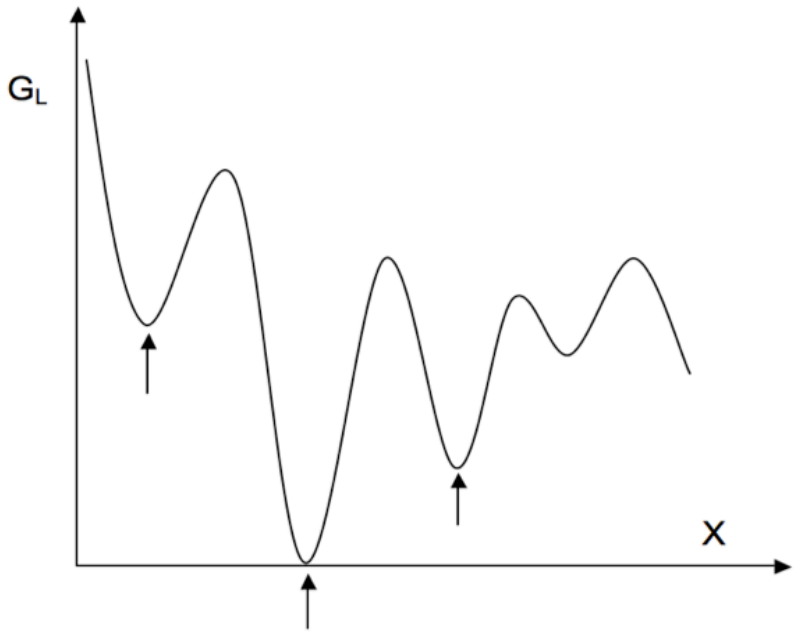

Figure 1.3 Landau free energy landscape. The occupation of a particular energy minimum corresponds to the system being characterized by a particular value of X.

1.4 Thermal Relaxation and the Approach to Equilibrium

In the limit of zero temperature, the system will remain indefinitely in any local energy minimum it may initially occupy, provided that the external conditions do not change, thereby creating a situation where the memory is absolutely persistent. In this limit, the only way to force the system to occupy a different metastable state is to change the external field H. Changing the external field H distorts the energy profile due to the –HX term in the Landau free energy expression, eventually transforming the G_L minimum into an inflection point, causing the system to make a spontaneous jump to the nearest local minimum. This event corresponds to a loss of stability and is called a **Barkhausen jump** [24,25]. The energy loss of the system during the jump is irreversibly dissipated as heat into the thermal bath.

With regard to Barkhausen jumps, it is important to understand that the term *spontaneous* implies that the evolution of the system to a new metastable configuration occurs in a short time relative to the rate at which the external field changes during the jump. Under these special conditions, denoted by the term rate-independent hysteresis, time is of no consequence. The external field plays the only role in forcing the system to pass from one local minimum to the next via a Barkhausen jump, which occurs upon the creation by the field of an instability threshold. However, at finite temperatures, there is always a chance for the system to escape the energy well it is occupying under the influence of thermal agitation, and in this sense, rate-independent hysteresis is a zero-temperature approximation. On slow time scales, random thermal fluctuations increase

the probability of the system making a spontaneous *thermally activated* jump to another metastable state. In particular, when the thermal agitation is sufficient to find the system at a local energy maximum separating the initial state occupied from neighbouring energy minima, a different state becomes accessible. In this way, the system probes progressively larger regions of phase space until thermodynamic equilibrium is reached, where the probability of the system to occupy any specific metastable state is governed by Boltzmann statistics.

When thermal effects play a significant role in allowing the exploration by the system of its free energy landscape, X(t) becomes a stochastic variable [20,26] reflecting the exchange of energy of the system with the thermal bath at a microscopic level. Since we are only interested in the average behaviour of X(t) over time scales long enough to track the macroscopic evolution of the system, we may use probabilistic methods and concepts.

Let P(X,t)dX represent the probability that the value of the state variable lies between X and X+dX at time t. P(X,t) thus characterizes the state of the system, and the value of X that we associate with a given state is the statistical-ensemble average over a large number of identical copies of the system:

$$\langle X(t) \rangle = \int XP(X,t)dX \qquad (1.4)$$

At sufficiently long times, the system will reach thermodynamic equilibrium, where the probability $P_{eq}(X)$ to find a given value of X is controlled by Boltzmann statistics:

$$P_{eq}(X) \equiv P(X, t \to \infty) \propto \exp\left(-\frac{G_L(X;H,T)}{k_B T}\right) \qquad (1.5)$$

If G_L varies rapidly with X relative to $k_B T$, then $P_{eq}(X)$ will exhibit sharp peaks around the local energy minima, and we can describe the problem in terms of discrete states. If P_i is the probability of finding the system around the i^{th} energy minimum, found by limiting the integral of P(X,t) to values of X in the neighbourhood of the minimum at X_i, then one can study $P_i(t)$, the probabilities as a function of time for each discrete state, with the constraint $\sum_i P_i = 1$.

1.5 Bistable Systems

Hysteretic systems can be described in terms of a complicated, multidimensional, multi-valleyed energy landscape with nonlocal memory effects, but studying them by beginning with such a complex description presents insurmountable conceptual and mathematical obstacles. Many fundamental aspects of the hysteresis phenomenon can be illustrated for the simple case of a bistable system, whose free energy is characterized by two minima only [20]. Since there are at most two metastable states available to the system, a system characterized in this way necessarily has only local memory.

Consider a system whose free energy is given by:

$$f(x) = x^4 - 2ax^2 \qquad (1.6)$$

where a is a positive constant. f(x) has two minima of equal magnitude located at $x = \pm a^{1/2}$ and a maximum at x = 0 depicted in Figure 1.4 with a = 1:

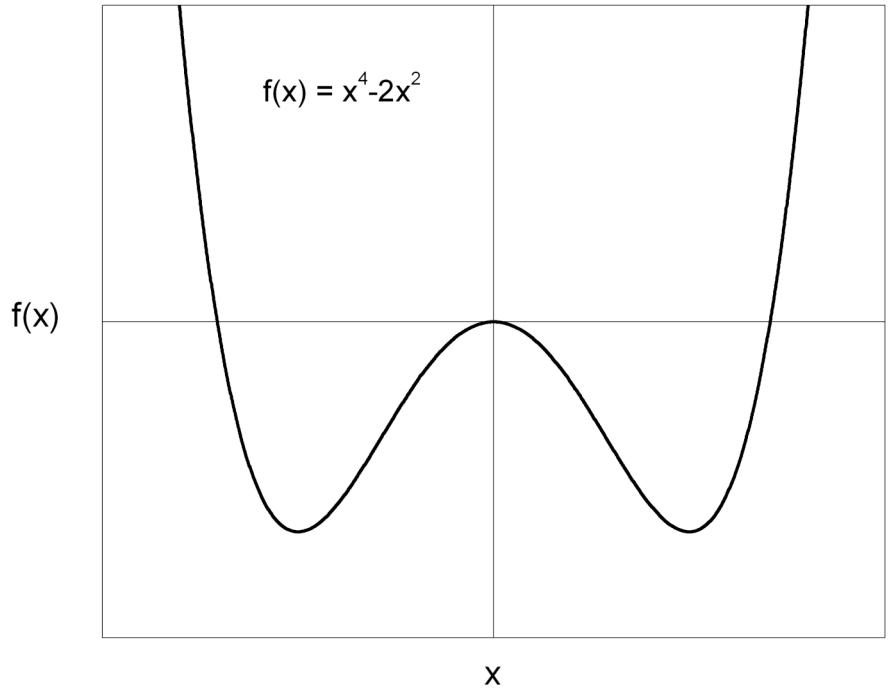

Figure 1.4 Plot of the free energy $f(x) = x^4 - 2ax^2$ with a = 1.0.

The Landau free energy under nonzero input h will be:

$$g_L(x;h) = x^4 - 2ax^2 - hx \qquad (1.7)$$

The metastable states under the application of a field h are found by applying the conditions $\partial g_L / \partial x = 0$ and $\partial^2 g_L / \partial x^2 > 0$, which identify local minima in g_L. When h = 0, the two wells have the same depth. When $h = h_c$, the minimum initially occupied by the system at $h < h_c$ becomes an inflection point, causing the system to make a

spontaneous and irreversible Barkhausen jump to the lower energy state. When $h > h_c$, only one minimum exists. By plotting the state variable x as a function of the input field h, a hysteresis loop, shown in Figure 1.5 is obtained. Despite having a simple structure, the loop arising from the bistable system manifests many of the structural features of hysteresis loops measured for real systems, as will now be explored.

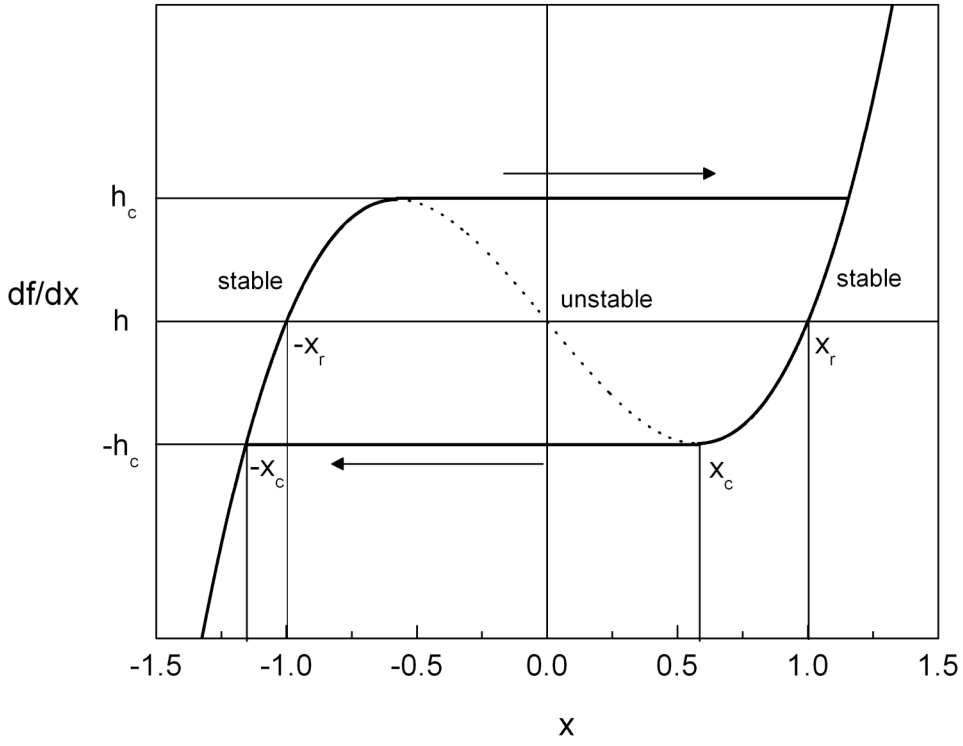

Figure 1.5 Plot of df/dx as a function of x. The stable portions are those segments for which there exists equilibrium between thermodynamic forces and the applied field. The dotted segment is unstable.

At h = 0, two stable states exist. These states are called remanent states, and the state variable has the value $x = x_r = \pm a^{1/2}$. The points where the system becomes unstable

and Barkhausen jumps take place are $h = h_c = 8(a/3)^{3/2}$, $x = -x_c = -(a/3)^{1/2}$, and $h = -h_c = -8(a/3)^{3/2}$, $x = x_c = (a/3)^{1/2}$.

From the thermodynamic viewpoint, the system gains energy from the external field as the minimum it occupies increases in energy and the well becomes more shallow. When the minimum becomes an inflection point, the energy gained from the field is rapidly transferred to the thermal bath during the jump to a lower energy state. In this way, the work done on the two-level system by the external field is transformed into heat.

The state x = 0 is an energy maximum, and thus cannot be realized for an individual subsystem. In the case where we have a spatially extended system, consisting of an ensemble of two-level subsystems, however, the condition $\langle x \rangle = 0$ can be realized with an appropriate *phase mixture*. Each **phase** or **domain** consists of two-level subsystems all of which are either in their $x = x_r$ state or in their $x = -x_r$ state. The relative volumes of the phases can then be adjusted so that the system can acquire values of $\langle x \rangle$ that span the entire interval $-x_r \le \langle x \rangle \le +x_r$. In Figure 1.6, phase coexistence corresponds to the total moment of the ensemble traversing the vertical broken line at h = 0; as the ensemble smoothly passes from $\langle x \rangle = -x_r$ to $\langle x \rangle = +x_r$ the fractional volume of the $-x_r$ domains adjusts continuously from 1 to 0.

Thermal effects become important when the system is coupled to a heat bath, and we can calculate the mean value of the state variable x by introducing the probabilities, p_+ and p_-, of finding the system occupying one of the two energy minima at x_+ and x_-. In this approximation [20, 27-29],

$$\langle x(t) \rangle = x_+ p_+ + x_- p_- = x_- + (x_+ - x_-)p_+ \qquad (1.8)$$

since $p_+ + p_- = 1$. For a statistical ensemble of identical systems, p_+ and p_- are proportional to the number of systems occupying the (+) and (-) minima, respectively. If we introduce the transition rates w_- and w_+, as the probability per unit time of a system occupying the (-) or (+) state making a transition into the (+) or (-) state, respectively, then $p_+(t)$ obeys the master equation,

$$\frac{dp_+}{dt} = w_- p_- - w_+ p_+ . \tag{1.9}$$

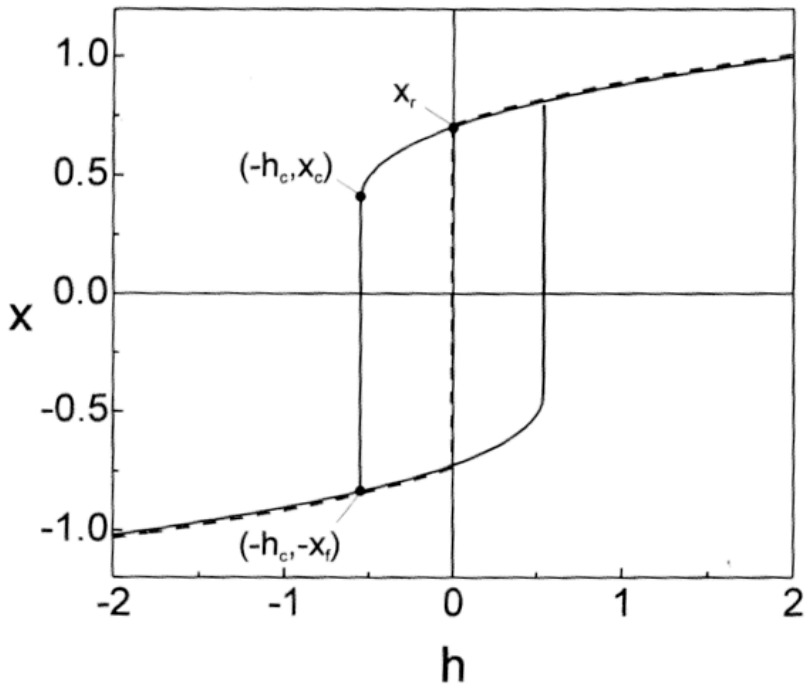

Figure 1.6 Solid line: The system moment x as a function of applied field h for a bistable system displays hysteresis. The broken line is the phase coexistence curve which is obtained for an ensemble of bistable systems with a mixture of phases or domains. *This figure was published in "Hysteresis in Magnetism" by Giorgio Bertotti, page 47. Copyright Academic Press (1998). Reprinted with permission.*

The flows from (-) to (+) and from (+) to (-) proceed independently of each other, and the master equation represents the total balance at any time t. The transition rates $w_{\pm}$ are found by the Arrhenius formula

$$w_{\pm} = \frac{1}{\tau_0} \exp\left(-\frac{\Delta g_{L\pm}}{k_B T} \right), \tag{1.10}$$

where T is the temperature, and $\Delta g_{L\pm} > 0$ are the two energy barriers depicted below:

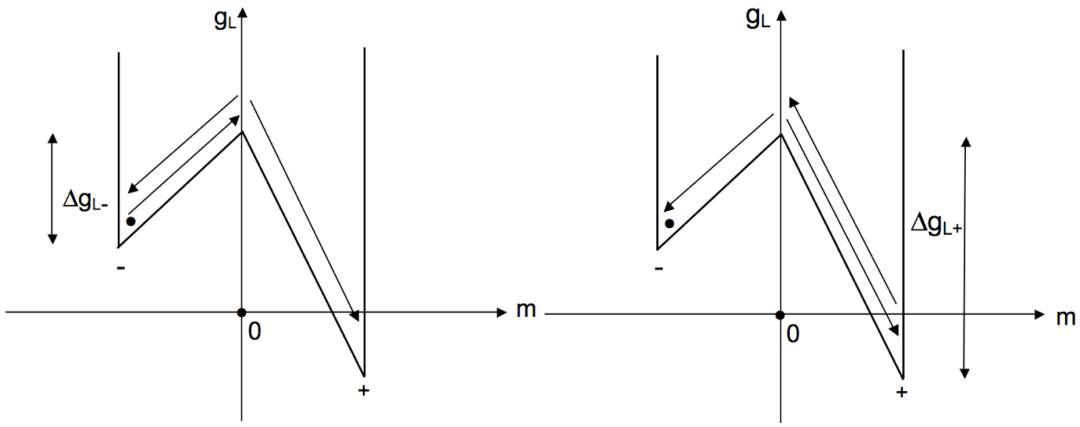

Figure 1.7 The energy barriers and relaxation paths of a bistable system influenced by thermal fluctuations.

The characteristic time constant τ_0 represents the time interval between each 'jump attempt' and physically is related to the curvature of the potential well [30]. The probability of finding a given system of the statistical ensemble at the top of the energy barrier relative to the (-) or (+) state is given by the Boltzmann factor, $\exp(-\Delta g_{L-}/k_B T)$ and $\exp(-\Delta g_{L+}/k_B T)$, respectively. The Arrhenius formula (1.10) is an expression for the

number of times per second that the system will be found on top of the barrier, since this state is dynamically unstable. The system has a probability of ½ of making a jump toward the other energy minimum every time it is found on top of the barrier.

The solution of the master equation (Eq(1.9))is

$$p_+(t) = p_{+,eq} + [p_+(0) - p_{+,eq}]\exp(-t/\tau) \tag{1.11}$$

where

$$p_{+,eq} = \frac{w_-}{w_+ + w_-} \quad \text{and} \quad \tau = \frac{1}{w_+ + w_-} \tag{1.12}$$

The relaxation is exponential, with a time constant τ. The two energy minima both acquire significant populations in the final equilibrium state only under the condition $\left|\Delta g_{L-} - \Delta g_{L+}\right| \le kT$. Otherwise, the larger barrier separating the states is such that the probability of a jump over that barrier is low and hence, only one of the two flows exists with any finite magnitude.

1.6 Hysteresis Loops, Magnetizing Curves, and Demagnetizing Procedures

We conclude this overview by describing a number of fundamental hysteresis loop parameters and magnetizing processes which are particularly relevant to an experimental characterization of hysteresis phenomena with reference to the schematic picture shown below in Figure 1.8:

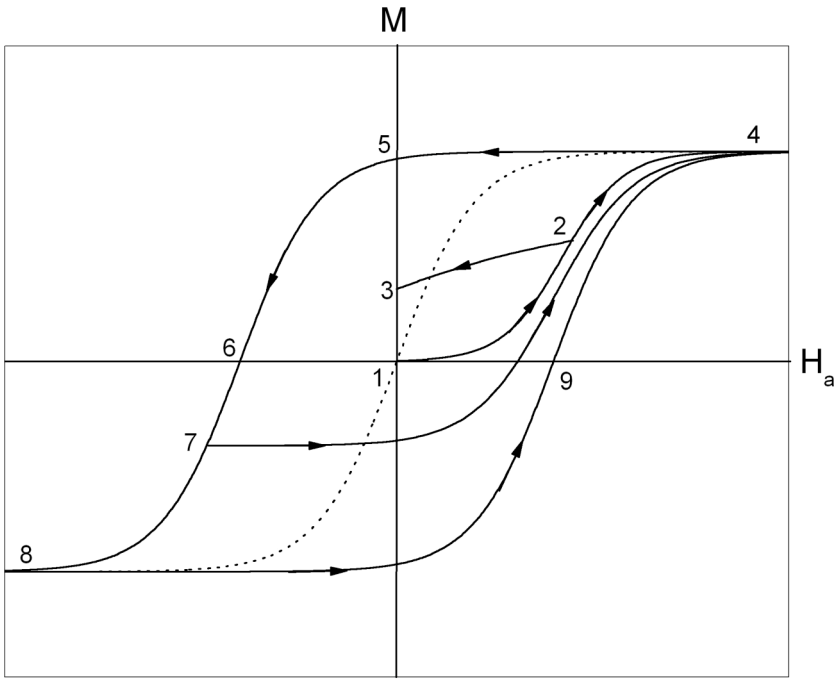

Figure 1.8 The identification of salient characterization parameters of a typical hysteresis loop.

(a) *Initial Magnetizing Curve*. Starting from the demagnetized state (M=0, H_a=0) at point 1, increasing the field yields the initial magnetizing curve 1-2-4.

(b) *Remanence.* Point 3 represents the resulting magnetization after the application of an external field to the system followed by field removal (path 1-2-3).

(c) *Saturation*. The state of the system is described by its domain structure, of which there can be many for given values of H_a and M. The past history of the material determines which domain structure will be realized and how it will evolve under further field changes. The application of a field of large enough amplitude will sweep away the existing domain structure, leaving the system in a state of uniform magnetization called the saturation state (point 4). Once saturation is reached, the subsequent evolution of the state is independent of its history prior to the application of the saturating field.

Saturation Remanent Magnetization or Saturation Remanence, M_r. Point 5 represents the magnetization remaining after the removal of a saturating magnetic field (path 1-2-4-5). The remanence is indicative of the fact that a ferromagnet can have a spontaneous magnetization, even in the absence of an external field. M_r is of the same order of magnitude as the spontaneous magnetization M_s, but may differ slightly due to geometrical or structural features.

(d) *Coercive Field.* The coercive field (point 6) is the reverse field required to reduce the magnetization from the remanent value to zero (path 5-6). The coercive field measures the order of magnitude of the fields that must be applied in order to reverse the magnetization of the material.

(e) *Return Branches*. Starting from saturation and reversing the field at a certain point (point 7) on the saturation loop forms a first-order return branch (path 7-4). Return branches provide experimental evidence that an infinite number of different magnetization curves can be associated with the same field interval.

(f) *Anhysteretic state*. The demagnetized state (point 1) is obtained by applying an oscillating field starting from a large initial value, and reducing the amplitude to smaller

and smaller values until the field reaches zero. This results in a spiraling magnetization curve ending at the origin. A sample that is demagnetized in this way is said to have been ac-demagnetized. Similarly, demagnetization can be achieved by superimposing an oscillating field of decreasing amplitude on a constant field H_a. The resulting state is the anhysteretic state. The anhysteretic curve (dotted line) is obtained by connecting the anhysteretic states resulting under different bias fields H_a. Since the memory of previous states occupied prior to demagnetization is completely erased by the oscillating field, the anhysteretic curve is independent of past history, and is essentially the skeleton around which hysteresis develops.

(g) *Thermally demagnetized state*. The demagnetized state can also be obtained by heating the system above the critical temperature or above the blocking temperature and then slowly cooling it down to the final temperature under constant field H_a. Both the anhysteretic and the thermally demagnetized state represent different ways of bringing the system immediately to the free energy minimum that the system would eventually occupy in thermodynamic equilibrium after waiting for an infinite time in a given applied field H_a. Hysteresis phenomena are a manifestation of the fact that the system is prevented from reaching equilibrium on the experimental time scale, and thus cause excursions from the minimum energy curve described by the backbone. Understanding the relationship between anhysteretic, thermally demagnetized, and minimum energy states is essential, but presents highly nontrivial difficulties, to describing hysteretic behaviour. The complexity of the free energy of a magnetic system makes finding detailed knowledge of its structure difficult. It is generally unknown where and how far from the minimum energy state the system is after a particular field history.

Barkhausen jumps. On a fine scale the magnetization curve $M(H_a)$ is not smooth but rather exhibits a staircase structure as a result of Barkhausen jumps (Figure 1.9). The nearly flat portions of the curve are a result of the domain structure undergoing springlike distortions under the influence of the applied field, while the nearly vertical parts are located at those fields which cause the domain structure to become unstable and jump to a new state. The observed signal, however, shows the occurrence of instabilities over many time scales and it is not generally as clear-cut.

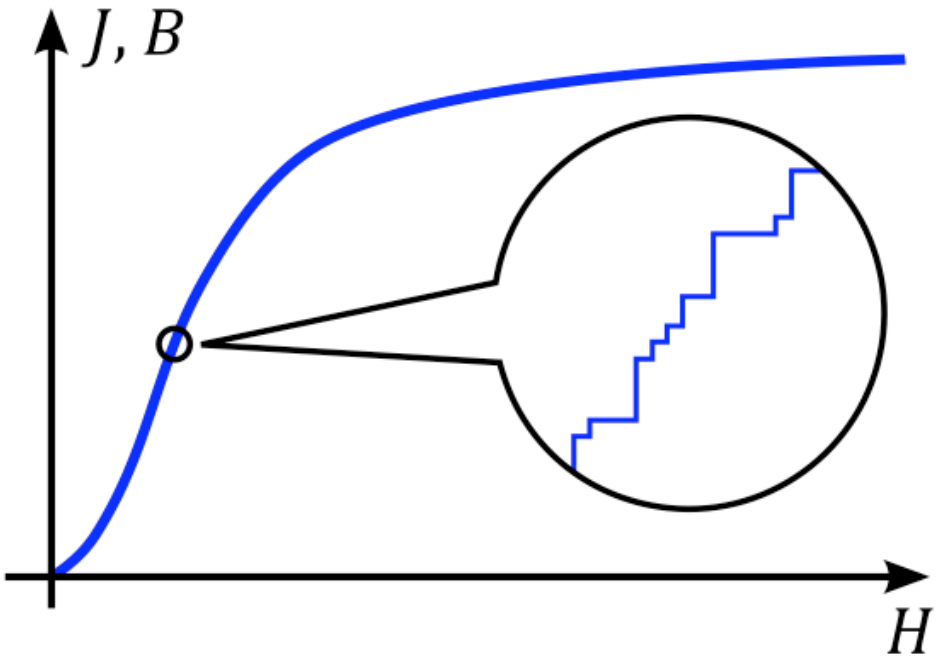

Figure 1.9 The initial magnetizing branch of a measured hysteresis loop. The inset shows the stepwise sequence of Barkhausen jumps which characterize the change in moment as a function of applied field. *This figure was published online at http://en.wikipedia.org/wiki/Barkhausen_effect, 2007. Permission was granted to reproduce this figure under the terms of the GNU Free Documentation License.*

1.7 References for Chapter 1

[1] A. Aharoni, *Introduction to the Theory of Ferromagnetism* (New York: Oxford University Press, 1996).

[2] R.M. Bozorth, *Ferromagnetism* (New York: IEEE Press, 1993).

[3] R.A. McCurrie, *Ferromagnetic Materials: Structure and Properties* (London: Academic Press, 1987).

[4] D.J. Craik and R.S. Tebble, *Ferromagnetism and Ferromagnetic Domains* (Amsterdam: North-Holland, 1965).

[5] B.D. Cullity, *Introduction to Magnetic Materials* (Reading, MA, USA: Addison-Wesley, 1972).

[6] A.H. Morrish, *The Physical Principles of Magnetism* (New York: Wiley, 1965).

[7] I.S. Jacobs and C.P. Bean, "Fine Particles, Thin Films and Exchange Anisotropy (Effects of Finite Dimensions and Interfaces on the Basic Properties of Ferromagnets), in G.T. Rado and H. Suhl, eds., *Magnetism*, Vol. III, 271-350 (New York: Academic Press, 1963-1973).

[8] K.H. Fischer and J.A. Hertz, *Spin Glasses* (Cambridge: Cambridge University Press, 1993).

[9] www.magtrol.com/tensioncontrol/index.html

[10] R. Cross, *Unemployment, Hysteresis, and the Natural Rate Hypotheses* (Blackwell: Oxford (1988).

[11] M. Setterfeld, *Rapid Growth and Relative Decline: Modelling Macroeconomic Dynamics with Hysteresis* (New York: St. Martin's Press, 1997).

[12] W. Dahui, W. Zigiang, and F. Ying, "Hysteresis phenomena of the intelligent driver model for traffic flow," Phys. Rev. E **76** 016105 (2007).

[13] M.B. Hu, W.X. Wang, R.Jiang, Q.S. Wu, and Y.H. Wu, "Phase transition and hysteresis in scale-free network traffic," Phys. Rev. E **75** 036102 (2007).

[14] B.S. Kerner, S.L. Klenov, A. Hiller, and H. Rehborn, "Microscopic features of moving traffic jams," Phys. Rev. E **73** 046107 (2006).

[15] H. Bachofen, "Lung tissue resistance and pulmonary hysteresis," J. Appl. Physiol. **24** 296 (1968).

[16] F.F. Tetenev, "Pulmonary elastic hysteresis under normal conditions and in emphysema," Bull. Exp. Biol. Med. **77** 608 (1974).

[17] A.C. Fisher and W.M. Hanemann, "The Hysteresis Phenomenon and Benefit Evalution for Pollution Control in Aquatic Ecosystems," *Department of Agricultural & Resource Economics, University of California, Berkeley*, *CUDARE Working Papers*, 361 (1985).

[18] S.R. de Groot and P. Mazur, *Non-Equilibrium Thermodynamics* (New York: Dover, 1984).

[19] G.D.C. Kuiken, *Thermodynamics of Irreversible Processes* (New York: Wiley, 1994).

[20] G. Bertotti, *Hysteresis in Magnetism* (San Diego: Academic Press, 1998).

[21] J.A. Ewing, "Experimental research in magnetism." Philosophical Transactions of the Royal Society of London, **176**, II (1895).

[22] H.B. Callen, *Thermodynamics* (New York: Wiley, 1960).

[23] E. Fermi, *Thermodynamics* (New York: Dover, 1956).

[24] B. Alessandro, C. Beatrice, G. Bertotti, and A. Montorsi, "Domain Wall Dynamics and Barkhausen Effect in Ferromagnetic Materials. I. Theory," J. Appl. Phys. **68**, 2901 (1990).

[25] B. Alessandro, C. Beatrice, G. Bertotti, and A. Montorsi, "Domain Wall Dynamics and Barkhausen Effect in Ferromagnetic Materials. II. Experiments," J. Appl. Phys. **68**, 2908 (1990).

[26] I.D. Mayergoyz, *Mathematical Models of Hysteresis* (New York: Springer-Verlag, 1991).

[27] W.F. Brown, Jr., "Thermal Fluctuations of Fine Ferromagnetic Particles," IEEE Trans. Magn. **15**, 1196 (1979).

[28] W.F. Brown, Jr., "Thermal Fluctuations of a Single-Domain Particle," Phys. Rev. **130**, 1677 (1963).

[29] L. Néel, “Theorie du Traînage Magnétique des Ferromagnétiques en Grains Fins avec Application aux Terres Cuites,” Ann. Géophys. **5**, 99 (1949), in French.

[30] J.J. Prejean and J. Souletie, “Two-level-systems in spin glasses: a dynamical study of the magnetizations below TG, application to CuMn systems,” J. Physique **41**, 1335 (1980).

Chapter 2: Micromagnetics

The goal of micromagnetics is to perform a point-by-point spatial reconstruction of the complete magnetization vector field $\vec{M}_{global}(\text{all } \vec{r})$ over the entire volume of the magnetic sample under prescribed conditions of applied field $\vec{H}_a$ and temperature T [1-7]. This volume has a free energy $G_L(X;\vec{H}_a,T)$, where X is some appropriate state variable, from which we can find the set of local minima by setting $dG_L/dX = 0$. Each minimum represents a possible metastable state. However, the energy minimization in this space-dependent approach is complicated by the fact that the state variable X is not simply a scalar quantity, but instead represents the complete magnetization vector field $\vec{M}_{global}(\text{all } \vec{r})$ over the entire body volume. The set of equations that express the conditions under which the energy of a particular magnetization configuration is minimized are called Brown's equations, after W.F. Brown [8,9] who pioneered the formulation of this problem in general terms.

Suppose we have a ferromagnetic body and we subdivide it (in imagination) into many elementary volumes ΔV, where ΔV is small enough on the scale over which the magnetization changes significantly to have uniform properties throughout, yet large enough to contain a significant number of atomic magnetic moments so that physical properties can be described using statistical and thermodynamic methods.

We designate the free energy of the local volume element ΔV around the position $\vec{r}$ by $\Delta G_L(\vec{M}_{local}(\vec{r}); \vec{H}_a, T)$, where $\vec{M}_{local}(\vec{r})$ is the local magnetization vector in ΔV and $\vec{H}_a$ is the externally applied field. There are five contributions to ΔG_L:

(a) Local Exchange. Due to the quantum mechanical exchange interaction $H_{ex} = -J_{ij}\vec{S}_i \cdot \vec{S}_j$ between elementary atomic spins $\vec{S}_i$ and $\vec{S}_j$, ΔV is characterized by a local magnetization vector $\vec{M}_{local}(\vec{r})$ with a magnitude equal to the spontaneous magnetization $M_s(T)$. Due to the isotropy of the exchange interaction, any direction is possible for $\vec{M}_{local}(\vec{r})$, and it is expected that, in general, magnetization vectors will point along different directions in different elementary volumes. Thus we can write $\vec{M}_{local}(\vec{r}) = M_s(T)\hat{m}_{local}(\vec{r})$ where $\hat{m}_{local}(\vec{r})$ is a local unit vector at $\vec{r}$. Since the dependence of the spontaneous magnetization M_s on applied field is weak at temperatures below the Curie temperature, it follows that the spontaneous moment, and hence the exchange energy, is a function of temperature only. At a fixed temperature T, the local exchange contribution to the free energy is thus a constant and will henceforth be neglected.

(b) Nonuniformity exchange energy. Exchange favours parallel alignment of the local magnetization vectors in neighbouring volume elements ΔV over the entire body. As a consequence, whenever $\vec{M}_{local}(\vec{r})$ changes orientation from point to point, neighbouring magnetic moments misalign, and this costs energy which is known as nonuniformity exchange energy. This nonuniformity energy can be expressed in terms of

the gradients $\vec{\nabla} M_{local,x}$, $\vec{\nabla} M_{local,y}$, $\vec{\nabla} M_{local,z}$. For a system with cubic symmetry, the lowest-order term in the energy is

$$\Delta F_{EX} = A\left(\left|\vec{\nabla} M_{local,x}\right|^2 + \left|\vec{\nabla} M_{local,y}\right|^2 + \left|\vec{\nabla} M_{local,z}\right|^2\right) \equiv A\left(\vec{\nabla}\vec{M}_{local}(\vec{r})\right)^2 \qquad (2.1)$$

where A is a phenomenological constant. Strictly speaking, ΔF_{EX} is not a purely local contribution to ΔG_L, since it depends on how $\vec{M}_{local}(\vec{r})$ varies from one volume element to another.

(c) Anisotropy. Anisotropy favours alignment of $\vec{M}_{local}(\vec{r})$ along certain local preferred directions, called easy axes. In a perfect single crystal where only magnetocrystalline anisotropy is important, the preferred directions do not change with position. However, in systems where random quenched-in stresses give rise to local stress anisotropy, the easy axes and the value of the anisotropy constants vary with position in space. If we denote the set of local preferred axes and anisotropy constants by $\vec{K}_{an}(\vec{r})$, the anisotropy energy of the volume element ΔV can be expressed in the form $\Delta F_{an} = f_{an}[\vec{M}_{local}(\vec{r}); \vec{K}_{an}(\vec{r})]\,\Delta V$ where f_{an} is the anisotropy energy density.

(d) Magnetostatic energy. Magnetostatic energy is the potential energy of the local magnetization vectors $\vec{M}_{local}(\vec{r})$ in their own magnetostatic field $\vec{H}_{mag}$. The contribution from each elementary volume is

$$\Delta F_{mag} = -\frac{\mu_0}{2}\vec{H}_{mag} \cdot \vec{M}_{local}\Delta V \qquad (2.2)$$

where $\vec{H}_{mag}$ is the solution of the following magnetostatic equations:

$$\vec{\nabla} \cdot \vec{H}_{mag} = -\vec{\nabla} \cdot (\vec{M}_{local}) \tag{2.3}$$

$$\vec{\nabla} \times \vec{H}_{mag} = 0 \tag{2.4}$$

These relationships are nonlocal in the sense that knowledge of $\vec{M}_{local}(\vec{r})$ in the neighbourhood of a certain point $\vec{r}$ is not sufficient to determine $\vec{H}_{mag}$. Even magnetic moments far away from $\vec{r}$ may contribute to the magnetostatic field at $\vec{r}$. Magnetostatic energy favours configurations where the magnetization follows closed paths inside the body, so that the net magnetic moment vanishes.

(e) Interaction with an applied field. This is the potential energy of the local magnetization vector $\vec{M}_{local}(\vec{r})$ in the applied magnetic field $\vec{H}_a$, and it is given by:

$$\Delta F_{app} = -\mu_0 \vec{H}_a \cdot \vec{M}_{local} \Delta V . \tag{2.5}$$

Combining all of these individual contributions and then summing up over all elementary volumes yields the complete micromagnetic free energy

$$G_L[\vec{M}_{global}(all\,\vec{r});\vec{H}_a] = \int_V \left(A\left(\vec{\nabla}\vec{M}_{local}\right)^2 + f_{an}(\vec{M}_{local};\vec{K}_{an}) - \frac{\mu_0}{2}\vec{H}_{mag} \cdot \vec{M}_{local} - \mu_0 \vec{H}_a \cdot \vec{M}_{local} \right) d^3r$$

(2.6)

where $G_L[\vec{M}_{global}(all\,\vec{r});\vec{H}_a]$ is a *functional*, since it depends on the complete vector field $\vec{M}_{global}(all\,\vec{r})$.

If thermal agitation does not play a significant role, the local minima in G_L represent states in which the system tends to persist for long times. In the limit of zero temperature, the set of all local G_L minima is the set of all possible states in which the system can be found under the influence of a particular external field. The behaviour of G_L should be viewed in the infinite-dimensional space of all possible magnetization vector fields $\vec{M}_{global}(all\,\vec{r})$. In this space, we can identify metastable states by certain configurations $\vec{M}_{meta}(all\,\vec{r})$ which have the property that $G_L[\vec{M}_{meta}(all\,\vec{r})] \le G_L[\vec{M}_{global}(all\,\vec{r})]$ for all other configurations $\vec{M}_{global}(all\,\vec{r})$ in the vicinity of $\vec{M}_{meta}(all\,\vec{r})$. Systems which can have a number of different metastable configurations $\vec{M}_{meta}(all\,\vec{r})$ with identical macroscopic values of the total moment $M(H_a,T)$ for the same applied field H_a and temperature T, exhibit non-local memory.

To minimize G_L and establish the metastable configurations $\vec{M}_{meta}(all\,\vec{r})$ we vary the direction of the local magnetization vector $\vec{M}_{local}(\vec{r})$ at each point $\vec{r}$ by a small arbitrary amount $\delta\vec{M}_{local}(\vec{r})$, $\vec{M}_{local}(\vec{r}) \Rightarrow \vec{M}_{local}(\vec{r}) + \delta\vec{M}_{local}(\vec{r})$, subject to the constraint $\delta\vec{M}_{local} = \vec{M}_{local} \times \delta\vec{\theta}$, where $\delta\vec{\theta}$ describes a small rotation of $\vec{M}_{local}(\vec{r})$ around an arbitrary axis identified by the direction of $\delta\vec{\theta}$. This yields

$$\delta G_L = \mu_0 \int_V (\vec{M}_{local} \times \vec{H}_{eff}) \cdot \delta\vec{\theta}\ d^3r - 2\oint_S A\left(\vec{M}_{local} \times \frac{\partial \vec{M}_{local}}{\partial n}\right) \cdot \delta\vec{\theta}\ da \qquad (2.7)$$

where

$$\vec{H}_{eff} = \frac{2}{\mu_0}\vec{\nabla}\cdot(A\vec{\nabla}\vec{M}_{local}) - \frac{1}{\mu_0}\frac{\partial f_{an}}{\partial \vec{M}_{local}} + \vec{H}_{mag} + \vec{H}_a \qquad (2.8)$$

and where $\partial / \partial n$ is the derivative along the outward normal to the surface of ΔV.

At an extremum, $\delta G_L = 0$ for an arbitrary variation $\delta\vec{\theta}$, which yields the following: (a) a stability condition $\vec{M}_{local} \times \vec{H}_{eff} = 0$ at each point in the volume, which amounts to $\vec{M}_{local}(\vec{r})$ aligning with $\vec{H}_{eff}$ in every single volume element throughout the material, and (b) a boundary condition $\vec{M}_{local} \times \frac{\partial \vec{M}_{local}}{\partial n} = 0$ on the surface, which is a consequence of the fact that the magnitude of $\vec{M}_{local}(\vec{r})$ is fixed at the spontaneous magnetization value $M_s(T)$.

Brown's equations suffice under equilibrium conditions. However, the formalism also demands a description of how the system will approach equilibrium when beginning from a non-equilibrium situation, and how the magnetization will respond to a time-varying applied field.

The field $\vec{H}_{eff}$ exerts a torque on the local magnetization vector $\vec{M}_{local}$, which leads to the equation of motion

$$\frac{\partial \vec{M}_{local}}{\partial t} = \gamma_G \vec{M}_{local} \times \vec{H}_{eff}\,. \qquad (2.9)$$

Eq(2.9) predicts that the magnetization vector will precess around the local field $\vec{H}_{eff}$ under non-equilibrium conditions, and thus will never approach equilibrium in the absence of dissipation mechanisms.

Dissipation-driven relaxation to equilibrium can be described phenomenologically by [8,10,11]

$$\vec{H}_{\perp} - \alpha_G \frac{\partial \vec{M}_{local}}{\partial t} = 0, \tag{2.10}$$

where $\alpha_G > 0$ and $\vec{H}_{\perp}$ is the component of $\vec{H}_{eff}$ perpendicular to $\vec{M}_{local}$. Precession and dissipation can then be combined into a single equation known as Gilbert's equation [8,11]

$$\frac{\partial \vec{M}_{local}}{\partial t} = \gamma_G \vec{M}_{local} \times \left(\vec{H}_{eff} - \alpha_G \frac{\partial \vec{M}_{local}}{\partial t} \right) \tag{2.11}$$

or a mathematically equivalent form known as the Landau-Lifshitz Equation [12]

$$\frac{\partial \vec{M}_{local}}{\partial t} = \gamma_L \vec{M}_{local} \times \left(\vec{H}_{eff} - \alpha_L \vec{M}_{local} \times \vec{H}_{eff} \right). \tag{2.12}$$

The solution of Brown's equations shows that changes in the external field $\vec{H}_a$ distort the free energy hypersurface and will eventually cause the metastable

configuration $\vec{M}_{meta}(\text{all } \vec{r})$ in which the system is trapped to lose stability when the local energy minimum occupied by the system is transformed into a saddle point. The system then evolves rapidly toward a new metastable configuration corresponding to a new local minimum. This sudden evolution corresponds to a Barkhausen instability.

The rigour which characterizes the exploration of micromagnetism, although deeply satisfying on an intellectual level, introduces formidable complexity into the solving of fundamental problems, and requires a detailed knowledge of microstructural features of materials while also demanding large, involved computations whose temporal rendering quickly exceeds tolerable limits. In contrast to micromagnetic models, theoretical approaches like the Preisach model, to be introduced shortly in Chapter 4, adopt a much broader perspective and attempt to formulate a general, unified framework for the joint description of metastability and thermal activation which is based on the premise that all magnetizing processes may be reduced to a sequence of Barkhausen instabilities, and on general energy considerations which are independent of the microstructural details of a specific material, no matter how complex. To quote Bertotti [1] "The situation has some resemblance to classical thermodynamics where certain general conclusions about the existence of thermodynamic potentials are deduced from purely macroscopic properties of thermodynamics, leaving to statistical mechanics the task of providing explicit expressions for these potentials based on microscopic models."

2.1 References for Chapter 2

[1] G. Bertotti, *Hysteresis in Magnetism* (San Diego: Academic Press, 1998).

[2] S. Shtrikman and J.K. Galt, "Ferromagnetic Domain Theory," in *Solid State Physics*, Vol. 3, H. Eherenreich, F. Seitz, and D. Turnbull, eds. (New York: Academic Press, 1956), 437-564.

[3] M.E. Schabes, "Micromagnetic Theory of Non-Uniform Magnetization Processes in Magnetic Recording Particles," J. Magn. Magn. Mat. **95**, 249 (1991).

[4] J.G. Zhu, "Micromagnetics of Thin-Film Media," in C.D. Mee and E.D. Daniel, eds., *Magnetic Recording Technology* (New York: McGraw-Hill, 1990), 5.1-5.78.

[5] H. Kronmuller, "Micromagnetic Background of Hard Magnetic Materials," in G.J. Long and F. Grandjean, eds., *Superparamagnets, Hard Magnetic Materials* (Dordrecht: Kluwer, 1991), 461-498.

[6] T. Schrefl, "Micromagnetics of Thin Films and Multilayers," in G. Hadjipanayis, ed., *Magnetic Hysteresis in Novel Magnetic Materials* (Dordrecht: Kluwer, 1997), 49-68.

[7] A. Aharoni, *Introduction to the Theory of Ferromagnetism* (New York: Oxford University Press, 1996).

[8] W.F. Brown, Jr., *Magnetostatic Principles in Ferromagnetism* (Amsterdam: North-Holland, 1962).

[9] W.F. Brown, Jr., Micromagnetics (New York: Krieger, 1978).

[10] L.D. Landau and E.M. Lifshitz, *Statistical Physics, Part II* (Oxford: Pergamom Press, 1980).

[11] A.H. Morrish, *The Physical Principles of Magnetism* (New York: Wiley, 1965).

[12] J.C. Mallinson, "On Damped Gyromagnetic Precession," IEEE Trans. Magn. **23**, 2003 (1987).

Chapter 3: Mechanisms for Moment Reversal

3.1 Introduction

The magnetization process is the result of a change in the micromagnetic magnetization vector field $\vec{M}_{global}(\text{all } \vec{r})$ characterizing the magnetic state of the body, brought about by a change in the applied magnetic field $\vec{H}_a$. This process is very complex and involves a large number of degrees of freedom. A realistic strategy for attacking a problem of this complexity is to reduce the magnetizing process to a superposition of independent elementary degrees of freedom. This philosophy paves the way for the Preisach formalism to be discussed in the next chapter. In section 3.2 the elementary contributions will be "particles" (real or fictitious) which reverse their magnetization by coherent rotation. In section 3.3 the moment reversal mechanism is domain wall motion, and the elementary degree of freedom will be a small segment of wall surface.

3.2 Coherent Rotation (The Stoner-Wohlfarth Model)

The basic premise underlying the concept of coherent rotation [1,2] is that a single magnetization vector is sufficient to describe the state of the system. A magnetic particle small enough to favour a single domain configuration is the best example of a system that is magnetized by this process. The magnetization is uniform and independent of position

in space, as is the change in magnetization when the magnetization vector rotates under the action of an external field.

Imagine a small magnetic particle, with no domains. Its magnetization in any arbitrary direction is always completely saturated in a particular direction at the spontaneous value M_s, and thus it is sufficient to give the orientation of its magnetization vector $\vec{M}(\vec{r})$ when describing its state. The particle may display magnetic anisotropy as a result of magnetocrystalline or shape effects. For simplicity, we consider a spheroidal particle composed of a material with uniaxial magnetocrystalline anisotropy, and assume also that the symmetry axis of the spheroid and the crystal anisotropy axis coincide.

The behaviour of the particle is controlled by two energy terms: (a) the energy of interaction with the external field $E_{EXT} = -\mu_0 \vec{M}(\vec{r}) \cdot \vec{H}_a$ and (b) the uniaxial anisotropy energy [1] $F_{AN} = KV \sin^2 \theta$, where θ is the angle between $\vec{M}$ and the easy axis, and V is the particle volume. The anisotropy axis is an easy magnetization direction, so $K > 0$.

The free energy G_L of the particle is thus

$$G_L(\theta; \vec{H}_a) = V[K \sin^2 \theta - \mu_0 M H_a \cos(\theta - \theta_H)] \qquad (3.1)$$

where θ_H is the angle between $\vec{H}_a$ and the easy axis. By introducing the dimensionless quantities

$$g_L = \frac{G_L}{2KV}, \ \vec{h}_a = \frac{\mu_0 M_s}{2K} \vec{H}_a = \frac{\vec{H}_a}{H_{an}}, \ H_{an} = \frac{2K}{\mu_0 M_s} \ , \qquad (3.2)$$

as well as the components of the applied field perpendicular and parallel to the easy axis, $h_{\perp} = h_a \sin\theta_H$ and $h_{\parallel} = h_a \cos\theta_H$, the free energy of the particle becomes

$$g_L(\theta;\vec{h}_a) = \frac{1}{2}\sin^2\theta - h_{\perp}\sin\theta - h_{\parallel}\cos\theta . \qquad (3.3)$$

For small applied fields $\vec{h}_a$ around zero, the condition $\partial g_L / \partial\theta = 0$ yields two local minimum, one stable and one metastable, separated by an energy maximum, while, for sufficiently large fields, only one local minimum is available, in which $\vec{M}$ is closely aligned with the field. Discontinuous changes in the orientation of the magnetization occur when one minimum and one maximum merge to form an inflection point. In general, the excitation energy barrier which must be overcome to induce a transition depends on the angle θ and exhibits a complex dependence on applied field. The calculus of the energy barriers has been studied in detail in the literature [1-3]. By imposing the conditions $\partial g_L / \partial\theta = 0$ and $\partial^2 g_L / \partial\theta^2 = 0$ we arrive at the following parametric representation of the instability condition (bifurcation set) for Barkhausen jumps:

$$\begin{aligned} h_{\perp} &= \sin^3\theta \\ h_{\parallel} &= -\cos^3\theta \end{aligned} \qquad (3.4)$$

where θ represents the orientation of $\vec{M}$ with respect to the easy axis in the state which is losing stability.

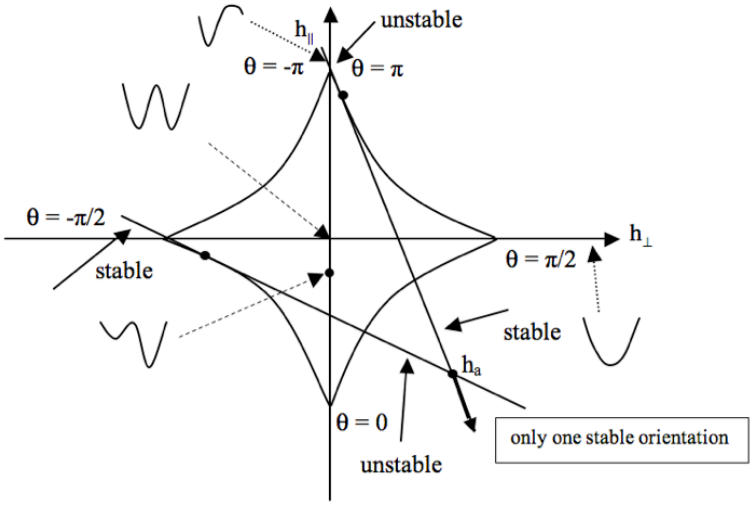

Figure 3.1 A Stoner-Wohlfarth astroid showing the free energy wells as a function of field. For applied fields outside the boundaries of the astroid, there exists only one stable orientation, while for applied fields inside the astroid, there are two solutions, one stable and one metastable.

The curve generated by the instability conditions Eq(3.4) when θ varies over the entire allowed interval (-π, π) is the astroid [4-7] shown in Figure 3.1. By eliminating θ from the instability conditions, the equation of the astroid can be written $h_{\perp}^{2/3} + h_{\parallel}^{2/3} = 1$. Outside the astroid, the system only has one state accessible to it; inside the astroid, two states are accessible, but the orientation realized depends on past history. The possible orientations of the moment $\vec{M}$ at each point are obtained by drawing tangent lines to the astroid which intersect with the field point. The possible states, one stable and one metastable, have magnetization vectors which lie parallel to the tangent lines, as shown in Figures 3.1 & 3.2.

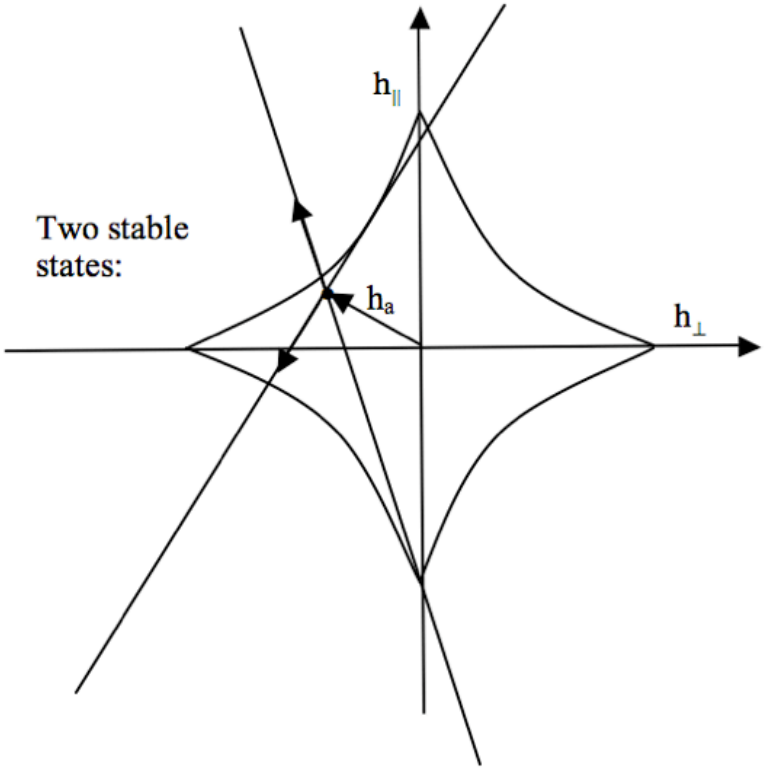

Figure 3.2 Determination of the two possible states for each applied field that exists within the boundaries of the astroid.

Tangent lines that are drawn through points where $-\pi < \theta < 0$ have stable orientations that point to the left, as shown in Figure 3.2, while tangent lines that are drawn through points where $0 < \theta < \pi$, have stable orientations that point to the right.

Figure 3.3 depicts the magnetization process applicable to the particular situation of a slowly varying, alternating magnetic field $\vec{h}_a$, but only shows the portion of the cycle for which the field intensity h_a increases from negative to positive values. The point representing the field slides back and forth along the fixed straight line. If the field oscillates with an amplitude such that the field point is contained inside the astroid, the magnetization simply oscillates around the initial occupied state, but insufficient field

energy is available to allow an instability point to form and thereby induce a transition from one state to another. However, when the field amplitude is large enough for the field point to cross the astroid boundary, the system responds in a qualitatively different way. At the moment the field point exits the astroid, the state occupied by the system loses stability and a Barkhausen jump takes place. By tracking the change in moment for a given value of θ_H under an alternating field of magnitude sufficient to cross the astroid, a hysteresis loop is obtained. Figure 3.4 below shows representative examples of these hysteresis loops for $0 \leq \theta_H \leq \pi/2$. In the special case of the field being exactly perpendicular to the anisotropy axis, i.e $\theta_H = \pi/2$, the hysteresis loop is closed (the response is perfectly reversible).

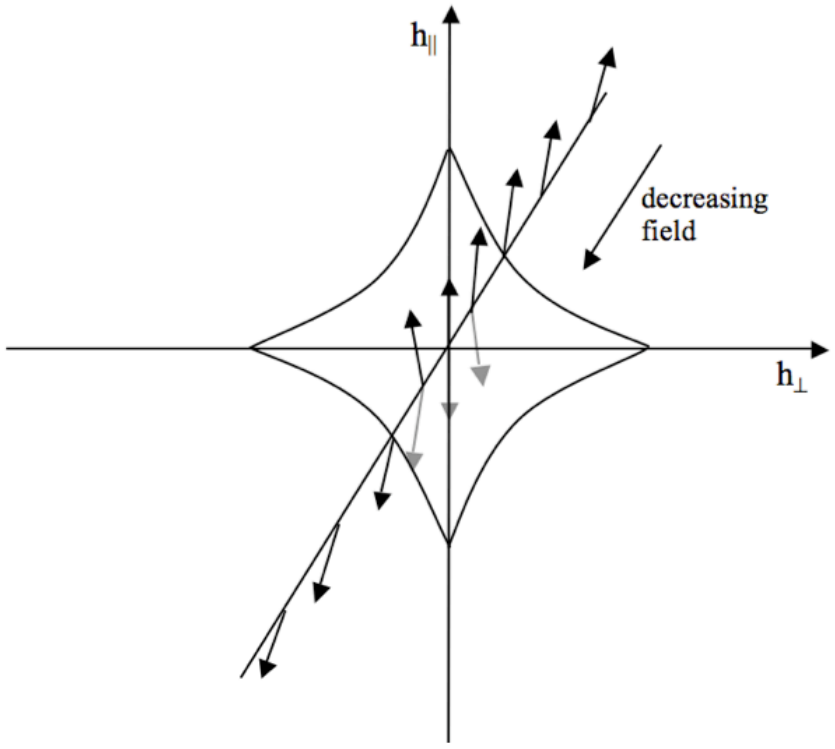

Figure 3.3 The magnetizing process for a changing magnetic field increasing in intensity from negative to positive values.

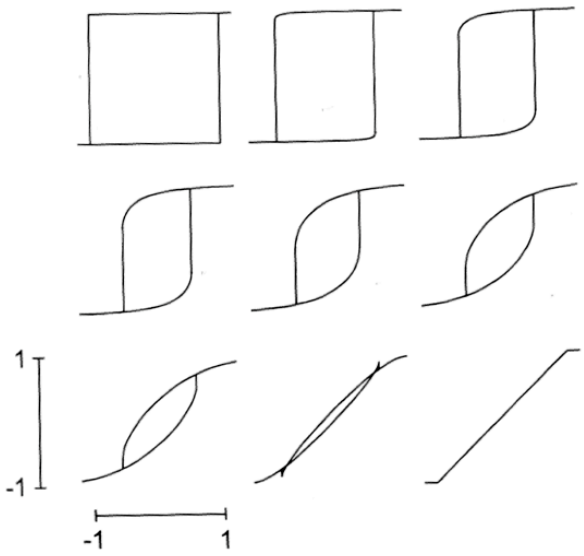

Figure 3.4 Hysteresis loops obtained from the Stoner-Wohlfarth astroid for various angles θ_H. *This figure was published in "Hysteresis in Magnetism" by Giorgio Bertotti, page 241.Copyright Academic Press. (1998). Reprinted with permission.*

3.3 Domain Walls

Attempts to image experimentally the magnetization vector field $\vec{M}(\vec{r})$ of bulk magnetic materials using optical techniques such as the Kerr effect and the Faraday effect, or electron beam deflection methods such as Lorentz microscopy, or magnetic probes such as the Bitter powder technique or magnetic force microscopy [8-12], show that the vector field appears to consist of relatively extensive regions of nearly uniform magnetization, called **domains**, separated by comparatively narrow interface layers known as **domain walls**. Over short spatial scales, exchange and anisotropy forces favour the parallel alignment of the atomic moments along a certain preferred direction to form a uniformly magnetized state. However, over large spatial scales, magnetostatic energy

becomes the dominant influence on the properties of the bulk magnetic structure, and favours a "fractured" configuration of numerous misaligned domains, over a single, uniformly magnetized configuration [4, 13-22].

To understand the reasons for this, recall that the magnetostatic field $\vec{H}_{mag}$ due to a magnetization vector field $\vec{M}(\vec{r})$ is equivalent to that produced by an effective volume pole density $\rho_m = -\vec{\nabla}\bullet\vec{M}$ and an effective surface pole density $\sigma_m = \vec{M}\bullet\hat{n}$, where $\hat{n}$ is the outward surface normal, and that the magnetostatic energy is proportional to the integral over all space of the square of the magnetostatic field $(H_{mag})^2$. The magnetostatic energy thus attains its absolute minimum when $\vec{H}_{mag}$ vanishes everywhere and, therefore, a low magnetostatic energy configuration is one where the magnetic pole densities ρ_m and σ_m are zero in as many locations as possible. This is known as the principle of *pole avoidance* [23]. Subdividing the material into misaligned magnetic domains reduces the pole density by placing positive and negative poles in close proximity, as illustrated in Figure 3.5 for the case of surface poles.

In principle, the micromagnetic approach can be used to explain the existence of domains and to predict the domain structures observed in real materials [12] by solving Brown's equations for the complete set of local minima corresponding to the metastable states available to the system. For a given field, there are as many domain structures as there are metastable states, that is, solutions to Brown's equations. In most situations, however, the problem is intractable due to the mathematical complexity of the procedure, and also due to the fact that structural disorder dominates the behaviour of real materials.

Domain theory is an attempt to reduce the micromagnetic formulation of the problem to a more tractable form. Domain theory postulates that it is possible to distinguish a sharp demarcation between the large regions where the magnitude and orientation of the magnetization is nearly uniform (domains) and the narrow interface layers where the magnetization changes rapidly from one orientation to another (domain walls). The atomic spins within the domain wall are misaligned with each other and with the easy direction and, consequently, the formation of domain walls costs both exchange and anisotropy energy. Furthermore, by neglecting the thickness of the wall, the wall becomes a two-dimensional surface with surface tension, thus significantly reducing the complexity of the original three-dimensional problem.

For classification purposes, domain walls are generally described in terms of the direction of the magnetization in neighbouring domains separated by the wall. For example, when the wall separates domains of opposite magnetization, it is called a 180-degree domain wall. For the special case of a 180-degree wall geometry and uniaxial anisotropy, a micromagnetic analysis [24] for a simple system in which the magnetization only changes direction along an axis perpendicular to the easy axis, and remains either parallel or anti-parallel to the easy axis, shows that complete magnetization reversal takes place in a spatial interval of $\delta_w = \pi\sqrt{\frac{A}{K_1}}$, which is generally taken to be a measure of the wall thickness. The total energy per unit surface γ_w stored in the domain wall (found by integrating the energy density g_L over all x) is given by $\gamma_W = 4\sqrt{AK_1}$, and amounts to the exchange and anisotropy energies densities being of the same order of magnitude inside the wall.

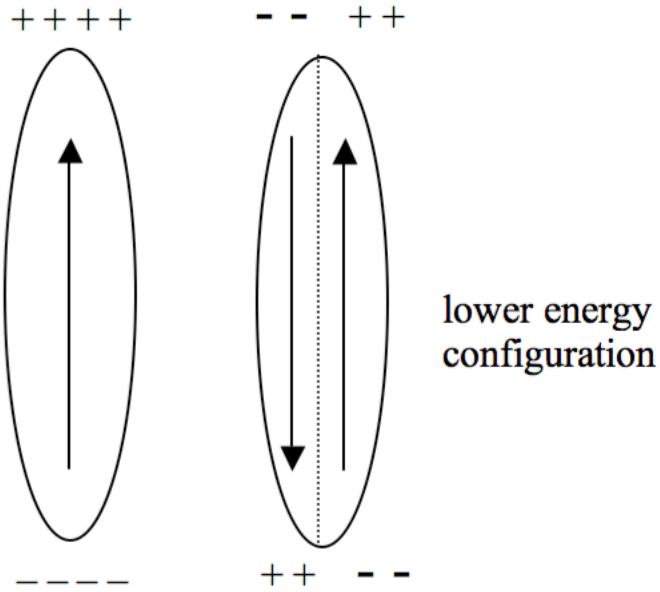

Figure 3.5 The reduction of magnetostatic energy that follows the formation of a domain.

3.4 Domain Wall Dynamics

If we neglect their finite thickness and internal structure, domain walls can be conceived of as geometrical surfaces which extend throughout the volume of a sample of magnetic material in an interconnected network, which evolves in response to changes in the external field through a random sequence of spatially localized deformations, each of which corresponds to a small fragment of the domain wall surface being displaced discontinuously and irreversibly from one location to another.

The equations that govern domain wall dynamics [1, 25-27] are identical to those in section 1.3, which describe the approach to equilibrium of any system that relaxes through a sequence of nonequilibrium thermodynamic states represented by a Landau

free energy $G_L(X;H,T) = F(X,T) - HX$, where X is some appropriate internal degree of freedom or state variable. As previously noted, equilibrium corresponds to a balance between the external field H_a and dF/dX, a gradient describing internal mechanisms:

$$dG_L/dX = H_a - dF/dX = 0 \tag{3.5}$$

If the system is not initially in equilibrium, X will change with time at a rate dX/dt which depends on dG_L/dX. However, sufficiently close to equilibrium, dX/dt may be expanded in powers of dG_L/dX and truncating the expansion after the first order term yields:

$$\gamma \frac{dX}{dt} = -\frac{\partial G_L}{\partial X} \tag{3.6}$$

where γ is a positive friction constant. The equality above is equivalent to stating that the velocity is proportional to the force, and hence the change in X with time is controlled by a viscous-like mechanism. Substituting for dG_L/dX from Eq(3.5) yields

$$\gamma \frac{dX}{dt} = H_a(t) - \frac{\partial F}{\partial X} = H_a(t) - H_F(X) \tag{3.7}$$

where $H_F(X) = dF/dX$ is an internal field. In the case of domain wall motion, the internal degree of freedom X is the position of the wall, or equivalently, the magnetic flux ϕ through the cross sectional area in which the magnetization reversal is taking place.

The free energy F is a function of the position X of the moving wall for two reasons. (a) The effect of the spatial variation of magnetostatic energy is intrinsically a nonlocal effect, and thus may give rise to a complex dependence of the system energy on wall position despite the apparent homogeneity of the medium surrounding a domain wall. (b) Structural disorder gives rise to spatial variations in the parameters used to describe the micromagnetic free energy, and hence introduces a spatial dependence into the exchange and anisotropy energy stored in the domain wall. As a consequence, H_F will contain two distinct contributions, a large-scale contribution, related primarily to magnetostatic effects, and a short-scale contribution, related to structural disorder. If the large-scale contribution to the free energy is approximated by a parabolic potential well, $F(X) = AX^2$, then

$$H_F(X) = 2AX + H_p(X). \tag{3.8}$$

The field $H_p(X)$ describes the random energy fluctuations around the large-scale curve and is called the pinning field.

To solve the domain wall equation of motion (Eq(3.7)) it is usual to express it as a pair of coupled equations in X and H_a as follows:

$$\gamma \frac{dX}{dt} = H_a - H_F(X)$$
$$\frac{dH_a}{dt} = r(t) \qquad (3.9)$$

where r(t) is the rate of change of the input field. If we further assume that the field H_a changes at a fixed rate r(t) = c, independent of time, then we can eliminate t from these two equations to obtain the differential equation for the trajectory $H_a(X)$ which the system follows in response to its free energy gradient $H_F(X)$:

$$\frac{1}{\gamma}\frac{dH_a}{dX} = \frac{c}{H_a - H_F(X)}. \qquad (3.10)$$

For a simple bistable system with a double well free energy $F(X) = X^4 - 2aX^2$, $H_F(X) = \partial F/\partial X = 4X^3 - 4aX$, and a phase portrait of domain wall motion can be obtained from Eq(3.10), where the possible trajectories in the (X,H_a) plane are plotted for a fixed, time-independent field change such as the one described. Each point in the (X,H_a) plane has only one possible trajectory passing through it (Figure 3.6).

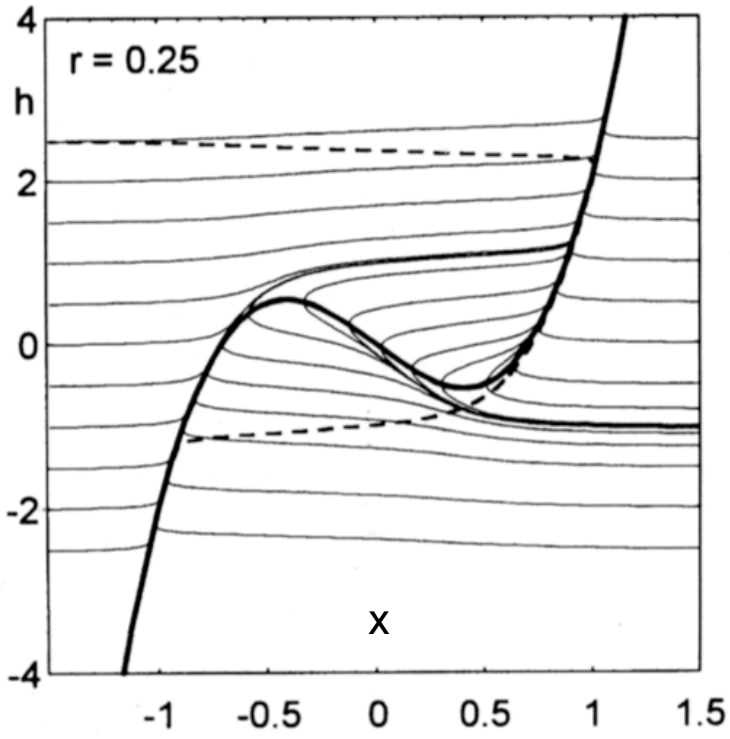

Figure 3.6 The phase portrait of domain wall motion from (3.10) for a field rate of r = 0.25. *This figure was published in "Hysteresis in Magnetism" by Giorgio Bertotti, page 58. Copyright Academic Press (1998). Reprinted with permission.*

If $c > 0$, then in the limit $c \to 0$, a possible solution of Eq(3.10) is $H_a \cong H_F(X)$ and $dH_a/dX \cong dH_F/dX$, provided that $dH_F/dX > 0$. Thus, H_a tracks $H_F(X)$. In those regions where $dH_F/dX < 0$, we simply set $dH_a/dX \cong 0$, whatever the value of $H_a - H_F(X)$. This is where a Barkhausen jump takes place. Thus, one obtains a trajectory made up of the stable branches of $H_F(X)$, joined by horizontal segments where Barkhausen jumps occur. This trajectory is shown as the dotted line in the Figure 3.7.

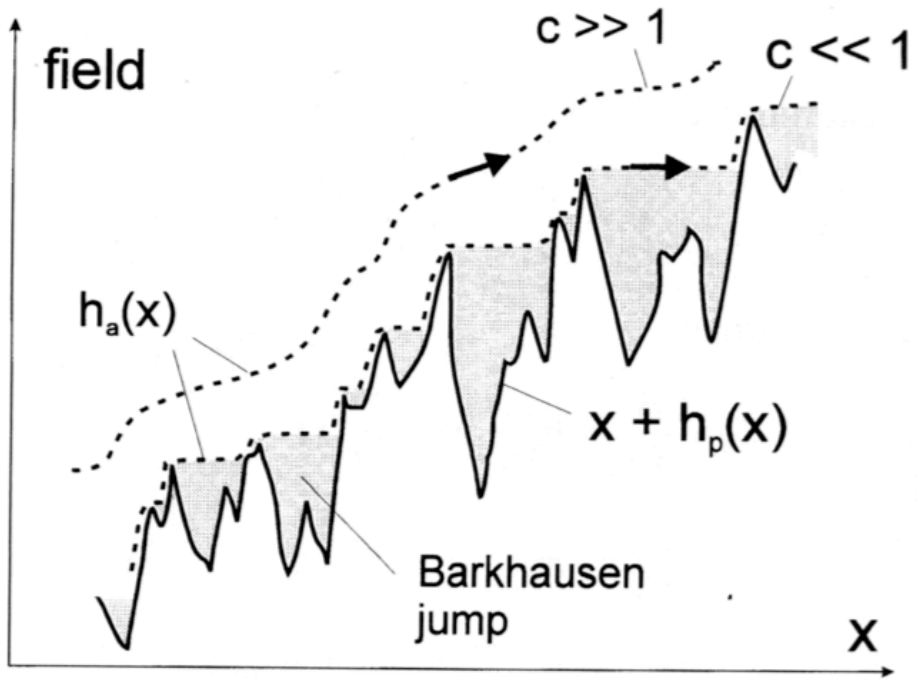

Figure 3.7 Phase portrait of domain wall motion for $c \rightarrow 0$. The Barkhausen jumps occur in those regions where $dh/dx \sim 0$. *This figure was published in "Hysteresis in Magnetism" by Giorgio Bertotti, page 272. Copyright Academic Press (1998). Reprinted with permission.*

The Barkhausen effect is evidence for the existence of domains, and can be observed aurally. For instance, by subjecting a magnetic specimen to a smoothly increasing field, the Barkhausen effect can be 'heard' with an amplifier and a loudspeaker connected to a magnetic search coil wrapped around the specimen. The speaker emits a crackling noise no matter how smoothly the field is changed, and it is this crackling that is indicative of abrupt changes in the magnetic moment as the field is changed [28].

An interesting application of the bistable double-well phase portrait shown in Figure 3.6 appears in a model, due to Zeeman [29], of the heart beat.

In Zeeman's model, there exists a state corresponding to relaxation of the heart muscle (diastole), a threshold that allows the triggering of an electrochemical wave which

forces a contraction of the heart muscle (systole), followed by an efficient and quick return to diastole. Completing the whole cycle results in a hysteresis loop, shown in Figure 3.8.

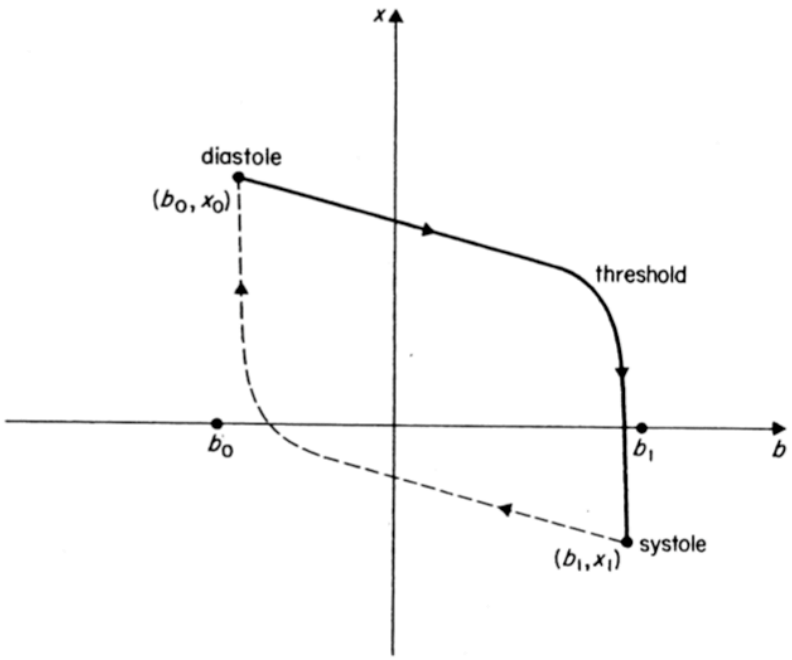

Figure 3.8 A hysteresis loop that describes the heartbeat cycle as it relaxes (diastole) and contracts (systole). *Reproduced with permission of Taylor & Francis Group LLC, from "Differential Equations and Mathematical Biology" by D.S. Jones and B.D. Sleeman, Copyright 1983; permission conveyed through Copyright Clearance Center, Inc.*

If the control variable is the electrical potential b (analogous to the role of the magnetic field H_a in magnetic systems) and the state variable is the muscle fibre length x (measured relative to a relaxed fibre of a length x_0 and analogous to the role of the magnetic moment in magnetic systems), then the coupled differential equations that are employed in Zeeman's model of the heartbeat are:

$$\begin{aligned} \varepsilon \frac{dx}{dt} &= -(x^3 - Tx + b) \\ \frac{db}{dt} &= x - x_0 \end{aligned} \tag{3.11}$$

where ε allows a rapid initial decrease/increase of the fibre length during the approach to systole/diastole, and the chemical control changes at a rate proportional to the muscle fibre extension.

Figure 3.9 shows the phase portrait of the dynamics of the coupled equations in Eq(3.11). As is, the flow along AB corresponds to the descending branch of the hysteresis loop, and represents the switch from diastole to systole, but CD does not represent a return to the diastolic state. To satisfy the requirement of a rapid return to equilibrium, an additional control variable, u, must be imposed to close the trajectory:

$$\begin{aligned} \varepsilon \frac{dx}{dt} &= -(x^3 - Tx + b) \\ \frac{db}{dt} &= x - x_0 + (x_0 - x_1)u \end{aligned} \tag{3.12}$$

Figure 3.10 shows the phase portrait that incorporates the additional control variable.

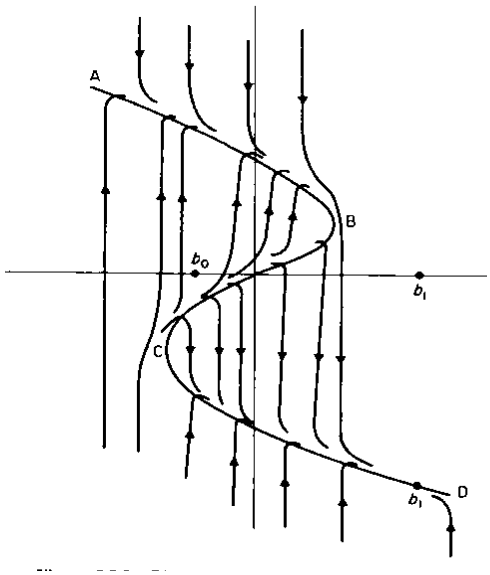

Figure 3.9 The phase portrait of a beating heart whose dynamics are described by Eq(3.11). Notice that the branch CD does not represent a return to the diastolic state. *Reproduced with permission of Taylor & Francis Group LLC, from "Differential Equations and Mathematical Biology" by D.S. Jones and B.D. Sleeman, Copyright 1983; permission conveyed through Copyright Clearance Center, Inc.*

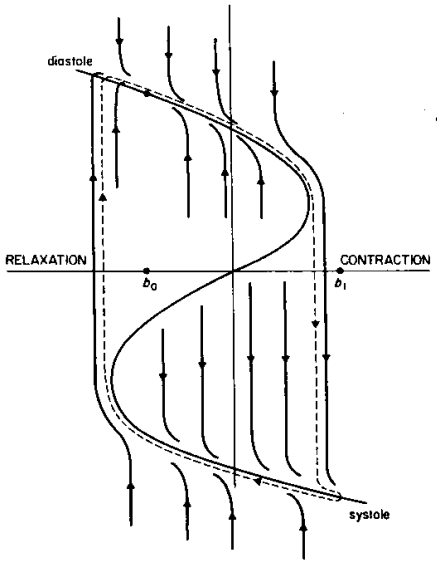

Figure 3.10. The phase portrait of a beating heart whose dynamics are described by Eq(3.12). Notice that with the addition of the control variable u, a repeating cycle can be observed, as required for a rapid return to equilibrium (diastole) from systole. *Reproduced with permission of Taylor & Francis Group LLC, from "Differential Equations and Mathematical Biology" by D.S. Jones and B.D. Sleeman, Copyright 1983; permission conveyed through Copyright Clearance Center, Inc.*

3.5 References for Chapter 3

[1] G. Bertotti, *Hysteresis in Magnetism* (San Diego: Academic Press, 1998).

[2] E.C. Stoner and E.P. Wohlfarth, "A Mechanism of Magnetic Hysteresis in Heterogeneous Alloys," Phil. Trans. Roy. Soc. A **240**, 599 (1948).

[3] Stancu, A, "Temperature and Time-Dependent Preisach Model for a Stoner-Wohlfarth Particle System," IEEE Trans. Mag. **34**, 3867 (1998).

[4] L.D. Landau and E.M. Lifshitz, *Electrodynamics of Continous Media*, 2nd Edition (Oxford: Pergamom Press, 1989).

[5] I.D. Mayergoyz, *Mathematical Models of Hysteresis* (New York: Springer-Verlag, 1991).

[6] M. Prutton, *Thin Ferromagnetic Films* (London: Butterworths, 1964).

[7] E.W. Lee and J.E.L. Bishop, "Magnetic Behavior of Single-Domain Particles," Proc. Phys. Soc. **89**, 661 (1966).

[8] G. Hadjipanayis, "Microstructure and Magnetic Domains," in J.M.D. Coey, ed., Rare-earth Iron Permanent Magnets (Oxford: Oxford University Press, 1996), 287-335.

[9] J.N. Chapman and K.J. Kirk, "Imaging Magnetic Structures in the Transmission Electron Microscope," in G. Hadjipanayis, ed., *Magnetic Hysteresis in Novel Magnetic Materials* (Dordrecht: Kluwer, 1997), 195-206.

[10] J.N. Chapman and K.J. Kirk, "Domains, Domain Walls and the Magnetization Reversal Process," in G. Hadjipanayis, ed., *Magnetic Hysteresis in Novel Magnetic Materials* (Dordrecht: Kluwer, 1997), 207-214.

[11] A. Tonomura, "Applications of Electron Holography," Rev. Mod. Phys. **59**, 639 (1987).

[12] M.R. Scheinfein, J. Unguris, J.L. Blue, K.J. Coakley, D.T. Pierce, R.J. Celotta, and P.J. Ryan, "Micromagnetics of Domain Walls at Surfaces," Phys. Rev. B **43**, 3395 (1991).

[13] C. Kittel, "Physical Theory of Ferromagnetic Domains," Rev. Mod. Phys. **21**, 541 (1949).

[14] C. Kittel and J.K. Galt, "Ferromagnetic Domain Theory," in Solid State Physics, Vol. 3, H. Eherenreich, F. Seitz, and D. Turnbull, eds. (New York: Academic Press, 1956), 437-564.

[15] J.F. Dillon, Jr., "Domains and Domain Walls," in G.T. Rado and H. Suhl, eds., *Magnetism, Vol. III* (New York: Academic Press, 1963-1973), 415-464.

[16] A. Aharoni, *Introduction to the Theory of Ferromagnetism* (New York: Oxford University Press, 1996).

[17] J.A.C. Bland and B. Heinrich, eds., *Ultrathin Magnetic Structures* (Berlin: Springer-Verlag, 1994).

[18] S. Chikazumi, *Physics of Magnetism* (New York: Wiley, 1964).

[19] D.J. Craik and R.S. Tebble, *Ferromagnetism and Ferromagnetic Domains* (Amsterdam: North-Holland, 1965).

[20] A.H. Eschenfelder, *Magnetic Bubble Technology* (Berlin: Springer-Verlag, 1981).

[21] M. Malozemoff and J.C. Slonczewski, *Magnetic Domain Walls in Bubble Materials* (New York: Academic Press, 1979).

[22] A. Hubert, *Theorie des Domänenwände in Geordenet Medien* (Berlin: Springer-Verlag, 1974) (in German).

[23] A. Hubert, "Stray-Field-Free Magnetization Configurations," Phys. Stat. Sol. **32**, 519 (1969); "Stray-Field-Free and Related Domain Wall Configurations in Thin Magnetic Films," Phys. Stat. Sol. **38**, 699 (1970).

[24] J. Miltat, "Domains and Domain Walls in Soft Magnetic Materials, Mostly," in R. Gerber, C.D. Wright, and G. Asti, eds., *Applied Magnetism* (Dordrecht: Kluwer, 1993), 221-308.

[25] J. Hale and H. Kocak, *Dynamics and Bifurcations* (New York: Springer-Verlag, 1991).

[26] J.P. Bouchaud and A. Georges, "Anomalous Diffusion in Disordered Media: Statistical Mechanisms, Models and Physical Applications," Phys. Rep. **195**, 127 (1990).

[27] G. Durin, A. Magni, and G. Bertotti, “Fractals, Scaling, and the Question of Self-Organized Criticality in Magnetization Processes,” Fractals **3**, 351 (1995).

[28] B.D. Cullity, *Introduction to Magnetic Materials*, (Reading, MA: Addison-Wesley), 1972.

[29] E. C. Zeeman, “Differential equations for the heartbeat and nerve impulse,” Dynamical systems (Proc. Sympos., Univ. Bahia, Salvador, 1971), 683-741, Academic Press, 1973.

Chapter 4: The Preisach Model

4.1 Introduction

The notion of constructing a generic hysteretic system from the superposition of many bistable elements is inevitably associated with the name of Ferenc Preisach [1], who introduced this notion into the literature in 1935 and who provided an elegant and illuminating graphical representation. Over the past several decades, the Preisach formalism has blossomed into a general mathematical and physical framework for the description of nonequilibrium phenomena in a variety of materials, including ferromagnets, fine magnetic grains, spin glasses, minerals, type II superconductors, amorphous glasses, rubber, and polymers below the vitreous transition, and composite materials [2-29]. The Preisach formalism is based on the premise that every magnetization process can be reduced to a sequence of Barkhausen events. Each such event is inherently bistable, in the sense that it corresponds to the system leaving one metastable state in favour of another metastable state of lower free energy, and each involves two characteristic energies, the free energy difference ΔF between the initial and final states, and the energy ΔE dissipated as heat during the event.

The working hypothesis is that the probability distribution $p(\Delta F, \Delta E)$ of characteristic energies exists and is an intrinsic property of any given material, prescribable in advance and independent of the specific field history to be imposed on the material. The

fundamental building block of the formalism is a one-dimensional, double well potential in a two-state configuration space, as shown in Figure 4.1. The state variable m may assume three possible values $m = \pm \mu$, and $m = 0$, where μ is a characteristic moment reversal associated with a single Barkhausen event, and the free energy F(m) is characterized by two energy levels $F(m = \pm\mu) = \pm \mu H_s$, separated by an energy maximum $F(m = 0) = \mu H_d$, where H_s and H_d are equivalent fields.

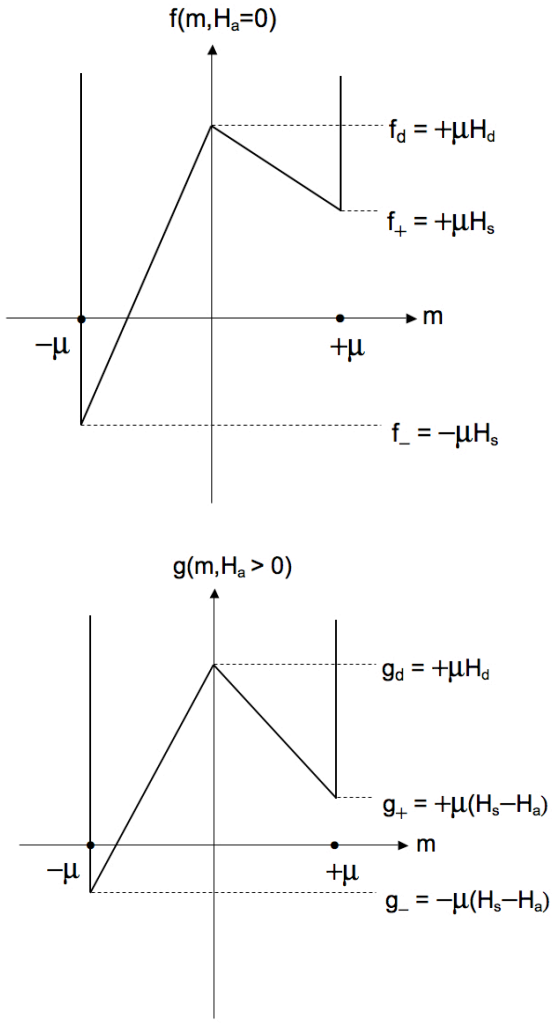

Figure 4.1: An elementary Preisach double-well potential in zero applied field (top). An elementary Preisach double-well potential in an applied field H_a (bottom).

Each elementary bistable unit is coupled linearly to the applied field H_a and its stability is controlled by the Gibbs free energy $G(m,H_a) = F(m)-mH_a$. When $H_a \geq H_s+H_d$, G exhibits only one local minimum at $m = +\mu$. Similarly, when $H_a \leq H_s - H_d$, only $m = -\mu$ is a minimum. In the intermediate case where $H_s - H_d < H_a < H_s + H_d$, G exhibits two local minima, one stable and one metastable.

4.2 The Preisach Plane

These stability conditions may be summarized conveniently in a graphical form using the Preisach plane, shown in Figure 4.2, defined by the rectangular coordinate axes H_d and H_s. Each Preisach element is located by its representative point with coordinates (H_d, H_s). The stability conditions partition the Preisach plane into three regions. All Preisach subsystems in region I are definitely in their $-\mu$ state, and all subsystems in region III are definitely in their $+\mu$ state. In region II, both states $+\mu$ and $-\mu$ are available. In principle, any subdivision of region II into $+\mu$ and $-\mu$ subregions is an acceptable metastable state for the system. However, in practice, we are concerned primarily with those subdivisions which have been created by a specific history of field applications and reversals.

In fact, any arbitrary field history starting at positive or negative saturation and ending with the field value H_a will partition the Preisach plane into only one $+\mu$ and one $-\mu$ region separated by a state line $C(H_d)$ which originates from the point ($H_d = 0$, $H_s = +H_a$) and consists of a chain of linear segments of alternating slope $dR/dH_d = +1$ and

$dR/dH_d = -1$ as shown in Figure 4.3. The shape of the state line $C(H_d)$ depends only on the sequence of field reversal points.

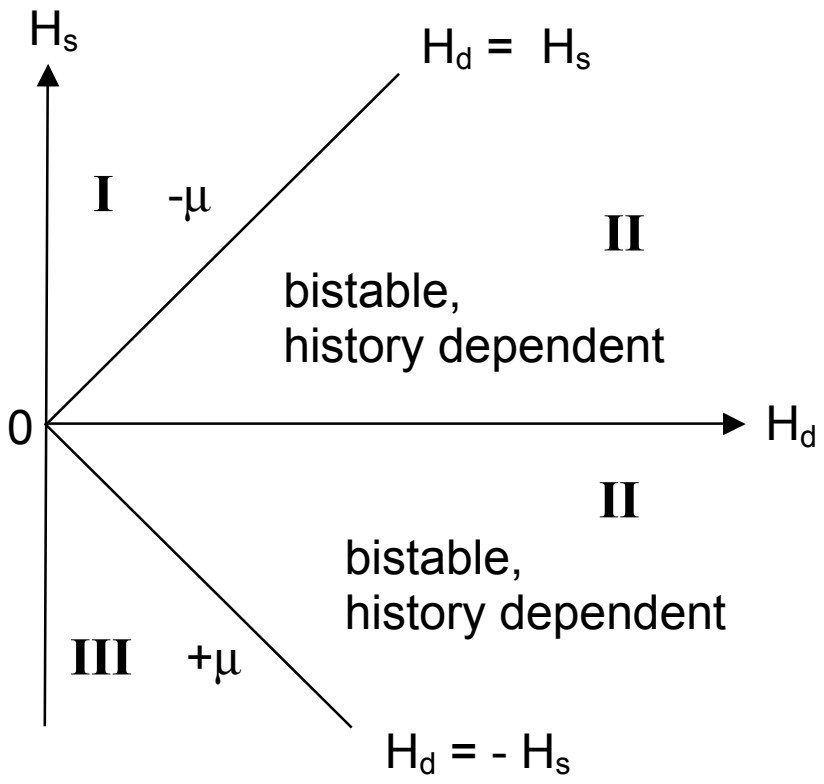

Figure 4.2: The Preisach plane in zero applied field. The stability conditions partition the plane into the three regions (I, II, III) illustrated above.

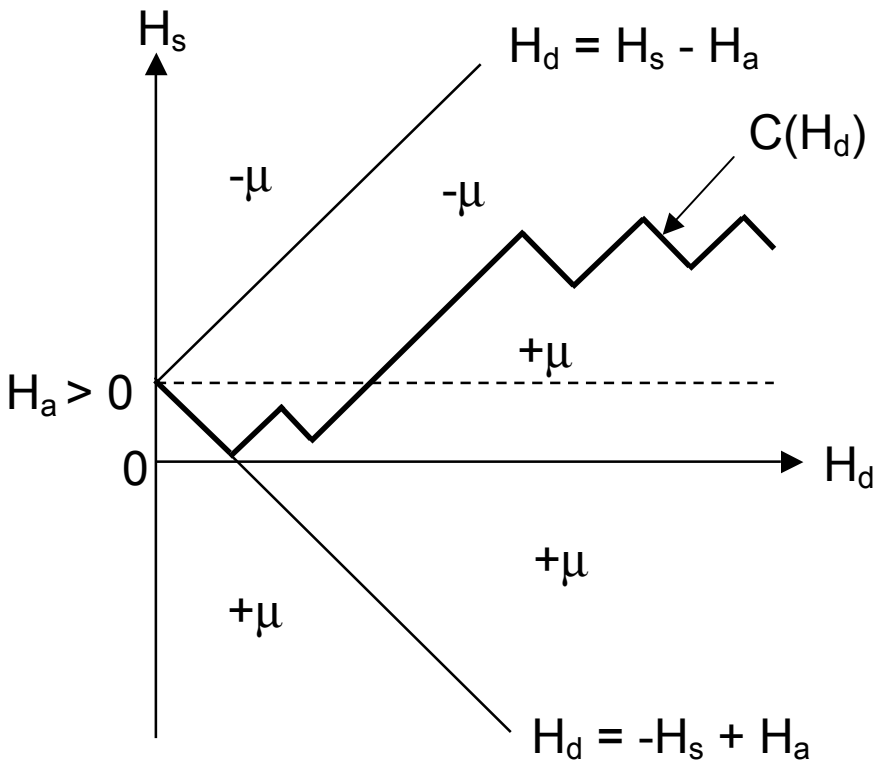

Figure 4.3: The Preisach configuration for an arbitrary field history starting at positive or negative saturation and ending at $H_a > 0$.

When a Barkhausen jump occurs, the free energy F changes by $|\Delta F| = 2\mu H_s$, while the Gibbs free energy suddenly decreases by $|\Delta G| = -\mu H_d$ and this energy is dissipated as heat. The characteristic field coordinates H_d and H_s of a Barkhausen element thus measure energy dissipated versus energy stored, respectively.

The response of each elementary bistable subsystem to a cyclic field sweep from $H_a = +\infty$ to $H_a = -\infty$ and back to $H_a = +\infty$ is thus the rectangular hysteresis loop shown in Figure 4.4. The loop width and loop asymmetry vary with the field coordinates (H_d,H_s). In principle, the loop height $\mu(H_d,H_s)$ may also vary from unit to unit.

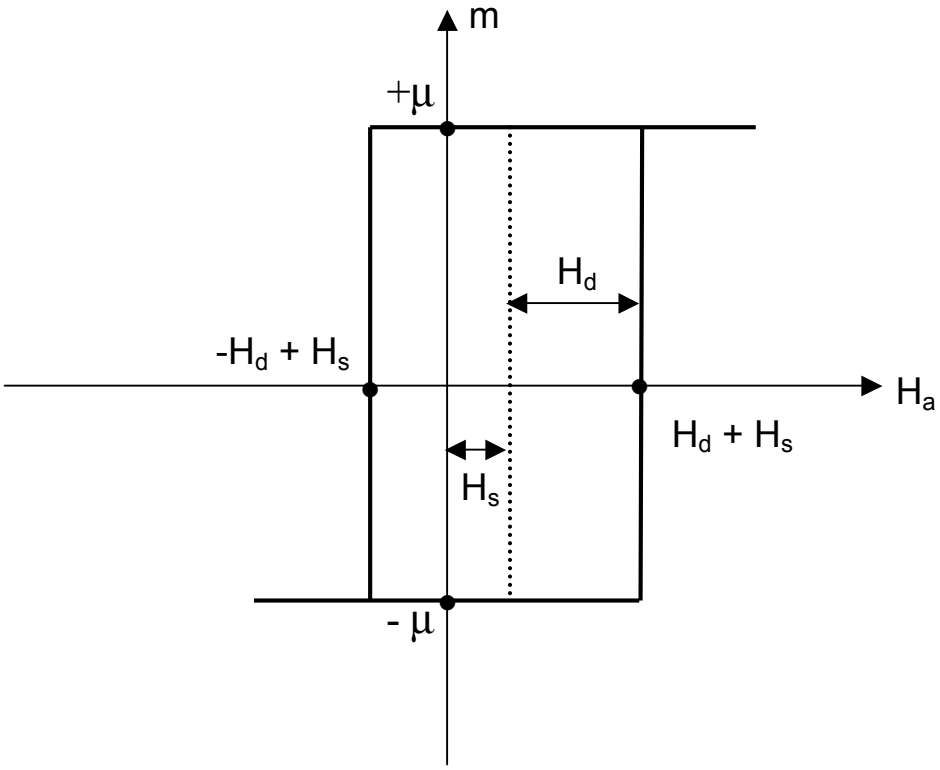

Figure 4.4: An elementary Preisach hysteresis loop.

4.3 Collections of Preisach Elements

Suppose that $n(H_d,H_s)$ is the density of Preisach elements normalized as

$$\int_0^{\infty} dH_d \int_{-\infty}^{\infty} dH_s n(H_d, H_s) = N$$

where N is the total number of Preisach elements. The total moment M in a state defined by a particular partition of the Preisach plane is then given by the weighted sum:

$$M = \int_0^{\infty} dH_d \int_{-\infty}^{\infty} dH_s \left[\pm\mu(H_d, H_s)\right]_{\text{partition}} n(H_d, H_s) \tag{4.1}$$

where the choice of $\pm\mu$ in the integrand depends on the specific process and partition.

Since the combination $\mu(H_d,H_s)n(H_d,H_s)$ appears only as a product in the integrand, it is usual to define an average subsystem moment $\bar{\mu}$ as

$$\bar{\mu} = \frac{1}{N} \int_0^{\infty} dH_d \int_{-\infty}^{+\infty} dH_s \mu(H_d, H_s) n(H_d, H_s) \tag{4.2}$$

and to define the Preisach density $p(H_d,H_s)$ as the fractional contribution of subsystems of type (H_d,H_s) to the saturation moment $M_{sat}=N\bar{\mu}$ as follows

$$p(H_d, H_s) = \frac{\mu(H_d, H_s) n(H_d, H_s)}{N\bar{\mu}} \tag{4.3}$$

normalized to unity:

$$\int_0^{\infty} dH_d \int_{-\infty}^{\infty} dH_s p(H_d, H_s) = 1 \tag{4.4}$$

in which case the total moment becomes:

$$M = \int_0^{\infty} dH_d \int_{-\infty}^{\infty} dH_s (\pm 1)_{\text{partition}} p(H_d, H_s)\,. \tag{4.5}$$

The Preisach distribution has the following general properties:

a. If, for any generic field-moment history $[H_a(t),M(t)]$, inversion to $[-H_a(t), -M(t)]$ also yields an admissible history, then the Preisach density $p(H_d,H_s)$ must be an even function of H_s:

$$p(H_d, H_s) = p(H_d, -H_s)$$

b. The Preisach description is substantially simplified if the Preisach density is factorizable. Two factorizations are compatible with the even symmetry with respect to H_s:

$$p(H_d, H_s) = f(H_d - H_s)g(H_d + H_s) \text{ and } p(H_d, H_s) = f(H_d)g(H_s)$$

where $g(H_s)$ is an even function of H_s.

The exchange, anisotropy, and magnetostatic energies which ultimately determine the energies of the metastable states, and hence the energy profiles of individual Preisach elements, depend explicitly on temperature. As a consequence, the Preisach distribution is also expected to be temperature-dependent. Furthermore, the entire Preisach distribution should collectively collapse into a delta-function $p(H_d, H_s) \to \delta(H_d)\delta(H_s)$ as the temperature T approaches the critical temperature T_C above which the material cannot sustain a spontaneously ordered magnetic configuration.

4.4 Energy Considerations

If we focus only on the fine-scale metastable state structure responsible for hysteresis, which is encoded at the level of the individual Preisach elements, and ignore large-scale

mean field effects which are expressible as a function of the total system moment M and the temperature T, and which describe the influence on a given elementary Preisach unit of the rest of the system taken as a whole, then the minimum free energy F_{min} will occur when all Preisach units are in their individual ground states with free energies $f = -\mu|H_s|$. It is natural to measure the free energy F of an arbitrary metastable configuration of the Preisach plane with state line $C(H_d)$, such as that shown in Figure 4.3, relative to F_{min}. It then follows that F will be given by the increase in free energy of those Preisach elements between $H_s = 0$ and $H_s = C(H_d)$ which have been trapped in their higher energy metastable minimum. For each such element $\Delta f = +2\bar{\mu}|H_s|$, and the total change in free energy is given by

$$F = N\int_0^{\infty} dH_d \int_0^{C(H_d)} dH_s \left(2\bar{\mu}|H_s|\right) p\left(H_d, H_s\right) = 2M_{sat} \int_0^{C(H_d)} dH_s H_s p\left(H_d, H_s\right). \qquad (4.6)$$

It follows that the Gibbs free energy G of this metastable configuration is given by

$$G = 2M_{sat}\int_0^{\infty} dH_d \int_0^{C(H_d)} dH_s (H_s + H_a) p(H_d, H_s). \qquad (4.7)$$

To find the state of minimum free energy G_{min}, we must calculate the variation δG in G when the state line $C(H_d)$ is varied infinitesimally by $\delta C(H_d)$, and then set $\delta G = 0$:

$$\delta G = 2M_{sat}\int_0^{\infty} dH_d \left[C(H_d) + H_a\right] \delta C(H_d) p\left(H_d, C(H_d)\right) = 0 \qquad (4.8)$$

which yields

$$C_{eq}(H_d) = -H_a . \tag{4.9}$$

Thus, in the absence of mean field effects, the equilibrium state line is a horizontal line at $H_s = -H_a$.

4.5 Properties of Preisach Magnetization Curves

Due to its internal mathematical structure, the magnetization curves predicted by the Preisach model exhibit two properties, independent of the details of their shape: return-point-memory and congruency.

Return-Point-Memory: If a Preisach system is brought from saturation to a field H_1 and then subjected to a field reversal from H_1 to H_2 followed by another field reversal back to H_1, then the original H_1 state line is restored exactly, and the system loses all memory of the intermediate field oscillation. (See Figure 4.5.)

Congruency: If, starting from saturation, a Preisach system is subjected to an arbitrary sequence of field reversals which eventually terminate in a minor loop defined by the field cycle $H_1 \rightarrow H_2 \rightarrow H_1$, then any other field history which starts at saturation and terminates in the same field cycle will produce a minor loop which is geometrically congruent to the first minor loop. (Figure 4.6)

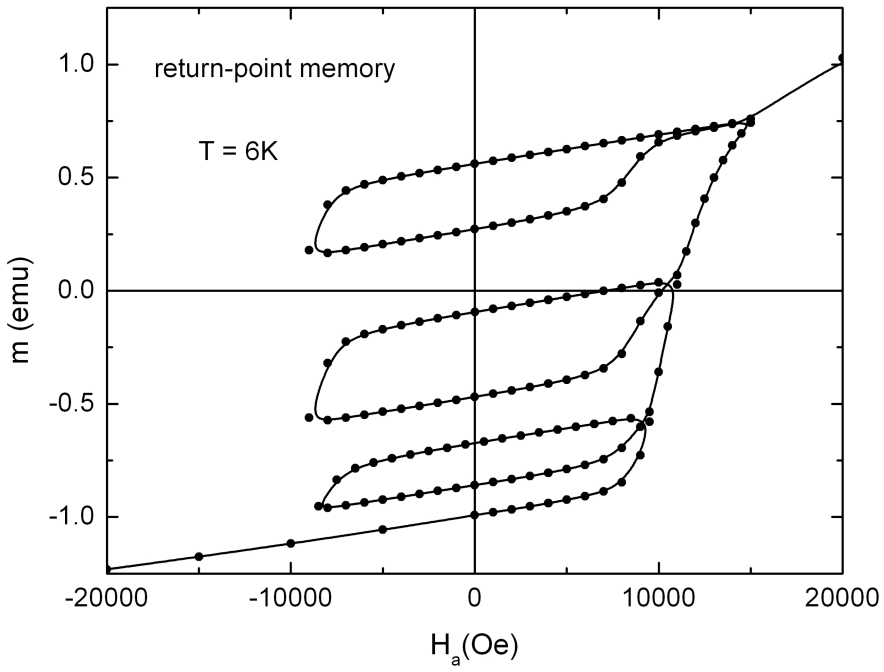

Figure 4.5: An experimental illustration of return-point memory, as measured at T = 6K on a ferromagnetic ruthenate, $Ca_{0.4}Sr_{0.6}RuO_3$.

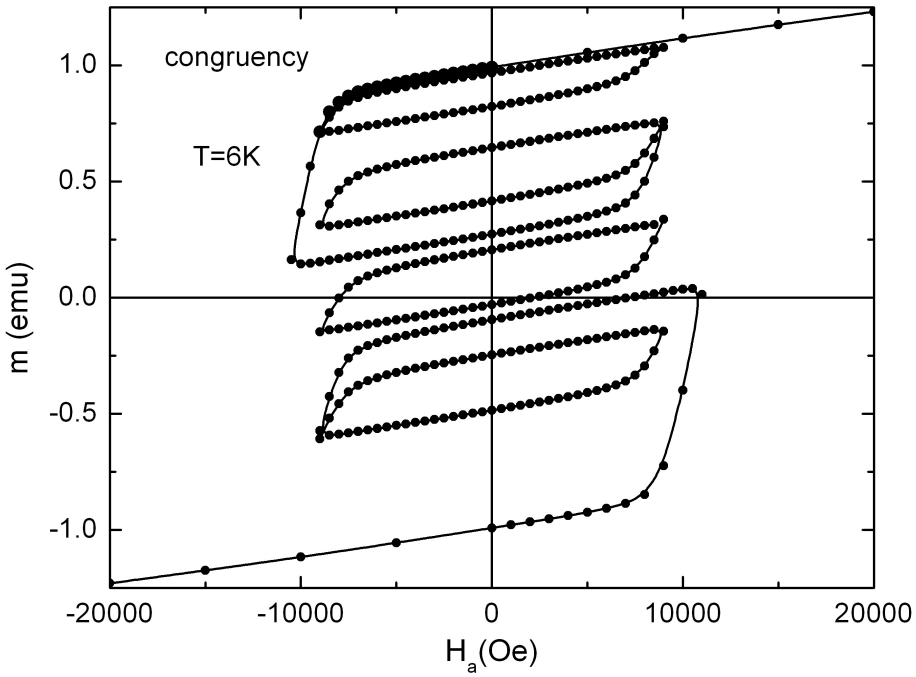

Figure 4.6: An experimental illustration of congruency, as measured at T = 6K on a ferromagnetic ruthenate, $Ca_{0.4}Sr_{0.6}RuO_3$.

The significance of these two properties is that they act as macroscopic fingerprints for the existence of the Preisach density $p(H_d,H_s)$ and can be employed as experimental tests of the validity of the Preisach decomposition. If these properties are obeyed by a given material, then it is certain that this material can be described by the Preisach model and that the decomposition of the micromagnetic free energy into bistable elements can be performed. However, these tests disclose no details regarding the structure of the distribution itself.

It is natural to ask whether it is possible to associate real physical entitites with the Preisach bistable subsystems. This identification would certainly appear to be straightforward for materials with a discrete microstructure, like an assembly of fine magnetic particles. Each particle has a total moment due to interatomic exchange forces and an anisotropy axis due to dipolar forces, which supplies the energy barrier, and it is straightforward to postulate a one-to-one correspondence between particles and Preisach units. However, the interpretation of a Preisach unit in ferromagnets or spin glasses pose more of a problem. Preisach apparently was keenly aware of the difficulty of justifying physically the existence of the elementary subsystems and thus simply presented his theory as a model system which exhibits hysteresis. Very significant progress in this regard was achieved by Neel [3] when he introduced his model of a random potential for a Bloch wall in a ferromagnet interacting with pinning forces. Neel was able to show the occurrence of a random distribution of square cycles for the magnetization, depending on the position of the wall in the potential, and was able to map the movement of domain walls onto an equivalent assembly of hypothetical fine grains.

In fact, it is possible to show rigorously that if the magnetization process is dominated by stochastic domain wall dynamics, and if the pinning field fluctuates in space according to the Wiener process, then both fingerprints of the Preisach decomposition, return-point-memory and congruency, will be obeyed. Furthermore, under these circumstances, the functional form of the Preisach density can be established explicitly by exploiting the properties of the Wiener process. This yields [9]:

$$p(H_d) = \frac{2}{\bar{H}_d} \frac{(H_d / \bar{H}_d)\coth\left(H_d / \bar{H}_d\right) - 1}{\sinh^2(H_d / \bar{H}_d)}. \tag{4.10}$$

4.6 Thermal Relaxation in the Preisach Model

The state of a Preisach system described by the state line $C(H_d)$ is in general a metastable state. At finite temperatures, as time elapses, this metastable state will relax toward the equilibrium configuration $C(H_d) = -H_a$. A discussion of the details of this relaxation process will be delayed to Chapter 6, where it is presented in the context of aging and memory effects.

4.7 References for Chapter 4

[1] F. Preisach, "Über die magnetische Nachwirkung," Z. Phys. **94**, 277 (1935).

[2] L. Néel, Théorie du traînage magnétique des substances massives dans le domaine de Rayleigh, Cah. Phys. Radium **11**, 49 (1950).

[3] L. Néel, "Some Theoretical Aspects of Rock-Magnetism", Philos. Mag. Supp. **4**, 191 (1955).

[4] L. Néel, Théorie des Lois d'Aimantation de Lord Rayleigh. I. Les Déplacements d'une Parois Isolée, Cahiers de Phys. **12**, 1 (1942).

[5] L. Néel, Cahiers de Phys. 12, 1 (1942).

[6] J.J. Préjean and J. Souletie, "Two-level systems in spin glasses: a dynamical study of the magnetizations below T_G, application to CuMn systems," J. Physique **41**, 1335 (1980).

[7] J. Souletie, "Hysteresis and after-effects in massive substances. From spin glasses to the sand hill," J. Phys., **44**, 1095 (1983).

[8] E. Della Torre, "Effect of Interaction on the Magnetization of Single Domain Particles," IEEE Trans. Audio **14**, 86 (1966).

[9] G. Bertotti, *Hysteresis in Magnetism* (San Diego: Academic Press, 1998).

[10] G. Bertotti, "Energetic and Thermodynamics Aspects of Hysteresis," Phys. Rev. Lett. **76**, 1739 (1996).

[11] G. Bertotti, "Dynamic Generalization of the Preisach Model of Hysteresis," IEEE Trans. Magn. **28**, 2599 (1992).

[12] V. Basso and G. Berotti, "Description of Magnetic Interactions and Henkel Plots by the Preisach Hysteresis Model," IEEE Trans. Magn. **30**, 64 (1994).

[13] I.D. Mayergoyz, "Mathematical Models of Hysteresis," Phys. Rev. Lett. **56**, 1518 (1986).

[14] C.E. Korman and I.D. Mayergoyz, "Preisach Model Driven by Stochastic Inputs as a Model for Aftereffect," IEEE Trans. Magn. **32**, 4204 (1996).

[11] A. Stancu and L. Spinu, "Temperature and time dependent Preisach model for a Stoner-Wohlfarth particle system," IEEE Trans. Magn. **34**, 3867 (1998).

[12] I.D. Borcia, L. Spinu, and A. Stancu, "Analysis of thermal critical curves in temperature and time dependent Preisach type models," Int. Journ. App. Electromag. Mech. **13**, 323 (2001).

[13] I.D. Borcia, L. Spinu, and A. Stancu, "A Preisach-Neel model with thermally variable variance," IEEE Trans. Mag. **38**, 2415 (2002).

[14] A. Stancu, C. Pike, L. Stoleriu, P. Postolache, D. Cimpoesu, "Micromagnetic and Preisach analysis of the First Order Reversal Curves (FORC) diagram," J. App. Phys. **93**, 6620 (2003).

[15] M. Cerchez, L. Stoleriu, and A. Stancu, "Identification of the generalised Preisach model parameters for systems with magnetostatic interactions," J. Optoelec. Adv. Mat. **5**, 351 (2003).

[16] A. Stancu, L. Stoleriu, P. Postolache, and R. Tanasa, "New Preisach model for structured particulate ferromagnetic media," J. Mag. Mag. Mat. **290**, 490 (2005).

[17] C. Enachescu, R. Tanasa, A. Stancu, F. Varret, J. Linares, and E. Codjovi, "First-order reversal curves analysis of rate-dependent hysteresis: The example of light-induced thermal hysteresis in a spin-crossover solid," Phys. Rev. B **72**, 054413 (2005).

[18] A. Stancu, P. Andrei, and L. Stoleriu, "Magnetic characterization of samples using first- and second-order reversal curve diagrams," J. App. Phys. **99**, 08D702 (2006).

[19] P. Andrei, A. Stancu, and A. Adedoyin, "Modeling of viscosity phenomena in models of hysteresis with local memory," J. Optoelec. Adv. Mat. **8**, 988 (2006).

[20] D. Cimpoesu, L. Spinu, and A. Stancu, "Temperature dependence of FORC diagrams in nanostructured materials," IEEE Trans. Mag. **42**, 3165 (2006).

[21] A. Stancu, "Identification procedures for Preisach-type models based on FORC diagrams," J. Optoelec. Adv. Mat. **8**, 1656 (2006).

[22] S.H. Charap and A. Ktena, "Vector Preisach Modeling," J. Appl. Phys. **73**, 5818 (1993).

[23] J. Oti and E. Della Torre, "A Vector Moving Model of Both Reversible and Irreversible Magnetizing Processes," J. Appl. Phys. 67, 5364 (1990).

[24] H.A.J. Cramer, "A Moving Preisach Vector Hysteresis Model for Magnetic Recording Media," J. Magn. Magn. Mat. **88**, 194 (1990).

[25] T. Song and R.M. Roshko, "Preisach Model for Systems of Interacting Superparamagnetic Particles," IEEE. Trans. Mag. **36**, 223 (2000).

[26] T. Song, R.M. Roshko, and E. Dan Dahlberg, "Modelling the irreversible response of magnetically ordered materials: a Preisach-based approach," J. Phys. Cond. Mat, **13**, 3443 (2001).

[27] P.D. Mitchler, E.D. Dahlberg, E.E. Wasseling, and R.M. Roshko, "Henkel Plots in a Temperature and Time Dependent Model," IEEE Trans. Magn. **32**, 3185 (1996).

[28] G. Biorci and D. Pescetti, "Analytical Theory of the Behavior of Ferromagnetic Materials," Il Nuovo Cimento **7**, 829 (1958).

[29] O. Benda, "Possibilities and Limits of the Preisach Model," J. Mag. Mag. Mat. **113**, 443 (1992).

Chapter 5

Equipment and Sample Preparation

5.1 Measuring the Magnetic Moment

5.1.1 The Physical Property Measurement System (PPMS)

A Physical Property Measurement System (PPMS Model 6000) manufactured by Quantum Design was used to obtain measurements of the magnetic moment as a function of temperature T, applied field H_a, and time t. The PPMS Model 6000 consists of a Probe (see Figure 5.1), a pump to control pressure, an aluminum dewar to contain the helium bath in which the PPMS probe is immersed, an electronic controller (Model 6000), a magnet controller, and a magnet power supply [1].

The PPMS probe is the essential hardware component of the measurement system, and sits within the liquid helium bath contained in the aluminum dewar. The probe integrates all of the fundamental temperature control hardware, the superconducting magnet, the helium-level meter, electrical connectors, gas lines, and sample puck connectors. The probe is constructed with several concentric stainless steel tubes, along with the inner and outer vacuum tubes, the sample tube, thermometers and heaters, the impedance assembly, the probe head, and the protective cap (open to helium).

The pump is direct drive and continuously pumps on the entire assembly to control the internal pressure of the sample tube and to help maintain thermal control.

The dewar is constructed out of aluminum and is used to contain the liquid helium bath and PPMS probe. The outer layer of the dewar is composed of reflective super insulation to aid in the minimization of helium consumption. The outer layer is evacuated and has layers of activated charcoal on the surface in contact with the cold liquid helium in order to maintain the vacuum set up inside.

The electronic controller (Model 6000) contains all of the gas control valves and system electronics for the PPMS. It is composed of a processor, a motherboard, a system bridge board (for temperature readings), and gas valves and gas lines to control temperature.

Finally, the magnet power supply is the current source for the superconducting magnet, while the control of the charging and discharging of the magnet is accomplished by the magnet controllers. The maximum magnetic field that can be reached in the dewar is 9T, and it has a stability of 0.05 G.

The PPMS probe is capable of performing DC magnetization measurements with a sensitivity between 2.5×10^{-5} and 5 emu, is capable of maintaining a sample chamber temperature below 4.2K (boiling point of helium) indefinitely, in addition to allowing smooth temperature transitions when both cooling and warming through 4.2K. The temperature range is $1.9K \leq T \leq 400K$ with an accuracy of $\pm 1\%$, and is stable to within $\pm 0.2\%$ for $T \leq 10K$, and $\pm 0.02\%$ for $T > 10K$. The sample chamber can hold a sample with a diameter of up to 3mm, and length of up to 8mm. For a complete block diagram illustrating the function of the PPMS system, see Figure 5.2.

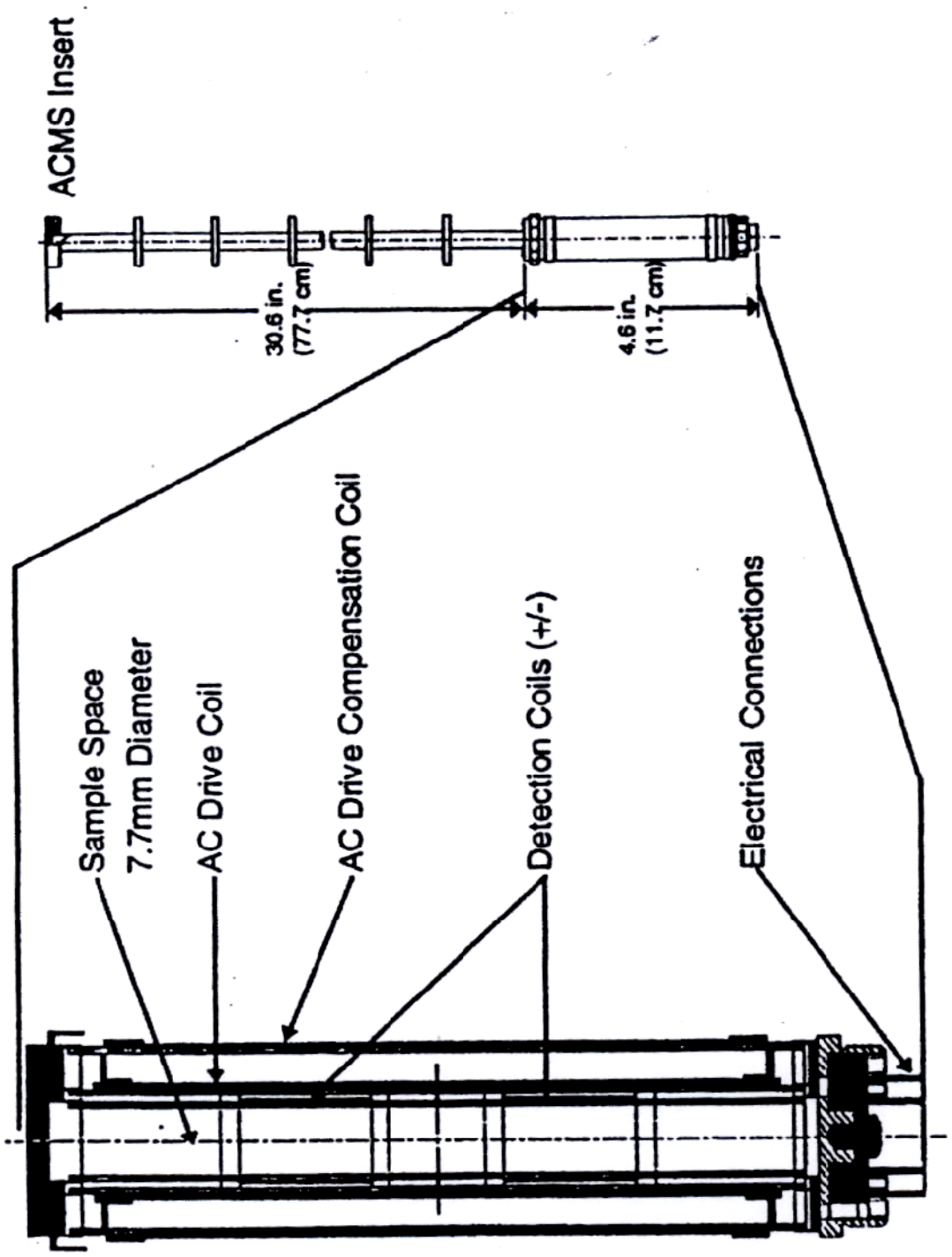

Figure 5.1: The PPMS Probe [1]

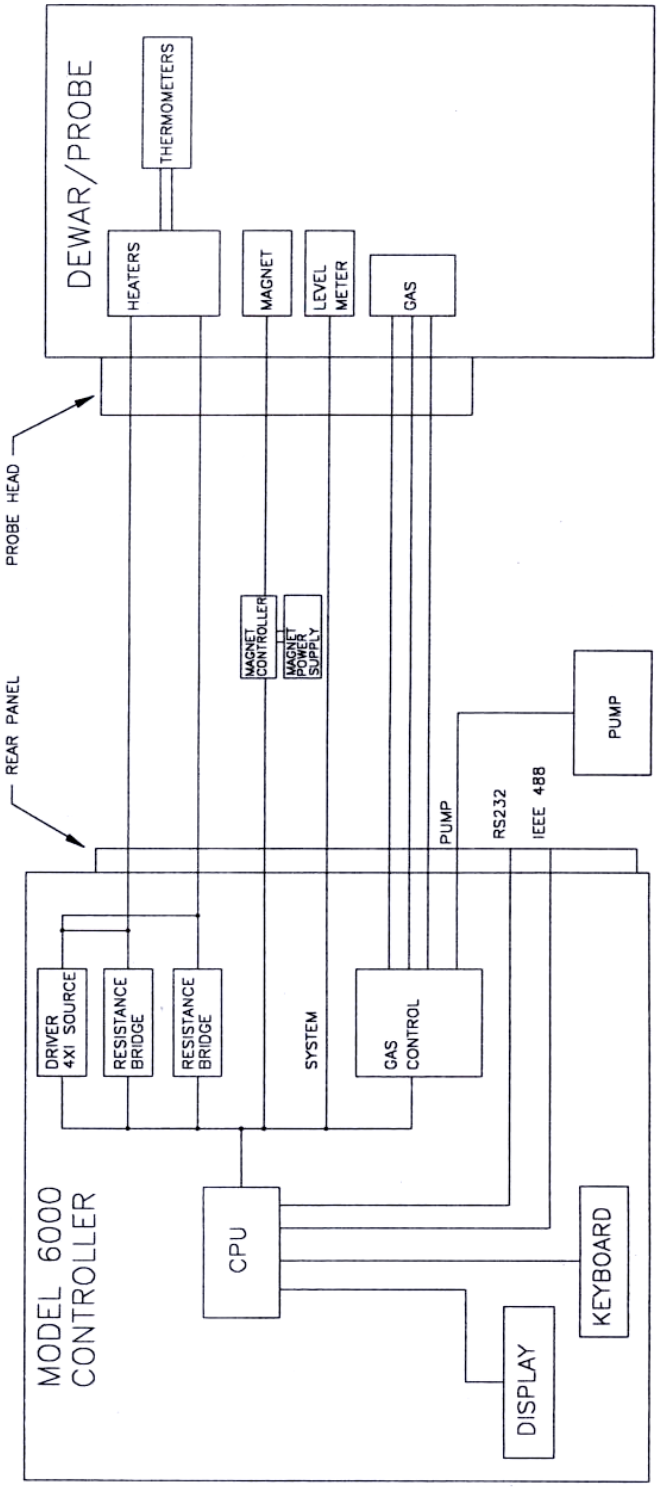

Figure 5.2: PPMS System block diagram [1].

5.1.2 The ACMS Insert

The ACMS insert (Figure 5.3) is an additional component of the assembly that is used to perform DC magnetization measurements, and houses the system's drive and detection coils, thermometer, and electrical connections [1]. The insert can be positioned directly inside the PPMS sample chamber, and its sample space lies directly within the uniform field region of the PPMS, allowing DC field and temperature control to be maintained.

The sample is held within the insert's coil set on the end of a thin, rigid sample rod. The sample holder is translated in the longitudinal direction by a DC servo motor in the sample transport assembly, which mounts to the top of the PPMS probe. The DC servo motor enables smooth and rapid longitudinal sample motion.

The ACMS includes an AC drive coil set that supplies a detection coil set and an alternating excitation field that inductively responds to the combined sample moment and excitation field. The copper drive and detection coils are positioned within the ACMS insert, concentric with the PPMS' superconducting DC magnet.

The drive coil is wound longitudinally around the detection coil set. The field amplitude that may be applied depends on both the frequency of the alternating applied field and the temperature maintained within the PPMS probes. However, the drive coil can generate alternating fields of up to ± 10 Oe in a frequency range of 10 Hz ≤ f ≤ 10 kHz at all temperatures. Larger amplitude fields can be applied as the temperature and frequency are reduced.

The detection coils are configured such that two sets of counterwound copper coils are connected in series and separated by several centimeters (first-order gradiometer

configuration), in order to electrically isolate the sample's signal from uniform background sources.

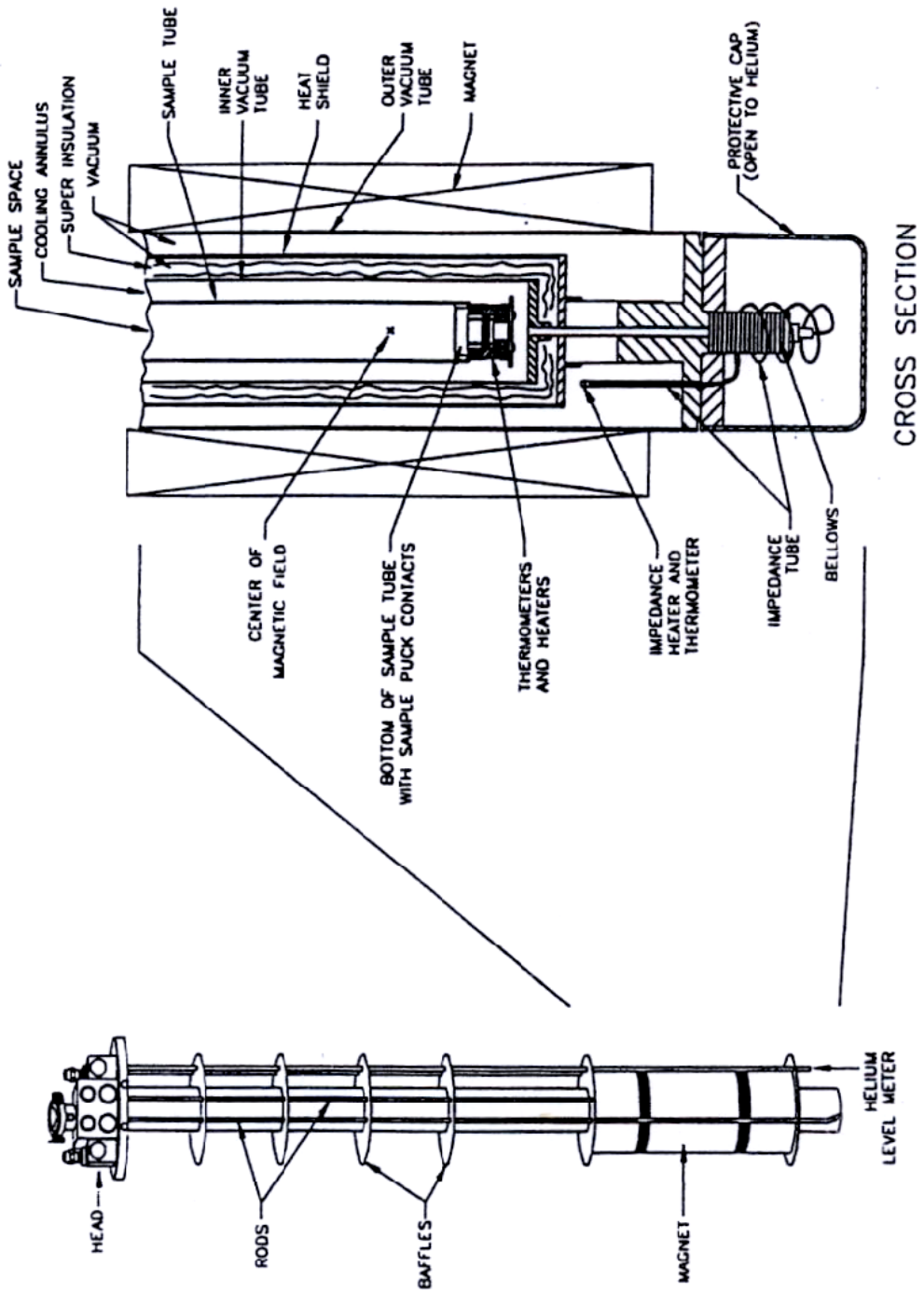

Figure 5.3: The ACMS insert and coil set [1].

During a typical DC measurement, a constant field is applied to the measurement region and the sample is moved rapidly through both sets of copper coils, inducing a signal in them according to Faraday's law. This measurement method is known as the **extraction** method. The servo motor translates the sample through the entire detection coil set in approximately 0.05s. The sample translation is synchronized with data acquisition by the transmission of a handshake signal from the servo motor to the digital signal processor (DSP) that triggers data acquisition. The ACMS acquires 4096 voltage readings during each translation of the sample and produces a voltage profile curve for each. The change in flux $\phi(t)$ caused by the moving sample induces a time-dependent voltage across the terminals of the pickup coils,

$$V(t) \propto \frac{d\varphi}{dt} \quad . \tag{5.1}$$

Thus, the voltage profile is simply the derivative with respect to time of the net magnetic flux through the coils. By integrating the voltage profile and fitting the known waveform for a dipole advancing through the detection coils to the resulting data using a regression algorithm, the total sample moment is found.

Outside the AC drive coil is a compensation coil. The two coils are counterwound and connected in series so that they receive the same excitation signal. Within the measurement region, there remains a net field, but outside the measurement region, the fields from the two coils combine to cancel. The compensation coil effectively confines the excitation fields to the volume of the coil set, thereby reducing the interaction of the

instrument with conductive materials outside the measurement region, such as the sample chamber walls, the magnet core, et cetera, by approximately three orders of magnitude.

During a typical DC measurement, the amplitude of the detection signal depends on both the speed of extraction and the magnetic moment of the sample. The ACMS extracts samples at speeds of ~ 100 cm/s thus minimizing the effects of time-dependent errors like drift, for example. Since the scan time is brief, several scans can be performed for each measurement, reducing the contributions of random error.

The software package accompanying the PPMS serves as an interface to the hardware and includes numerous automatic protocols to assist in positioning the sample, demagnetizing and determining a number of sample characteristics, in addition to monitoring the atmosphere of the sample chamber. Sequences are easily written and executed using the built-in software package, thus allowing us to automatically measure hysteresis loops, field cooled magnetization, thermoremanent magnetization (TRM), zero field cooled magnetization, and isothermal remanent magnetization (IRM) as a function of field, temperature, and time, and to view the results graphically in real time.

5.1.3 The Vibrating Sample Magnetometer (VSM)

A number of our experimental magnetic measurements were made utilizing a Princeton Measurements Corporation Model 3900 MicroMag^{TM} Vibrating Sample Magnetometer (Princeton Measurements Corporation, 1995) is housed in the Institute for Rock Magnetism at the University of Minnesota. The VSM is a computer-controlled magnetic measurement device that is highly sensitive and capable of measuring the

magnetic properties of a large array of magnetic materials. A schematic diagram of the VSM is shown in Figure 5.4 [2].

As a result of the fact that the field in the vicinity of a magnetic material is spatially-dependent, the field existing at any specific point in space can be altered by translating the magnetized body. Thus, the VSM works by vibrating a sample vertically at the midpoint of the field produced by a magnet. An electric current is induced in pickup coils placed near the vibrating sample as a result of the vibration, proportional to the magnetic moment and of the same frequency as the frequency of vibration of the sample. Thus, the change in flux $\varphi(t)$ caused by the vibrating sample, induces a time-dependent voltage across the terminals of the pickup coils (Eq(5.1)), where $\varphi(t)$ is proportional to the field induced in the pickup coils by the sample. Specific signal processing techniques guarantee that the measurement resulting from this process will depend only on the amplitude of the moment and not of the drive amplitude. It is possible to calibrate the absolute moment and the sensitivity of the pickup coils by performing the measurement with a sample of known magnetization.

The mechanical transducer assembly vibrates the sample at a frequency of 83.0 Hz, and allows precision three dimensional translation, vibration isolation, and continuous rotation about a vertical axis with the aid of computer control.

The magnetometer has a sensitivity of 5 μemu, defined as the standard deviation at room temperature operation at one second averaging time per point. The magnetometer is capable of measuring moments in the range 50 μemu $\leq m \leq$ 10 emu. The accuracy of the measured moments is 2% as compared to calibration with a pure nickel standard.

Since the measured magnetic quantity is the total moment and not the magnetization, knowing the volume of the sample is important when comparing absolute values of the measurements. Also, the shape of the sample determines the degree to which demagnetization effects play a role. Although the data processing abilities of the VSM include correction factors for demagnetization effects and normalization for sample mass or volume, the absolute values of the measured moments are not essential to interpreting and comparing data and amount to no more than scaling factors. Thus, although our values are irrelevant to a certain extent on an absolute scale, the relative values of the measured moments are very accurate, based on the high sensitivity of the VSM.

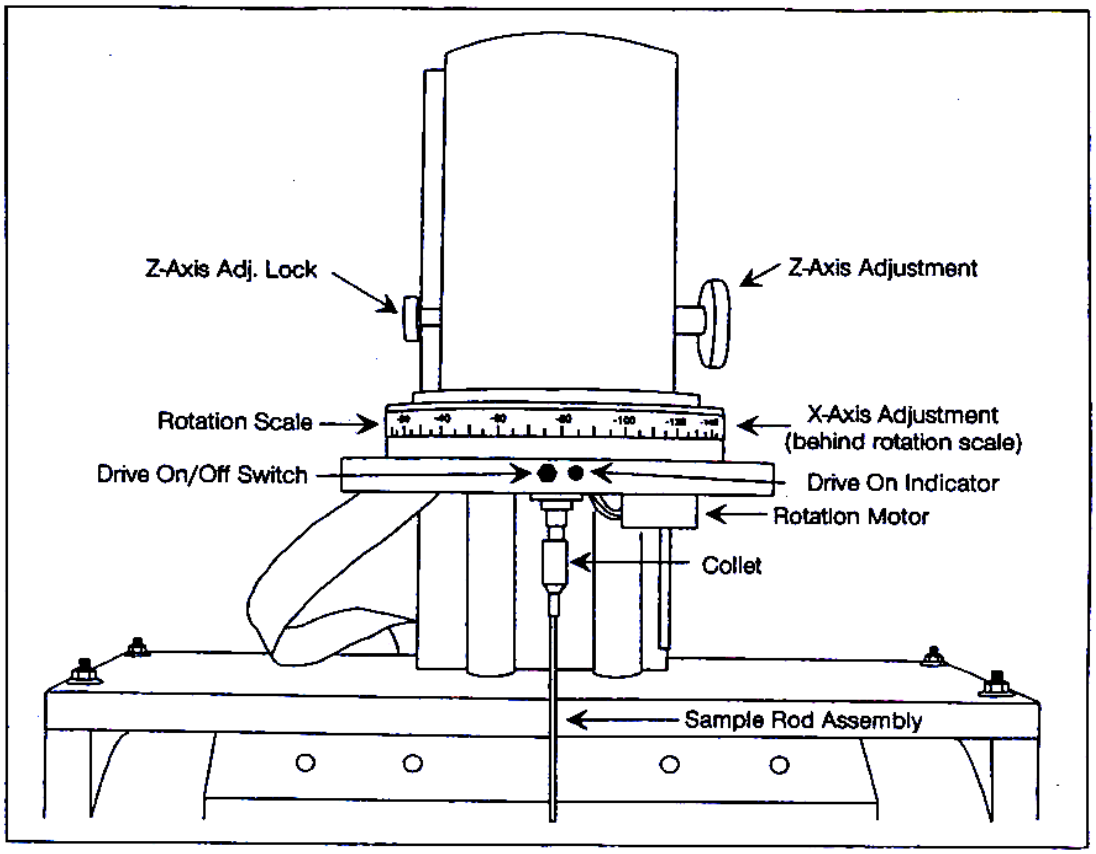

Figure 5.4: Schematic of the Vibrating Sample Magnetometer, shown from the front of the translation stage [2].

The applied field is generated by a high-performance laboratory electromagnet with a 4-inch pole face diameter with pole caps tapering to 2 inches. The maximum field range for this system is ±18 kOe. The applied field is recorded continuously with the aid of a built-in Hall-effect gaussmeter that is accurate to within 2% ± 1 Oe. Because of this high degree of accuracy, the null field in the sample chamber can also be determined accurately. The magnet power supply is a bipolar, wideband pulse-width modulated power amplifier that uses a feedback signal to regulate the field, thus allowing precise servo-control under static or field sweeping conditions. The maximum magnet slew rate is 20 kOe/s with an option to pause for magnetic field stabilization before a new measurement is taken. The electromagnet also allows for a rapid settling of the field, making it particularly convenient for measuring hysteresis loops.

The pick up coils are mounted on the ends of the pole pieces, while the sample is mounted at the end of a glass rod suspended in the electromagnet gap. The sample chamber is composed of fused silica. The sample holder is composed of high purity boron nitride, capable of withstanding high temperatures, and allows vertical mounting of the sample in the chamber.

The VSM system is also equipped with a high-temperature oven that uses a continuous flow of He gas at a rate of two to four liters per minute to stabilize at temperatures greater than the ambient temperature. The oven is capable of heating to 750°C and is accurate to 0.75% ± 2.2K. A thermocouple of designation type K, is a chromel/alumel construction that is reliable for temperatures -200°C ≤ T ≤ 1250°C, and is mounted ¼ inch from the heater and is used to monitor and control the internal

temperature. The sample chamber is located directly above the thermocouple. The temperature controller is integrated into the system and a temperature change that covers the whole operating region can occur in eight to ten minutes. For a schematic of the oven assembly see Figure 5.5.

The software package accompanying the VSM includes a variety of automatic procedures to assist in positioning the sample, demagnetizing and determining a number of sample characteristics. We performed measurements of hysteresis loops, field cooled (FC) magnetization, thermoremanent magnetization (TRM), zero field cooled (ZFC) magnetization as a function of field, temperature, and time with the VSM.

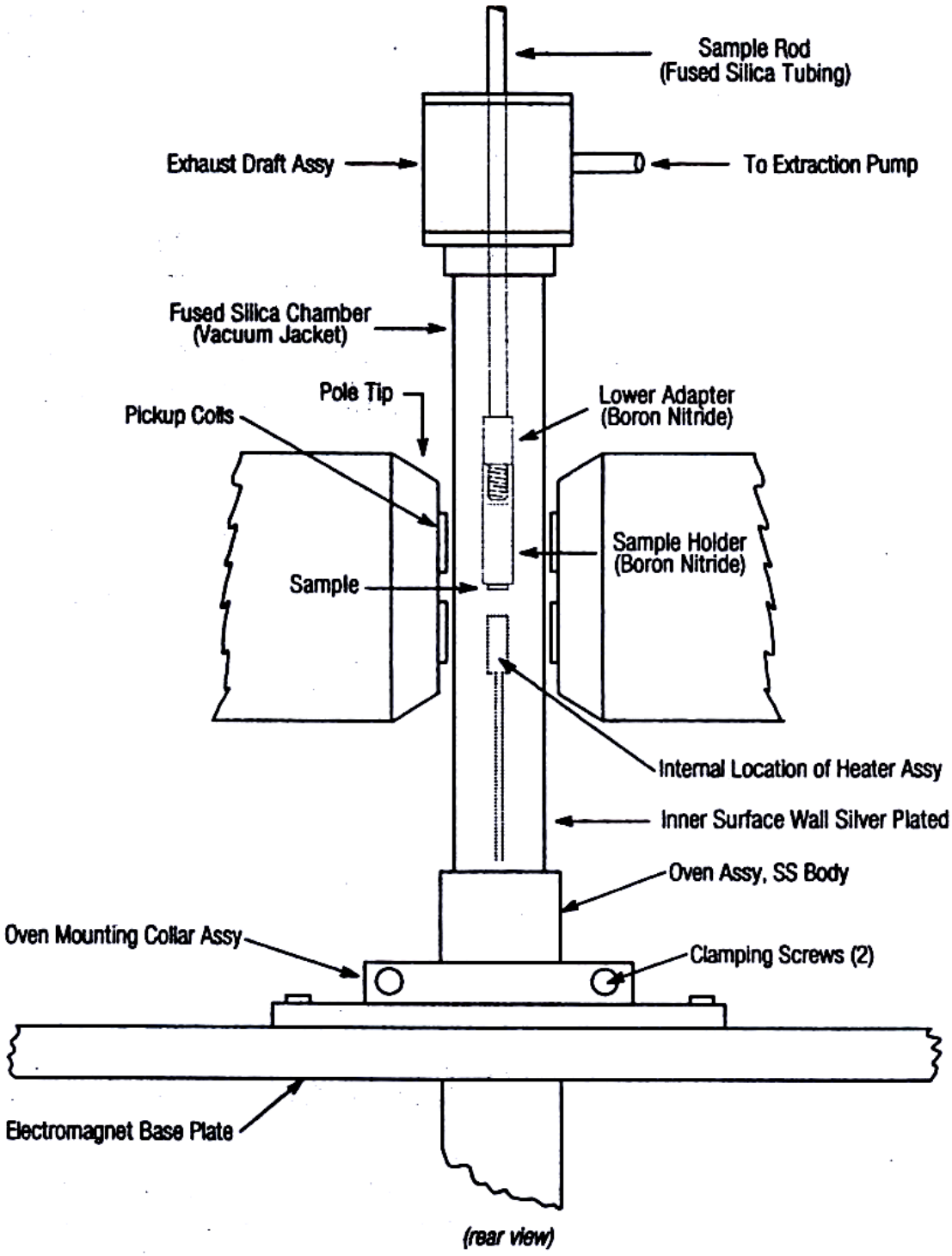

Figure 5.5: The oven assembly of the VSM [2].

5.2 Magnetic Systems and Sample Preparation

A variety of experiments were performed to investigate numerous aspects of hysteretic behaviour in magnetic systems with a variety of chemical compositions and microstructures, which are important for reasons of both fundamental and technological interest. These ranged from discrete suspensions of nanodimensional magnetite particles, which are of considerable interest as information storage media and for use as biosensors (Section 5.2.1), to minerals like Tiva Canyon Tuff, (Section 5.2.2), to exchange-bond disordered ferromagnetic perovskites, which are employed for read-write applications in hard disk drives (Section 5.2.3), and finally to a thin film of nanodimensional Fe particles embedded in an insulating matrix of alumina (Section 5.2.4).

5.2.1 Magnetite

Magnetite is the most important and fundamental oxide in rock magnetism, and as a result, it is desirable to acquire a comprehensive understanding of its magnetic properties as a rock-forming mineral. Magnetite has also become important in technological applications. Collections of nanodimensional magnetic particles are utilized in biosensors, and are particularly useful if the individual particles are fabricated to have smooth surfaces, spheroidal shapes, narrow size distributions, and are chemically stable [3].

The crystal structure of magnetite is an inverse cubic spinel (*Fd*3*m*, $[Fe^{3+}]_A[Fe^{2+}Fe^{3+}]_BO_4$, where lattice site A is surrounded by 4 oxygen ions tetrahedrally, and lattice site B is surrounded by 6 oxygen ions octahedrally. One unit cell of the crystal

structure is comprised of eight (Fe_3O_4) molecules. Magnetite is a typical ferrimagnetic substance, with the magnetic moments of the iron ions in the octahedral and tetrahedral sites in the crystal arranged in an antiparallel configuration. The ferromagnetic critical temperature T_C is 578ºC, and bulk magnetite has a saturation magnetization of ~ 92 emu/gram.

The sample of magnetite used for the purposes of our investigation, is a compressed powder of nanodimensional magnetite (Fe_3O_4) particles immobilized in an organic binder.

The magnetite particles were provided by Professor Y.K. Hong of the University of Idaho, and were synthesized by the chemical coprecipitation process [4]. The starting materials consisted of Iron (II) chloride tetrahydrate – 99% $Fe_2Cl_2 \cdot 4H_2O$, iron (III) nitrate nonahydrate – 98% $Fe(NO)_3 \cdot 9H_2O$, and sodium hydroxide solution – 97% NaOH, all provided by Fisher Chemicals Co. The molar ratio of Fe^{2+} to Fe^{3+} was established at 1 to create spherical magnetite nanoparticles with an average particle size of 7 nm. Final production of the magnetic particles by coprecipitation was accomplished with the addition of a 0.1 mol ferrous chloride and 0.1 mol ferric nitrate mixed solution to a strongly stirred 3 mol sodium hydroxide solution in de-ionized water at a temperature of 88ºC for a duration of ten minutes. The precipitated product was decanted with a permanent magnet, then washed with de-ionized water to eliminate the remaining cations and anions, and subsequently dried at a temperature of 50ºC for a total time of 6 hours in a dryer oven.

A vibrating sample magnetometer was used to characterize the magnetic properties of individual magnetite nanoparticles. The hysteresis curve measured at 300K

has a vanishingly small coercive field, in contrast with that of bulk magnetite, whose coercive field at 300K is about $H_c \sim 115\text{-}150$ Oe. The difference was attributed to the superparamagnetic behaviour of nanodimensional magnetite particles. The measured saturation magnetization of the magnetite particles is 49 emu/gram (a reduction of approximately a factor of two from the bulk value, the reduction being a result of the increase in surface effects with decreasing particle size [5, 6]. Transmission electron micrography was used to determine that the spherical magnetite particles ranged in diameter from 5-10 nm, with an average particle diameter of 7 nm.

5.2.2 Tiva Canyon Tuff

Tiva Canyon Tuff is a volcanic rock that was supplied by the Institute for Rock Magnetism at the University of Minnesota, and was acquired at various depths from the Yucca Mountain, Nevada, USA, near the Nevada Test site and future repository for the USA's depleted nuclear fuel [7]. It is comprised of grains of titanomagnetite, $Fe_{3-x}Ti_xO_4$ with $x \cong 0.1$ which are embedded rigidly and randomly in a volcanic glass. What makes the tuff such a superb sample to study is that the titanomagnetite grains are essentially non-interacting and consist of a mixture of stable single-domain and superparamagnetic grains.

Titanomagnetite is a solid solution of ulvöspinel (Fe_2TiO_4) and magnetite, both with the inverse spinel structure, that forms with the substitution $2Fe^{3+} \Leftrightarrow Fe^{2+} + Ti^{4+}$. The relative ratio of magnetite to ulvöspinel in the solid solution changes the Curie temperature T_C from the nominal values of $T_C \sim 578$ºC for pure magnetite, and ~ -150ºC

for pure ulvöspinel.The dependence of T_C on % molar concentration of Fe_2TiO_4 is shown in Figure 5.6 [8].

The titanomagnetite grains in the Tiva Canyon Tuff are acicular (needle-like), have a narrow grain size distribution and are spatially well separated. When the Tuff was initially deposited, the cooling rate varied as a function of height above the base of the unit, leaving the quickly-cooled base with extremely fine oxides that are less than 10 nm in diameter, and leaving the much more slowly-cooled top layer with oxides greater than 1000 nm in diameter that are essentially single-domain, in that they resemble, as closely as possible, ideal Stoner-Wohlfarth grains. Once the tuff was excavated, the material was homogenized by the Institute for Rock Magnetism, by crushing and mixing the cores, first using a Braun "Chipmunk Crusher," then a rotary disc mill, before using a ball mill to complete the process.

High temperature susceptibility measurements give evidence of a single ordered phase, while peaks in the temperature derivative of the susceptibility imply an ordering temperature of $T_C \sim 550°C$. Furthermore, the particles have an average grain volume of 5.75×10^{-23} m^3, a length to width ratio of ~ 0.3, and a length of about 87 nm.

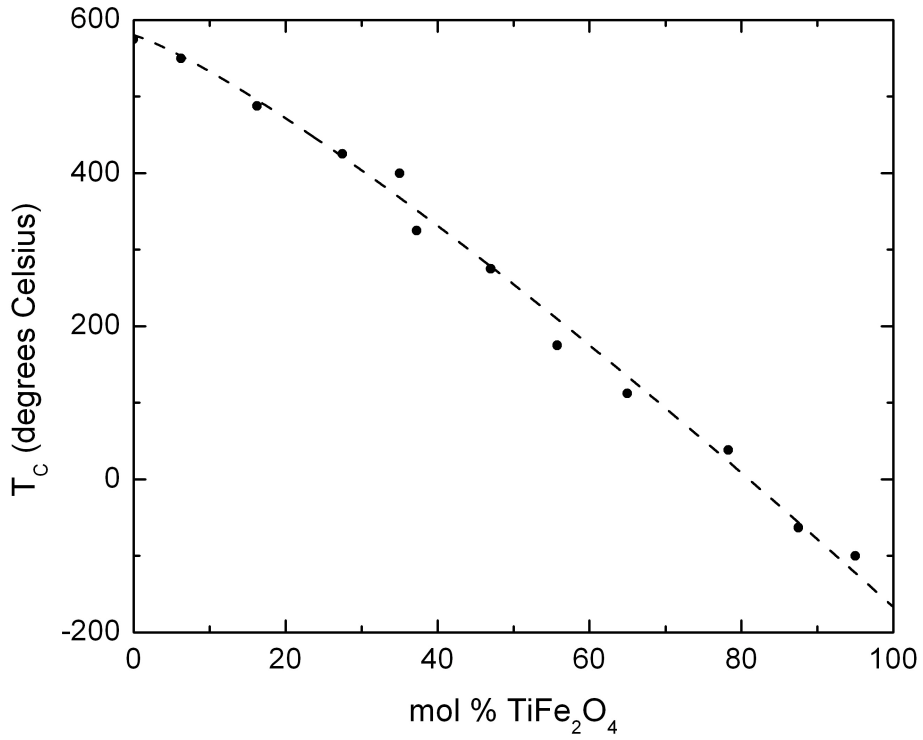

Figure 5.6: Dependence of the Curie temperature T_C on percent molar concentration of $TiFe_2O_4$ in a solid solution of Fe_3O_4 - $TiFe_2O_4$. [8]

5.2.3 Ferromagnetic Ruthenates ($Ca_xSr_{1-x}RuO_3$)

$Ca_xSr_{1-x}RuO_3$ is a polycrystalline mixed ruthenate with an orthorhombically distorted perovskite structure and a single magnetically active species (Ru). The limiting members of the series (x = 0 and x = 1) are a long-range ferromagnet and a highly exchange-enhanced paramagnet, respectively. The manifestation of extreme magnet behaviour is a consequence of the degree to which the RuO_6 octahedra are distorted. The distortion is minimal in the x = 0 member, and significant in the isostructural x =1 member.

Polycrystalline samples of $Ca_xSr_{1-x}RuO_3$ were supplied by one of our colleagues, Dr. G. Williams of the University of Manitoba, and were prepared utilizing a conventional solid-state reaction method [9]. Stoichiometric quantities of $SrCO_3$ (99.99%), $CaCO_3$ (99.99%), and RuO_2 (99.99%) powders were mixed together and heated at 900°C for a period of 24 hours in air, with six intermediate grindings. The final compounds were single phase, as confirmed by subsequent powder X-ray diffraction measurements. After heating, the compounds were pressed into circular disks with a typical thickness of 1 mm and a diameter of 5 mm, and were then annealed in air at a temperature of 1300°C for a period of 24 hours. Scanning electron microscope images reveal a sintered network of "particles" with an average "particle" size of approximately 1 μm.

The systems investigated for our purposes have Ca fractions x = 0.2, 0.4, and 0.6, and all three are exchange bond-disordered ferromagnets with paramagnetic-ferromagnetic critical temperatures T_C (x = 0.2) ≈ 120K, T_C (x = 0.4) ≈ 75K, and T_C (x = 0.6) ≈ 45K.

5.2.4 Nanodimensional Fe Particles Embedded in an Insulating Matrix of Alumina (Fe/Al_2O_3)

$Fe_{40}Al_{24}O_{36}$ (atomic ratio) is a nano-structured granular film. Thin films are used in applications such as magnetic recording and microelectronics, where thermal stability becomes extremely important. They are also of practical significance due to their

potential for exhibiting giant magnetoresistance effects (GMR) for use in magnetoelectronics [10, 11].

Granular films of $Fe_{40}Al_{24}O_{36}$ were fabricated by a group from Lanzhou University in China [12], and were deposited onto a glass substrate by rf reactive sputtering from a composite target comprised of Al chips, of 6 mm diameter, placed homogeneously on a disk of pure Fe having a diameter of 80 mm.

To determine the resulting structure of the films, X-ray diffraction (XRD) and transmission electron microscopy (TEM) were used. XRD patterns showed that the Fe particle sizes are not uniform, but have diameter sizes which having a range of 2-4 nm. Furthermore, since no diffraction peaks were present indicating a crystalline Al_2O_3 structure, it can be concluded that Al_2O_3 exists in the amorphous phase. The thickness of the film is approximately 1 μm.

The Langevin formula was fit to measurements of M against H to determine that the films exhibit paramagnetic behaviour at room temperature, and that the magnetic moments of the large and small particles are 3.38×10^4 μ_B and 4.25×10^3 μ_B, respectively.

5.3 References for Chapter 5

[1] Physical Property Measurement System (PPMS) Hardware & Options Manual, Quantum Design, 1996.

[2] Model 3900 MicroMag^{TM} VSM Magnetometer Instruction Manual, Princeton Measurements Corporation, 1995. (VSM)

[3] R.L. Edelstein, C.R. Tamanaha, P.E. Sheehan, M.M. Miller, D.R. Baselt, L.J. Whitman, and R.J. Colton, "The BARC biosensor applied to the detection of biological warfare agents," Biosens. Bioelectron. 14, 805 (2000).

[4] S.H. Gee, Y.K. Hong, D.W. Erickson, M.H. Park, and J.C. Sur, "Synthesis and aging effect of spherical magnetite (Fe_3O_4) nanoparticles for biosensor applications," J. Appl. Phys. 93, 7560 (2003).

[5] O. Iglesias and A. Labarta, "Finite-size and surface effects in maghemite nanoparticles: Monte Carlo simulations," Phys. Rev. B 63, 184416 (2001).

[6] F. Bodker, A. Morup, and S. Linderoth, "Surface effects in metallic iron nanoparticles," Phys. Rev. Lett. 72, 282 (1994).)

[7] B.S. Carter-Stiglitz, P.A. Solheid, R. Egli, and A.P. Chen, "Tiva Canyon Tuff," The IRM Quarterly, Spring 2006, page 1, Vol. 16 No. 1.

[8] Takesi Nagata, *Rock Magnetism* (Tokyo: Maruzen Company Limited, 1961).

[9] C. Viddal, R.M. Roshko, H. Kunkel, L. Wei, X.Z. Zhou, and G. Williams, "Critical Behaviour and Irreversibility in a Mixed Perovskite $Ca_{0.6}Sr_{0.4}RuO_3$," J. Mag. Mag. Mat. 272, 652 (2004).

[10] M. N. Baibich, J.M. Broto, A. Fert, F.N.V. Dau, F. Petroff, P. Eitenne, G. Creuzet, A. Friederich, and J. Chazelas, "Giant Magnetoresistance of (001)Fe/(001)Cr Magnetic Superlattices," Phys. Rev. Lett. 61, 2472 (1988).

[11] G.A. Prinz, "Magnetoelectronics," Science, 282, 1660 (1998).

[12] Shi Hui Ge, Shi Bin Zhang, Jun Hong Chi, Zhen Gang Zhang, Cheng Xian Li, and Run Jin Gan, "The giant magnetoresistance effect of Fe-Al-O nano-structured granular films," J. Phys. D. 33, 917 (2000).

Chapter 6
Aging, Memory and Rejuvenation in Collections of Two-Level Subsystems

6.1 Introduction

Spin glasses [1-3] have been an active field of research for the last three decades, yet many questions regarding the nonequilibrium relaxation dynamics in the spin-glass phase remain unresolved [4-7]. A spin glass is a collection of magnetic moments which undergo an apparently cooperative phase transition, below a well-defined critical temperature T_G, into a magnetically frozen state in which the moments are locked into an orientationally random configuration which lacks the long-range uniform or periodic order typical of conventional frozen magnetic states like ferromagnets and antiferromagnets. In order to produce such a state, it appears that two ingredients are necessary. There must be a **competition** between the interactions which couple the magnetic moments so that no single configuration of moments is able to satisfy all of the interactions simultaneously (this is commonly referred to as "frustration"), and the interactions must be at least partially **random**, implying that there must be some structural disorder in the spatial arrangement of the moments.

The three defining characteristics of the nonequilibrium relaxation dynamics of spin glasses are aging [8], memory [9], and rejuvenation [10, 11]. **Aging** refers to the

observation that the magnetic response depends on the time t_a for which the system is held at constant temperature following cooling from above to below T_G , and is visible directly as a relaxation of the moment (or the frequency dependent susceptibility) as a function of observation time t in the cooling field, or through the appearance of structural anomalies in the time dependence of the relaxation isotherms following field application or removal at an observation time t which coincides with the aging time ($t \approx t_a$). **Memory** refers to the observation that if cooling in a field (zero or nonzero) below T_G is temporarily halted and the system is aged at a constant temperature T for a time t_a before cooling is resumed, then the magnetic response exhibits a "step" (in the field cooled case) or a "dip" (in the zero field cooled case) at the aging temperature T when the system is subsequently warmed from low temperatures in a field. **Rejuvenation** refers to the observation that if aging at temperature T is followed by a temperature shift from T to $T \pm \Delta T$ then, for sufficiently large shifts ΔT, the system relaxes as if it was unaffected by the previous aging at T and had been cooled directly to $T \pm \Delta T$. However, if the system is subsequently cycled back to the initial temperature T, then the relaxation at long times may be superposed onto the original relaxation curve by means of a simple shift, indicating that the system has preserved a **memory** of the original aging in spite of the rejuvenation at $T \pm \Delta T$.

The interpretation of nonequilibrium relaxation dynamics in spin glasses is usually conducted within one of two competing theoretical frameworks. In **mean field "phase space" models** [12-15], the dynamical evolution of the system is pictured as a random walk among metastable states organized on an hierarchical tree which bifurcates continuously as the system is cooled below T_G. In **"real space" droplet excitation**

models [16-22], the dynamics are associated with the logarithmically slow growth of domains pinned by the disorder, and the fragility of the spin glass state to changes in temperature is described through the concept of an **overlap length** $L_{\Delta T}$, which defines the length scale over which the equilibrium configurations at two neighbouring temperatures T and $T \pm \Delta T$ are identical and beyond which they are completely uncorrelated. In either case, the evolution of the system with time proceeds through the mechanism of thermal activation over energy barriers which grow with decreasing temperature and, consequently, we are led to enquire whether any of the common mathematical representations of hysteresis, all of which involve a thermal- and field-activated migration through a corrugated, metastable free energy landscape, might not also exhibit some form of nonequilibrium, age-dependent relaxation dynamics. The question is particularly relevant in the context of dense assemblies of magnetic nanoparticles, which they have become fashionable to refer to as **superspin glasses** in order to emphasize the comparatively large size of the magnetic moment (typically on the order of $10{,}000\mu_B$), where slow dynamics potentially originate from two possible sources, one collective and one non-collective. The non-collective source is simply the broad distribution of single-particle anisotropy energy barriers $E_A=KV$ (K is the anisotropy energy density and V is the volume of the particle) which leads to a correspondingly broad distribution of single-particle relaxation times $\tau = \tau_0 \exp(E_A/kT)$. The collective source is the frustrated state formed by the strong dipolar interactions between the particles coupled with the randomness in the particle positions and anisotropy axis orientations.

In this section, we present detailed numerical simulations of magnetic relaxation isotherms of a Preisach collection of two-level subsystems in response to all of the standard field and temperature histories which are typically imposed experimentally to probe the relaxation dynamics of spin glasses. The purpose was to search for evidence of nonequilibrium aging phenomena in Preisach assemblies, and to explore their relationship and possible relevance to spin glass and superspin glass dynamics. These simulations show that Preisach systems do indeed exhibit aging, memory and, potentially, rejuvenation effects, analogous to those observed in real nanoparticulate assemblies and other spin glasses, including certain properties which have traditionally been assumed to be a unique signature of collectively ordered, frustrated spin glasses and superspin glasses, such as the "flatness" of the field-cooled magnetization below the critical temperature, and memory effects in the zero-field cooled magnetization.

6.2 Thermal Relaxation of a Preisach Ensemble of Two-Level Subsystems

The application of a magnetic field H_a (positive or negative) to a Preisach ensemble of two-level subsystems creates two distinct subpopulations as shown in Figure 6.1: (a) subsystems with $H_s \le -H_d + H_a$ or with $H_s \ge H_d + H_a$ which have only one free energy minimum and moments which are saturated at $m = +\mu$ or $m = -\mu$, respectively, and (b) subsystems with $-H_d + H_a \le H_s \le H_d + H_a$ which have two free energy minima and two positive free energy excitation barriers, a lower barrier $W_L \equiv \mu H_L = \mu\left(H_d - \left|H_s - H_a\right|\right)$ with relaxation time constant $\tau_L = \tau_0 \exp\left(W_L / kT\right) = \tau_0 \exp\left(H_L / H_f\right)$ where $H_f = kT/\mu$ is the

thermal fluctuation field [23], and a higher barrier $W_H \equiv \mu H_H = \mu\left(H_d + \left|H_s - H_a\right|\right)$ with relaxation time constant $\tau_H = \tau_0 \exp\left(W_H / kT\right) = \tau_0 \exp\left(H_H / H_f\right)$.

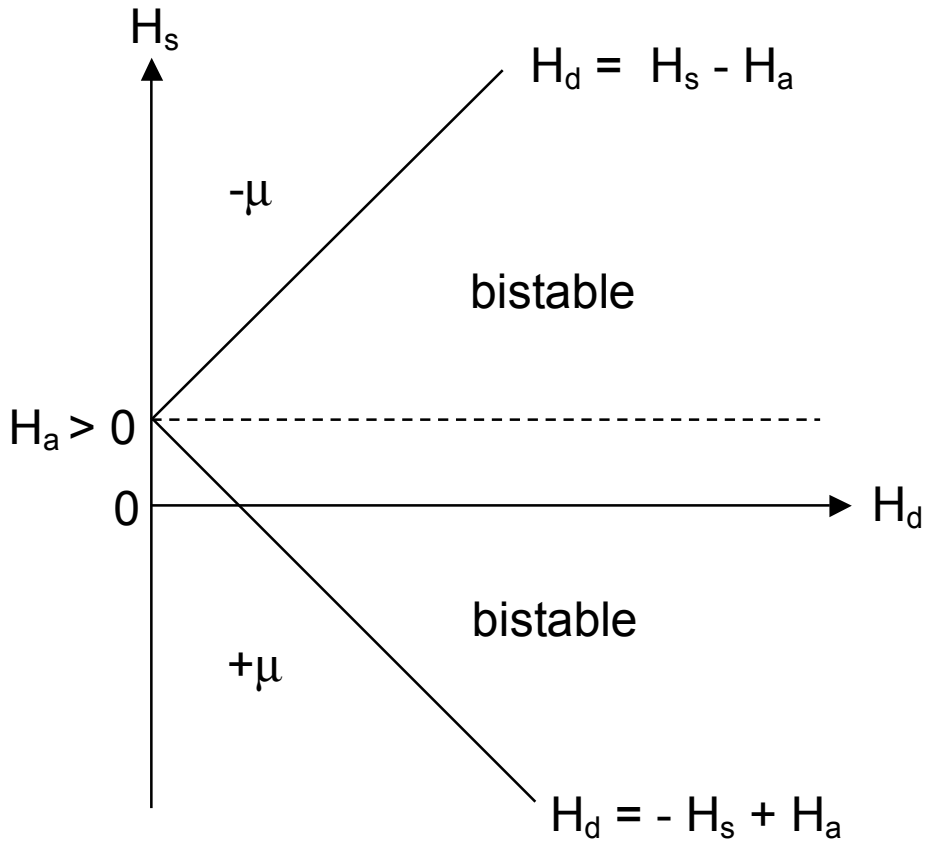

Figure 6.1: The configuration of the Preisach plane in an applied field $H_a > 0$ at T = 0.

Only the bistable subsystems in category (b) can participate in thermally driven relaxation phenomena, and the time constant for these relaxation processes is $\tau = \tau_L \tau_H / \left(\tau_L + \tau_H\right)$. However, due to the exponential dependence of τ_L and τ_H on barrier height W, it follows that $\tau_L << \tau_H$ for all subsystems for which $\left(H_H - H_L\right) / H_f \cong \left|H_s - H_a\right| / H_f \geq 1$, that is, for which the magnitude of the energy level

splitting $|H_s - H_a|$ exceeds the thermal fluctuation field H_f. Thus $\tau \cong \tau_L$ for essentially all but the degenerate subsystems, and the thermal relaxation time constant for a bistable subsystem is given by $\tau \cong \tau_0 \exp\left[\tau\left(H_d - |H_s - H_a|\right)/kT\right] = \tau_0 \exp\left(H_L/H_f\right)$.

If a subsystem (H_d, H_s) is prepared in an initial (t = 0) state with level occupation probabilities ($P_+(0)$, $P_-(0)$) which does not correspond to the equilibrium configuration under the prevailing experimental conditions (H_a,T), then the subsystem level occupation probabilities $P_\pm(t)$ and the ensemble average subsystem moment $\langle m(t) \rangle = \mu[P_+(t)-P_-(t)]$ $= \mu[2P_+(t)-1]$ will relax exponentially as $\exp(-t/\tau)$ toward their thermal equilibrium values (see Section 1.5 of Chapter 1). Substituting the subsystem relaxation time constant $\tau = \tau_L = \tau_0 \exp(H_L/H_f)$ into the exponential relaxation factor yields:

$$g\left(t,H_L\right) = \exp\left(-\frac{t}{\tau}\right) = \exp\left[-\frac{t}{\tau_0}\exp\left(-H_L/H_f\right)\right]. \qquad (6.1)$$

If $g(t,H_L) = 1$, no relaxation has yet occurred, while if $g(t,H_L) = 0$, relaxation to the equilibrium configuration is complete. Figure 6.2(a) shows a plot of $g(t,H_L)$ as a function of the logarithm of the observation time $\ln(t/\tau_0)$ for two fixed values of the lower barrier height, $H_L/H_f = 5$ and $H_L/H_f = 10$. On a logarithmic time scale, the transition from the initial nonequilibrium configuration to the final equilibrium configuration is spread over an observation time interval $\Delta\ln(t/\tau_0) \sim 3$ centred at $\ln(t/\tau_0) = H_L/H_f$, the ratio of the excitation barrier H_L to the fluctuation field H_f. Alternatively, we may plot $g(t,H_L)$ as a function of H_L/H_f for a fixed experimental observation time $t = t_{exp}$, as shown in Figure

6.2(b) for two different values of the observation time, $t_{exp}/\tau_0 = 2.2x10^4$ and $t_{exp}/\tau_0 = 10^9$. This expression defines a "thermal relaxation front [24]" centered at $H_L/H_f = \ln(t_{exp}/\tau_0) = 10$ for $t_{exp}/\tau_0 = 2.2x10^4$ and at $H_L/H_f = \ln(t_{exp}/\tau_0) = 20.7$ for $t_{exp}/\tau_0 = 10^9$, of width $\Delta H_L/H_f \sim 3$. The front separates the subsystems into 3 subpopulations, subsystems with $H_L/H_f < \ln(t_{exp}/\tau_0) - \Delta H_L/H_f$ which are completely relaxed to equilibrium, subsystems with $H_L/H_f > \ln(t_{exp}/\tau_0) + \Delta H_L/H_f$ which have not yet begun to relax, and subsystems with $\ln(t_{exp}/\tau_0) - \Delta H_L/H_f < H_L/H_f < \ln(t_{exp}/\tau_0) + \Delta H_L/H_f$ which are actively relaxing at this time t_{exp}. The relaxation front in Figure 6.2(b) propagates from left to right with increasing observation time.

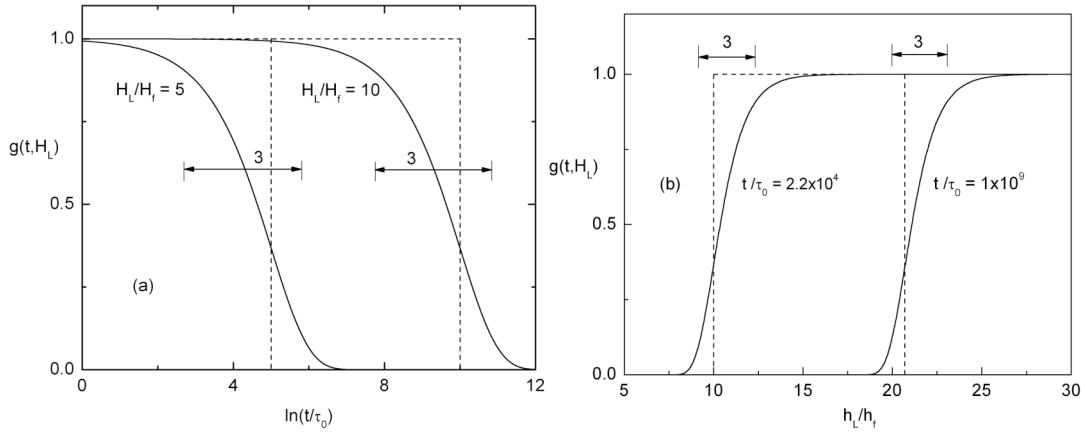

Figure 6.2: (a) A plot of the relaxation factor $g(t, H_L)$ in Eq(6.1) as a function of $\ln(t/\tau_0)$ for two fixed values of the lower barrier height H_L/H_f. (b) A plot of the relaxation factor as a function of H_L/H_f for two fixed values of the observation time t/τ_0. The dotted lines are step function approximations to the real relaxation factor.

The relaxation response M(t) of the entire Preisach ensemble in a field H_a at temperature T is obtained by superposing the relaxation contributions from all of the individual Preisach subsystems:

$$M(t) = N\mu \int_0^{\infty} dH_d \int_{-\infty}^{+\infty} dH_s \left[2P_+(t) - 1\right] p(H_d, H_s). \qquad (6.2)$$

If the Preisach distribution $p(H_d,H_s)$ is constant over characteristic field intervals ΔH_d and ΔH_s on the order of H_f , then the contribution to the ensemble moment in Eq(6.2) from the actively relaxing subsystems in the transition layer of width $3H_f$ in Figure 6.2(b) is proportional to the integral $\int dH_d \int dH_s \; g(t, H_d, H_s)$ over the relaxation frontal boundary $g(t,H_L)$. For fixed H_d, the integral over H_s can be approximated to excellent accuracy by replacing the exponential factor $g(t,H_L)$ by a vertical step function, as shown by the dotted lines in Figure 6.2(b). In this limit, there is a one-to-one correspondence between a particular experimental observation time t_{exp} and a specific barrier height H_L, so that the single subsystem relaxation response function in Figure 6.2(a) also reduces to a step function (dotted lines). The "critical" condition for the thermal activation (on warming) or thermal deactivation (on cooling) of bistable subsystems is then represented geometrically in the Preisach plane as a sharp thermal boundary defined by $H_T = H_f \ln\left(t_{exp}/\tau_0\right) = H_d - \left|H_s - H_a\right| = H_L$, which subdivides the Preisach plane into two subpopulations, subsystems with $H_L < H_T$ which are in thermal equilibrium, and subsystems with $H_L > H_T$ which are trapped in their t = 0 nonequilibrium configuration,

as shown in Figure 6.3. However, it is important to keep in mind that, in reality, this thermal boundary has an intrinsic "thermal fuzziness" $\Delta H_T \sim 3\, H_f$.

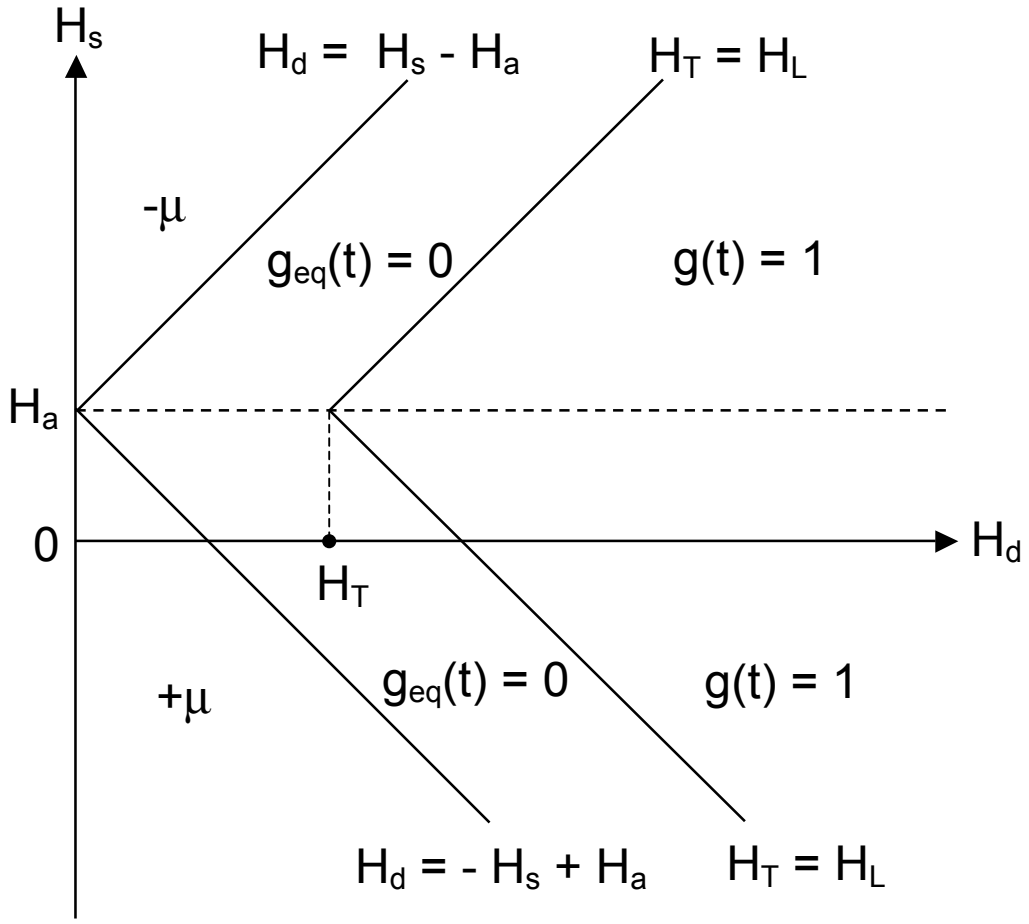

Figure 6.3: A geometrical representation of the entire Preisach ensemble in a field H_a at a temperature T. The region labelled $g_{eq}(t) = 0$ represents subsystems which are in thermal equilibrium. The region labelled g(t)=1 represents subsystems which are trapped in their initial nonequilibrium configuration.

6.3 Modeling Changes in Temperature: Cooling, Warming and Temperature Cycling

In both phase space (hierarchical) and real space (droplet excitation) models of spin glasses, aging and memory effects are intimately related to the sensitivity of the free energy landscape or to the fragility of the domain configuration to changes in temperature. A rigorous exploration of aging and memory effects in collections of two-level subsystems thus demands a precise model representation for the various experimental cooling, warming and temperature cycling protocols normally employed to probe spin glass relaxation dynamics. We have adopted the following representation.

All changes in temperature are modeled as a sequence of two steps. The first step is an instantaneous "quench" to the target temperature T from the previous temperature $T \pm \Delta T$, which resets the relaxation clock to $t = \tau_0$ and hence the thermal viscosity field to $H_T = 0$, while temporarily freezing the entire Preisach plane at its previous configuration. The second step is a temperature stabilization pause at T of duration t_{stab} , during which the thermal viscosity field grows continuously from $H_T = 0$ to $H_T = H_f \ln(t_{stab}/\tau_0)$, and the thermal boundary H_T sweeps smoothly through the Preisach plane, driving all subsystems with lower barriers $H_L < H_T$ to thermal equilibrium at T, and leaving all subsystems with $H_L > H_T$ trapped in their previous configurations. For a particular subsystem with characteristic fields (H_d,H_s), the condition $H_T = H_f \ln\left(t_{stab}/\tau_0\right) = H_L = H_d - \left|H_s - H_a\right|$ defines the **blocking temperature** $T_B = \mu\left(H_d - \left|H_s - H_a\right|\right) / \left(k \ln\left(t_{stab}/\tau_0\right)\right)$. For $T > T_B$, the subsystem relaxation time τ is shorter than the experimental stabilization (measurement)

time t_{stab} ($\tau < t_{stab}$) , the subsystem reaches thermal equilibrium during the time scale of the experiment, and the subsystem moment is given by $m_{eq} = \mu \tanh[\mu(H_a - H_s) / kT]$. For $T < T_B$, the Boltzmann occupation probabilities of the two subsystem levels are permanently frozen at their $T = T_B$ values and the subsystem moment is permanently frozen at $m_B = \mu \tanh[\mu(H_a - H_s)/kT_B]$. If cooling or warming with a fixed stabilization time t_{stab} is interrupted temporarily at a preselected temperature T_a, at which the system is aged for a time $t_a >> t_{stab}$, then subsystems with lower barriers between $(kT_a/\mu) \ln(t_{stab}/\tau_0) < H_L < (kT_a/\mu) \ln((t_{stab}+t_a)/\tau_0)$, which would have failed to reach thermal equilibrium at T_a during uninterrupted cooling or warming, now have sufficient time to equilibrate at T_a. When cooling or warming is resumed after aging, and the system is quenched instantaneously and incrementally to $T_a \pm \Delta T$ followed by stabilization for t_{stab}, this aged "pocket" of subsystems will remain trapped (blocked) in their T_a-configurations, leaving a "permanent" imprint on the configuration of the ensemble. It is this imprint which distinguishes the aged system from the unaged system, and which is responsible for the various memory effects described below. However, it is important to remember that the approximation by which the real relaxation front is replaced by a perfectly sharp transition (Figure 6.2) can potentially produce "artificial" aging imprints which are effectively wiped out when the "thermal fuzziness" H_f of the thermal front is taken into consideration. Thus, for an "aging imprint" to survive as a physically reality, **the difference between the thermal boundary $H_{Ta} = (kT_a/\mu) \ln((t_{stab}+t_a)/\tau_0)$ immediately after aging and the thermal boundary $H_{T\pm} = (k(T_a \pm \Delta T)/\mu) \ln(t_{stab}/\tau_0)$ immediately after the temperature change, $\Delta H_T = H_{Ta} - H_{T\pm}$, must be not only positive (that is,**

$H_{T\pm} < H_{Ta}$**), but also large in comparison with H_f** $\left(\Delta H_T = H_{Ta} - H_{T\pm} >> H_f > 0\right)$. As a corollary, it follows that a **negative value** of $\Delta H_T = H_{Ta} - H_T\pm$ (that is $H_{T\pm} > H_{Ta}$) necessarily **wipes out** all evidence of aging and consequently leaves no aging imprint.

When presenting model simulations, it is convenient to express fields and temperatures in dimensionless units, and to identify these with lowercase letters. Thus all fields H (and field dispersions) are reduced to the median dissipation field H_{dm} as $h = H/H_{dm}$, and all temperatures T are expressed in terms of the reduced thermal fluctuation field $h_f = H_f / H_{dm} = kT/(\mu H_{dm})$. This convention will be adhered to throughout the remainder of this chapter.

As an illustration of the effects of the experimental time constant t_{stab} on standard magnetic response functions, Figure 6.4(a) shows numerical simulations for two different measurement (stabilization) times $t_{stab} = 2.2x10^4\tau_0$ and $t_{stab} = 4.9x10^8\tau_0$, of the temperature dependence of the field cooled (FC) moment and the zero field cooled (ZFC) moment of an ensemble of two-level subsystems described by a product of a lognormal and a Gaussian distribution of characteristics fields $p(h_d,h_s) = (2\pi\sigma_d^2 h_d^2)^{-1/2} \exp[-(\ln h_d)^2/(2\sigma_d^2)] (2\pi\sigma_s^2)^{-1/2}\exp(-h_s^2/2\sigma_s^2)$ with $\sigma_d = 0.5$ and $\sigma_s = 0.5$. The FC moment is obtained by cooling in a reduced field $h_a = 0.1$ from a reference temperature $h_{f,ref}$ which exceeds the highest blocking temperature of the assembly to $h_f = 0$, assuming the same stabilization time t_{stab} at all temperatures, while the ZFC moment is obtained by cooling in zero field $h_a = 0$ to $h_f = 0$ followed by the application of a field $h_a = 0.1$ and then by warming, once again assuming the same stabilization pause t_{stab} at all temperatures.

According to Figure 6.4(a), increasing the experimental measuring time t_{stab} enhances the in-field response of both the FC and ZFC branches, precisely as observed experimentally.

Figure 6.4(b) shows numerical simulations of the temperature dependence of the field cooled (FC) moment and the zero field cooled (ZFC) of an ensemble of two-level subsystems with the same lognormal distribution of dissipation fields as above, $f(h_d) = (2\pi\sigma_d^2 h_d^2)^{-1/2} \exp[-(\ln h_d)^2/(2\sigma_d^2)]$ with $\sigma_d = 0.5$, but with a **bimodal** Gaussian distribution of bias fields $g(h_s) = (8\pi\sigma_s^2)^{-1/2}\exp[-(h_s-h_{s0})^2/2\sigma_s^2] + (8\pi\sigma_s^2)^{-1/2}\exp[-(h_s+h_{s0})^2/2\sigma_s^2]$ with $\sigma_s = 0.5$ and $h_{s0} = 1.5$. In contrast to the behaviour observed in Figure 6.4(a), the FC moment in Figure 6.4(b) increases with increasing temperature, much like the behaviour reported for real spin glasses, and an increase in the experimental measuring time t_{stab} has the opposite effect on the two branches, suppressing the magnitude of the FC moment and enhancing the magnitude of the ZFC moment.

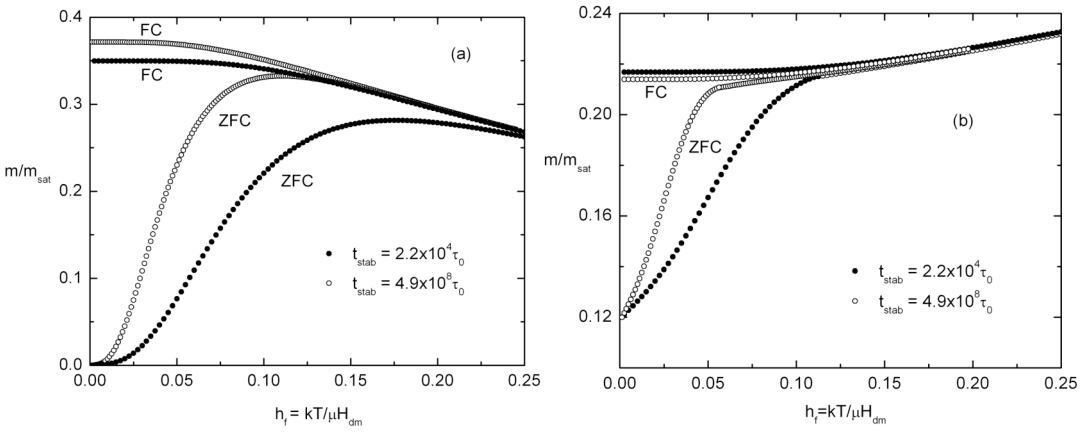

Figure 6.4: (a) Numerical simulations of the temperature dependence of the field cooled (FC) moment and the zero field cooled (ZFC) moment of an ensemble of two-level subsystems with a lognormal distribution of dissipation fields and a gaussian distribution of bias fields, in an applied field $h_a = 0.1$, for two different stabilization times. (b) Numerical simulations of the temperature dependence of the FC moment and the ZFC moment of an ensemble of two-level subsystems with the same lognormal distribution of dissipation fields as in (a) but with a bimodal Gaussian distribution of bias fields in an applied field $h_a = 1.1$.

6.4 Aging

The principal experimental signatures of aging in atomic spin glasses and superspin glasses are summarized in Figure 6.5. Figure 6.5(a) shows the time dependence of the FC moment of a $Fe_{0.5}Mn_{0.5}TiO_3$ Ising spin glass at several constant temperatures below T_G following field cooling from above T_G [25]. The relaxation is monotonically upward at higher temperatures, monotonically downward at lower temperatures, and crosses over from downward at short times and to upward at longer times at intermediate temperatures. Figure 6.5(b) shows the time dependence of the real part of the frequency dependent susceptibility of an assembly of FeC nanoparticles after cooling through T_G and stabilizing at a fixed temperature below T_G [26]. The susceptibility relaxes monotonically downward with time. Figure 6.5(c) shows the time dependence of the TRM of an assembly of ferritin (iron-storage protein) nanoparticles after cooling from above to below T_G in a field H_a = 200 Oe, aging the system for various times t_w at constant temperature in constant field, and then removing the field [27]. The TRM relaxation isotherms exhibit a systematic shift toward longer observation times with increasing wait time. Figure 6.5(d) shows the relaxation rate S = dm/dlnt of a CuMn spin glass after zero field cooling from above to below T_G, aging the system for various times t_w at constant temperature in zero field, and then applying a positive probing field [28]. The relaxation rate exhibits a maximum at an observation time which is essentially coincident with the aging time t_w. Figure 6.5(e) shows the same experiment as that in Figure 6.5(d) performed on a frozen ferrofluid of γ-Fe_2O_3 nanoparticles [29]. Once again,

the relaxation rate exhibits a age-dependent maximum which propagates toward longer observation times with increasing age.

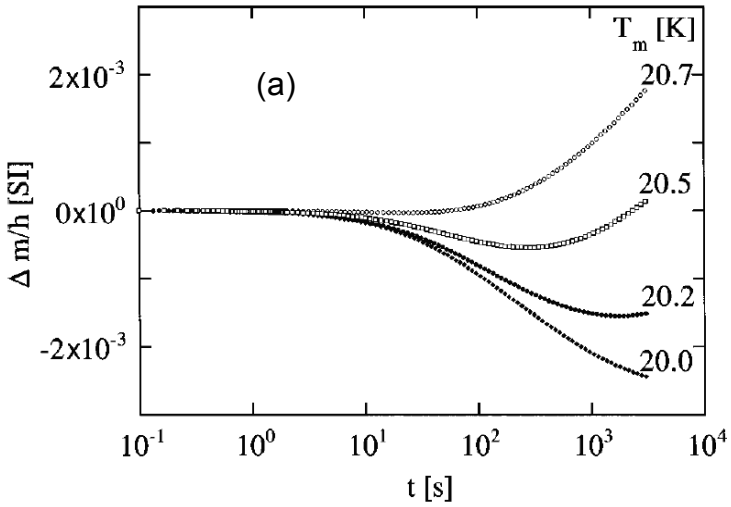

Figure 6.5(a): The time dependence of the FC moment of a $Fe_{0.5}Mn_{0.5}TiO_3$ Ising spin glass at various temperatures below the glass temperature T_G. Reprinted figure with permission from Jonsson, Jonason, and Nordblad, Physical Review B **59**, 9402 (1999). Copyright 1999 by the American Physical Society. http://link.aps.org/abstract/PRB/v59/p9402

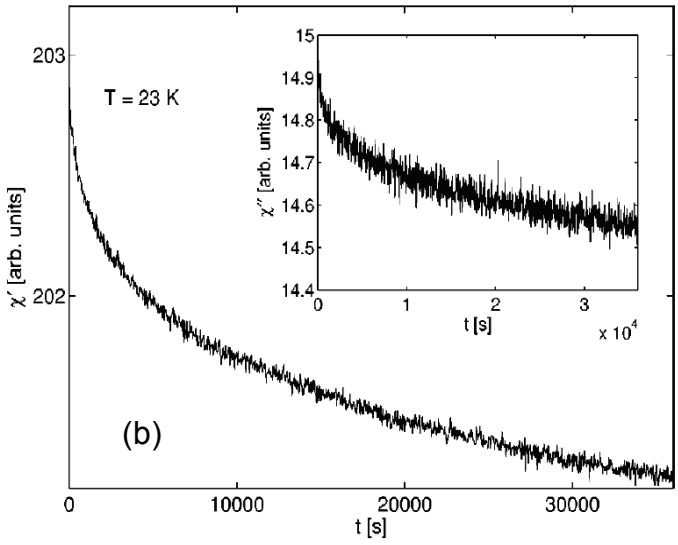

Figure 6.5(b): The time dependence of the real part of the frequency dependent susceptibility of an assembly of FeC nanoparticles after cooling from above T_G and stabilizing at $T < T_G$. Reprinted figure with permission from Jönsson, Hansen, and Nordblad, Physical Review B **61**, 1261 (2000). Copyright 2000 by the American Physical Society. http://link.aps.org/abstract/PRB/v61/p1261

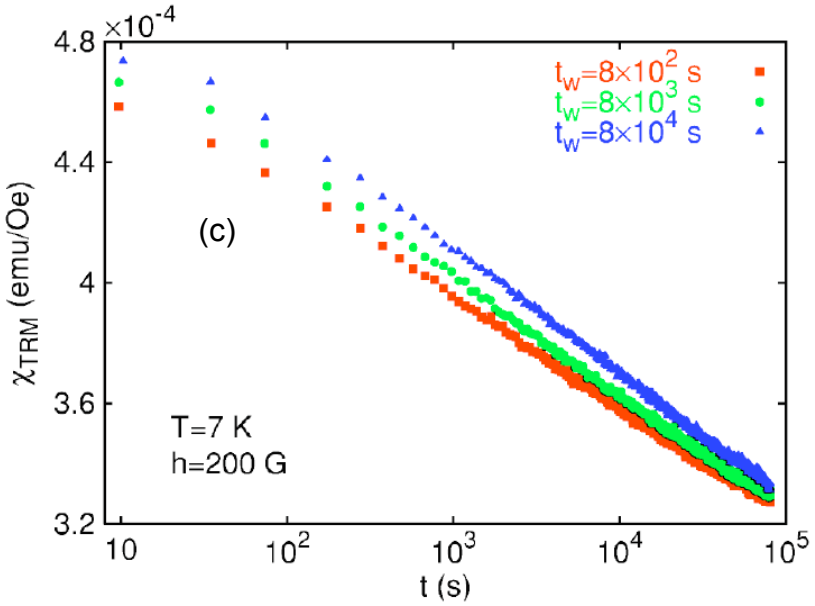

Figure 6.5(c): The time dependence of the TRM of an assembly of ferritin nanoparticles after cooling from above T_G in a field of H_a = 200 Oe and aging the system for various waiting times t_w at fixed temperature, followed by removal of the field. Reprinted figure with permission from Sasaki, Jönsson, Takayama and Mamiya, Physical Review B **71**, 104405 (2005). Copyright 2005 by the American Physical Society. http://link.aps.org/abstract/PRB/v71/e104405

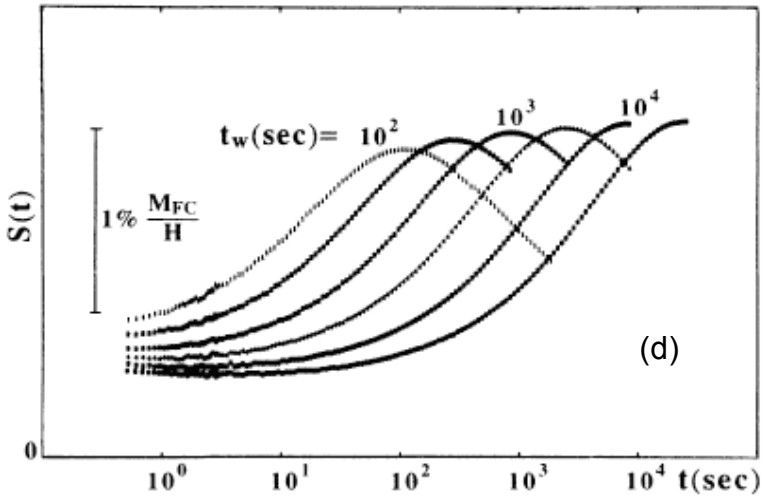

Figure 6.5(d): The relaxation rate (S = dm/dlnt) of a CuMn spin glass after cooling in zero field from above T_G, aging the system at constant temperature for various times t_w, followed by the application of a positive field. Reprinted figure with permission from Granberg, Sandlund, Nordblad, Svedlindh, and Lundgren, Physical Review B **38**, 7097 (1988). Copyright 1988 by the American Physical Society. http://link.aps.org/abstract/PRB/v38/p7097

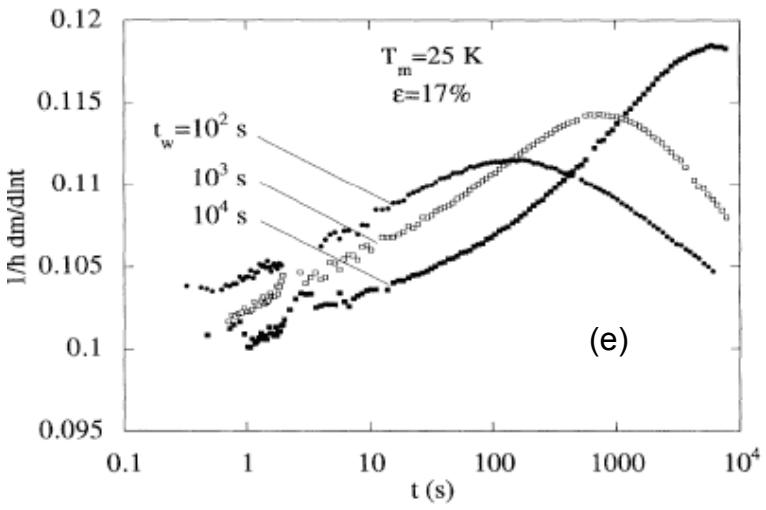

Figure 6.5(e): The same experiment as in 3(d), but performed on a frozen ferrofluid of γ-Fe_2O_3 nanoparticles. Reprinted Figure with permission from Jonsson, Mattson, Djurberg, Khan, Nordblad, and Svedlindh, Physical Review Letters **75**, 4138 (1995) Copyright 1995 by the American Physical Society. http://link.aps.org/abstract/PRL/v75/p4138

Numerical simulations of the aging experiments described above, performed on a model ensemble of two-level subsystems, show that aging is also a characteristic of a collection of interacting entities which relax independently over individual free energy barriers. Figure 6.6(a) shows a geometrical representation in the Preisach plane of the aging of the FC moment at a fixed aging temperature $h_{fa} = kT_a/(\mu H_{dm})$ in a constant field h_a, following cooling from a reference temperature $h_{f,\,ref} = kT_{ref}/(\mu H_{dm})$, which exceeds all of the subsystem blocking temperatures, to h_{fa} with a cooling stabilization time constant $t_{stab} = t_c$. The dashed diagonal lines in Figure 6.6(a) with vertex at $h_d = h_{Ta,c} = h_{fa}\ln(t_c/\tau_0)$ show the location of the thermal relaxation front immediately following thermal stabilization at h_{fa}, and the solid diagonal boundaries with vertex at $h_d = h_{Ta} = h_{fa}\ln((t_c+t_a)/\tau_0)$ show the location of the thermal front after aging for a time t_a. The subsystems to the left of the dashed lines relaxed to equilibrium during stabilization,

while the subsystems between the dashed and solid boundaries relaxed to equilibrium during the subsequent aging. Figure 6.6(b) shows numerical simulations of the relaxation of the FC moment for two model ensembles, with identical lognormal distributions of dissipation fields $f(h_d) = (2\pi\sigma_d^2 h_d^2)^{-1/2} \exp[-(\ln h_d)^2/(2\sigma_d^2)]$ with $\sigma_d = 0.5$, but with different distributions of bias fields, one a simple Gaussian $g(h_s) = (2\pi\sigma_s^2)^{-1/2}\exp(-h_s^2/2\sigma_s^2)$ with $\sigma_s = 0.5$, and the other a bimodal Gaussian $g(h_s) = (8\pi\sigma_s^2)^{-1/2}\exp[-(h_s-h_{s0})^2/2\sigma_s^2] +(8\pi\sigma_s^2)^{-1/2}\exp[-(h_s+h_{s0})^2/2\sigma_s^2]$ with $\sigma_s = 0.5$ and $h_{s0} = 1.5$. The relaxation was calculated at a reduced temperature $h_{fa} = 0.1$, and in reduced fields $h_a = 0.8$ for the simple Gaussian, and $h_a = 1.1$ for the bimodal Gaussian. The FC moment of the simple Gaussian system relaxes upward with increasing wait time, while the FC moment of the bimodal system relaxes downward. It is clear from Figure 6.6(a) that, in both cases (and, in fact, in all subsequent experimental simulations), the relaxation originates physically from that group of subsystems (labels italicized in Figure 6.6(a)) which were blocked in low moment states $|m_B(h_{fB})|$ at thermal fluctuation fields $h_{fB} > h_{fa}$ and subsequently allowed to reach thermal equilibrium at the lower thermal fluctuation field h_{fa} where the moment is closer to saturation $|m_{eq}(h_{fa})| > |m_B(h_{fB})|$. For the simple Gaussian distribution, the contribution from subsystems below the line $h_s = +h_a$ with positive moments dominates, and the moment relaxes upward. For the bimodal distribution, the contribution from subsystems above the line $h_s = +h_a$ with negative moments dominates, and the moment relaxes downward. Figure 6.7(a) shows Preisach representation of the relaxation of the TRM at the instant of removal of the field h_a from the aged FC state in Figure 6.6(a). Figure 6.7(b) shows numerical simulations of the time dependence of the TRM after field

cooling to $h_{fa} = 0.04$ in a field $h_a = 0.01$ followed by field removal, for three different FC aging times $t_a = 10^{11}\tau_0$, $10^{12}\tau_0$, and $10^{13}\tau_0$ for a lognormal-simple Gaussian Preisach density with $\sigma_d = 0.5$ and $\sigma_s = 0.01$. Figure 6.7(c) shows the relaxation rate defined by S = - dTRM/dlnt for each of the relaxation isotherms in Figure 6.7(b). Each of the TRM relaxation isotherms exhibits a change in slope at an observation time which is essentially coincident with the aging time, that is, at $\ln t \sim \ln t_a$. Lastly, Figure 6.8(a) shows the Preisach representation of the relaxation of the ZFC moment at the instant that a positive field is applied to an aged ZFC state. Figure 6.8(b) shows numerical simulations of the time dependence of the relaxation rate $S = dm_{ZFC}/d\ln t$ of three ZFC relaxation isotherms for a system with a lognormal-simple Gaussian Preisach density with $\sigma_d = 0.5$ and $\sigma_s = 0.2$ which has been cooled to $h_{fa} = 0.1$ at $t_c = 2.2\text{x}10^4\tau_0$, and aged at h_{fa} for $t_a = 2.6\text{x}10^{10}\tau_0$, $1.4\text{x}10^{12}\tau_0$, and $7.9\text{x}10^{13}\tau_0$ before applying a field $h_a = 0.2$. As before, the relaxation rate exhibits structure, in this case a local maximum, at an observation time which is coincident with the aging time.

Proponents of droplet domain theories of spin glasses have long insisted that aging of the ZFC moment is a unique signature of cooperatively ordered magnetic states with spin glass correlations, and completely incompatible with model ensembles of independently relaxing elements [27, 30]. This study clearly shows that, while interactions between the Preisach elements are indeed a necessary prerequisite for the observation of ZFC aging effects, and that these aging effects disappear when the interaction field distribution collapses to a δ-function, $g(h_s) \rightarrow \delta(h_s)$, there is no

requirement that these interactions necessarily originate from collective ordering phenomena.

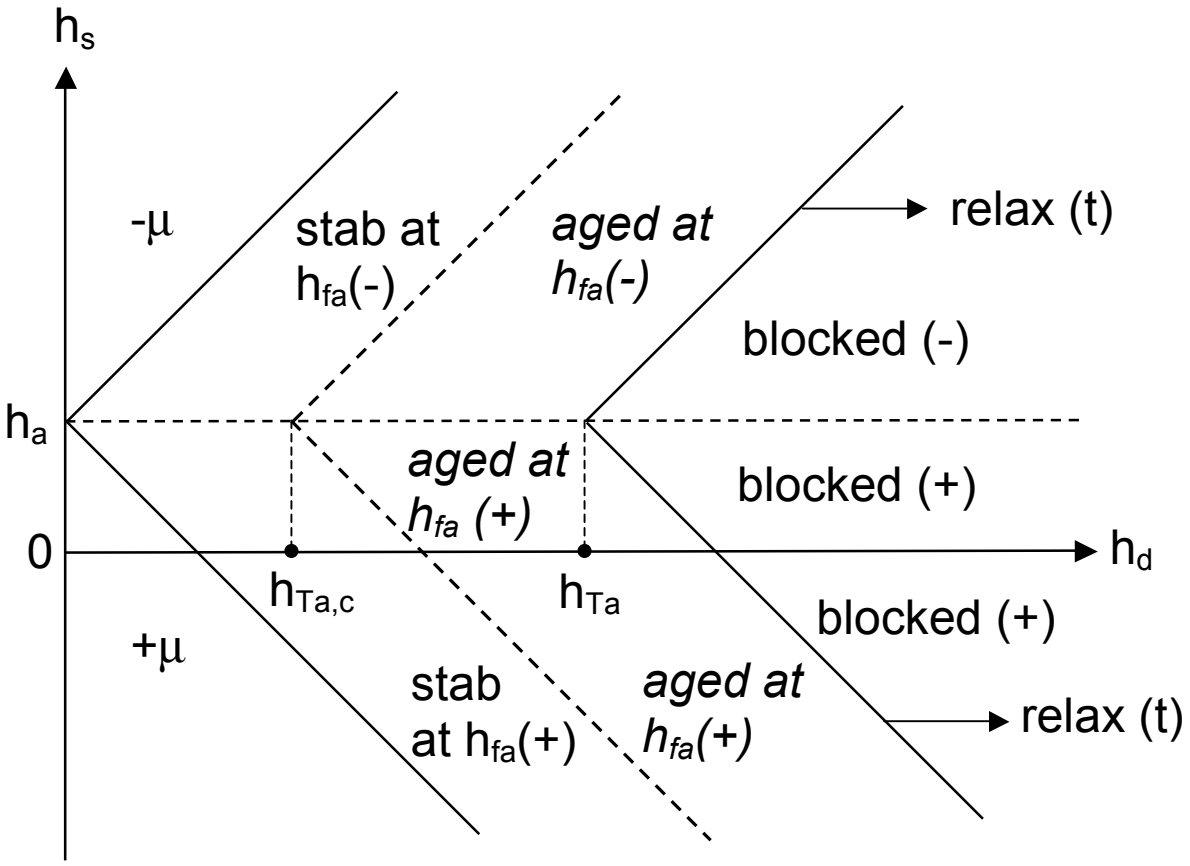

Figure 6.6(a): A geometrical representation in the Preisach plane of the aging of the FC moment at a fixed aging temperature h_{fa} in a constant field $h_a > 0$.

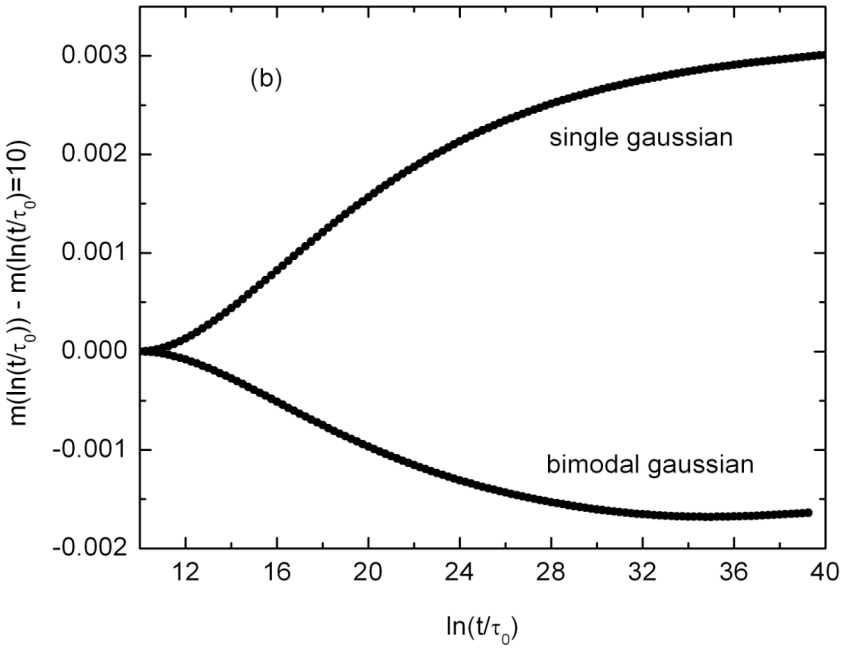

Figure 6.6(b): Numerical simulations of the relaxation of the FC moment for two model ensembles, both with lognormal distributions of dissipation fields, but each with different distributions of bias fields: one a single gaussian, the other a bimodal gaussian.

There is also compelling evidence to suggest that the distribution of bias fields may indeed be bimodal in high density nanoparticulate assemblies. Micromagnetic simulations [31] of the magnetization process in systems of ellipsoidal particles with uniaxial anisotropy, coupled by magnetostatic interaction fields, and governed by Landau-Lifshitz-Gilbert dynamics, performed for various packing fractions and easy axis orientations show that, for high packing fractions and highly oriented easy axes, the distribution of interaction fields evolves from a single-peaked distribution with a positive mean at positive saturation, to a double-peaked distribution with zero mean near the zero moment coercive field state, to a single-peaked distribution with a negative mean at negative saturation. This behaviour is attributed to the formation of "superferromagnetic

cluster domains" of magnetic particles which are analogous to traditional domains in bulk atomic ferromagnets, in the sense that the particle moments within a given cluster are aligned by the strong intracluster magnetostatic interactions along a common direction which varies from cluster to cluster. Cluster growth in response to a change in field is analogous to ferromagnetic domain growth in the sense that the border between clusters moves as particles from one cluster switch into the direction of the particles in the neighbouring cluster. The interactions described by the bimodal distribution are the interactions between clusters rather than the interactions between individual particles.

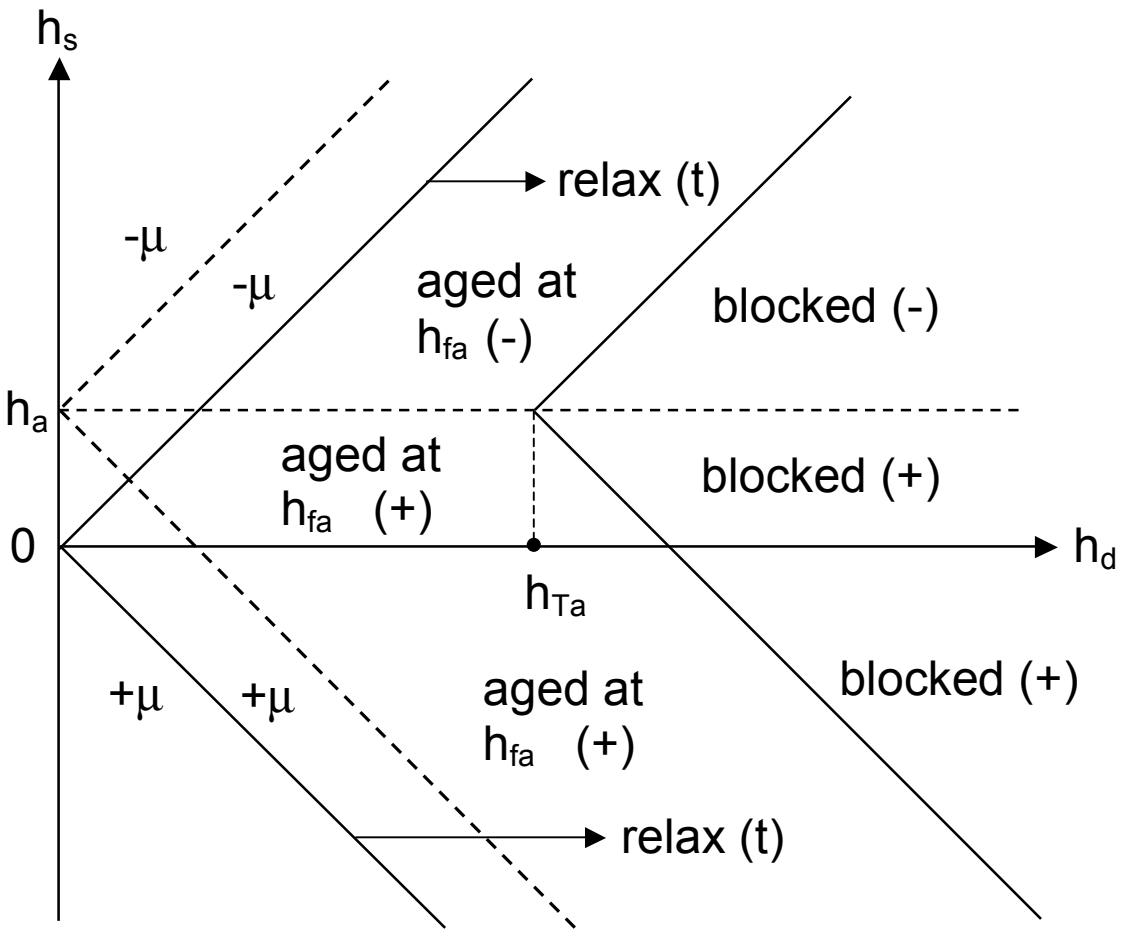

Figure 6.7(a): The Preisach representation of the relaxation of the TRM at the instant of field removal from the aged FC state depicted in Figure 6.6(a).

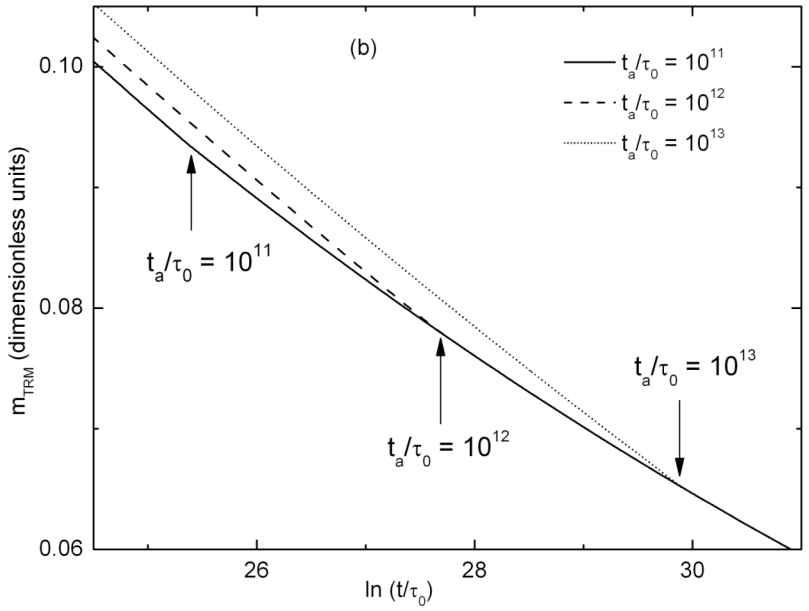

Figure 6.7(b): Numerical simulations of the time dependence of the TRM after field cooling in a constant field $h_a = 0.01$, and aging for three different times t_a / τ_0, followed by field removal.

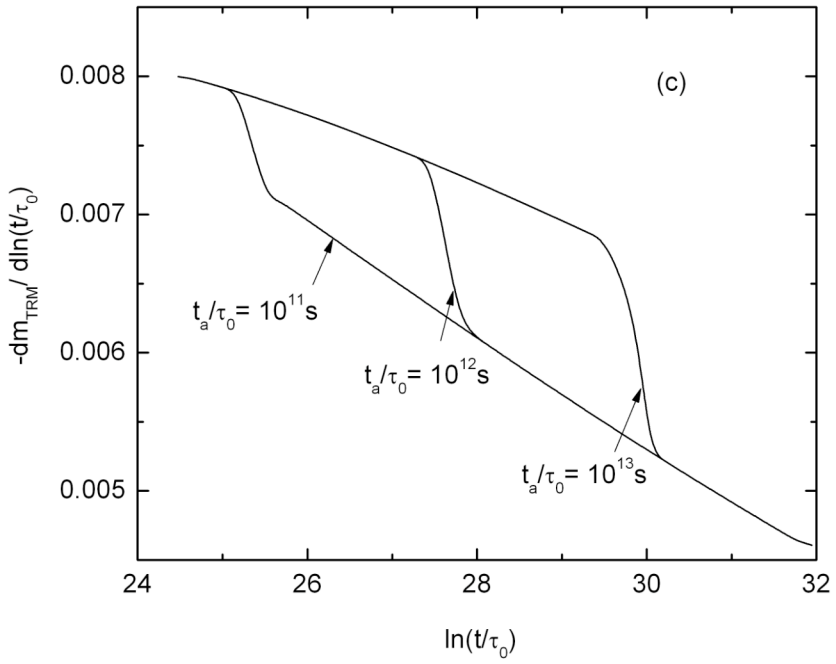

Figure 6.7(c): The relaxation rate as a function of $\ln(t/\tau_0)$ for each of the relaxation isotherms in Figure 6.7(b).

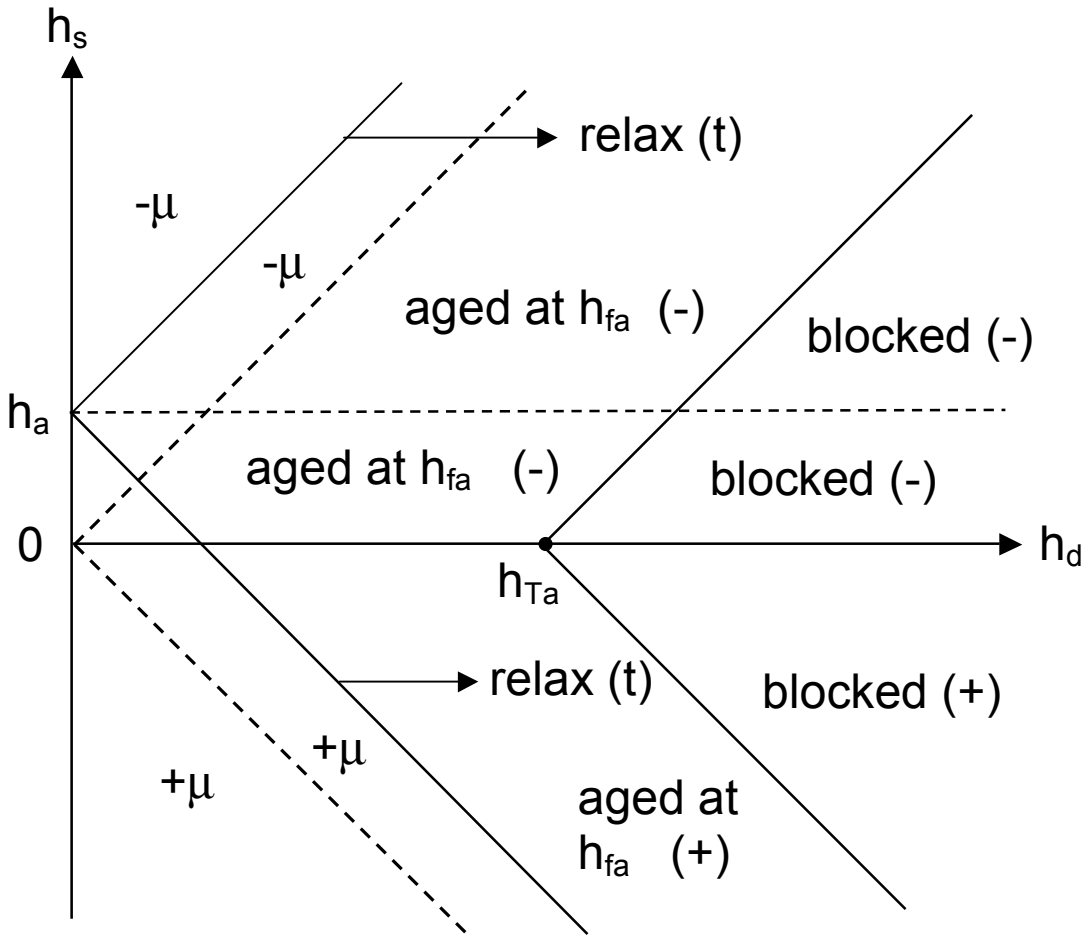

Figure 6.8(a): The Preisach representation of the relaxation of the ZFC moment at the instant that a positive field $h_a > 0$ is applied to the aged ZFC state.

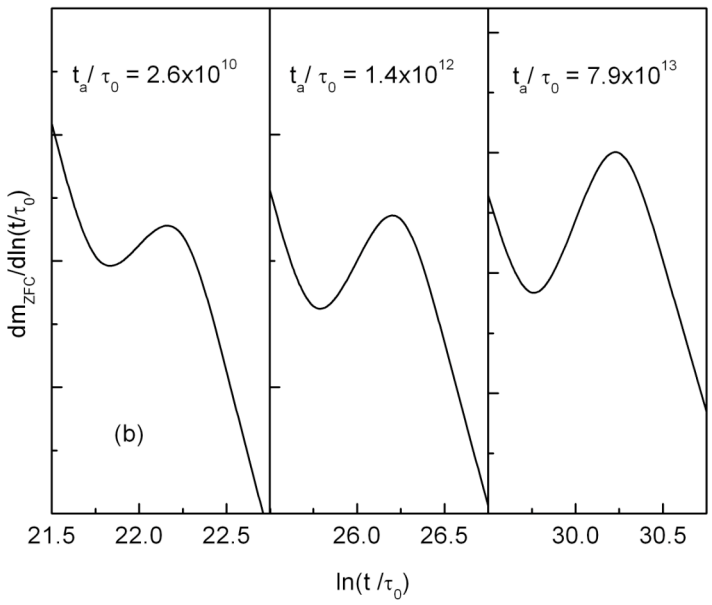

Figure 6.8(b): Numerical simulations of the time dependence of the relaxation rate of ZFC relaxation isotherms that have been aged for the three different aging times noted in each panel, following application of a positive field $h_a = 0.2$.

6.5 Memory

When a spin glass is cooled, memory of the cooling process is imprinted on the spin structure. The principal experimental signatures of memory in atomic spin glasses and superspin glasses are summarized in Figure 6.9. Figure 6.9(a) shows **memory steps** in the temperature dependence of the FC moment of a short-ranged Ising atomic spin glass $Fe_{0.5}Mn_{0.5}TiO_3$ which has been cooled in a field $H_a = 0.5$ Oe from above the glass temperature $T_G = 21$K at a constant rate of 0.4K/min with the exception of two temporary stops, one at T = 18K for 2h and another at T = 15K for 3h, and subsequently warmed from the lowest measurement temperature T = 11.5K [25]. During each of the isothermal aging pauses, the FC moment relaxes downward and persists at the lower level when

cooling is resumed. When the system is warmed, the warming curve tends to merge with the cooling curve, but only at temperatures well above the corresponding aging temperature. Figure 6.9(b) shows **memory dips** in the temperature dependence of the imaginary component χ'' of the frequency dependent susceptibility of a Cu-13.5at%Mn atomic spin glass measured on warming after the system has been subjected to two temporary aging stops on the order of 10^4s at T = 50K and T = 40K during cooling from above T_G = 68K [32]. The susceptibility on warming clearly exhibits two memory dips below the reference curve measured at a constant cooling rate in the absence of thermal pauses. Finally, Figure 6.9(c) shows a "genuine" **memory dip** in the ZFC moment of a dense assembly of Fe_3N nanoparticles for which cooling in **zero magnetic field** from above the ordering temperature has been interrupted temporarily by aging at constant temperature T = 40K for 9000s followed by further cooling, the application of a field H_a , and warming [27]. The figure shows that the difference $m_{ZFC} - m_{ZFC}(ref)$ between the ZFC moment measured on warming after interrupted cooling, and the reference ZFC moment measured without interrupted cooling exhibits a clear minimum at the aging temperature. As mentioned earlier, proponents of droplet domain theories contend [27] that "genuine" ZFC anomalies like that in Figure 6.9(c) are a unique signature of spin glasses, and provide a definitive criterion for distinguishing cooperatively ordered spin glasses from sequentially blocked superparamagnets.

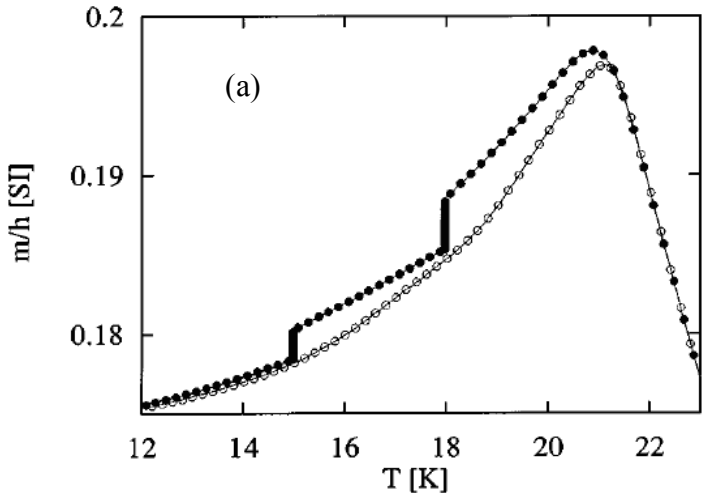

Figure 6.9(a): Memory steps in the temperature dependence of the FC moment of $Fe_{0.5}Mn_{0.5}TiO_3$ after having been cooled in a constant field with temporary stops at T = 18K and T = 15K, followed by warming. Reprinted figure with permission from Jonsson, Jonason, and Nordblad, Physical Review B **59**, 9402 (1999). Copyright 1999 by the American Physical Society. http://link.aps.org/abstract/PRB/v59/p9402

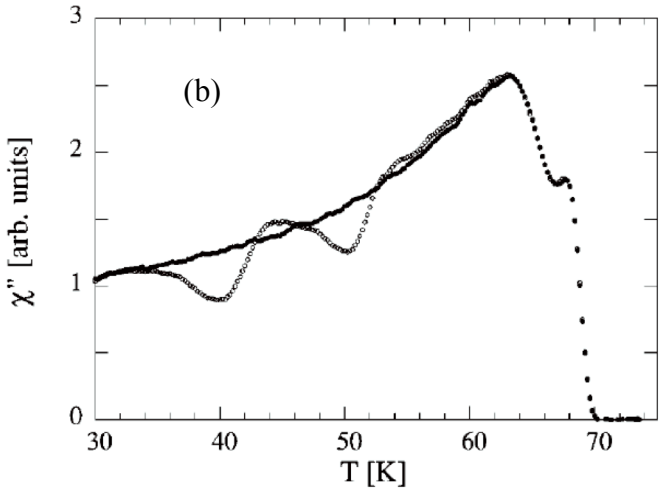

Figure 6.9(b): Memory dips in the temperature dependence of the imaginary component of the frequency dependent susceptibility of a Cu-13.5at%Mn spin glass measured on warming after having been aged at two different temperatures, T = 50K and T = 40K, during cooling. Reprinted figure with permission from Jonsson, Jonason, Jönsson, and Nordblad, Physical Review B **59**, 8770 (1999). Copyright 1999 by the American Physical Society. http://link.aps.org/abstract/PRB/v59/p8770

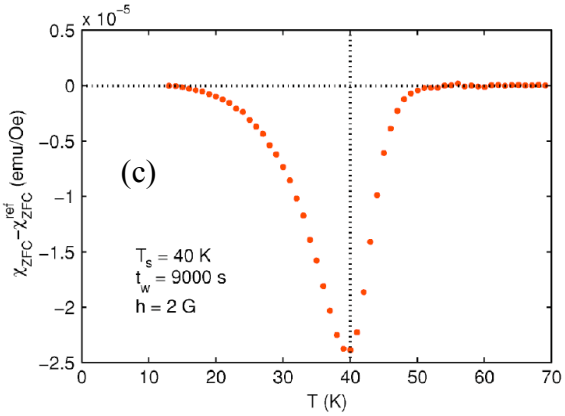

Figure 6.9(c): A memory dip in the ZFC moment of a dense assembly of Fe_3N nanoparticles for which aging at T=40K has occurred during cooling, followed by further cooling, the subsequent application of a positive field, and warming. Reprinted figure with permission from Sasaki, Jonsson, Takayama, and Mamiya, Physical Review B **71**, 104405 (2005). Copyright 2005 by the American Physical Society. http://link.aps.org/abstract/PRB/v71/e104405

Numerical simulations show that memory steps and memory dips are also characteristics of Preisach ensembles of two-level subsystems which relax independently over individual free energy barriers. Figure 6.10(a) shows the configuration of the Preisach plane for a system which has been cooled in a field h_a to h_{fa} with time constant t_c, aged at h_{fa} for a time t_a , and then cooled to $h_f = 0$ with time constant t_c , before warming with time constant $t_w = t_c$. Figure 6.10(b) shows numerical simulations of the temperature dependence of both the cooling and warming curves for an ensemble of two-level subsystems with a lognormal-bimodal Gaussian Preisach density with parameters $\sigma_d = 0.5$, $h_{s0} = 1.5$, and $\sigma_s = 0.5$, for which cooling in a field $h_a = 1.1$ with a fixed time constant $t_c = 2.2\text{x}10^4\tau_0$ has been twice interrupted temporarily, once at $h_{fa} = 0.12$ to age for $t_a = 4.9\text{x}10^8\tau_0$, and again at $h_{fa} = 0.06$ also to age for $t_a = 4.9\text{x}10^8\tau_0$, before cooling to $h_f = 0.02$ and then warming with time constant $t_w = 2.2\text{x}10^4\tau_0$. The cooling curve shows

two downward steps at the two aging temperatures, and the warming curve shows memory of each aging event through a tendency to approach and merge with the cooling curve above the corresponding aging temperature, precisely as observed experimentally.

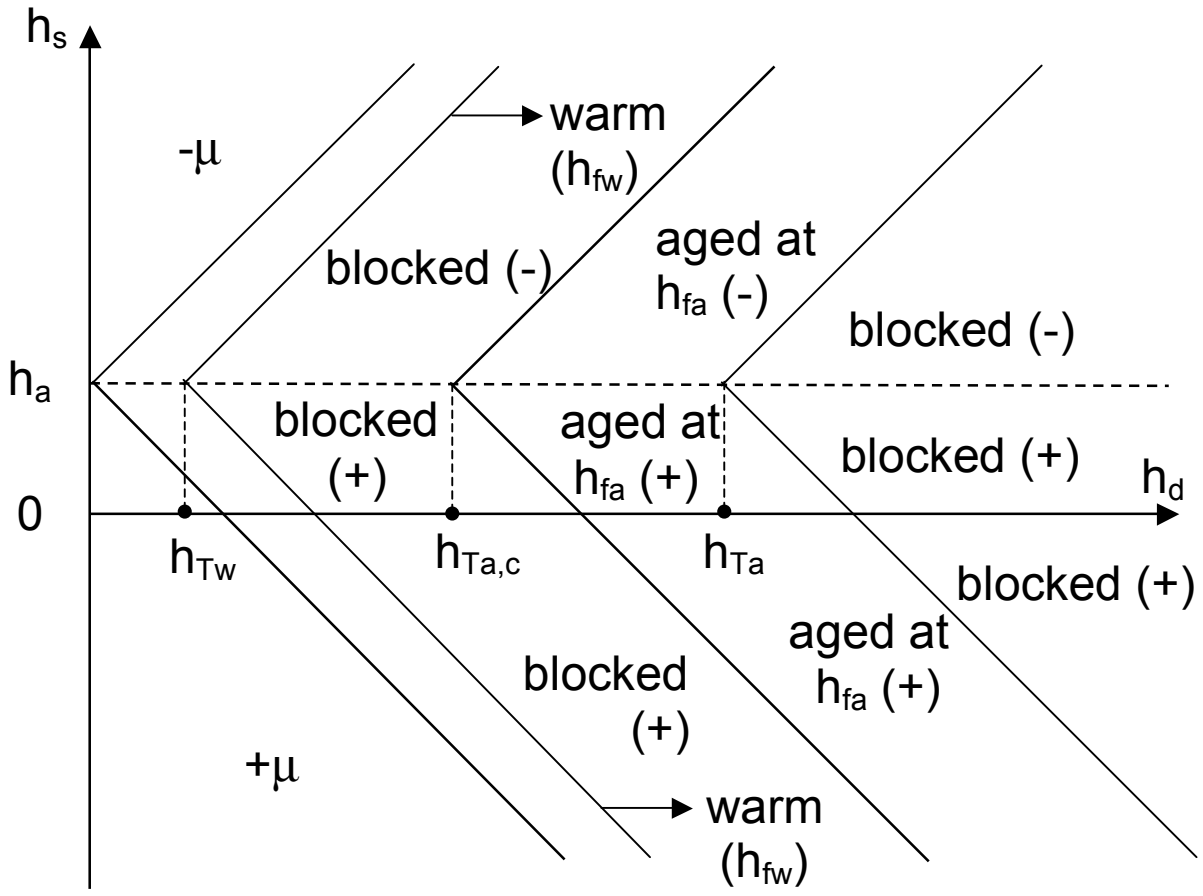

Figure 6.10(a): The Preisach representation of a system that has been cooled in a field $h_a > 0$ to a temperature h_{fa}, aged, then cooled to $h_f = 0$, and warmed.

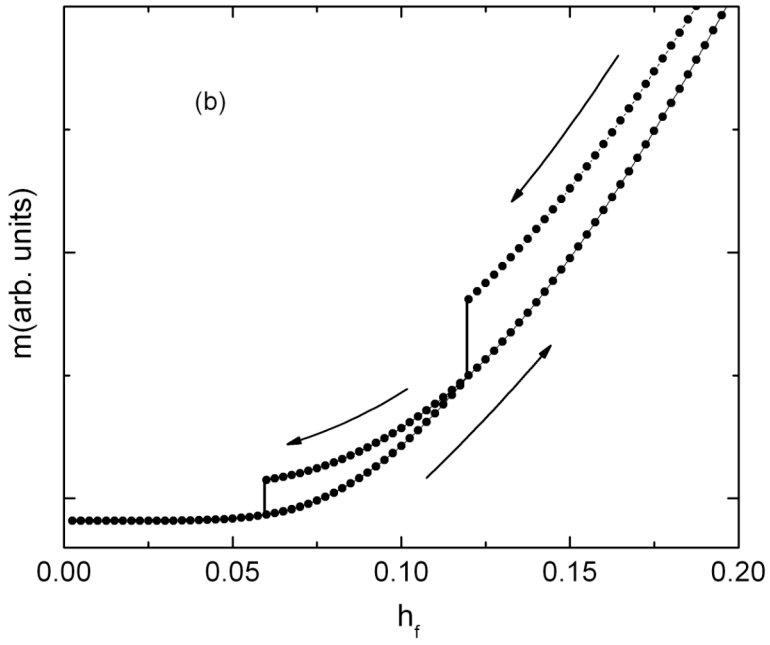

Figure 6.10(b): Numerical simulations of the temperature dependence of the FC moment in a constant field $h_a = 1.1$ for a Preisach ensemble which has been aged during cooling at two different temperatures $h_f = 0.12$ and $h_f = 0.06$, and then warmed. The upper set of data corresponds to cooling, and the lower set of data corresponds to warming.

Figure 6.11(a) shows the configuration of the Preisach plane at the instant of application of a positive field h_a for a system which has been previously cooled to a temperature T_a in zero field $h_a = 0$ and aged at h_{fa} for a time t_a . Figure 6.11(b) shows numerical simulations of the temperature dependence of the difference $\Delta m_{ZFC} = m_{ZFC}(\text{aged}) - m_{ZFC}(\text{unaged})$ between the aged ZFC moment calculated on warming and the unaged (reference) ZFC moment also calculated on warming, for an ensemble of two-level subsystems with a lognormal-single Gaussian Preisach density with distribution parameters $\sigma_d = 0.5$ and various values of σ_s , and with $h_a = 0.7$, $h_{fa} = 0.1$, $t_c = 2.2\text{x}10^4\tau_0$, $t_a = 8.9\text{x}10^6\tau_0$, and $t_w = 2.2\text{x}10^4\tau_0$. The difference shows a dip in the neighbourhood of

the aging temperature h_{fa}, which becomes progressively more pronounced as the dispersion of bias fields increases, emphasizing that the ZFC memory effect depends on the existence of interactions between the subsystems, and vanishes in the limit $\sigma_s \rightarrow 0$. There is, however, no requirement that these interactions be collective in any sense.

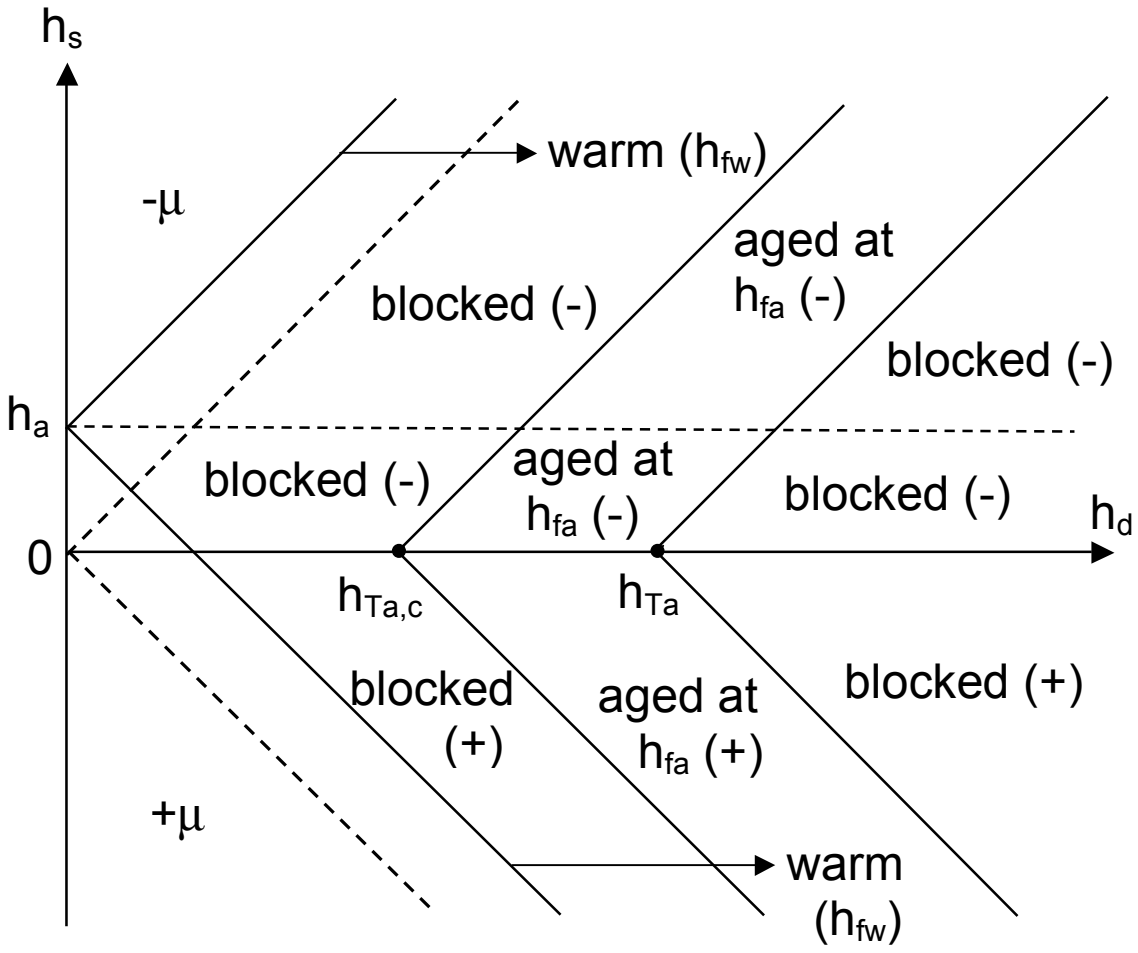

Figure 6.11(a): The Preisach representation at the instant of field application of a system which has been previously cooled to a temperature h_{fa} in zero field and aged in zero field.

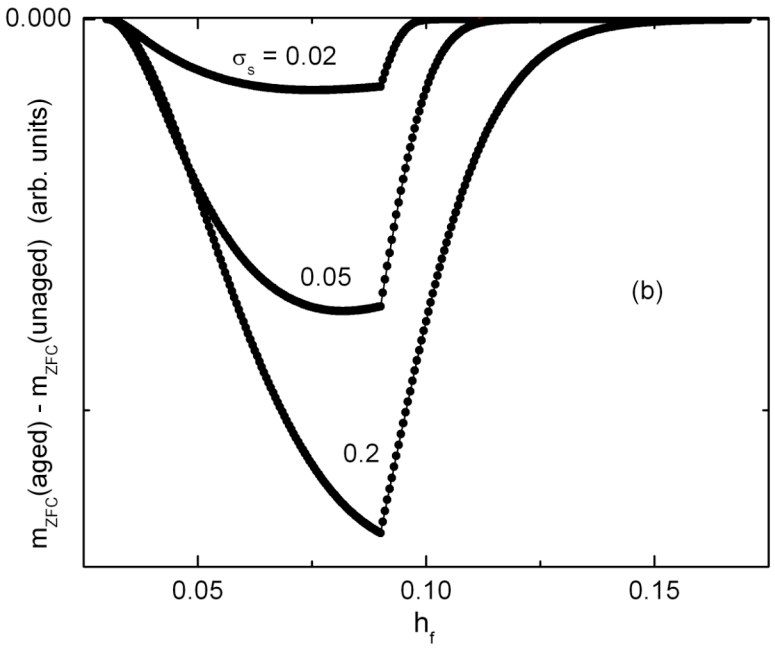

Figure 6.11(b): Numerical simulations of the difference between the aged ZFC moment and the unaged ZFC moment on warming.

6.6 Temperature Cycling, Rejuvenation, and Memory

Figure 6.12 shows measurements of the relaxation of the imaginary component χ'' of the frequency dependent susceptibility as a function of time t for an atomic $Ag_{0.89}Mn_{0.11}$ spin glass [11] with a critical temperature T_G = 32.8K which has been (a) aged for $t_a = 10^4$s at a series of temperatures T_a = 30K-ΔT followed by a positive temperature shift to T_m=30K where the relaxation is observed for a further $t_a = 10^4$s (Figure 6.12(a)) and, (b) aged for $t_a = 10^4$s at a series of temperatures T_a = 30K+ΔT followed by a negative temperature shift to T_m = 30K where the relaxation is observed for

a further $t_a = 10^4$s (Figure 6.12(b)). In both cases, if the temperature shift ΔT is sufficiently large, most of the aging accomplished at $T_a = 30K \pm \Delta T$ is virtually wiped out by the shift to T_m=30K, and the relaxation at T_m is essentially the same as if the system had been cooled directly to T_m=30K without any aging. That is, the system behaves as if it had been **completely rejuvenated**. In this limit, the measured relaxation curve at T_m=30K superposes almost perfectly onto the unperturbed "virgin" 30K relaxation curve with only a minor shift t_{eff} in the time scale. However, as the temperature shift ΔT becomes smaller, progressively more of the aging imposed on the system at $T_a = 30K \pm \Delta T$ survives the temperature shift, the rejuvenation effect becomes progressively weaker, the relaxation at T_m departs progressively further from the "virgin" 30K relaxation curve, and a progressively more significant time shift t_{eff} is required to achieve superposition. The insets in Figures 6.12(a) and 6.12(b) show that the superposition is never perfect, and always exhibits a **transient deviation**, which is below the "virgin" curve for $\Delta T > 0$ and above the "virgin" curve for $\Delta T < 0$.

Figure 6.12(c) shows a temperature cycling experiment performed on the $Ag_{0.89}Mn_{0.11}$ spin glass, which consists of aging at 30K for 3000s, followed by a negative temperature shift to 28K for 3000s, and finally by a positive temperature shift back to 30K. The system is essentially completely rejuvenated following the temperature shift to 28K. When the original temperature is recovered, the relaxation curve shows an initial transient, but eventually joins smoothly onto a time-shifted "virgin" 30K relaxation curve. Thus, in spite of the strong rejuvenation at 28K, the system eventually **heals** from

the effects of the perturbation at 28K while preserving some **memory** of the original aging at 30K.

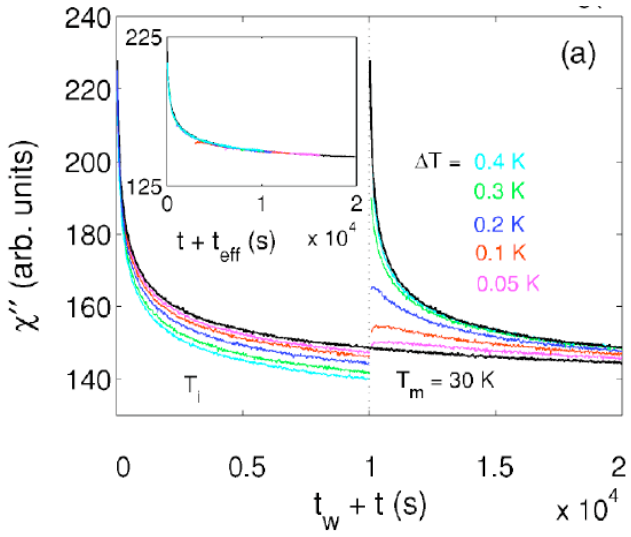

Figure 6.12(a): Measurements of the relaxation of the imaginary component of the frequency dependent susceptibility as a function of time of an atomic $Ag_{0.89}Mn_{0.11}$ spin glass which has been aged at a series of temperatures below 30K, followed by a positive temperature shift to 30K where the relaxation is continued.

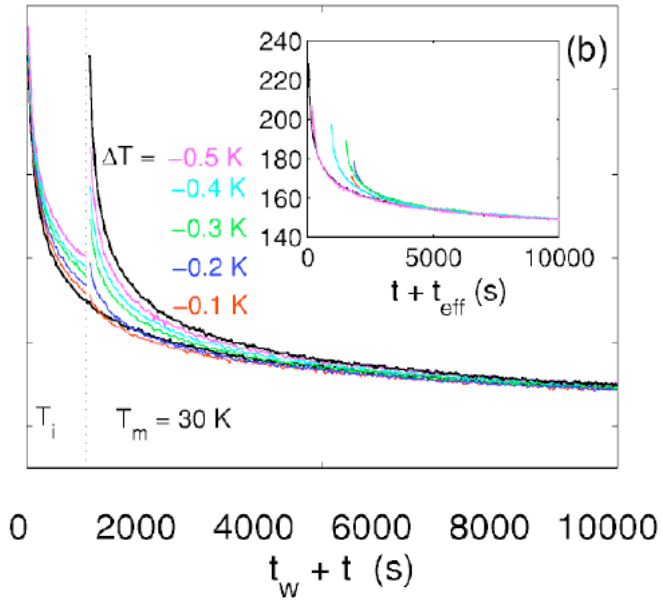

Figure 6.12(b): Measurements of the relaxation of the imaginary component of the frequency dependent susceptibility as a function of time of an atomic $Ag_{0.89}Mn_{0.11}$ spin glass which has been aged at a series of temperatures above 30K, followed by a negative temperature shift to 30K where the relaxation is observed further.

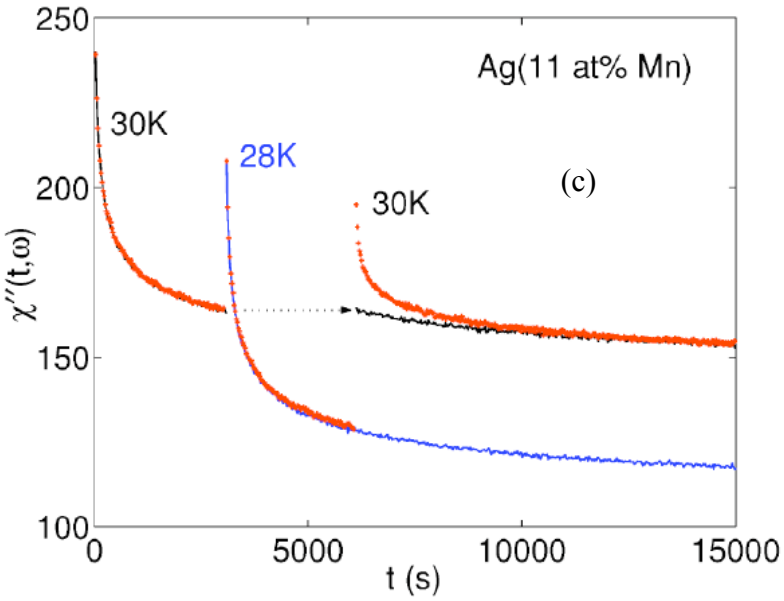

Figure 6.12(c): A temperature cycling experiment performed on an $Ag_{0.89}Mn_{0.11}$ spin glass. The cycling consisted of aging at T = 30K, cooling to 28K and aging, followed by warming to 30K and measuring the subsequent relaxation. Figures 6.12(a), (b), and (c) are reprinted with permission from Jönsson, Mathieu, Nordblad, Yoshino, Katori, and Ito, Physical Review B **70**, 174402 (2004). Copyright 2004 by the American Physical Society. http://link.aps.org/abstract/PRB/v70/e174402

The behaviour of superspin glasses in response to temperature shift and temperature cycle protocols differs from that of atomic spin glasses in several significant respects. Figure 6.13 shows measurements of the relaxation of the imaginary component χ'' of the frequency dependent susceptibility as a function of time t for the strongly interacting nanoparticulate Fe_3N superspin glass [33] with critical temperature $T_G \sim 60K$. Figure 6.13(a) shows a T-shift experiment which consists of a quench from $T_{ref} = 120K$ to $T_i = 42K$, followed by aging at T_i for $t_a \sim 10^4$s and then by a negative temperature shift to $T_m = 40K$. Figures 6.13(b) and 6.13(c) show the relaxation of the susceptibility χ'' with time t during all three stages of negative and positive T-cycle experiments consisting of the sequence $T_m(t_{w1}) \rightarrow T_m \pm \Delta T(t_{w2}) \rightarrow T_m$. The insets show that the susceptibility

relaxes with time in all three stages of the cycling process, and the main body of these figures shows the relationship between the initial and final stages of the relaxation at T_m following superposition of the third stage data onto the virgin reference isothermal relaxation curve at T_m by time shifting through $t_{eff}(\Delta T)$. The time shift t_{eff} for T-cycle experiments is negative for $\Delta T < 0$ and positive for $\Delta T > 0$. In contrast with the behaviour of atomic spin glasses, **complete rejuvenation is never observed** in the nanoparticulate Fe_3N superspin glass even for the largest temperature shifts ΔT investigated experimentally. Furthermore, the magnitude of the time shift $|t_{eff}|$ required to achieve superposition onto the virgin (or, equivalently, the perfectly rejuvenated) relaxation curve at T_m varies directly with the amplitude $|\Delta T|$ of the temperature shift.

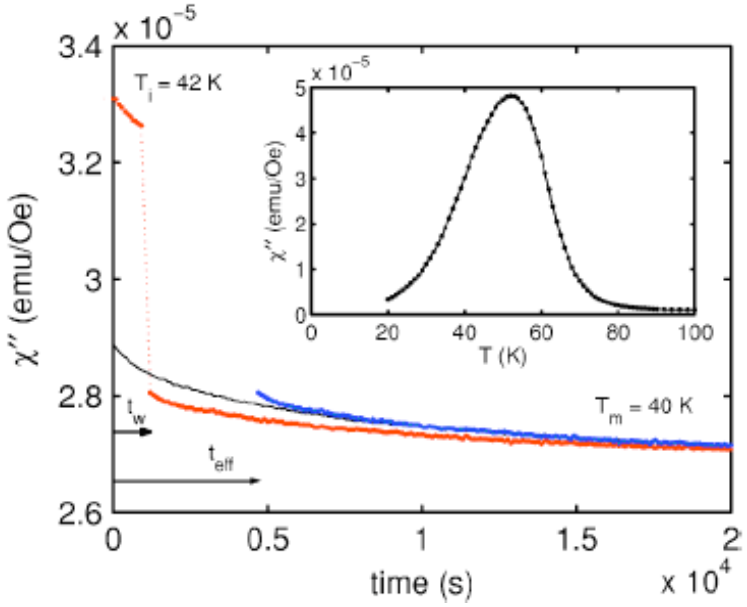

Figure 6.13(a): Measurements of the relaxation of the imaginary component of the frequency dependent susceptibility as a function of time for a Fe_3N superspin glass. The glass was cooled to $T_i = 42K$, aged for 1000s, and then subjected to a negative temperature shift to $T_m = 40K$ and allowed to relax further. Reprinted figure with permission from Jönsson, Yoshino, Mamiya, and Takayama, Physical Review B **71**, 104404 (2005). Copyright 2005 by the American Physical Society. http://link.aps.org/abstract/PRB/v71e104404

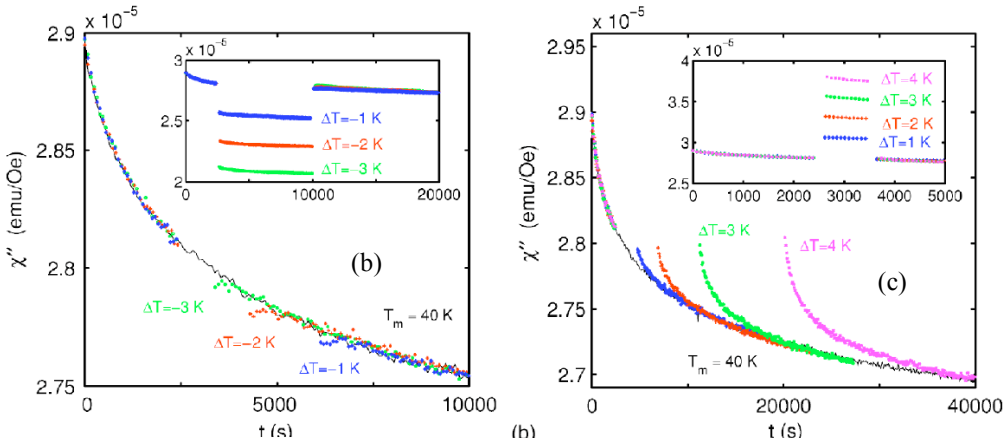

Figures 6.13(b) and 6.13(c): Measurements of the relaxation of the imaginary component of the frequency dependent susceptibility as a function of time during all three phases of negative and positive temperature cycling experiments. The main body of each figure shows the superposition of the third phase data onto the virgin isothermal reference curve at T_m by shifting the data in time by $t_{eff}(\Delta T)$. The insets show the relaxation of the susceptibility with time. Reprinted figures with permission from Jönsson, Yoshino, Mamiya, and Takayama, Physical Review B **71**, 104404 (2005). Copyright 2005 by the American Physical Society. http://link.aps.org/abstract/PRB/v71/e104404

Numerical simulations show that **rejuvenation and transient effects** are also characteristics of Preisach ensembles of two-level subsystems which relax independently over individual free energy barriers. Figure 6.14(a) shows the configuration of the Preisach plane for a system which has been cooled in a field h_a to a temperature h_{fa} with time constant t_c , aged at h_{fa} for a time t_a , and then warmed to a temperature h_{f+} with time constant $t_w = t_c$. When $h_{Ta} = h_{fa} \ln(t_a/\tau_0) > h_{T+} = h_{f+} \ln(t_w/\tau_0)$, this procedure leaves an "aging imprint" at h_{f+} consisting of a group of subsystems which have been aged at h_{fa} and which have "survived" the temperature shift to h_{f+} . Figure 6.14(b) shows numerical simulations of the relaxation of the moment as a function of time t/τ_0 for an ensemble of two-level subsystems with a lognormal-bimodal Gaussian Preisach density with parameters $\sigma_d = 0.5$, $h_{s0} = 1.5$, and $\sigma_s = 0.2$, which has been cooled in a field $h_a = 1.1$ with

time constant $t_c = 2.2x10^4\tau_0$, aged for a time $t_a = 2x10^{12}\tau_0$ at a series of temperatures h_{fa} = 0.075, 0.085, 0.09, 0.094, 0.096, 0.097, 0.099, and then subjected to a **positive temperature shift** to $h_{f+} = 0.1$ with a warming time constant $t_w = 2.2x10^4\tau_0$. The inset in Figure 6.14(b) shows the details of the relaxation response at $h_{f+} = 0.1$ on magnified vertical and horizontal scales. For all aging temperatures $h_{fa} > 0.07$, $h_{Ta} - h_{T+} > 3h_f$ and the aging imprint is real. Notice that the relaxation response at $h_{f+} = 0.1$ following the temperature shift is strongly rejuvenated for "large" temperature shifts $\Delta h_f = h_{f+} - h_{fa} >$ 0.02. In this regime, the increase in the total (negative) moment of those subsystems with $h_s > + h_a$ which were aged to equilibrium at h_{fa} and then re-equilibrated following the temperature shift to $h_{f+} = 0.1$ exceeds the decrease in the total moment of those subsystems which were blocked during the original cooling process and subsequently aged at h_{fa} , and the system essentially behaves as if it had been cooled directly to $h_{f+} =$ 0.1 with time constant $t_c = 2.2x10^4\tau_0$ and then allowed to relax, that is, the system appears to be **completely rejuvenated**. However, as the temperature shift $\Delta h_f = h_{f+} - h_{fa}$ becomes smaller, the re-equilibration effect becomes progressively weaker, the aging effect gradually becomes more dominant, progressively more of the aging at h_{fa} survives the temperature shift, and the relaxation response deviates progressively further below the "virgin" relaxation curve at $h_{f+} = 0.1$ and merges with the rejuvenated curve at progressively later times. We refer to this situation as **partial rejuvenation**. Thus, according to the two-level subsystem formalism, the deviations below the rejuvenated relaxation curve observed for small temperature shifts, and referred to as **transients** in the context of the spin glass investigations described above, are actually an intrinsic

characteristic of the relaxation response originating directly and naturally from the competition between the re-equilibration and aging processes.

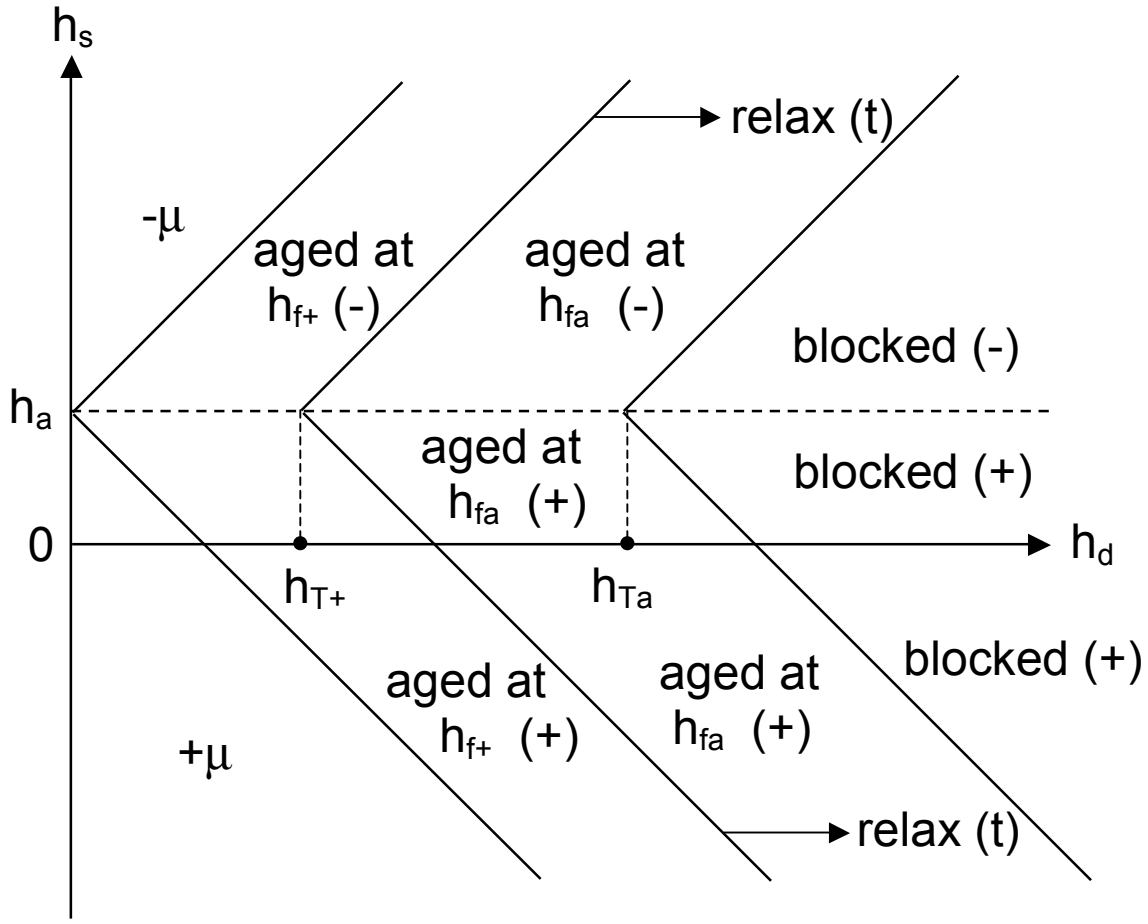

Figure 6.14(a): The Preisach representation of a system that has been cooled in a constant field $h_a > 0$ to a temperature h_{fa}, aged at h_{fa} for a time t_a, and them warmed to a temperature h_{f+}. This protocol leaves an aging imprint on those subsystems labeled 'aged at h_{fa}.'

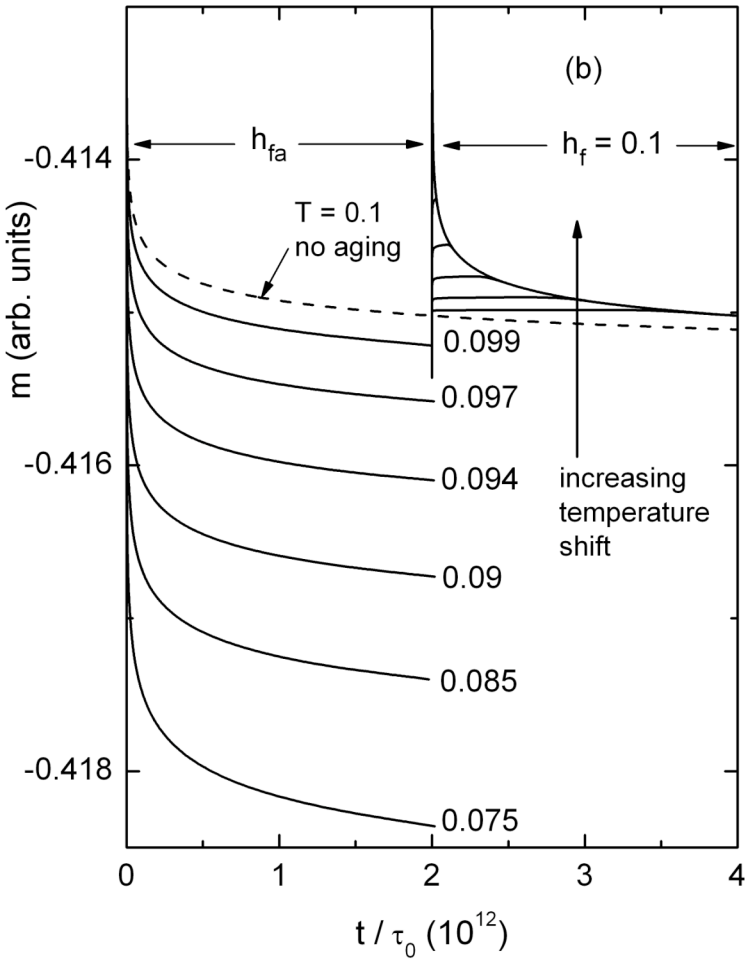

Figure 6.14(b): Numerical simulations of the relaxation of the moment as a function of t/τ_0 for a collection of subsystems that were cooled in a constant field $h_a = 1.1$, aged for a time $t_a / \tau_0 = 2x10^{12}$ at the series of temperatures listed next to each virgin relaxation curve, and then subjected to a positive temperature shift to $h_{f+} = 0.1$.

Figure 6.15(a) shows the configuration of the Preisach plane for a system which has been cooled in a field h_a to a temperature h_{fa} with time constant t_c , aged at h_{fa} for a time t_a , and then cooled to a temperature h_{f-} with time constant t_c . Since $h_{Ta} = h_{fa} \ln(t_a/\tau_0)$ $> h_{T-} = h_{f-} \ln(t_c/\tau_0)$ for all $h_{fa} > h_{f-}$, this procedure **always** leaves an "aging imprint" at h_{f-} As a consequence, negative temperature shifts are **incapable of inducing complete**

rejuvenation. This is indeed confirmed by the numerical simulations in Figure 6.15(b), which show the relaxation of the moment as a function of time t/τ_0 for an ensemble of two-level subsystems with a lognormal-bimodal Gaussian Preisach density with parameters $\sigma_d = 0.5$, $h_{s0} = 1.5$, and $\sigma_s = 0.2$, which has been cooled in a field $h_a = 1.1$ with time constant $t_c = 2.2\text{x}10^4\tau_0$, aged for a time $t_a = 2\text{x}10^{12}\tau_0$ at a series of temperatures h_{fa} = 0.102, 0.104, 0.106, 0.108, 0.11, and then subjected to a **negative temperature shift** to $h_{f-} = 0.1$ with a cooling time constant $t_c = 2.2\text{x}10^4\tau_0$. A close inspection of this figure also reveals that the model systematics under negative temperature shifts are precisely the opposite to those observed in Figure 6.14(b) under positive temperature shifts, in the sense that the rejuvenation time (that is, the time interval between the instant of the temperature shift from h_{f-} to h_f and the instant that the relaxation curve joins the virgin (unaged) h_f relaxation isotherm) is shortest for the smallest temperature shift from h_{f-} = 0.102 to $h_f = 0.1$, and increases monotonically as the magnitude of the temperature shift increases. This behaviour is contrary to that reported in atomic spin glasses, where the largest temperature shifts (positive or negative) always induce the strongest rejuvenation (see Figures 6.12(a) and (b)), but is, however, very similar to the behaviour observed in nanoparticulate superspin glasses (see Figure 6.13(c)), which also happen to be particularly compatible, from a microstructural point of view (an ensemble of "big spins" [24]), with the spirit of the Preisach formalism.

.

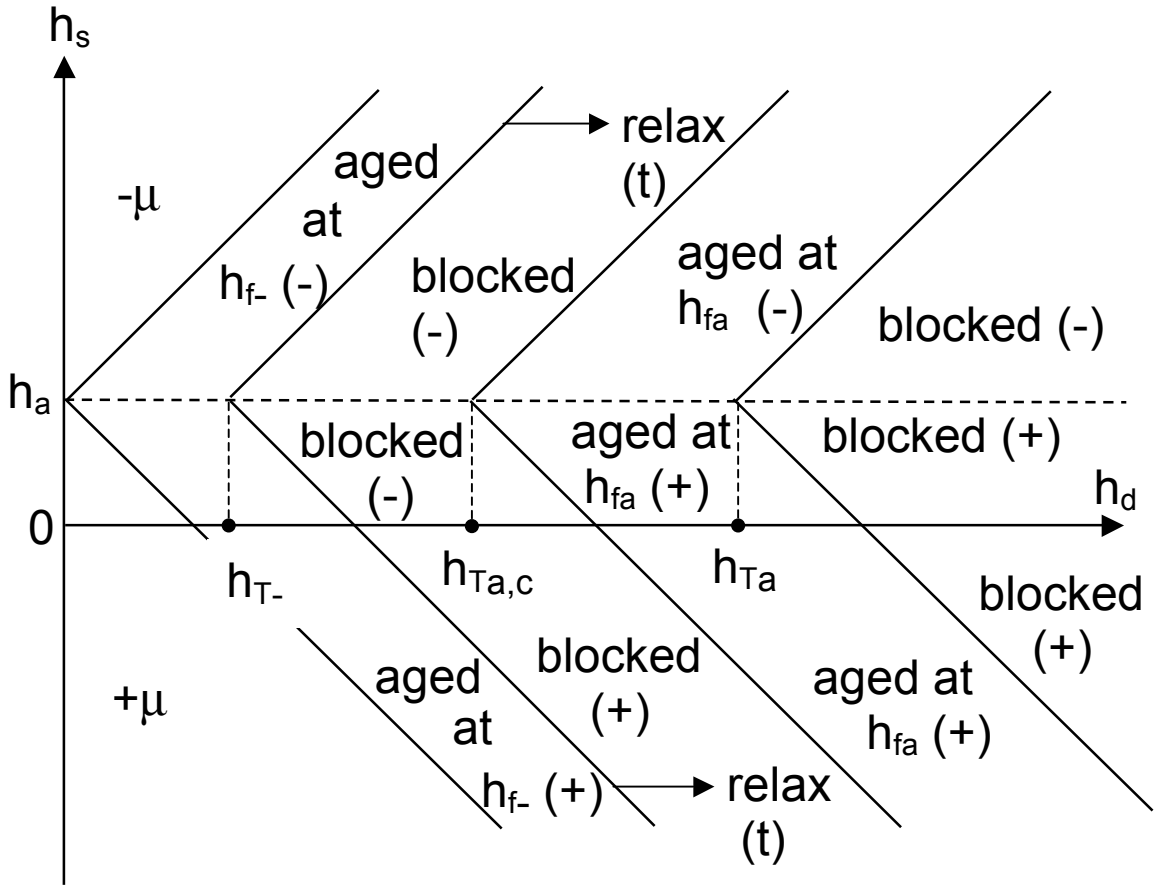

Figure 6.15(a): The Preisach representation of a system that has been cooled in a constant field $h_a > 0$ to a temperature h_{fa}, aged at h_{fa} for a time t_a, and then cooled to a temperature h_{f-}. This protocol leaves an aging imprint on those subsystems labeled 'aged at h_{fa}.'

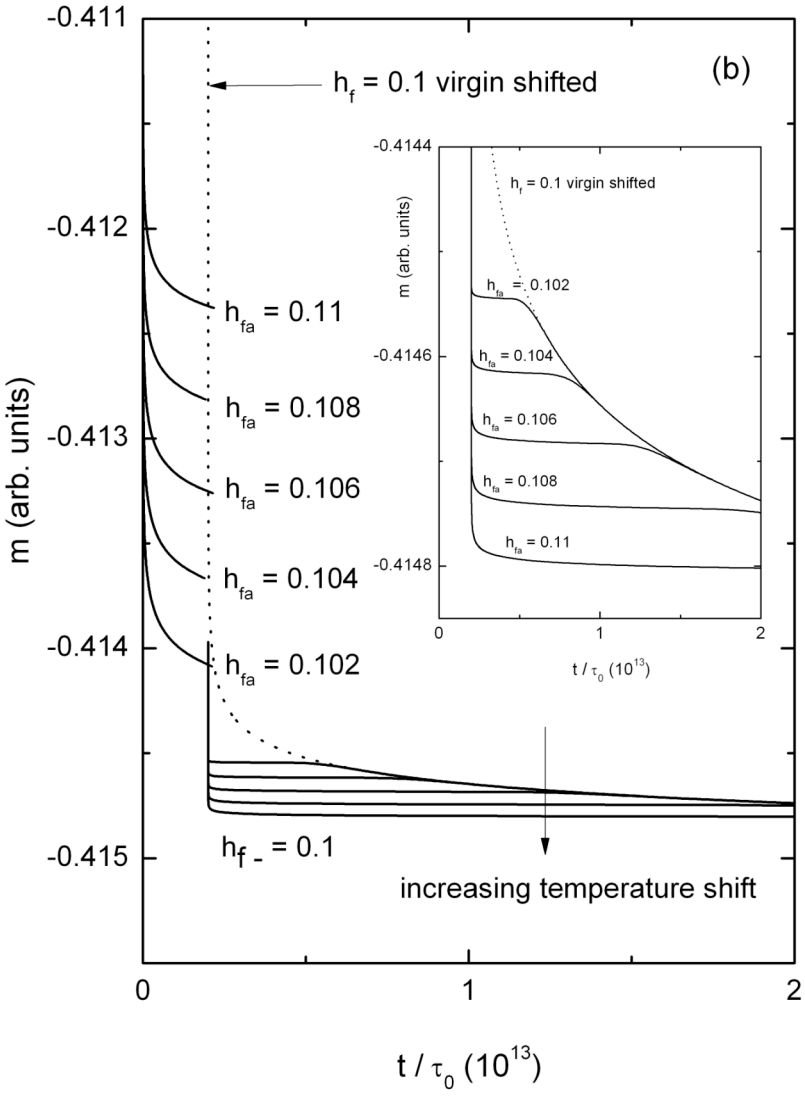

Figure 6.15(b): Numerical simulations of the relaxation of the moment as a function of t/τ_0 for a collection of subsystems which have been cooled in a constant field $h_a = 1.1$, aged for a time $t_a / \tau_0 = 2x10^{12}$ at the series of temperatures listed next to each virgin relaxation curve, then subjected to a negative temperature shift to $h_{f-} = 0.1$. The inset shows a magnified image of early time relaxation at h_{f-}.

6.7 References for Chapter 6

[1] K. H. Fischer and J. A. Hertz, *Spin Glasses* (Cambridge: Cambridge University Press, 1991).

[2] D. Chowdhury, *Spin Glasses and Other Frustrated Systems* (Princeton: Princeton University Press, 1986).

[3] V.S. Dotsenko, "Physics of Spin-Glass State," Physics – Uspekhi **36**, 455 (1993).

[4] See the thesis by K. Jonason, "Dynamics of Complex Magnetic Systems" (Uppsala: Acta Universitatis Upsaliensis, 1999), for a comprehensive recent review of the principal features of spin glass dynamics and their interpretation within the context of droplet domain theories of spin glasses.

[5] J.-P. Bouchaud, L. F. Cugliandolo, J. Kurchan, and M. Mezard, in *Spin Glasses and Random Fields*, edited by A.P. Young (Singapore: World Scientific, 1997), pp. 161-223.

[6] J.-P. Bouchaud, in *Soft and Fragile Matter*, edited by M. E. Cates and M. R. Evans (Bristol: IOP, 2000).

[7] P. Nordblad, "Spin glasses: model systems for non-equilibrium dynamics," J. Phys. Cond. Mat. **16**, S715 (2004).

[8] L. Lundgren, P. Svedlindh, P. Nordblad, and O. Beckman, "Dynamics of the Relaxation-Time Spectrum in a CuMn Spin-Glass," Phys. Rev. Lett. **51**, 911 (1983).

[9] K. Jonason, E. Vincent, J. Hammann, J.-P. Bouchaud, and P. Nordblad, "Memory and Chaos Effects in Spin Glasses," Phys. Rev. Lett. **81**, 3243 (1998).

[10] P. Granberg, L. Lundgren, and P. Nordblad, "Non-equilibrium relaxation in a Cu(Mn) spin glass," J. Magn. Magn. Mater. **92**, 228 (1990).

[11] P. E. Jonsson, R. Mathieu, P. Nordblad, H. Yoshino, H. A. Katori, and A. Ito, "Nonequilibrium dynamics of spin glasses: Examination of the ghost domain scenario," Phys. Rev. B **70**, 174402 (2004).

[12] J. Hammann, M. Lederman, M. Ocio, R. Orbach, and E. Vincent, "Spin-glass dynamics: Relation between theory and experiment: a beginning," Physica A **185**, 278 (1984).

[13] E. Vincent, J. Hammann, and M. Ocio, *Recent Progress in Random Magnets*, edited by D. H. Ryan (Singapore: World Scientific, 1992), p. 207.

[14] Ph. Refregier, E. Vincent, J. Hammann, and M. Ocio, "Ageing phenomena in a spin-glass: effect of temperature changes below T_g," J. Phys., Paris **48**, 1533 (1987).

[15] E. Vincent, J.-P. Bouchaud, J. Hammann, and F. Lefloch, "Contrasting effects of field and temperature variations on ageing in spin glasses," Phil. Mag. B **71**, 489 (1995).

[16] A. J. Bray and M. A. Moore, "Chaotic Nature of the Spin-Glass Phase," Phys. Rev. Lett. **58**, 57 (1987).

[17] D. S. Fisher and D. A. Huse, "Equilibrium behavior of the spin-glass ordered phase," Phys. Rev. B **38**, 386 (1988).

[18] D. S. Fisher and D. A. Huse, "Nonequilibrium dynamics of spin glasses," Phys. Rev. B **38**, 373 (1988).

[19] D. S. Fisher and D. A. Huse, "Directed paths in a random potential," Phys. Rev. B **43**, 10728 (1991).

[20] H. Yoshino, A. Lemaitre, and J.-P. Bouchaud, "Multiple domain growth and memory in the droplet model for spin-glasses," Eur. Phys. J. B **20**, 367 (2001).

[21] F. Scheffler, H. Yoshino, and P. Maass, "Real space normalization group approach to spin-glass dynamics," Phys. Rev. B **68**, 060404(R) (2003).

[22] H. Yoshino, "Dynamics of ghost domains in spin-glasses," J. Phys. A **36**, 10819 (2003).

[23] L. Néel, "Theorie du traînage magnetique des ferromagnetiques en grains fins avec applications aux terres cuites," Ann. Geophys. **5**, 99 (1949).

[24] J. Souletie, "Hysteresis and after-effects in massive substances. From spin-glasses to the sand hill," J. Physique **45**, 1095 (1983).

[25] Jonsson, Jonason, and Nordblad, "Relaxation of the field-cooled magnetization of an Ising spin glass," Phys. Rev. B **59**, 9402 (1999).

[26] Jönsson, Hansen, and Nordblad, "Nonequilibrium dynamics in an interacting Fe-C nanoparticle system," Phys. Rev. B **61**, 1261 (2000).

[27] M. Sasaki, P.E. Jönsson,H. Takayama, and H. Mamiya, "Aging and memory effects in superparamagnets and superspin glasses," Phys. Rev. B **71**, 104405 (2005).

[28] Granberg, Sandlund, Nordblad, Svedlindh, and Lundgren, "Observation of a time-dependent spatial correlation length in a metallic spin glass," Phys. Rev. B **38**, 7097 (1988).

[29] Jonsson, Mattson, Djurberg, Khan, Nordblad, and Svedlindh, "Aging in a Magnetic Particle System," Phys. Rev. Lett. **75**, 4138 (1995).

[30] R. Mathieu, P. Jonsson, D. N. H. Nam, and P. Nordblad, "Memory and superposition in a spin glass," Phys. Rev. B **63**, 092401 (2001).

[31] M. Cerchez, L. Stoleriu, and A. Stancu, "Interaction effects in high density magnetic particulate media," Physica B **343**, 48 (2004).

[32] Jonsson, Jonason, Jönsson, and Nordblad, "Nonequilibrium dynamics in a three-dimensional spin glass," Phys. Rev. B **59**, 8770 (1999).

[33] Jönsson, Yoshino, Mamiya, and Takayama, "Absence of strong rejuvenation in a superspin glass," Phys. Rev. B **71**, 104404 (2005).

Chapter 7

Probing the Temperature Dependence of the Free Energy Landscape in Magnetic Materials with Persistent Memory: A Scaling Approach based on Viscosity Isotherms

7.1. Introduction

The magnetic properties of all magnetic materials which exhibit persistent memory and a history dependent response to an external field stimulus are functions of *temperature*, and the interpretation of the measured temperature dependence of important design parameters, like the coercive field and the saturation remanence, and of standard macroscopic response functions, like the field cooled (FC) moment, the zero field cooled (ZFC) moment, the thermoremanent moment (TRM), the isothermal remanent moment (IRM), and moment and remanence hysteresis loops, continues to pose a significant challenge. Figure 7.1 illustrates the types of complex thermal profiles which are typically encountered in experimental characterizations of magnetic materials with a nanoparticulate microstructure, in this case for an assembly of Fe nanoparticles embedded in a thin film of alumina. The main body of the figure shows the temperature dependence of the FC moment, the ZFC moment, the TRM, and the IRM measured in a fixed field of $H_a = 6$ Oe. As we have seen, systems with permanent memory are

characterized by a highly corrugated free energy hypersurface in a multidimensional configuration space [1], and their evolution through configuration space consists of a sequence of irreversible transitions between metastable configurations, in which the system is temporarily trapped in a local minimum and then liberated either by field-induced distortions of the free energy landscape, or by random energy exchanges with a heat bath, which trigger the spontaneous escape of the system from metastable states by thermal activation over local energy barriers, or by some combination of these. The temperature dependence of the measured magnetic response of the material is thus shaped by a complex coexistence of two processes: (a) thermal overbarrier activation events, which relax the system toward thermodynamic equilibrium, and (b) the explicit evolution with temperature of the free energy landscape itself, which ultimately originates from the explicit dependence on temperature of intrinsic material parameters, such as anisotropy constants and the spontaneous magnetization. The purpose of the current investigation is to explore a general strategy [2,3] for isolating and quantifying the contributions from these two processes, and hence for reconstructing the spectrum of intrinsic metastable state excitation barriers and its evolution with temperature.

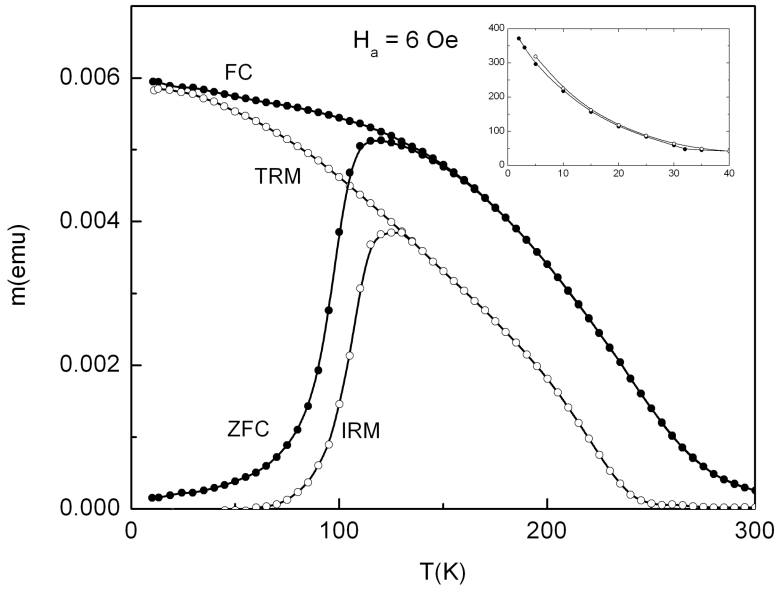

Figure 7.1: The temperature dependence of the FC moment, the ZFC moment, the TRM, and the IRM of an assembly of Fe nanoparticles embedded in a thin film of alumina measured in an applied field of $H_a = 6$ Oe.

7.2. Modelling Magnetic Viscosity Isotherms

Thermal fluctuations introduce a dependence on observation time t into the measured response functions of systems which are out-of-equilibrium, and the key to unraveling the intricate relationship between landscape evolution and thermal activation lies in the interpretation of magnetic relaxation isotherms. In magnetic materials, the relaxation of the magnetic properties that accompanies the spontaneous approach to equilibrium is also of considerable practical interest, particularly in connection with the limitations that it imposes on the ultimate bit size of storage media and on the stability of permanent magnets, both of which depend on the preservation of a stable magnetic state.

Model magnetic systems composed of a Preisach ensemble of elementary metastable two-level subsystems provide a unified treatment of hysteresis and thermal

relaxation [1, 4] which is particularly well adapted for studying the combined effects of thermal overbarrier activation and landscape evolution on macroscopic response functions [5, 6], including relaxation isotherms. The unification rests on the assumption that hysteresis and thermal relaxation involve a common set of energy barriers which are to be regarded as an **intrinsic property of the material at any given temperature**, in the sense that these barriers would define the response of the system in the hypothetical limit where all changes in applied field and temperature could be accomplished instantaneously (that is, in the limit $t \rightarrow \tau_0$). Thermal activation events are modeled by an effective activation moment reversal μ and are driven by a fictitious random thermal fluctuation field with amplitude $H_f = kT/\mu$ [7] which mimics the action of thermal perturbations. For purposes of the current investigation, we focus on a particular class of relaxation experiments which are conventionally referred to in the literature as "viscosity" isotherms (although the term "viscosity" has a much more general significance). The experimental protocol consists of temperature stabilization, followed by the application of a positive saturating field $H_a \rightarrow \infty$, and then by recoil to a negative holding field $H_a < 0$, after which the relaxation of the magnetic moment is recorded as a function of observation time t in fixed field H_a at fixed temperature T. The Preisach representation of the viscosity protocol is shown in Figure 7.2. The subsystems which are primarily responsible for the relaxation of the ensemble moment with time are those with characteristic fields $(H_d,H_s) = (H_d, H_a \leq H_s \leq H_d + H_a)$ (the $+\mu$ region above the horizontal dashed line in Figure 7.2), which are trapped in their higher energy metastable $+\mu$ state immediately following field reversal to H_a, and which will eventually experience

a moment reversal with time into a negative equilibrium moment configuration $m_{eq} = \mu \tanh[\mu(H_a - H_s)/kT] < 0$. The remaining subsystems are either purely and permanently monostable, with time independent moments $+\mu$ or $-\mu$, or are bistable but with a positive moment which relaxes from $+\mu$ to the positive equilibrium configuration $m_{eq} > 0$, without sign reversal.

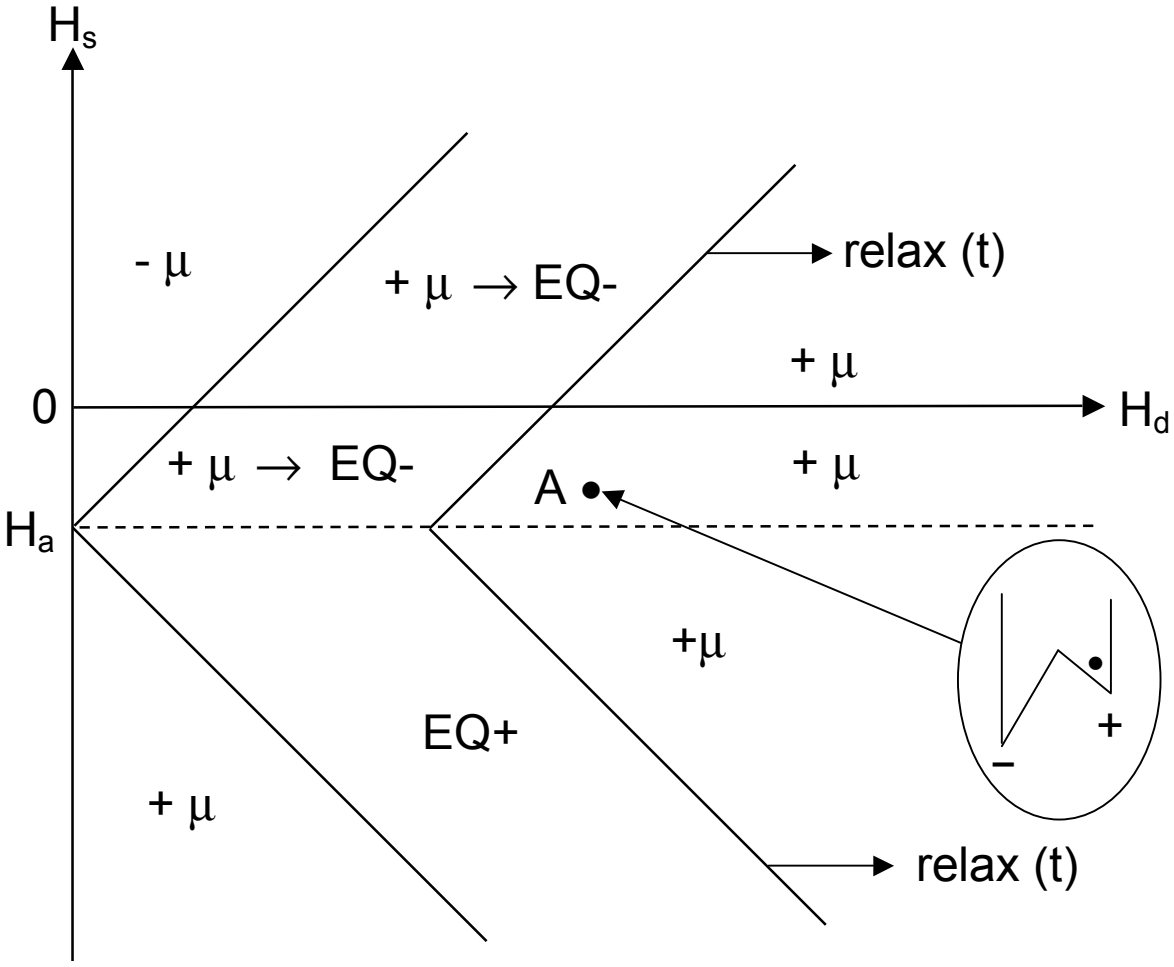

Figure 7.2: The Preisach representation of the experimental protocol for measuring viscosity isotherms. The subsystems in the region labeled $+\mu$ are those which experience a moment reversal to a negative equilibrium moment configuration with time. "A" is a typical subsystem in this region, and its free energy profile is sketched in the lower right hand corner of the figure.

Suppose that we consider a typical subsystem within the region labelled as $+\mu$ in Figure 7.2 such as subsystem "A", with characteristic fields (H_d,H_s) and with a free energy profile sketched on the lower right of the figure. If we adopt the same approximations to treat the thermal relaxation of two-level subsystems as those discussed in detail in Chapter 6.2, then subsystem A will remain trapped in its $+\mu$ configuration until a time $t = t_r$ at which the thermal viscosity field $H_T = H_f \ln(t_r / \tau_0)$ precisely matches the lower subsystem energy barrier $H_L = H_d - H_s + H_a$, at which point the subsystem moment will instantaneously invert to its equilibrium value m_{eq}. Thus, the condition for thermal activation of subsystem A is:

$$H_f \ln(t_r / \tau_0) = H_d - H_s + H_a \qquad (7.1)$$

or, equivalently,

$$\ln(t_r / \tau_0) = (1/H_f)H_a + (1/H_f)(H_d - H_s) \; . \qquad (7.2)$$

Thus, according to the model, the logarithm of the reversal time $\ln(t_r / \tau_0)$ for a single subsystem is predicted to vary **linearly** as a function of the holding field H_a, with a slope which is the inverse of the thermal fluctuation field H_f and with an intercept which yields the intrinsic zero field excitation barrier $H_L = H_d - H_s$ for the subsystem.

Of course, measured relaxation isotherms are actually a superposition of a multitude of relaxation events involving the entire ensemble of Preisach subsystems, each

with its own characteristic reversal time t_r, and the value of $\ln(t_r/\tau_0)$ for the **ensemble** must be determined by integrating over the entire Preisach plane in Figure 7.2:

$$M(t) = N\mu \int_0^{\infty} dH_d \int_{-\infty}^{+\infty} dH_s \, \Theta\left[H_f \ln(t/\tau_0) - \left(H_d - |H_s - H_a| \right) \right] p(H_d, H_s) \qquad (7.3)$$

where $\Theta(x)$ is a step-function defined by:

$$\left.\begin{aligned} \Theta(x) &= +1, && \text{for} \quad x < 0 \\ &= \tanh\left[(H_a - H_s)/H_f \right], && \text{for} \quad x > 0 \end{aligned}\right\}. \qquad (7.4)$$

We have generated model simulations of viscosity isotherms numerically for a Preisach ensemble of two-level subsystems described by a Preisach density of characteristic fields $p(H_d,H_s)$ consisting of the product $p(H_d,H_s) = f(H_d)\, g(H_s)$ of a lognormal distribution of dissipation fields H_d and a Gaussian distribution of bias fields H_s:

$$\begin{aligned} p(H_d,H_s) &= f(H_d)\, g(H_s) \\ &= (2\pi\sigma_d^2 H_d^2)^{-1/2} \exp\left[-(\ln H_d/H_{dm})^2/(2\sigma_d^2) \right] (2\pi\sigma_s^2)^{-1/2} \exp(-H_s^2/2\sigma_s^2) \, . \end{aligned} \qquad (7.5)$$

As in our previous discussions, all fields and field dispersions are normalized to the median dissipation field H_{dm} as $h = H/H_{dm}$ and all temperatures are expressed in terms

of the reduced thermal fluctuation field $h_f = H_f/H_{dm} = kT/(\mu H_{dm})$. The microstructural properties of a specific magnetic material are encoded in the Preisach distribution function $p(h_d,h_s)$, and microstructural disorder is expressed through the dispersions σ_d and σ_s of characteristic fields, with vanishing dispersions corresponding to the hypothetical limit of an ensemble of perfectly identical, aligned, noninteracting particles. We initially assume that the Preisach distribution, and hence the landscape of metastable states and free energy excitation barriers, possesses **no explicit dependence on temperature**. The implications of relaxing this restriction will be discussed shortly.

Figures 7.3(a) through 7.3(d) show four sets of model relaxation isotherms for four different Preisach distributions with characteristic field dispersions (σ_d,σ_s) = (0.1,0.5), (0.5,0.1), (0.5,0.5) and (1.0,1.0), respectively, representing varying degrees of structural disorder. The shapes of the four distributions, and the extent to which the subsystems are dispersed over the Preisach plane, are compared in Figure 7.4, which shows "limiting" contour plots of constant density in the Preisach plane, defined in each case as the value of $p(h_d,h_s)$ for which $p(h_d,h_s) / p_{max}(h_d,h_s) = 0.01$. Each set of isotherms in Figure 7.3 was generated for a series of negative holding fields h_a between $h_a = 0$ (top curve) and $h_a = -1.2$ (bottom curve), and each is plotted as a function of the thermal viscosity field $h_T = h_f \ln(t/\tau_0)$ over the same field interval $0 \le h_T \le 1.4$. Since the only source of temperature dependence in the model other than the fluctuation field h_f is the comparatively weak dependence on temperature associated with the equilibrium subsystem moment $m_{eq} = \tanh[(h_a - h_s)/h_f]$, it follows that such plots yield **universal curves** in the sense that, for a given distribution, each relaxation curve in a given holding

field h_a is valid for all temperatures h_f and for all observation times t. The curvature of the relaxation isotherms in Figure 7.3 is most pronounced, and the approach to equilibrium in the limit $h_T \rightarrow \infty$ is most rapid, when the distribution is narrow along either the h_d or h_s axis (as in Figures 7.3(a) and 7.3(b)) subject, of course, to the particular functional forms chosen for the distributions. As the subsystem distribution becomes broader and more uniform, the relaxation becomes progressively more gradual and featureless, and the approach to equilibrium extends to progressively longer time scales (Figures 7.3(c) and 7.3(d)). Structural disorder places severe limits on our experimental ability to probe the complete spectrum of metastable state excitation barriers. The vertical lines in Figure 7.3 illustrate those portions of the universal curves which would be visible in an experiment performed at three different reduced temperatures $h_f = 0.005$, 0.015, and 0.03, and over a limited observation time window $10^{10} \leq t/\tau_0 \leq 10^{13}$, which is typical of commercial magnetometers (assuming $\tau_0 = 10^{-9}$s). It is clear that, even for quite modest levels of structural disorder, only a short quasi-logarithmic fragment of the complete relaxation response function is visible in an experiment performed at one temperature, over a restricted observation time window. Structural disorder also affects the equilibrium moment of the ensemble. Each isotherm in Figure 7.3 converges to an equilibrium moment which is dependent on the holding field h_a. This particular effect is specifically related to disorder in the distribution of bias fields and hence to the dispersion σ_s. In the equilibrium limit $h_T \rightarrow \infty$, and in the presence of an applied field h_a, the Preisach plane is subdivided into two subpopulations, subsystems with bias fields $h_s > h_a$ which have negative equilibrium moments (either $m_{eq} = -\mu$ or $m_{eq} = \tanh[(h_a - h_s)/h_f] < 0$), and

subsystems with bias fields $h_s < h_a$ which have positive equilibrium moments (either $m_{eq} = +\mu$ or $m_{eq} = \tanh[(h_a - h_s)/h_f] > 0$). For all nonzero applied fields $h_a < 0$, the population of negative moment subsystems exceeds the population of positive moment subsystems, and it is this imbalance which is responsible for the field dependence of the equilibrium moment observed in Figure 7.3. In the limit $\sigma_s \rightarrow 0$, all subsystems have negative equilibrium moments and, if the weak dependence of $m_{eq} = \tanh(h_a/h_f)$ on temperature h_f is neglected, all viscosity isotherms converge to negative saturation $m \rightarrow -1$ independent of σ_d (with the obvious exception of the $h_a = 0$ isotherm, which always converges to zero moment in equilibrium.)

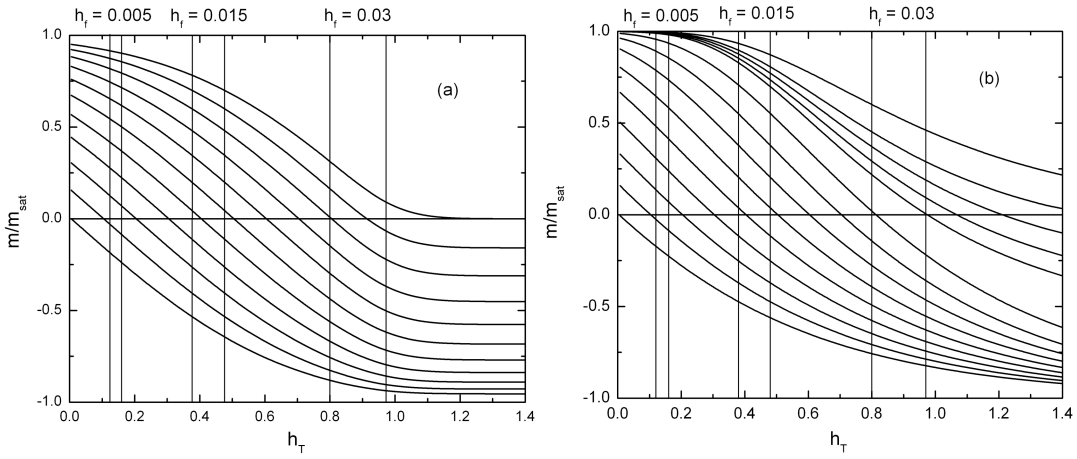

Figure 7.3: Model relaxation isotherms for Preisach distributions with characteristic field dispersions (σ_d, σ_s) = (a) (0.1,0.5), (b) (0.5,0.1).

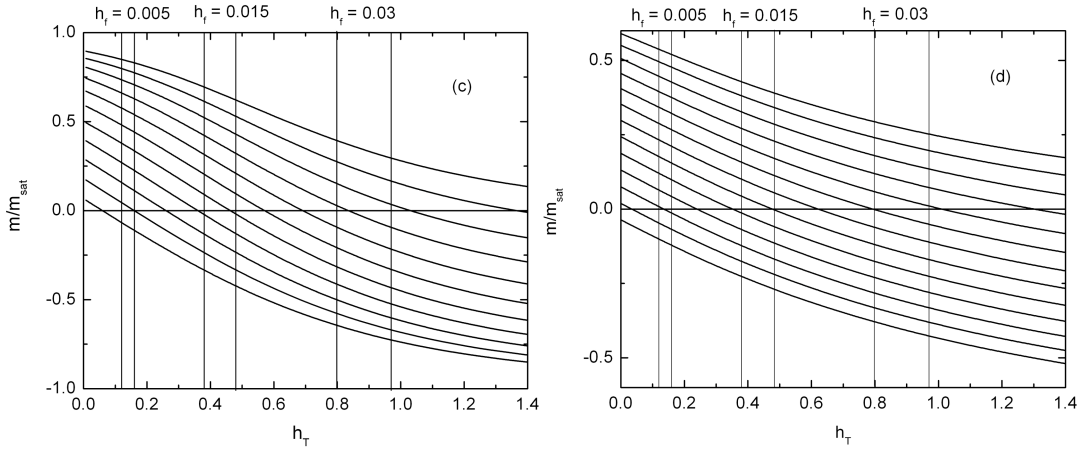

Figure 7.3 (cont'd): For characteristic field dispersions (c) (0.5,0.5), and (d) (1.0,1.0).

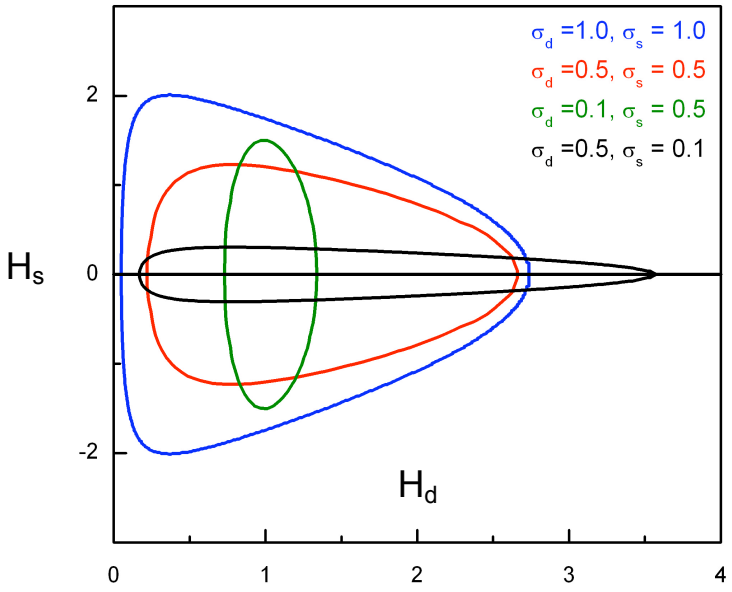

Figure 7.4: Contour plots of constant density $p(H_d,H_s)/p_{max}(H_d,H_s)$ in the Preisach plane for each of the four Preisach distributions with dispersions (σ_d, σ_s) listed in the figure.

Guided by our analysis of the relaxation response of a single subsystem in Eq(7.1) and (7.2), according to which the logarithm of the time $\ln(t_r/\tau_0)$ at which the moment reverses sign is predicted to vary **linearly** as a function of the holding field H_a, with a

slope which is the inverse of the thermal fluctuation field H_f, we focus attention on the zero moment (m=0) crossing points of the relaxation isotherms in Figure 7.3. Figure 7.5 shows a plot of the "critical" thermal viscosity field $h_{Tr} = h_f \ln(t_r / \tau_0)$, at which the relaxation isotherm in a particular holding field reverses sign, as a function of the holding field h_a, for each of the four sets of relaxation isotherms in Figure 7.3. Since the individual isotherms from a given set are universal functions of h_T, it follows that each of the plots in Figure 7.5 also defines a **universal curve**, valid for all thermal reversal fields h_{Tr}, that is, for all temperatures h_f and for all reversal times t_r. In spite of their universal character, however, it is important to emphasize that only a fragment of each curve is actually accessible in an experiment performed at a fixed temperature and over a finite experimental time window and that, from an experimental perspective, each curve must be assembled segment-by-segment from measurements performed over a wide range of temperatures which ideally spans the entire irreversible phase. The three pairs of horizontal lines in Figure 7.5 show the segments of the universal curves that would be accessible experimentally within the same temperature-time windows as those which defined the vertical lines through the relaxation isotherms in Figure 7.3.

In the following sections, we propose and implement a general analytical strategy for reconstructing the spectrum of intrinsic metastable state excitation barriers of a magnetic material and its evolution with temperature which exploits, as its basis, the concept of the universal curve, as shown in Figure 7.5. Before articulating the details of the strategy, we first summarize the principal characteristic features of these curves, as revealed by numerical simulations. (1) Starting from the limit of low viscosity fields h_{Tr}

$\rightarrow 0$, that is, low temperatures $T \rightarrow 0$ and/or short reversal times $t_r \rightarrow \tau_0$, the universal curves for all Preisach distributions, independent of their shape, exhibit a regime which is **linear in holding field h_a**, and identical in form to Eq(7.2) obeyed by a single subsystem, with a slope $\Delta h_{Tr} / \Delta h_a = 1$ exactly and an intercept along the h_a-axis equal to the coercive field h_{ci} of the intrinsic ($t \rightarrow \tau_0, h_T \rightarrow 0$) major hysteresis loop:

$$h_{Tr} = h_f \ln(t_r / \tau_0) = h_a + h_{ci} . \qquad (7.6)$$

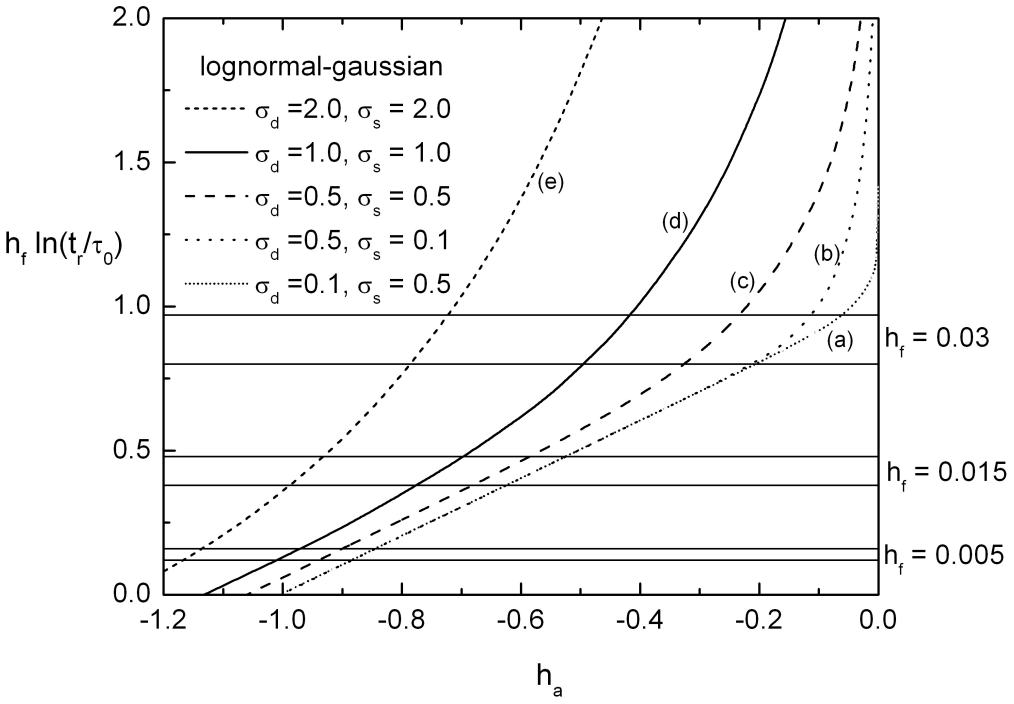

Figure 7.5 A plot of the thermal viscosity fields h_{Tr} at which the relaxation isotherms in Figure 7.3 reverse sign as a function of holding field h_a. Each of these plots defines a universal curve for a particular Preisach distribution of dissipation and bias fields (listed for each curve).

(2) While the principle of the existence of the linear regime is general and independent of the details of the Preisach distribution, the range of validity of the linear regime does

depend on the precise values chosen for the dispersions σ_d and σ_s. For distributions which are sufficiently narrow, the linear regime can extend over a wide range of holding fields, as illustrated by the universal curves labeled (a), (b) and (c) in Figure 7.5. In fact, in the limit where one of the two dispersions vanishes ($\sigma_d \rightarrow 0$ or $\sigma_s \rightarrow 0$) and the corresponding distribution $f(H_d)$ or $g(H_s)$ collapses to a δ-function, the linear relation is rigorously valid over the **entire range** of holding fields, and the universal curve reduces exactly to the straight line in Eq(7.6). However, as structural disorder becomes progressively more significant and the distribution becomes progressively broader, the range of validity of the linear regime shrinks dramatically, and linear behaviour is restricted to a progressively smaller range of holding fields close to the intrinsic coercive field h_{ci}, and to very low viscosity fields $h_{Tr} \rightarrow 0$, as illustrated by the universal curves labeled (d) and (e) in Figure 7.5. (3) For fields outside the linear regime, the universal curve always deviates **above** the limiting straight line for vanishing dispersions. These deviations become progressively more severe as $h_a \rightarrow 0$, and eventually culminate in a **divergent slope** at $h_a = 0$. The origin of these deviations from linearity is easy to appreciate from an inspection of the Preisach diagram in Figure 7.6. The straight line in this figure which intersects the h_s-axis at $-h_{ci}$ shows the location of the **intrinsic** coercive field boundary, which bisects the distribution and reduces the total moment to zero in the limit $h_T \rightarrow 0$ (that is, $t \rightarrow \tau_0$). The integrated moment of the subsystems to the left of this line, all of which are in their $-\mu$ state, exactly cancels the integrated moment of the $+\mu$ subsystems to the right of the line. The figure also shows the configuration of the plane in the presence of a negative holding field $h_a > -h_{ci}$ and a finite thermal viscosity field $h_T >$

0, chosen so as to satisfy the linear relationship $h_{Tr} = h_a + h_{ci}$ in Eq(7.6). These two configurations are clearly not identical, and differ in the orientations of the subsystems in the **shaded** region, which is $+\mu$ when $h_T > 0$, compared with $-\mu$ when $h_T = 0$. It follows that a thermal fluctuation field $h_{Tr} > h_a + h_{ci}$ is needed in order to reduce the moment to zero whenever $h_a > -h_{ci}$. This "correction" becomes progressively more significant as $h_a \rightarrow 0$, and leads to a progressively more severe upward deviation of the universal curve from linearity. When either $\sigma_d << 1$ or $\sigma_s << 1$, the shaded region in Figure 7.6 is essentially unoccupied, and the deviation from linearity is negligible (except, of course, when $h_a = 0$ exactly, in which case $h_{Tr} \rightarrow \infty$). (4) When thermal effects are **not restricted exclusively** to thermal overbarrier activation events, and when the free energy landscape itself is allowed to evolve explicitly with temperature, then the principle of universality breaks down. Thus, if either the Preisach distribution of free energy barriers, defined by the intrinsic material parameters (H_{dm}, σ_s, σ_d), or the spontaneous subsystem moment μ depend explicitly on temperature, then a plot of h_{Tr} as a function of h_a will, in general, no longer be universal and will **fracture** into an **infinite family of isothermal curves**, each with properties which reflect the characteristics of the ensemble at that specific temperature. There is only one instance of landscape evolution for which this infinite family of isotherms will not fracture and for which a plot of h_{Tr} as a function of h_a will continue to yield a common universal curve, and that is the special case where the temperature dependence of the landscape is localized exclusively in the intrinsic median dissipation field $H_{dm}(T)$, with all other intrinsic material parameters (μ, σ_s, σ_d) being rigorously independent of temperature provided, of course, that each individual

isothermal curve is scaled to its own intrinsic dissipation field $H_{dm}(T)$ along both field axes h_{Tr} and h_a.

Based on the properties summarized above, we suggest the following experimental protocol for analyzing viscosity isotherms. At each temperature T, viscosity isotherms are measured over the widest possible range of negative holding fields H_a such that moment reversal is observed at times $t = t_r$ which span the entire experimentally available time window, that is, $10s \le t \le 10^4 s$ for a typical commercial magnetometer.

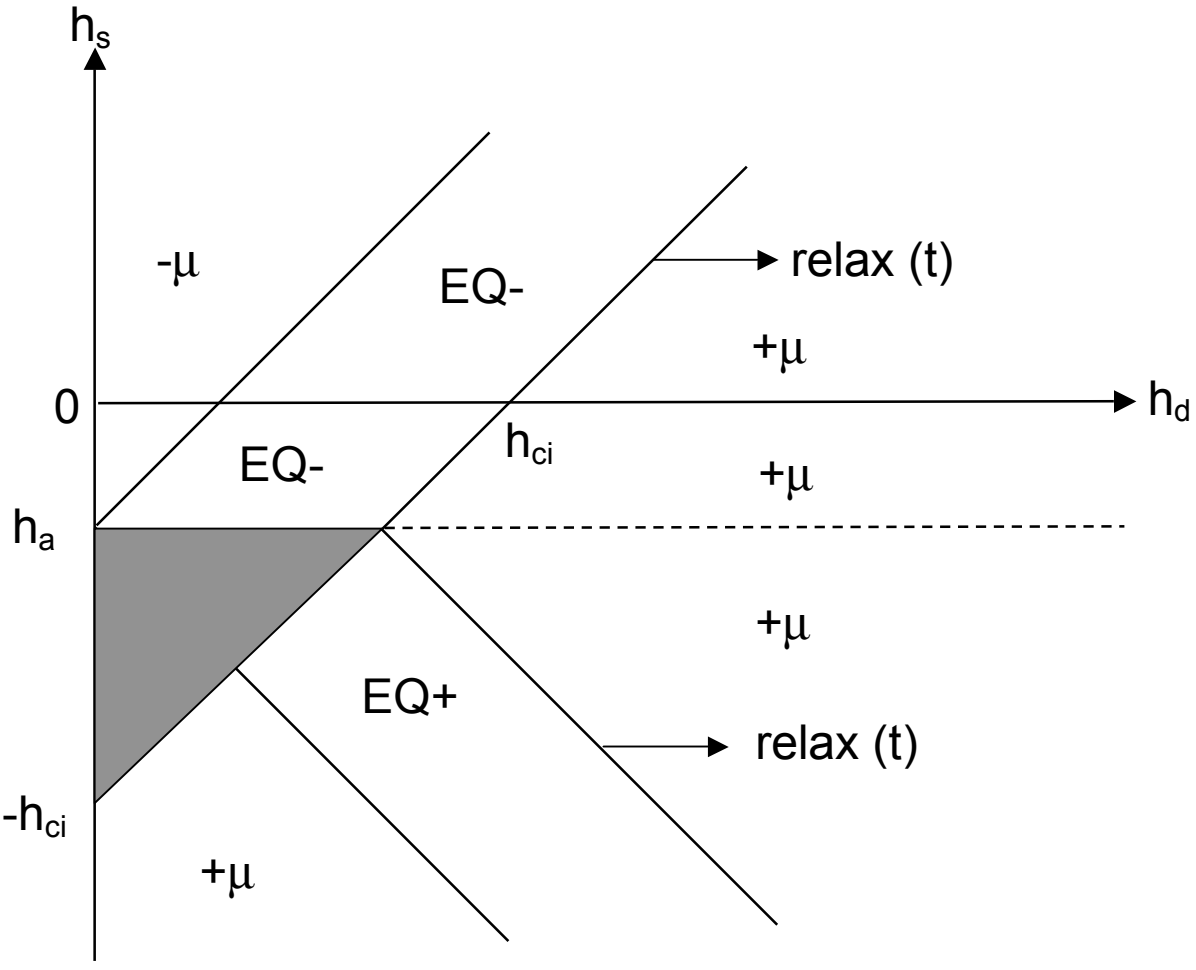

Figure 7.6: Preisach diagram depicting the origin of the deviations from linearity of universal curves. The shaded region is that region which is responsible for the nonlinear variation of h_{Tr} with applied field h_a.

These measurements are repeated over a wide range of closely spaced temperatures which ideally spans the entire irreversible phase. A plot of $T \ln(t_r/\tau_0)$ as a function of H_a, consisting of a sequence of (ideally overlapping) isothermal segments, is constructed, and the microscopic time constant τ_0 is adjusted, within physically reasonable bounds $10^{-13}\text{s} \le \tau_0 \le 10^{-9}\text{s}$, until the individual segments align to form a convincing universal curve, or until it is established conclusively that alignment is not possible. In the case where alignment is not convincing, it may be concluded that the observed temperature dependence of the material response functions originates exclusively from thermal overbarrier activation events within a temperature independent free energy landscape, and the plot will terminate, in the limit of low temperatures $T \to 0$, in a linear regime with a slope $\Delta[T \ln(t_r/\tau_0)] / \Delta H_a = \mu/k$ which yields the intrinsic spontaneous subsystem moment μ (that is, the intrinsic elementary activation moment reversal) and an intercept along the H_a-axis which yields the coercive field H_{ci} of the intrinsic major hysteresis loop, and hence the mean intrinsic dissipation barrier H_{dm} (assuming reversible effects are negligible), corresponding to the hypothetical limit ($T = 0$ and/or $t = \tau_0$) where thermal fluctuations could be eliminated. Fits of the universal curve to model simulations would then complete the description of the spectrum of intrinsic excitation barriers by establishing the dispersions σ_d and σ_s of characteristic fields H_d and H_s. When the intrinsic properties of the system, as summarized in the distribution of characteristic fields $p(H_d, H_s, T)$ and the subsystem moment $\mu(T)$, are allowed to vary explicitly with temperature, the model formalism predicts that universality will break down and that the

$Tln(t_r/\tau_0)$-versus-H_a plot will fracture into an infinite family of isothermal curves. Thus, the absence of universality for reasonable values of the microscopic characteristic time τ_0 may be interpreted as a signature of the **coexistence of thermal relaxation and landscape evolution**. Under these circumstances, fits of model simulations of $Tln(t_r/\tau_0)$-H_a curves to experimental data, as proposed above, are of very limited use for purposes of determining the intrinsic material parameters (μ, H_{dm}, σ_s, σ_d), since only a tiny fragment of each isothermal curve is available experimentally for purposes of comparison, and further analytical progress depends on the implementation of drastic simplifying assumptions which can only be justified a posteriori, by model comparisons with other experimental response functions, specifically the temperature dependence of the FC, ZFC, thermoremanent and isothermal remanent moments. As stated earlier, there is only one instance of landscape evolution for which it is possible to pursue a reconstruction of the entire universal curve, and that is the special case in which the temperature dependence of the intrinsic material parameters is limited exclusively to the median dissipation field $H_{dm}(T)$, with all other material parameters (μ, σ_s, σ_d) being rigorously independent of temperature. Under these conditions it is still possible to achieve universality, with the entire infinite family of isothermal curves collapsing onto a common universal curve, provided that each isothermal curve is scaled to its own intrinsic median dissipation field $H_{dm}(T)$.

Finally, it is important to point out that the magnetic response of most real magnetic materials to changes in applied field contains a reversible component, which originates from purely elastic, non-dissipative processes like reversible moment rotation

or domain wall flexing, or from the presence of populations of very small magnetic grains with energy barriers which are too low to be resolved in all applied fields of practical interest. A convenient way to include contributions of this nature within the Preisach formalism is to introduce a new distribution function $p_{rev}(H_s)$ which describes a collection of purely reversible subsystems, concentrated exclusively along the $H_d = 0$ axis in the Preisach plane [1]. Each reversible subsystem is characterized only by a bias field H_s, and each possesses only one energy minimum in all applied fields. The total Preisach distribution then becomes a weighted superposition of a distribution $p_{irrev}(H_d,H_s)$ of metastable subsystems (with non-vanishing dissipation fields $H_d \neq 0$) and a distribution $p_{rev}(H_s)$ of purely reversible subsystems (with $H_d = 0$), as follows:

$$p(H_d,H_s) = (1\text{-}f)\, p_{irrev}(H_d,H_s) + f\, p_{rev}(H_s) \tag{7.7}$$

where $0 \leq f \leq 1$. The total moment of the system is then the sum of an irreversible, history-dependent component M_{irrev} and a purely reversible component M_{rev} which depends only on the instantaneous value of the applied field H_a:

$$\begin{aligned} M(H_a,T,t) &= M_{irrev}(\text{history of } H_a,T,t) + M_{rev}(H_a,T) \\ &= N\mu(1-f)\int_{-\infty}^{+\infty} dH_s \int_{0}^{+\infty} dH_d\; p_{irrev}(H_d,H_s) + N\mu f \int_{0}^{H_a} dH_s\; p_{rev}(H_s) \end{aligned} \tag{7.8}$$

The thermal viscosity field $H_T = H_f \ln(t/\tau_0)$ appears exclusively in the first term in Eq(7.8), and consequently it is this dissipative term which is solely responsible for any

time dependence which is observed in the magnetic response, as well as for any temperature dependence arising specifically from thermal fluctuations. The second, purely reversible term is independent of time, but may depend on temperature T. For viscosity measurements, which are performed in negative holding fields $H_a < 0$, the reversible term is also negative, $M_{rev}(H_a) < 0$, and consequently this term imposes a uniform field-dependent downward shift on to each of the relaxation isotherms in Figure 7.3, all of which are purely dissipative in origin. This has the effect of reducing all of the reversal times t_r in Figure 7.3 which, in turn, distorts the universal plots of $Tln(t_r/\tau_0)$ versus H_a in Figure 7.5 by shifting every point on these curves downward parallel to the $Tln(t_r/\tau_0)$ axis, by an amount which depends on the holding field H_a. If the reversible term is independent of temperature, then the universality of the $Tln(t_r/\tau_0)$ versus H_a plot will be preserved , and consequently it will still be possible to conclude that the temperature dependence of the magnetic response originates exclusively from thermal fluctuations. However, the distortion of the universal curve will tend to invalidate some of the specific conclusions listed earlier. In particular, the initial slope of the linear regime of the universal curve in the limit of low temperatures and/or short observation times (if it still exists) is no longer a measure of the true elementary moment reversal μ, and the absolute value of the intercept along the H_a-axis will underestimate the true median intrinsic dissipation field H_{dm}. If the reversible term introduces an extra dependence on temperature beyond the linear dependence which appears in the thermal fluctuation field $H_f = kT/\mu$, then the distortions of the $Tln(t_r/\tau_0)$ versus H_a plot will become temperature dependent, and this will act to destroy the universality of the $Tln(t_r$

$/\tau_0$) versus H_a plot. In this case, universality loses its significance as a diagnostic tool for establishing the dominance of thermal fluctuations over barrier growth.

We now present applications of the analytical strategy proposed above to five magnetic materials with a spectrum of magnetic and microstructural characteristics.

7.3 Tiva Canyon Tuff

Figures 7.7 through 7.9 summarize the experimental measurements of the field, temperature, and time dependence of the magnetic response of a sample of Tiva Canyon Tuff, which is a magnetic rock consisting of nanodimensional particles of titanomagnetite $Fe_{3-x}Ti_xO_4$ (with $x \cong 0.1$) embedded rigidly and randomly in a volcanic glass.

Figure 7.7 shows a typical hysteresis loop measured at T = 15K by repeated application, removal, and reapplication of the magnetic field in increments of $\Delta H_a = 20$ Oe, starting from a thermally demagnetized inital state (achieved by cooling to T = 15K in zero field $H_a = 0$ from a reference temperature $T_{ref} = 325$K in the superparamagnetic regime, where the magnetic response is completely reversible), and then proceeding to a maximum positive field $H_a = 4.0$ kOe close to technical saturation, and terminating at a maximum negative field $H_a = -2.5$ kOe . The measurements in Figure 7.7 include the initial magnetizing curve, the initial magnetizing remanence (IRM), the descending branch of the major hysteresis loop, and the demagnetizing remanence.

Figures 7.8(a) through 7.8(e) show typical measurements of the temperature dependence of the field cooled (FC) moment, the zero field cooled (ZFC) moment, and the thermoremanent moment (TRM) in a series of applied fields H_a. The FC moment was measured by first thermally demagnetizing the sample in zero applied field $H_a=0$ at a reference temperature $T_{ref}=325$K, followed by the application of a positive field H_a, then by cooling in the field at a rate of about 10K/min to the lowest measurement temperature T=10K, and then by incremental warming in steps of $\Delta T=5$K. The TRM was measured

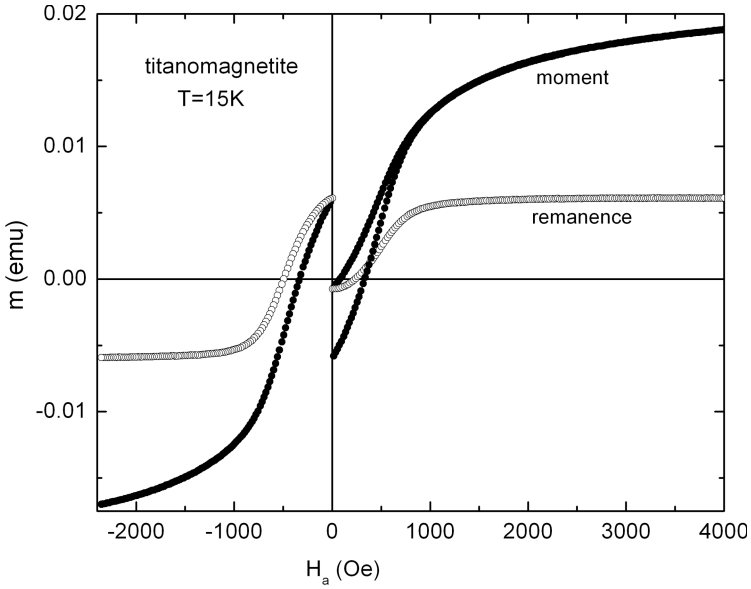

Figure 7.7: A hysteresis loop measured at T=15K for Tiva Canyon Tuff. The solid circles are the moment and the open circles are the remanent moment.

by field cooling from T_{ref}=325K to T=10K, followed by field removal, and then by incremental warming. The ZFC moment was measured by cooling in zero applied field from T_{ref}=325K to T=10K, followed by the application of a positive field H_a at T=10K, and then by incremental warming. The data in Figure 7.8 exhibit a number of structural features which are characteristic of materials that are conventionally classified as superparamagnets. Microstructurally, such materials typically consist of an ensemble of physically distinct magnetic grains, and the material exhibits a gradual and progressive loss of magnetic response (known as "blocking") upon cooling, as the individual grains fall of out thermal equilibrium sequentially, and as their individual moments drop below their thermal equilibrium values. Most notable among these structural features is a bifurcation temperature $T_{bif} \cong 150K$ which lies well below the critical ordering temperature of the constituent magnetic grains ($T_C \cong 800K$ for $Fe_{2.9}Ti_{0.1}O_4$). It is at this

temperature that the FC and ZFC moments bifurcate into two distinct branches, accompanied by the appearance of remanence (TRM) and hysteresis, and is the temperature that separates a high temperature reversible (equilibrium) regime where the FC and ZFC moments are identical and decay very gradually with temperature and the remanent moment is negligible, from a low temperature irreversible regime, where the system is unable to reach thermal equilibrium within the time scale of the experimental measurement (in this case, $t_{exp} \sim 100s$). The FC/ZFC bifurcation in low applied fields $H_a \leq 20$ Oe is quite significant in this particular sample, a behaviour which tends to be indicative of weak inter-granular coupling[8-11]. As we shall see, this is indeed confirmed by the subsequent analysis. To the list of structural features characteristic of superparamagnets, it is appropriate to add the presence of a broad maximum in the temperature dependence of the ZFC moment which is located just below the bifurcation temperature, and which propagates systematically toward lower temperatures with increasing applied field.

Figures 7.9(a) through 7.9(d) show representative measurements of viscosity isotherms performed at four different temperatures within the irreversible regime, in a series of negative holding fields $H_a < 0$ (listed in each figure), over an experimental observation time window $10s \leq t \leq 10^4 s$, and plotted on a logarithmic time scale. At each temperature, the material was first subjected to a positive saturating field $H_{sat} = 10$ kOe, followed by recoil to a negative holding field H_a, chosen so that the "critical" time $t = t_r$ at which the relaxation isotherm reverses sign (that is, passes through zero moment, $m = 0$) lies within the experimentally available time window, after which the decay of the

moment was recorded as a function of observation time at fixed temperature and in fixed magnetic field. The measurements presented here were performed on a magnetic mineral in its "natural" state, as extracted from the Earth, and, as a consequence, the magnetic signal is relatively weak and the viscosity data are relatively noisy. Nevertheless, within the limitations imposed by the scatter and also by the width of the experimental time window, the functional form of the decay in Figure 7.9 may be characterized as quasi-logarithmic.

Figure 7.10 summarizes the complete set of "reversal time" data for Tiva Canyon Tuff, obtained from measurements like those shown in Figure 7.9 performed over a range of temperatures $8K \leq T \leq 80K$ that spans a significant portion of the irreversible regime, in the form of a plot of $Tlnt_r$ as a function of holding field H_a, where t_r is the time at which a relaxation isotherm measured at temperature T in a holding field H_a reverses sign.

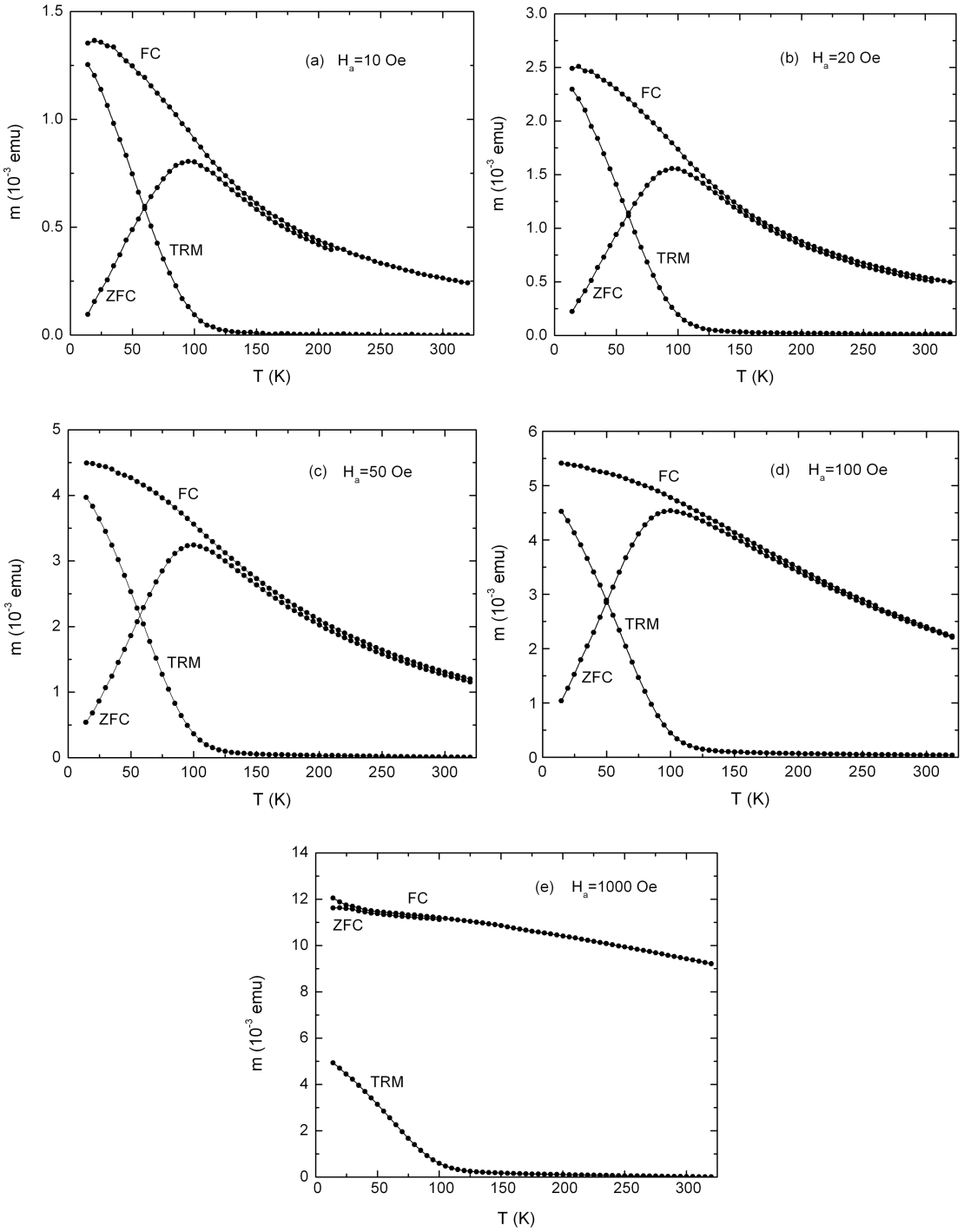

Figure 7.8: Measurements of the FC moment, ZFC moment, TRM, and IRM of Tiva Canyon Tuff in applied fields of (a) $H_a = 10$ Oe, (b) $H_a = 20$ Oe, (c) $H_a = 50$ Oe, (d) $H_a = 100$ Oe and (e) $H_a = 1000$ Oe. The solid lines are guides to the eye.

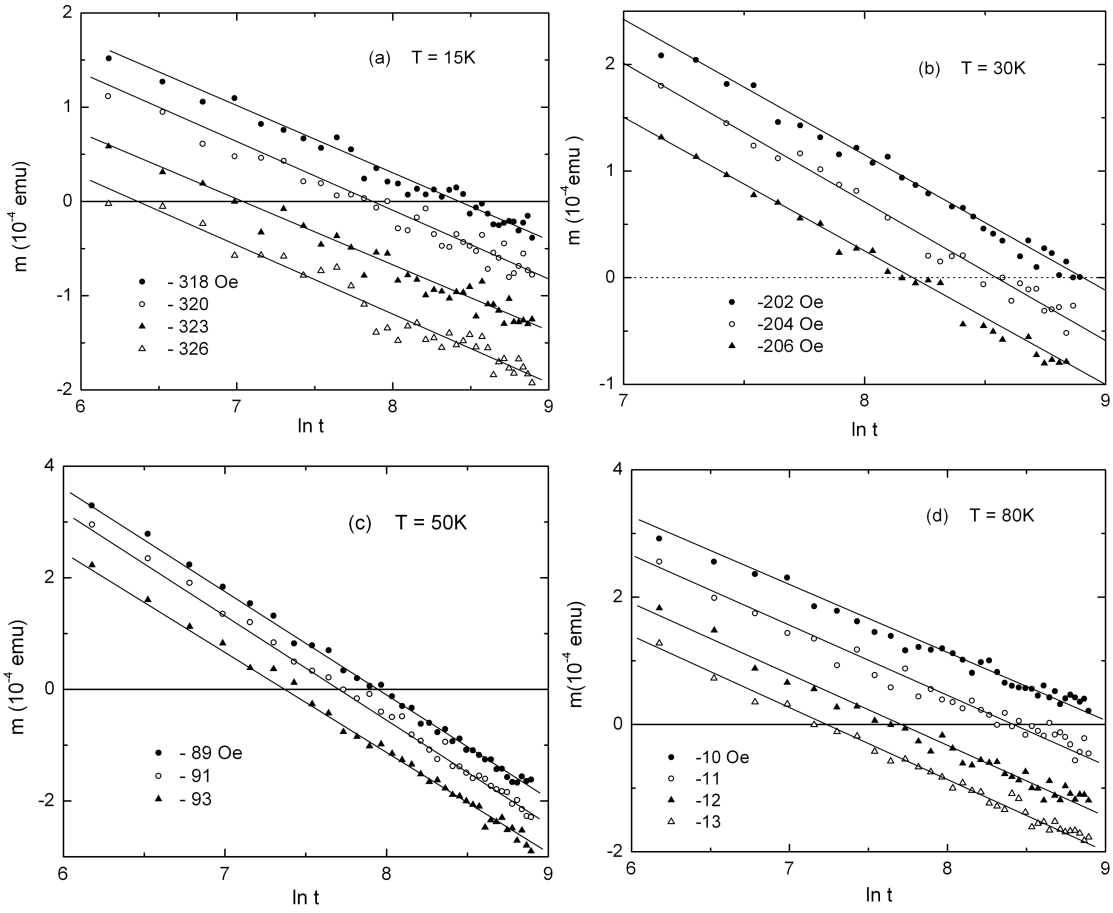

Figure 7.9: Measurements of viscosity isotherms of Tiva Canyon Tuff in a series of negative holding fields at temperatures: (a) T = 15K, (b) T = 30K, (c) T = 50K, and (d) T=80K. The fields in which each isotherm was measured are listed in each panel. The straight lines are guides to the eye.

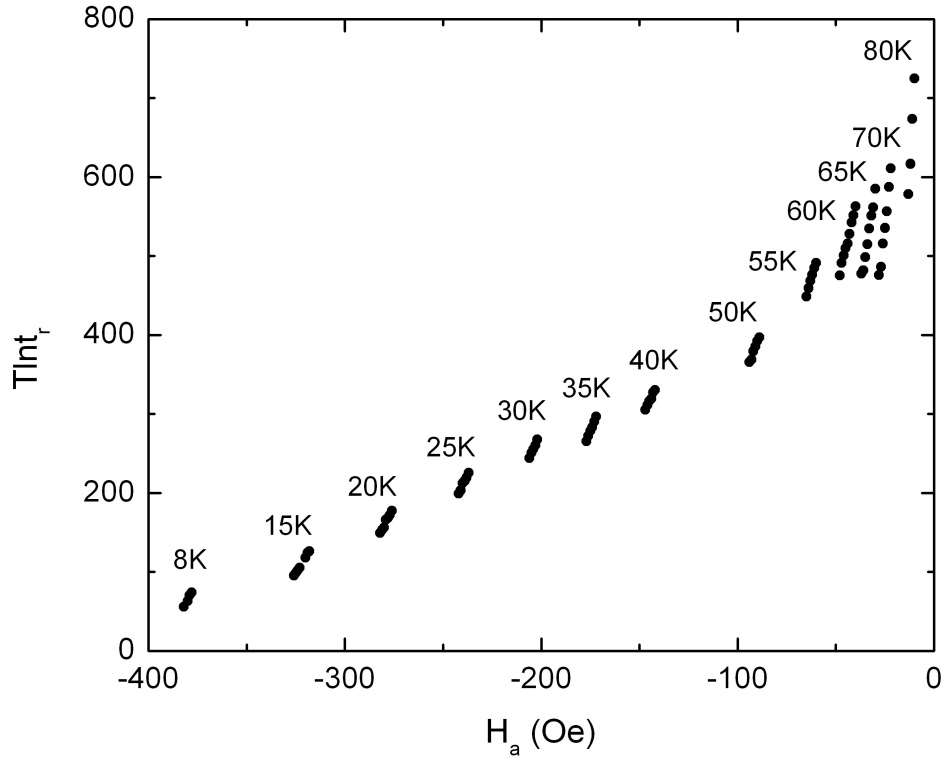

Figure 7.10: Reversal time data expressed in the form $Tlnt_r$ and plotted a function of the holding field H_a for a range of temperatures from T = 8K to T = 80K listed in the figure.

As the first step toward establishing the physical origins of thermal effects in Tiva Canyon Tuff, and the relative importance of the roles played by thermal fluctuations and barrier growth, the "reversal time" data in Figure 7.10 have been replotted in Figure 7.11 in the form $Tln(t_r/\tau_0)$ versus H_a, for a series of values of τ_0 lying within the range $10^{-18}s \le \tau_0 \le 10^{-6}s$, in order to search for evidence of universality. The main body of Figure 7.11 shows the complete plots over the entire range of temperatures and holding fields investigated experimentally, while the inset shows a magnified view in the limit of low fields and high temperatures. An inspection of this figure shows that there are four values of τ_0 for which the "reversal time" data scale convincingly onto universal curves

of roughly comparable quality, namely, $\tau_0 = 10^{-13}$ s, 10^{-12} s, 10^{-11} s, and 10^{-10} s, all of which fall within physically acceptable limits, as defined in the literature [12-14]. For values of τ_0 outside this range, deviations from universality become progressively and systematically more severe (see inset). The existence of the universal curves allows us to conclude, at least tentatively (for reasons to be discussed later in this section), that the temperature dependence of the magnetic response of this particular assembly of titanomagnetite nanoparticles is shaped almost exclusively by thermal overbarrier activation events within a fixed free energy landscape which does not itself evolve explicitly with temperature.

As predicted by the model simulations of universal curves shown in Figure 7.5, the four experimental universal curves in Figure 7.11 each exhibit a regime which is linear in applied field H_a, and with a relatively wide range of validity -450 Oe < H_a < -150 Oe, as illustrated by the straight lines in Figure 7.11. According to the model, the slope of the linear regime yields the mean characteristic elementary moment reversal μ, while the intercept along the H_a-axis yields the intrinsic coercive field H_{ci}, and hence a first estimate for the median intrinsic dissipation field H_{dm}. The preliminary estimates for the parameters (μ, H_{dm}) obtained from the slope and intercept, respectively, of the four straight lines in Figure 7.11 are listed below in Table 7.1.

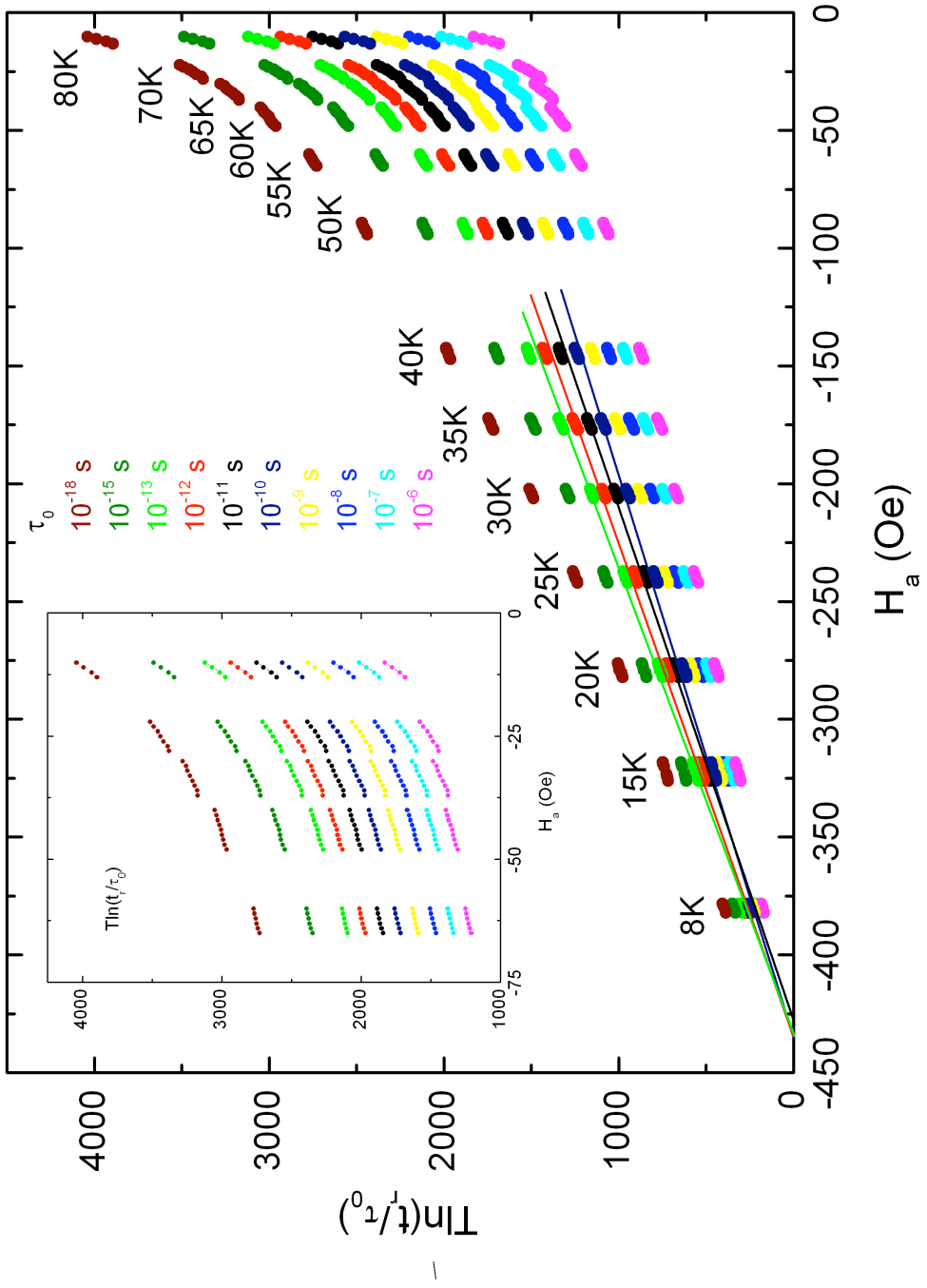

Figure 7.11: $T\ln(t_r/\tau_0)$ versus H_a plots shown over the entire range of temperatures and holding fields for a series of values of τ_0. The straight lines through the four curves with $10^{-13} \le \tau_0 \le 10^{-10}$ s show the linear portions of each universal curve. The inset is a magnified version of the $T\ln(t_r/\tau_0)$ versus H_a plots in the limit of low fields and high temperatures.

Table 7.1: Preliminary Universal Curve Simulation Parameters

τ_0 (s)	μ (10^{-16}emu)	H_{dm} (Oe)	σ_d	σ_s
10^{-13}	7.0 ± 0.5	434 ± 11	0.5±0.05	0.1 ± 0.05
10^{-12}	6.6 ± 0.5	434 ± 10	0.5±0.05	0.1± 0.05
10^{-11}	6.3 ± 0.4	425 ± 14	0.5±0.05	0.1± 0.05
10^{-10}	5.8 ± 0.4	435 ± 7	0.5±0.05	0.1± 0.05

Once initial estimates for μ and H_{dm} have been established, and the thermal fluctuation field $H_f = kT/\mu$ is known, a functional form may be chosen for the Preisach distribution $p(H_d,H_s)$, and the dispersions σ_d and σ_s of characteristic fields H_d and H_s determined by comparing model simulations of universal curves like those shown in Figure 7.5 to the measured universal curves in Figure 7.11, for various combinations of σ_d and σ_s. Figure 7.12 shows the best model representations of the four universal curves with $10^{-13} \leq \tau_0 \leq 10^{-10}$ s in Figure 7.11, assuming a Preisach density of characteristic fields $p(H_d,H_s)$ consisting of the product $p(H_d,H_s) = f(H_d)\, g(H_s)$ of a lognormal distribution of dissipation fields H_d and a Gaussian distribution of bias fields H_s, as given in Eq(7.5). In all four cases, the best description was achieved with the same combination of dispersions, $\sigma_d = 0.5$ and $\sigma_s = 0.1$ (Table 7.1).

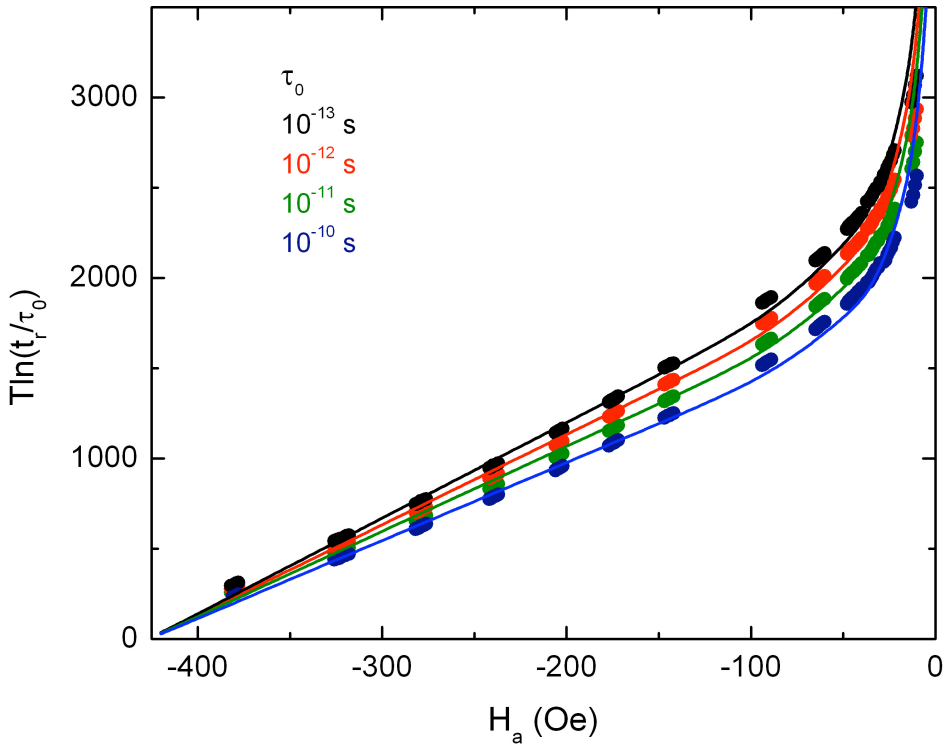

Figure 7.12: The best model representations of the four universal curves whose values of τ_0 fall within physically acceptable limits. The representations assume a Preisach density consisting of a product of a lognormal distribution of dissipation fields and a Gaussian distribution of bias fields, with dispersions of $\sigma_d = 0.5$ and $\sigma_s = 0.1$ respectively.

Although the viscosity-based thermal fluctuation analysis presented above is certainly compelling, it is nevertheless incomplete, and the entire set of model parameter values (μ, H_{dm}, σ_d, σ_s) in Table 7.1 must be regarded as preliminary, since the analysis entirely ignores contributions from reversible magnetizing processes, which form a significant component of the magnetic response of Tiva Canyon Tuff. This reversible contribution is most evident in measurements of hysteresis loops like that shown in Figure 7.7, primarily

through the large ratio of the saturation moment $M_{sat}(H_a \rightarrow \infty)$ to the saturation isothermal remanent moment $IRM_{sat}(H_a \rightarrow \infty)$. As previously discussed toward the end of Section 7.2, a proper description of systems like Tiva Canyon Tuff requires the superposition of two distinct distributions of characteristic fields, one distribution $p_{irrev}(H_d,H_s)$ to describe dissipative, time-dependent processes, and another distribution $p_{rev}(H_s)$ to describe purely reversible processes, as indicated in Eq(7.7) and Eq(7.8). The introduction of a reversible term can have a profound effect on the properties of model relaxation isotherms, and on the shape and characteristics of the $T\ln(t_r/\tau_0)$ versus H_a plots, generated from a dissipative distribution alone. As a consequence, it is necessary to revisit the original model simulations in Figure 7.12 in order to ascertain the extent to which the original physical interpretation, as summarized by the parameter values in Table 7.1, survives the superposition substantially intact. The first step in this process is to choose a suitable functional form for the distribution $p_{rev}(H_s)$ of purely reversible subsystems. For reasons of computational simplicity, the following exponential form was adopted

$$p_{rev}(H_s) = \lambda \exp(-\lambda |H_s|) \quad , \qquad (7.9)$$

where λ is a constant, independent of H_s, but possibly temperature-dependent. Next, estimates for the reversible parameters f and λ were determined by fitting model simulations of hysteresis loops to the measured hysteresis loop in Figure 7.7, using the superposition in Eq(7.8). For purposes of establishing the shape of the reversible response function, the effects of thermal fluctuations are irrelevant, and the fit was performed by

setting the thermal viscosity field $H_T = 0$ (that is, setting $\mu = \infty$) and the intrinsic coercive field H_{dm} equal to the measured remanent coercive field $H_{cr}(T = 15K) = 500$ Oe, and by adopting the original estimates for the dispersions $\sigma_d = 0.5$ and $\sigma_s = 0.1$ listed in Table 7.1. This procedure yielded best fit values for λ and f of $\lambda = 6.7 \times 10^{-4}$ Oe^{-1} and f = 0.7.

With the reversible component thus defined, numerical simulations of viscosity isotherms and reversal time plots of $T\ln(t_r/\tau_0)$ as a function of H_a were generated once again assuming the superposition in Eq(7.8). The original parameter values μ, H_{dm}, σ_d, and σ_s were revised as necessary in order to achieve the best overall representation of the measured universal curves in Figure 7.12. The results of these simulations are shown by the solid curves in Figure 7.13 for the two universal data sets with $\tau_0 = 10^{-13}$ and $\tau_0 = 10^{-10}$ s , and the corresponding sets of best fit parameter values are listed in Table 7.2. In order to better appreciate the nature of the distortions caused by introduction of the reversible component, the dashed line in Figure 7.13 shows the $T\ln(t_r/\tau_0)$ versus H_a plot for the dissipative component alone using the moment μ required to describe the data with $\tau_0 = 10^{-13}$ s. A comparison of the final parameter values in Table 7.2 with the preliminary estimates in Table 7.1 shows that the inclusion of a reversible term necessitates reductions in both μ and σ_s, and an increase in H_{dm}. However, the essential features of the original interpretation remain fundamentally unaltered. In particular, Tiva Canyon Tuff may be classified as a material which is *fluctuation-dominated* in the sense that the temperature dependence of the irreversible component of the magnetic response originates primarily from a thermally activated migration through a free energy landscape

which does not evolve explicitly with temperature, at least over the temperature range T < 150K where non-equilibrium history-dependent and time-dependent effects are observed.

Table 7.2: Final Universal Curve Simulation Parameters

τ_0 (s)	μ (10^{-16}emu)	H_{dm} (Oe)	σ_d	σ_s / H_{dm}	f	λ (10^{-4} Oe^{-1})	M_{sat} (emu)
10^{-13}	4.9± 0.5	650 ± 11	0.5 ±0.1	0.05 ±0.02	0.7 ±0.1	6.7 ±0.5	0.02
10^{-12}	4.6 ± 0.5	650 ± 10	0.5 ±0.1	0.05 ±0.02	0.7 ±0.1	6.7 ±0.5	0.02
10^{-11}	4.4± 0.5	650 ± 14	0.5 ±0.1	0.05 ±0.02	0.7 ±0.1	6.7 ±0.5	0.02
10^{-10}	4.0 ± 0.5	650 ± 7	0.5 ±0.1	0.05 ±0.02	0.7 ±0.1	6.7 ±0.5	0.02

Once the distribution $p_{irrev}(H_d,H_s)$ of dissipative subsystems and the distribution $p_{rev}(H_s)$ of reversible subsystems as well as the characteristic elementary moment reversal μ are known, the characteristics of the spectrum of metastable state excitation barriers of Tiva Canyon Tuff are in principle completely defined, and it is possible to predict the results of other experimental measurements such as hysteresis loops and the FC/ZFC/TRM measurements shown in Figure 7.8(a) to 7.8(e). Such predictions provide an important and necessary internal consistency check on the validity of the thermal fluctuation analysis performed above, and the conclusions reached thereby, since these response functions are themselves also highly sensitive probes of the structure of the free energy landscape, and particular structural features of the response functions, as well as their systematic variation with applied field and temperature, have been linked to particular Preisach distribution parameters, specifically, to the two dispersions of characteristic

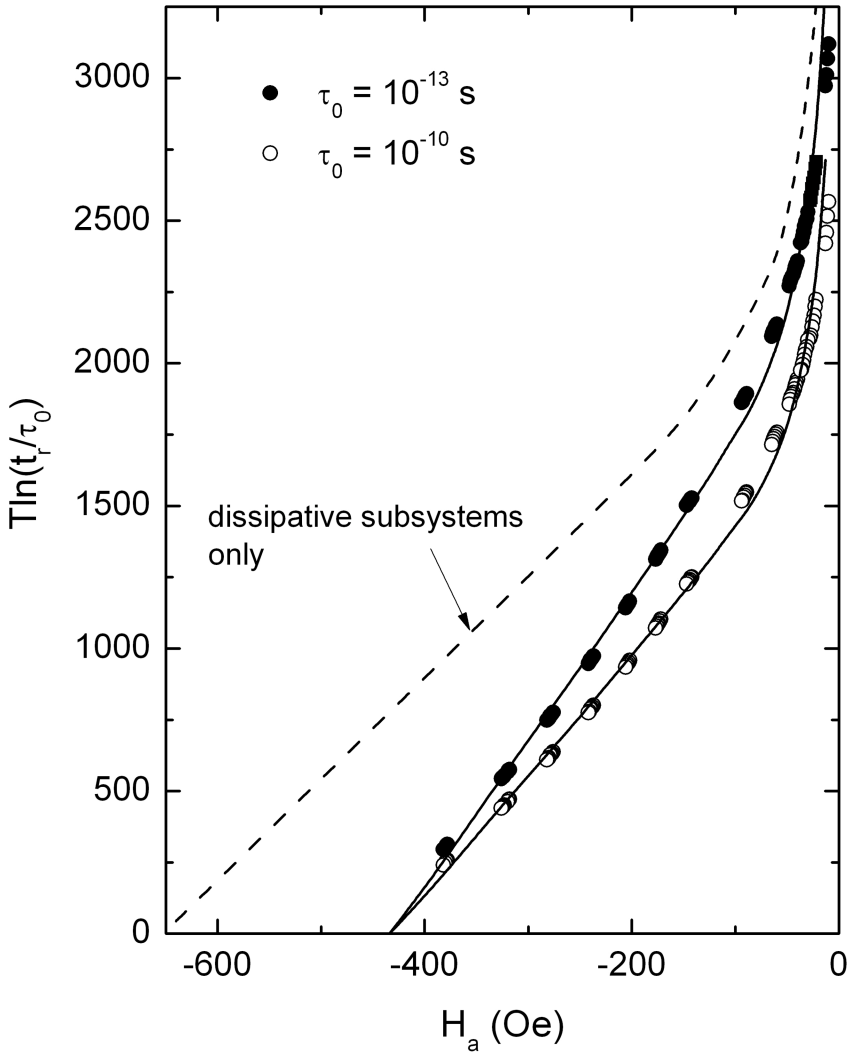

Figure 7.13: Numerical simulations of reversal time plots (solid curves) for universal data sets with $\tau_0 = 10^{-13}$ s and $\tau_0 = 10^{-10}$ s. The simulations incorporate both dissipation and reversible Preisach distributions. The dotted curve shows the reversal time plot for the dissipative component only.

fields σ_d and σ_s [6, 9]. Figures 7.14(a) through 7.14(e) shows numerical model simulations of the same sequence of FC/ZFC/TRM measurements shown in Figure 7.8, and the solid curves in Figure 7.15 show numerical model simulations of the hysteresis loop in Figure 7.7 superposed onto the measured loop. In order to achieve the most

faithful reproduction of the experimental data, minor adjustments were necessary to a few of the model parameters, specifically a reduction in the mean elementary moment reversal to $\mu = 3x10^{-16}$ emu, reductions to some of the applied fields H_a in the FC/ZFC/TRM sequence below the nominal experimental values and, in the case of the hysteresis loop, a reduction in the dispersion of dissipation fields to $\sigma_d = 0.4$. However, in all cases, these adjustments are consistent with the tolerances established by the analysis, and the need for such adjustments is even less significant in light of the fact that the viscosity measurements in Figure 7.9 and the hysteresis/FC/ZFC/TRM measurements in Figures 7.7 and 7.8 were performed on two different magnetometers. Tables 7.3 and 7.4 summarize the parameter values used to generate the FC/ZFC/TRM and hysteresis loop simulations, respectively.

Table 7.3: FC/ZFC/TRM Simulation Parameters

τ_0 (s)	t_{exp}(s)	μ (10^{-16}emu)	H_{dm} (Oe)	σ_d	σ_s / H_{dm}	f	λ (10^{-4} Oe^{-1})	M_{sat} (emu)
10^{-12}	10^2	3.0 ± 0.5	650 ± 10	0.5 ±0.1	0.05 ±0.02	0.7 ±0.1	6.7 ±0.5	0.02

Table 7.4: Hysteresis Loop Simulation Parameters

τ_0 (s)	t_{exp}(s)	μ (10^{-16}emu)	H_{dm} (Oe)	σ_d	σ_s / H_{dm}	f	λ (10^{-4} Oe^{-1})	M_{sat} (emu)
10^{-12}	10^2	3.0 ± 0.5	650 ± 10	0.4 ±0.1	0.05 ±0.02	0.7 ±0.1	6.7 ±0.5	0.02

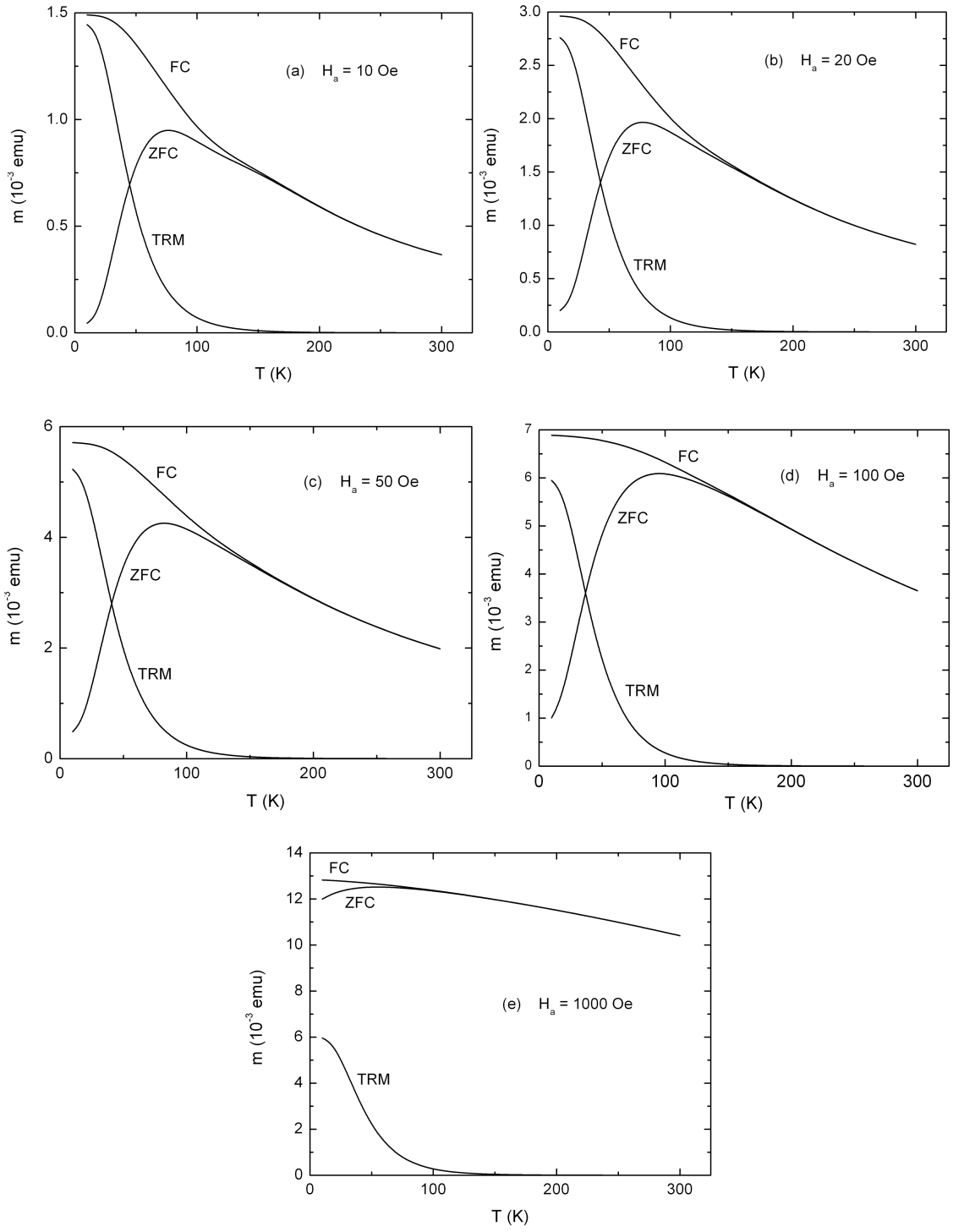

Figure 7.14: Numerical model simulations of the same sequence of FC/ZFC/TRM measurements shown in Figure 7.8, for the simulation parameters listed in Table 7.3: (a) H_a = 10 Oe, (b) H_a = 20 Oe, (c) H_a = 50 Oe, (d) H_a = 100 Oe, and (e) H_a = 1000 Oe.

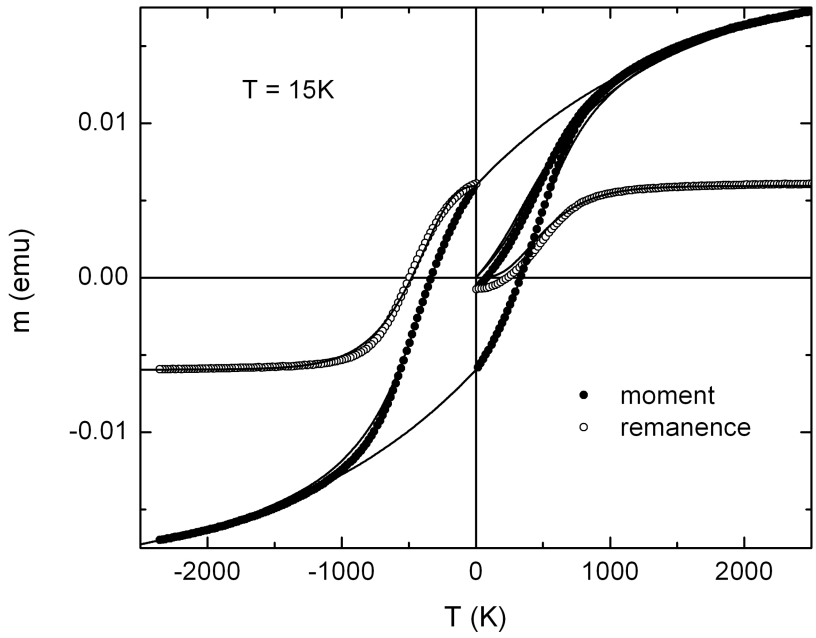

Figure 7.15: Numerical model simulation (solid curves) of the measured hysteresis loop (dots) shown in Figure 7.7 for the model simulation parameters listed in Table 7.4.

7.4 Nanoparticulate Magnetite

Figures 7.16 through 7.18 summarize the principal characteristics of the field and temperature and time dependence of the measured magnetic response of a compressed powder of nanodimensional magnetite (Fe_3O_4) particles immobilized in an organic binder.

Figures 7.16(a), (b) and (c) show representative hysteresis loops measured at T = 5K, 10K and 15K, following thermal demagnetization in zero field from a reference temperature T_{ref} = 325K, by repeated application, removal, and reapplication of the magnetic field in increments of ΔH_a = 100 Oe, starting from the demagnetized state and then proceeding to a maximum positive field H_a = 6.0 kOe close to technical saturation, and terminating at a maximum negative field H_a = -6.0 kOe . The measurements in these figures include the initial magnetizing curve, the initial magnetizing remanence (IRM), the descending and ascending branches of the major hysteresis loop, and the demagnetizing remanence. Figure 7.16(d) shows plots of the measured coercive field H_c and the measured remanent coercive field H_{cr} as a function of temperature over the interval $5K \leq T \leq 80K$.

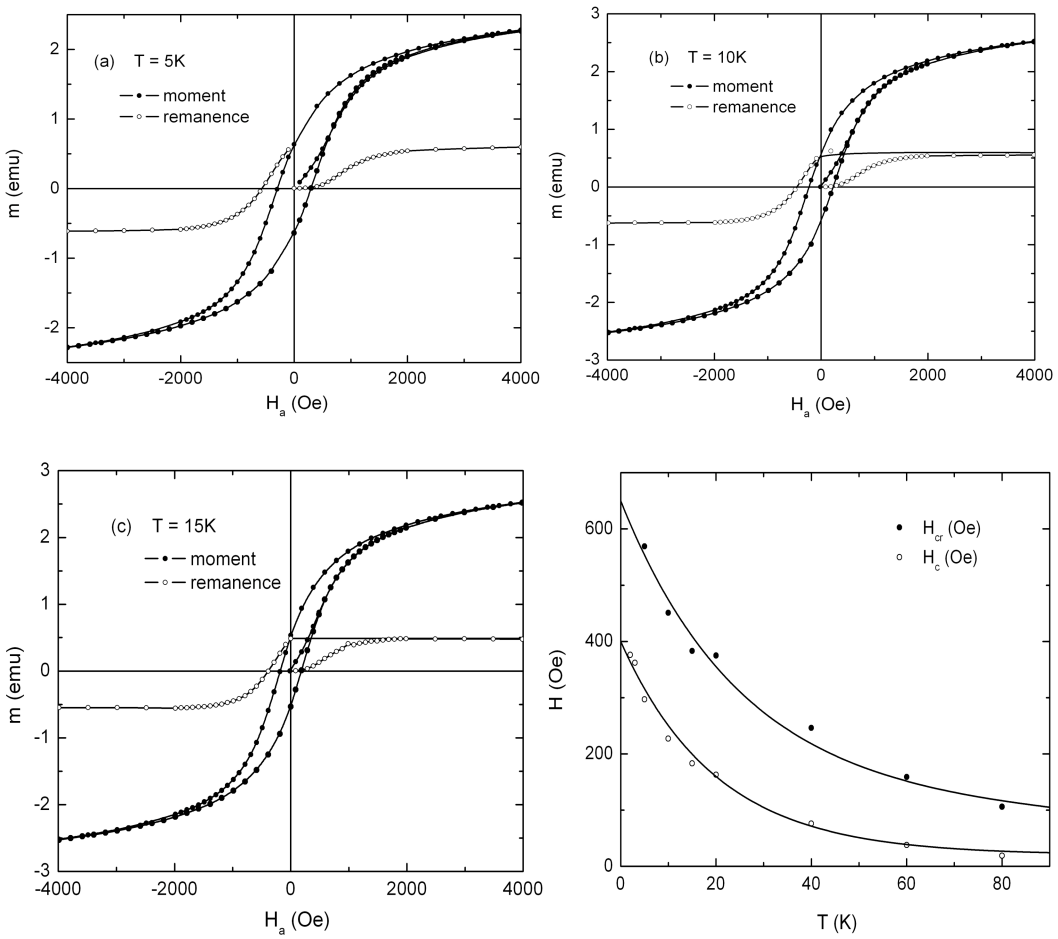

Figure 7.16: Measured hysteresis loops for a nanoparticulate magnetite powder at temperatures of (a) T = 5K, (b) T = 10K, (c) T = 15K. (d) The temperature dependence of the measured coercive field (open circles) and the measured remanent coercive field (solid circles) for the magnetite powder. The solid lines are guides to the eye.

Figures 7.17(a) through 7.17(d) show representative measurements of the temperature dependence of the field cooled (FC) moment, the zero field cooled (ZFC) moment, the thermoremanent moment (TRM) and the isothermal remanent moment (IRM) between 10K $\leq$ T $\leq$ 300K in a series of applied fields H_a. The experimental protocols for the FC moment and the TRM were identical to those described for Tiva Canyon Tuff in the Section 7.3. The ZFC moment and the IRM were measured by first

thermally demagnetizing the sample in zero applied field $H_a = 0$ at a reference temperature T_{ref}=325K, then cooling in zero applied field to the lowest measurement temperature T=10K, followed by the application of a positive field (to obtain the ZFC moment), then field removal (to obtain the IRM), and then by field reapplication and incremental warming to the next measurement temperature, where the field removal and reapplication protocol was repeated. The response functions of the magnetite powder in Figure 7.17 share many of the same superparamagnetic characteristics as those of titanomagnetite in Figure 7.8, including a bifurcation temperature $T_{bif} \cong 250$K which lies well below the bulk ferrimagnetic critical temperature $T_C \cong 850$K of pure magnetite, a purely reversible high temperature regime ($T > T_{bif}$), and an irreversible low temperature regime ($T < T_{bif}$) where the moment bifurcates into two distinct FC and ZFC branches, accompanied by a simultaneous bifurcation of the remanent moment into distinct IRM and TRM branches. In spite of their overall similarity, the behaviour of magnetite and titanomagnetite nevertheless differs in one important respect: the thermal profile of the low field FC moment in magnetite is quite flat, particularly below the bifurcation point and, consequently, the divergence between the FC and ZFC branches is weak, in comparison with titanomagnetite, where the rapid variation of the FC moment with temperature, which persists down to the lowest measurement temperatures, leads to a strong divergence of the FC and ZFC branches.

Figures 7.18(a) through 7.18(e) show representative measurements of viscosity isotherms performed at five different temperatures within the irreversible regime, in a series of negative holding fields $H_a < 0$ (listed in each figure), over an experimental

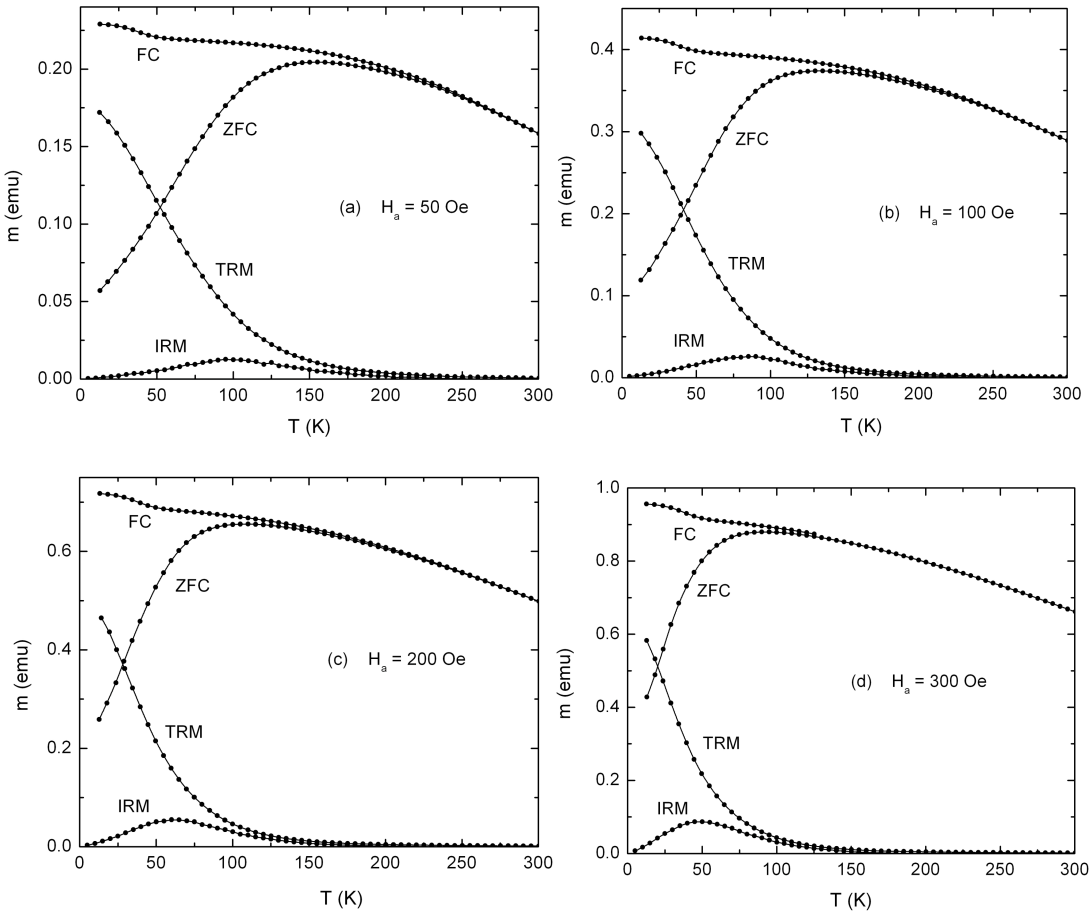

Figure 7.17: Measurements of the FC moment, ZFC moment, TRM, and IRM for nanoparticulate magnetite in fields of (a) H_a = 50 Oe, (b) H_a = 100 Oe, (c) H_a = 200 Oe, and (d) H_a = 300 Oe. The solid lines are guides to the eye.

observation time window $10s \leq t \leq 10^4 s$, and plotted on a logarithmic time scale. The experimental protocol was identical to that described in Section 7.3 for Tiva Canyon Tuff, but with a different positive saturating field H_{sat} =10 kOe. As before, only a logarithmic or quasi-logarithmic fragment of the complete relaxation isotherm is visible within the limited experimental time window.

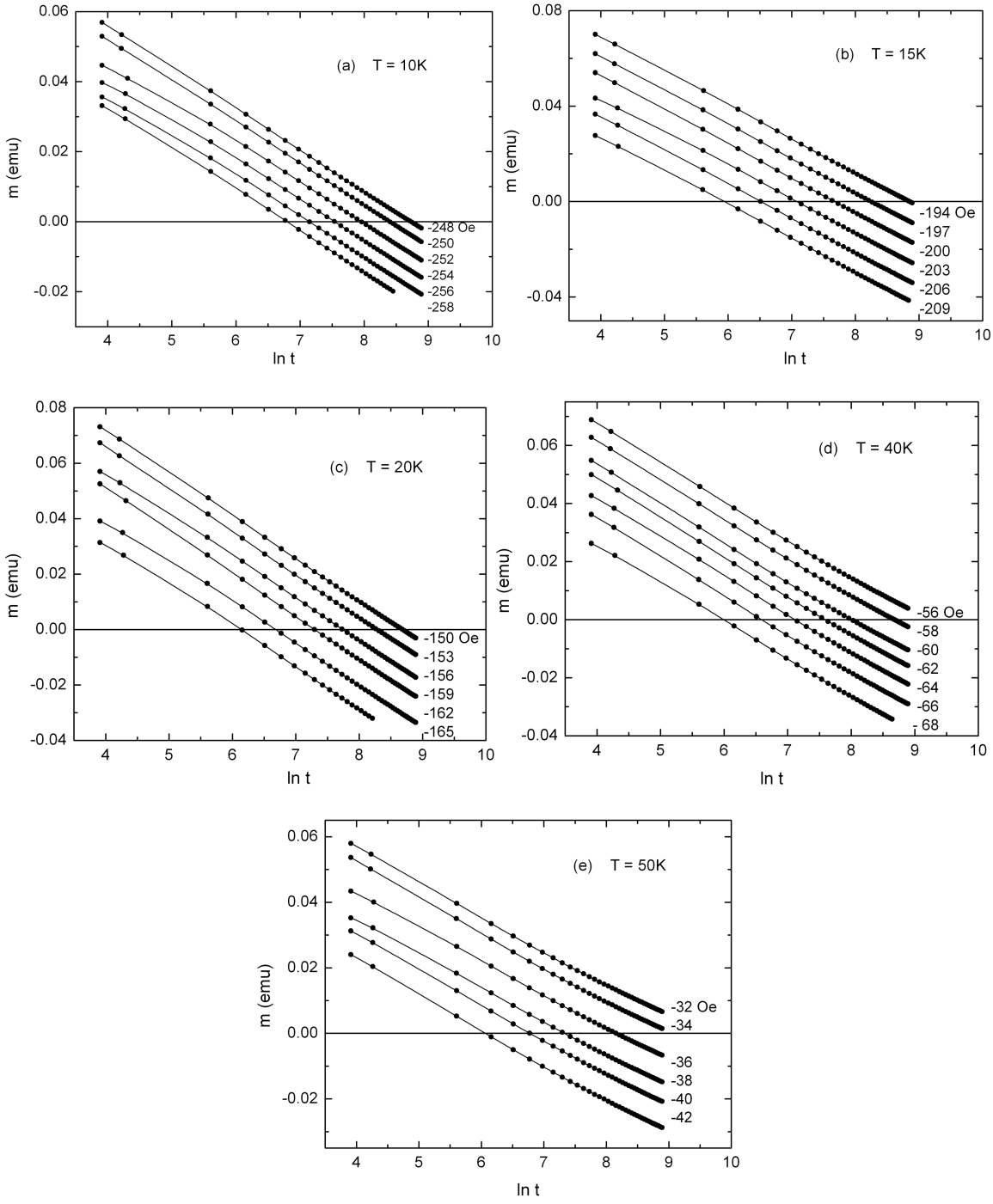

Figure 7.18: Measurements of viscosity isotherms for nanoparticulate magnetite in a sequence of holding fields (listed in each figure) at temperatures (a) T = 10K, (b) T = 15K, (c) T = 20K, (d) T = 40K, and (e) T = 50K. The solid lines are guides to the eye.

The analytical strategy described in Section 7.3 for Tiva Canyon Tuff was repeated, in precisely the same sequence, for the system of magnetite nanoparticles, and the results are summarized in Figures 7.19 through 7.22 and in Tables 7.5 through 7.8. Figure 7.19 shows plots of the "reversal time" data obtained from the viscosity isotherms in Figure 7.18 in the form $T\ln(t_r/\tau_0)$ versus H_a, for a series of values of τ_0 lying within the range $10^{-18}\text{s} \le \tau_0 \le 10^{-6}\text{s}$. The inset in this figure shows a magnified view of the behaviour of these plots in the limit of low fields and high temperatures. As before, values of τ_0 from the centre of the range, specifically $\tau_0 = 10^{-12}$ s and $\tau_0 = 10^{-11}$ s, yield the most acceptable universal behaviour, with deviations from universality becoming progressively more severe for values of τ_0 approaching the extreme ends of the range. For purposes of the current analysis, we have adopted a value of $\tau_0 = 10^{-11}$ s. The solid curve in Figure 7.19 shows the best model representation of the measured universal curve for $\tau_0 = 10^{-11}$ s, assuming a single, purely dissipative Preisach density of characteristic fields $p_{irrev}(H_d,H_s)$ consisting of the product of a lognormal distribution of dissipation fields H_d and a Gaussian distribution of bias fields H_s. Table 7.5 summarizes the preliminary values of the model parameters (μ, H_{dm}, σ_d, σ_s), neglecting reversible contributions. Estimates for the reversible parameters f and λ, as defined in Section 7.3, were then determined by fitting model simulations of hysteresis loops to the measured hysteresis loop for T = 5K in Figure 7.15(a), using the superposition in Eq(7.8) and the reversible distribution function defined in Eq(7.9). As before, the fit was performed by setting the thermal viscosity field $H_T = 0$ (that is, by setting $\mu = \infty$) and the intrinsic coercive field

H_{dm} equal to the measured remanent coercive field $H_{cr}(T = 5K) = 550$ Oe, and by adopting the original estimates for the dispersions $\sigma_d = 1.0$ and $\sigma_s = 1.0$ listed in Table 7.1. This procedure yielded best fit values for λ and f of $\lambda = 7.0 \times 10^{-4}$ Oe^{-1} and $f = 0.67$. Once the reversible component of the magnetic response was defined, model simulations of viscosity isotherms were performed assuming the complete superposition of dissipative and reversible Preisach densities in Eq(7.8), and comparisons with the experimental plot of $T\ln(t_r/\tau_0)$ versus H_a in Figure 7.19 for $\tau_0 = 10^{-11}$ s were revisited, and the parameters in Table 7.5 were revised as necessary. The solid curve in Figure 7.20 shows the best model description of the data, and the dashed curve shows the contribution from the purely dissipative subsystems alone. Table 7.6 summarizes the complete set of model parameter values. A comparison of Tables 7.5 and 7.6 shows that the principal effects of including a reversible term are significant reductions in the elementary moment reversal μ, and in both dispersions σ_d and σ_s below the preliminary, dissipation-only estimates.

Table 7.5: Preliminary Universal Curve Simulation Parameters

τ_0 (s)	μ (10^{-16}emu)	H_{dm} (Oe)	σ_d	σ_s
10^{-11} s	2.6 ±0.6	365 ± 5	1.0 ±0.2	1.0 ±0.2

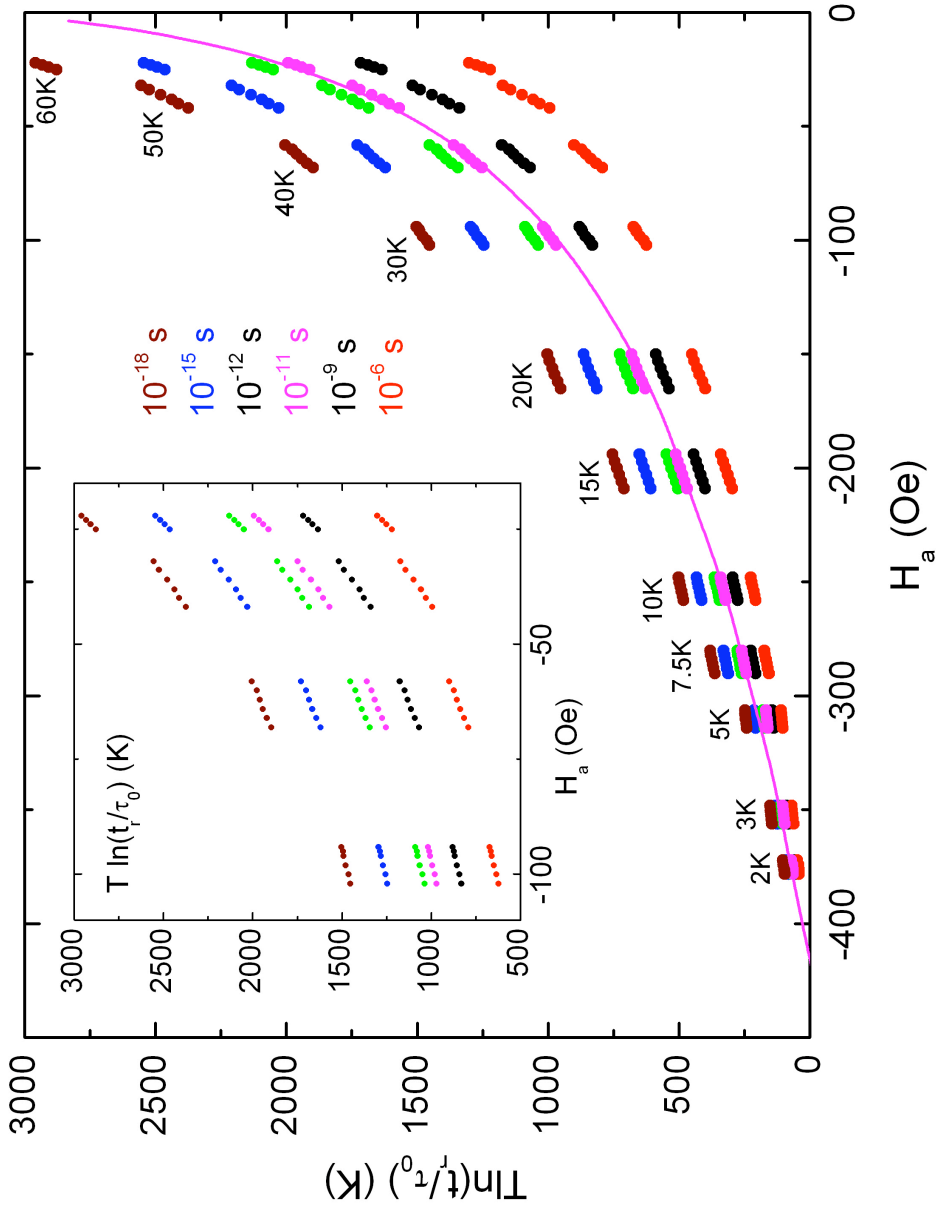

Figure 7.19: Reversal time plots ($T\ln(t_r/\tau_0)$ versus H_a) for a series of values of τ_0. The solid curve is the best model representation of the universal curve for $\tau_0 = 10^{-11}$ s, and assumes a Preisach density consisting of a product of a lognormal distribution of dissipation fields and a Gaussian distribution of bias fields, with dispersions of $\sigma_d = 1.0$ and $\sigma_s = 1.0$.

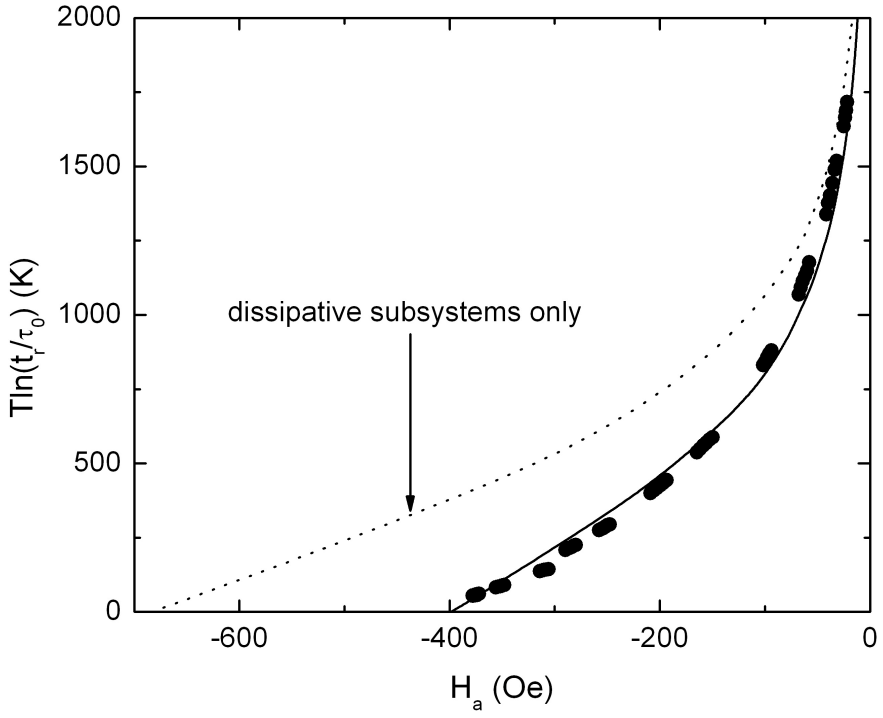

Figure 7.20: A model simulation of the reversal time plot (smooth curve) for the universal data set with $\tau_0 = 10^{-11}$ s (solid dots). The simulation incorporates a distribution of purely reversible subsystems as well as a distribution of dissipative subsystems with Preisach dispersions of $\sigma_d = 0.6$, and $\sigma_s = 0.4$. The dotted curve is the plot for the dissipative distribution alone (no reversible component).

Table 7.6: Final Universal Curve Simulation Parameters

τ_0 (s)	μ (10^{-16}emu)	H_{dm} (Oe)	σ_d	σ_s	f	λ (10^{-4} Oe^{-1})	M_{sat} (emu)
10^{-11}	1.8 ± 0.5	650 ± 10	0.6 ±0.2	0.4 ±0.2	0.67 ±0.05	7.0 ±2.0	2.55

Once the characteristics of the entire ensemble of two-level subsystems have been defined, and the spectrum of metastable state excitation barriers as well as the thermal fluctuation field are known, the model acquires predictive capability which may be

exploited to confirm the validity of the viscosity analysis. The solid curves in Figure 7.21(a) through 7.21(c) show numerical model simulations of moment and remanence hysteresis loops at T = 5K, 10K and 15K, superposed directly onto the measured loops from Figure 7.16, while Figures 7.22(a) through 7.22(d) show numerical model simulations (smooth curves) of the same sequence of FC/ZFC/TRM/IRM measurements shown in Figure 7.17. As before, minor adjustments were necessary to a few of the model parameters in Table 7.6 in order to optimize the correspondence with the experimental data, specifically an increase in the mean elementary moment reversal to $\mu = 2.5 \times 10^{-16}$ emu as well as to some of the applied fields H_a above the nominal experimental values in the FC/ZFC/TRM/IRM sequence and, in the case of the hysteresis loops, an increase in the dispersion of dissipation fields to $\sigma_s = 0.5$ and in the reversible parameter λ to $\lambda = 8.0 \times 10^{-4}$ Oe^{-1}. However, in all cases, these adjustments are consistent with the tolerances established by the viscosity analysis. Table 7.7 and Table 7.8 summarize the parameter values used to generate the hysteresis loop and the FC/ZFC/TRM/IRM simulations, respectively.

We remarked earlier in this section that the single most striking contrast between the measured FC/ZFC response functions of magnetite and those of Tiva Canyon Tuff in low magnetic fields was the comparative flatness of the FC moment and the comparative weakness of the FC/ZFC divergence below the bifurcation point in magnetite with respect to Tiva Canyon Tuff. A comparison of the model parameters for the two systems in Table 7.2 and Table 7.6, as deduced from the viscosity analyses, reveals that the two systems have remarkably similar characteristics (which might have been anticipated to

some extent given that the two materials are chemically so similar) with one important exception, the dispersions σ_s of bias fields, which differ by an order of magnitude, with σ_s(magnetite) = 0.4 and σ_s(titanomagnetite) = 0.05. This is no coincidence. Model simulations of FC/ZFC/TRM/IRM response functions based on Preisach collections of two-level subsystems have shown [5] that the field and temperature dependence of the FC moment (and the TRM) are encoded almost exclusively in the dispersion of bias fields σ_s. (By contrast, the field and temperature dependence of the ZFC moment and the IRM are encoded primarily in the dispersion σ_d of dissipation fields, and are relatively insensitive to the dispersion σ_s of bias fields [5].) Since the role of the bias field H_s within the Preisach formalism is to lift the degeneracy of the two-level subsystems, it is frequently interpreted as an interaction field (particularly if the microstructure is discrete and granular), and we conclude that the difference in the behaviour of the FC/ZFC moments observed experimentally in the two systems is directly correlated with the strength of the interparticle interactions, which are significant in magnetite where the particle packing density is high, and weak in titanomagnetite where the particle distribution is comparatively dilute. This situation is correspondingly manifested in the model dispersion of bias fields, which is wide (σ_s = 0.4) in magnetite and narrow (σ_s = 0.05) in Tiva Canyon Tuff.

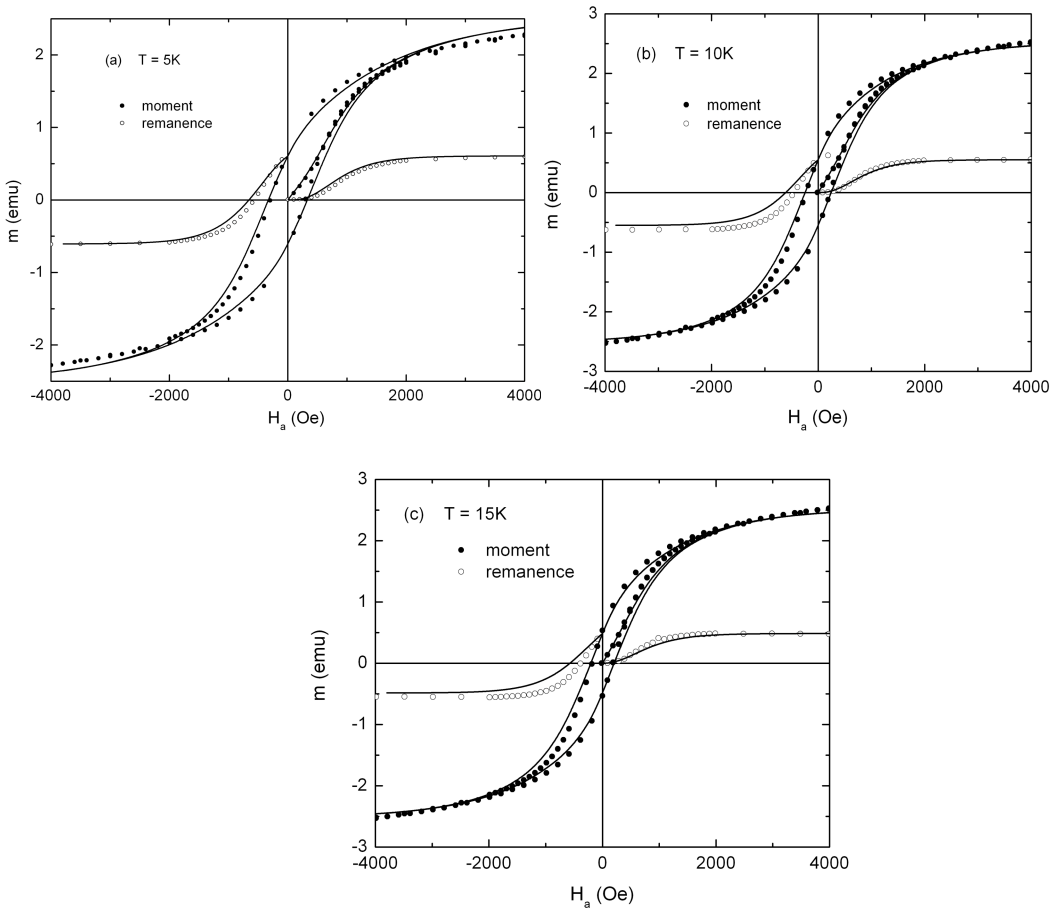

Figure 7.21: Model simulations (solid lines) of hysteresis loops using the parameters in Table 7.7, superposed over measured hysteresis loops for nanoparticulate magnetite at (a) T = 5K, (b) T = 10K, and (c) T = 15K.

Table 7.7: Hysteresis Loop Simulation Parameters

τ_0 (s)	t_{exp} (s)	μ (10^{-16}emu)	H_{dm} (Oe)	σ_d	σ_s	f	λ (10^{-4} Oe^{-1})	M_{sat} (emu)
10^{-11}	10^2	2.0 ± 0.5	650 ± 10	0.6 ±0.2	0.5 ±0.2	0.71 ±0.05	8.0 ±2.0	2.55

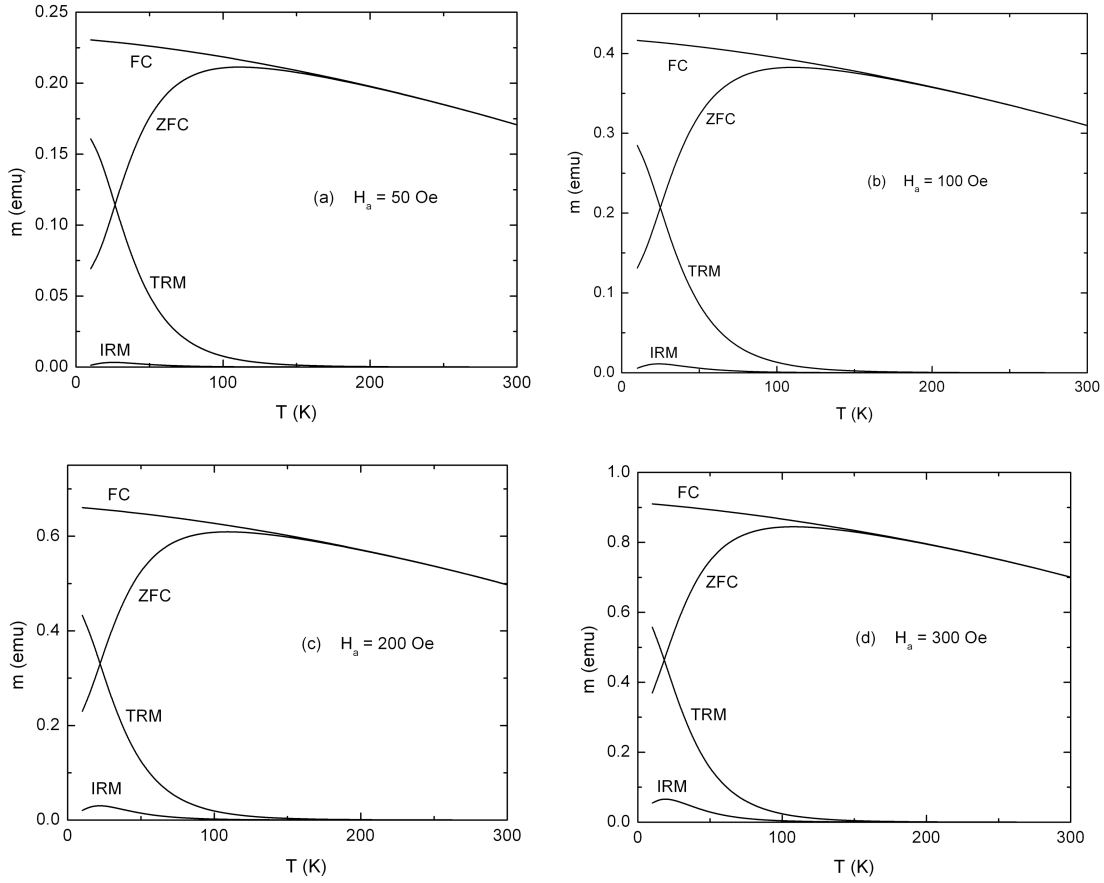

Figure 7.22: Model simulations of the same sequence of FC/ZFC/TRM/IRM measurements for nanoparticulate magnetite shown in Figure 7.17, with the simulation parameters listed in Table 7.8: (a) H_a = 50 Oe, (b) H_a = 100 Oe, (c) H_a = 200 Oe, and (d) H_a = 300 Oe.

Table 7.8: FC/ZFC/TRM Simulation Parameters

τ_0 (s)	t_{exp}(s)	μ (10^{-16}emu)	H_{dm} (Oe)	σ_d	σ_s	f	λ (10^{-4} Oe^{-1})	M_{sat} (emu)
10^{-11}	10^2	2.5 ± 0.5	650 ± 10	0.6 ±0.2	0.4 ±0.2	0.67 ±0.5	6.0 ±2.0	2.55

7.5 Ferromagnetic Ruthenates

We now turn our attention to a series of three magnetic systems with quite different magnetic characteristics from those of the previous two nanoparticulate materials. All three are members of a family of polycrystalline mixed ruthenates with chemical formula $Ca_xSr_{1-x}RuO_3$, an orthorhombically distorted perovskite structure, and a single magnetically active species Ru [15, 16]. The systems investigated here have Ca fractions x = 0.2, x = 0.4, and x = 0.6, and all three are exchange bond-disordered ferromagnets with paramagnetic-ferromagnetic critical temperatures $T_C(x = 0.2) \approx 120K$, $T_C(x = 0.4) \approx 75K$, and $T_C(x = 0.6) \approx 45K$.

7.5.1 $Ca_xSr_{1-x}RuO_3$ with x = 0.6

Figures 7.23 through 7.25 summarize the principal characteristics of the field, temperature, and time dependence of the measured magnetic response of $Ca_{0.6}Sr_{0.4}RuO_3$.

Figures 7.23(a) through 7.23(g) show seven representative hysteresis loops measured at T = 5K, 6K, 8K, 10K, 12K, 14K and 16K, following thermal demagnetization in zero field from a reference temperature $T_{ref} = 80K$, by repeated application, removal, and reapplication of the magnetic field in increments of $\Delta H_a = 500$ Oe, starting from the demagnetized state and then proceeding to a maximum positive field $H_a = 50kOe$ close to technical saturation, and terminating at a maximum negative field $H_a = -50kOe$. The measurements in these figures include the initial magnetizing curve, the initial magnetizing remanence (IRM), the descending branch of the major hysteresis loop, and the demagnetizing remanence. Figure 7.23(h) shows plots of the

measured coercive field H_c (solid dots) and the measured remanent coercive field H_{cr} (open circles) as a function of temperature over the interval $2.5K \leq T \leq 18K$. An inspection of Figure 7.23(h) shows that the measured coercive fields of $Ca_{0.6}Sr_{0.4}RuO_3$ in the limit of low temperatures ($T \leq 10K$) are a factor of 20-30 times larger than those in either of the nanoparticulate systems studied in Sections 7.3 and 7.4, and also that the magnitudes of the two coercive fields H_c and H_{cr} are virtually identical, indicating that reversible processes in the ruthenates play a much less significant role than they do in the superparamagnetic nanoparticulates.

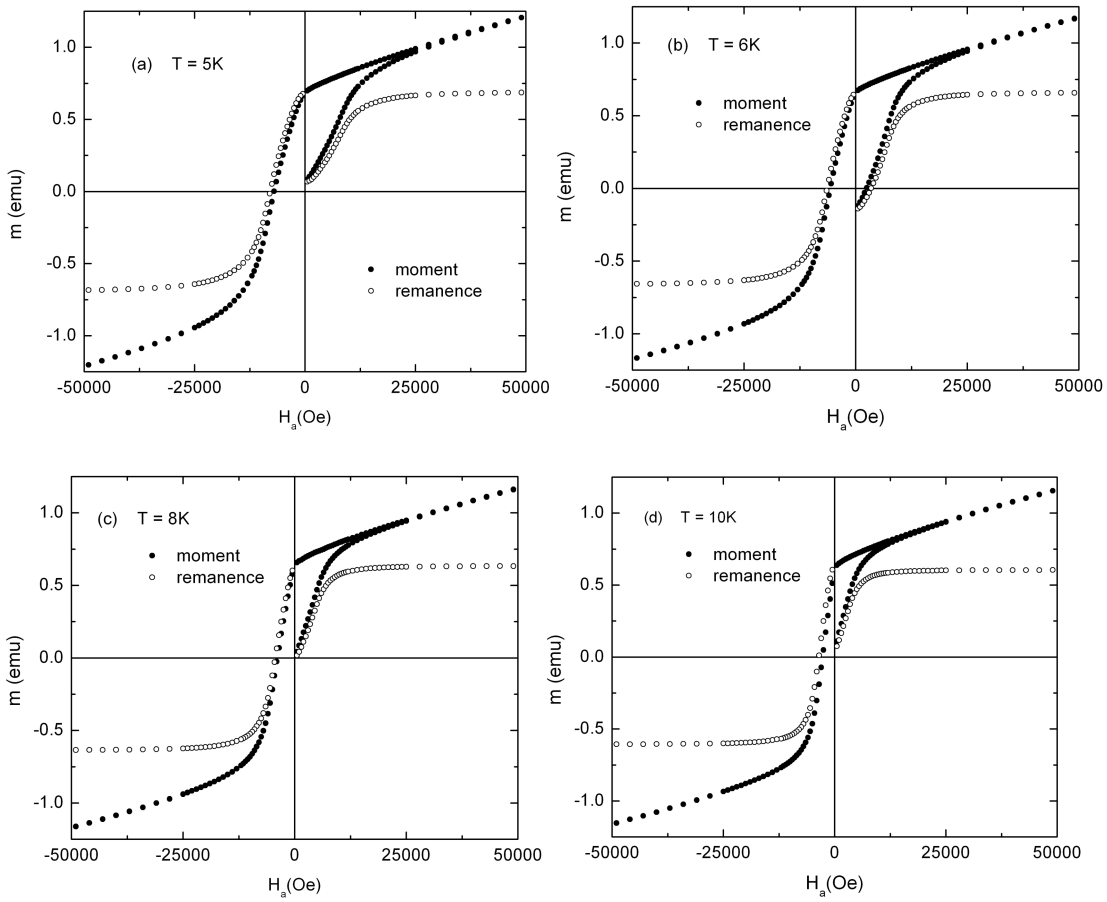

Figure 7.23: Measured hysteresis loops for $Ca_{0.6}Sr_{0.4}RuO_3$ at (a) T = 5K, (b) T = 6K, (c) T = 8K, and (d) T = 10K.

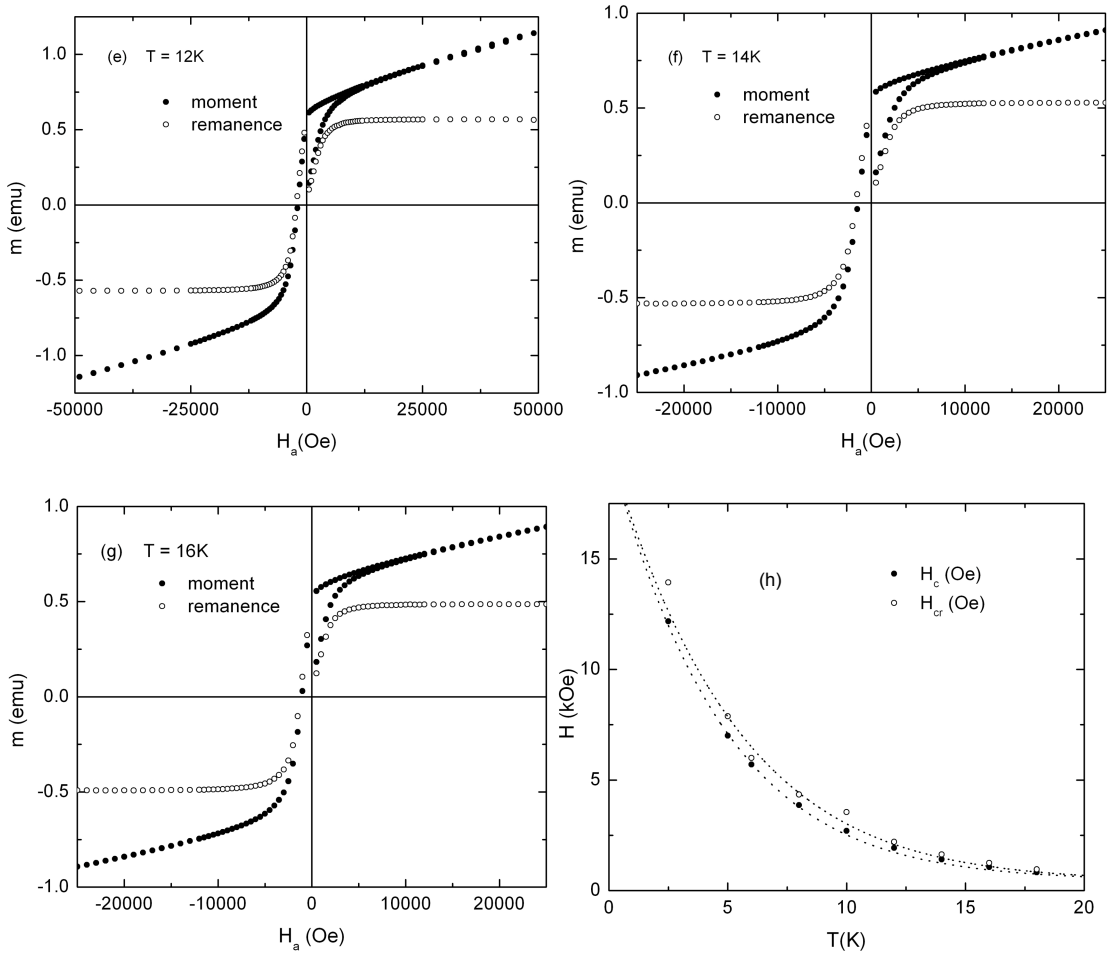

Figure 7.23 cont'd: Measured hysteresis loops for $Ca_{0.6}Sr_{0.4}RuO_3$ at (e) T = 12K, (f) T = 14K, (g) T = 16K. (h) Measured coercive field H_c (solid circles) and measured remanent coercive field H_{cr} (open circles) for $Ca_{0.6}Sr_{0.4}RuO_3$. The dotted lines are guides to the eye.

Figures 7.24(a) through 7.24(f) show representative measurements of the temperature dependence of the field cooled (FC) moment, the zero field cooled (ZFC) moment, the thermoremanent moment (TRM) and the isothermal remanent moment (IRM) between $5K \leq T \leq 55K$ in a series of applied fields H_a = 300Oe, 500Oe, 800Oe, 1000Oe, 2000Oe and 4000Oe. The experimental measurement protocols were identical to those described for the nanoparticulates in Sections 7.3 and 7.4 (with the exception of the reference demagnetizing temperature T_{ref} = 80K), and will not be repeated here. There are

clear structural similarities between the FC/ZFC/TRM/IRM response functions of the ferromagnetic ruthenate in Figure 7.24 and the corresponding response functions of the nanoparticulates in Sections 7.3 and 7.4: specifically, a bifurcation temperature $T_{bif} \approx$ 45K, below which the moment splits into two distinct FC and ZFC branches, and the remanent moment splits into two distinct TRM and IRM branches, and a maximum in the temperature dependence of both the ZFC moment and the IRM. In spite of these superficial similarities, the response functions of the ruthenate and the nanoparticulates nevertheless differ in several important respects. (1) In low applied fields, the bifurcation temperature for the ruthenate is essentially coincident with the critical temperature ($T_{bif} \approx T_C$), in contrast with the situation in the nanoparticulates, where $T_{bif} << T_C$. (2) The magnitude of the FC moment of the ruthenate decreases significantly with increasing temperature throughout the entire irreversible regime and, as a consequence, the magnetic response in the high temperature reversible phase is negligible in comparison with the low temperature response in the magnetically ordered phase in the limit $T \rightarrow 0$. This behaviour is characteristic of a material which undergoes a cooperative phase transition from a high temperature paramagnetic phase where the response originates from individual, uncoupled atomic moments, to a low temperature collectively frozen ferromagnetic phase where the atomic moments align spontaneously under the influence of the quantum mechanical exchange interaction, and respond cooperatively to changes in field. It is the rapid growth of the spontaneous moment with decreasing temperature as the system is cooled below T_C and through the ferromagnetic phase which is responsible for the temperature dependence of the FC moment observed in Figure 7.24. By contrast, in the nanoparticulate assemblies, the crossover from the irreversible blocked phase to the

reversible superparamagnetic phase occurs at temperatures well below the critical ordering temperature of the individual grains, where the spontaneous moment has ceased to evolve significantly with temperature and, as a consequence, the magnetic response in the two regimes is comparable. (3) In the ruthenate system, the magnitude and the thermal profile of the remanent moment both bear a close resemblance to those of the corresponding in-field moment, as can be seen by comparing the IRM to the ZFC moment, and the TRM to the FC moment in each of the six panels of Figure 7.24. In the nanoparticulates, the IRM is typically only a small fraction of the ZFC moment, and the maximum in the IRM is displaced toward lower temperatures relative to the maximum in the ZFC moment, while the FC and TRM branches diverge rapidly with increasing temperature. The data analyses described in Sections 7.3 and 7.4 show that these relationships between the branches in nanoparticulates are a signature of materials in which effects of temperature are limited exclusively to random energy exchanges with a heat bath and in which the moment induced by the application of a field originates predominantly from thermal overbarrier activation events.

Figures 7.25(a) through 7.25(f) show representative measurements of viscosity isotherms performed at six different temperatures T = 8K, 12K, 16K, 24K, 26K and 34K within the ferromagnetic phase, in a series of negative holding fields $H_a < 0$ (listed in each figure), over an experimental observation time window $10s \leq t \leq 10^4 s$, and plotted on a logarithmic time scale. The experimental protocol was identical to that described for the nanoparticulates in Sections 7.3 and 7.4, but with a different positive saturating field H_{sat} = 40kOe. As before, only a logarithmic or quasi-logarithmic fragment of the complete relaxation isotherm is visible within the limited experimental time window.

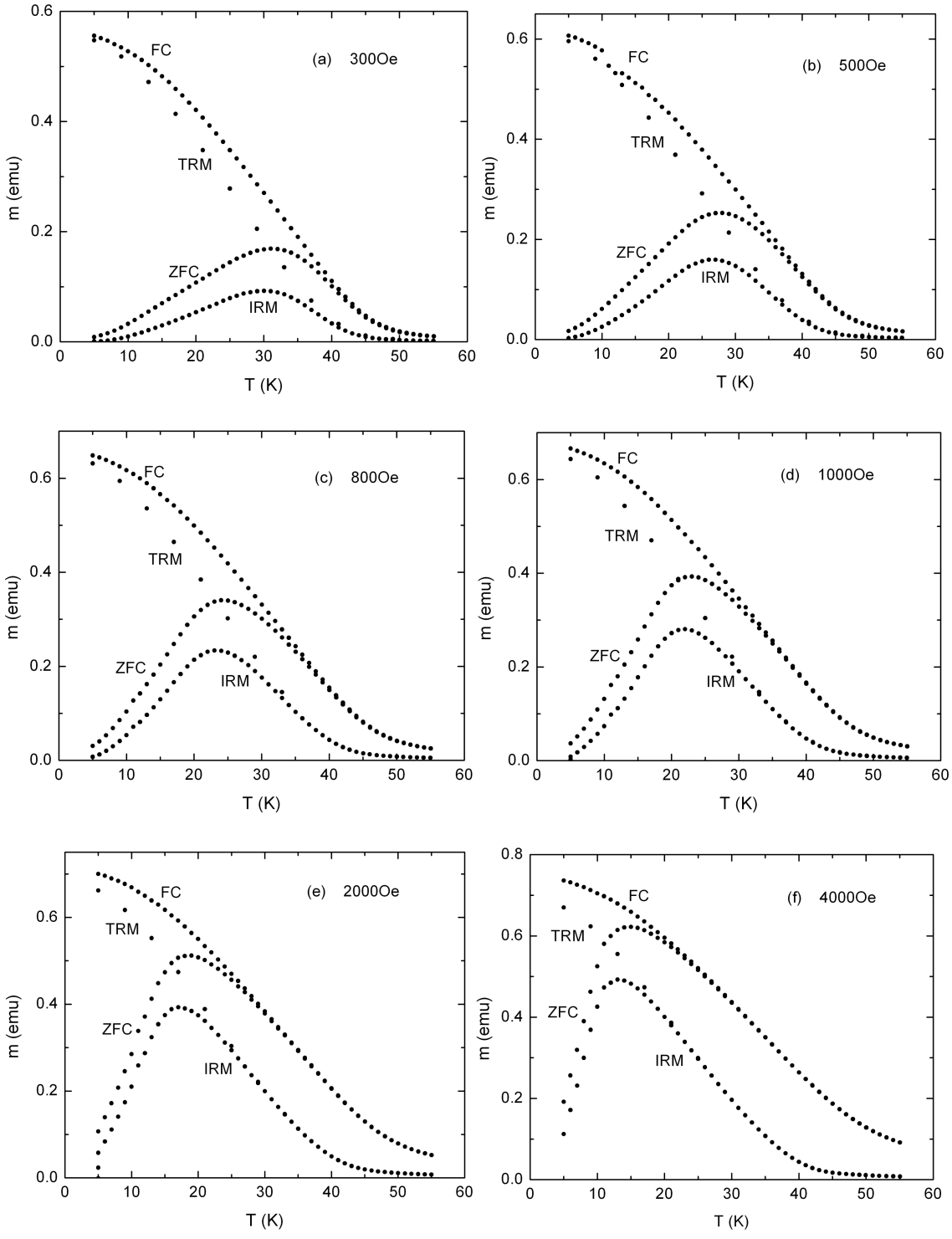

Figure 7.24: The measured FC moment, ZFC moment, TRM and IRM for $Ca_{0.6}Sr_{0.4}RuO_3$ in fields of (a) H_a = 300 Oe, (b) H_a = 600 Oe, (c) H_a = 800 Oe, (d) H_a = 1000 Oe, (e) H_a = 2000 Oe, and (f) H_a = 4000 Oe.

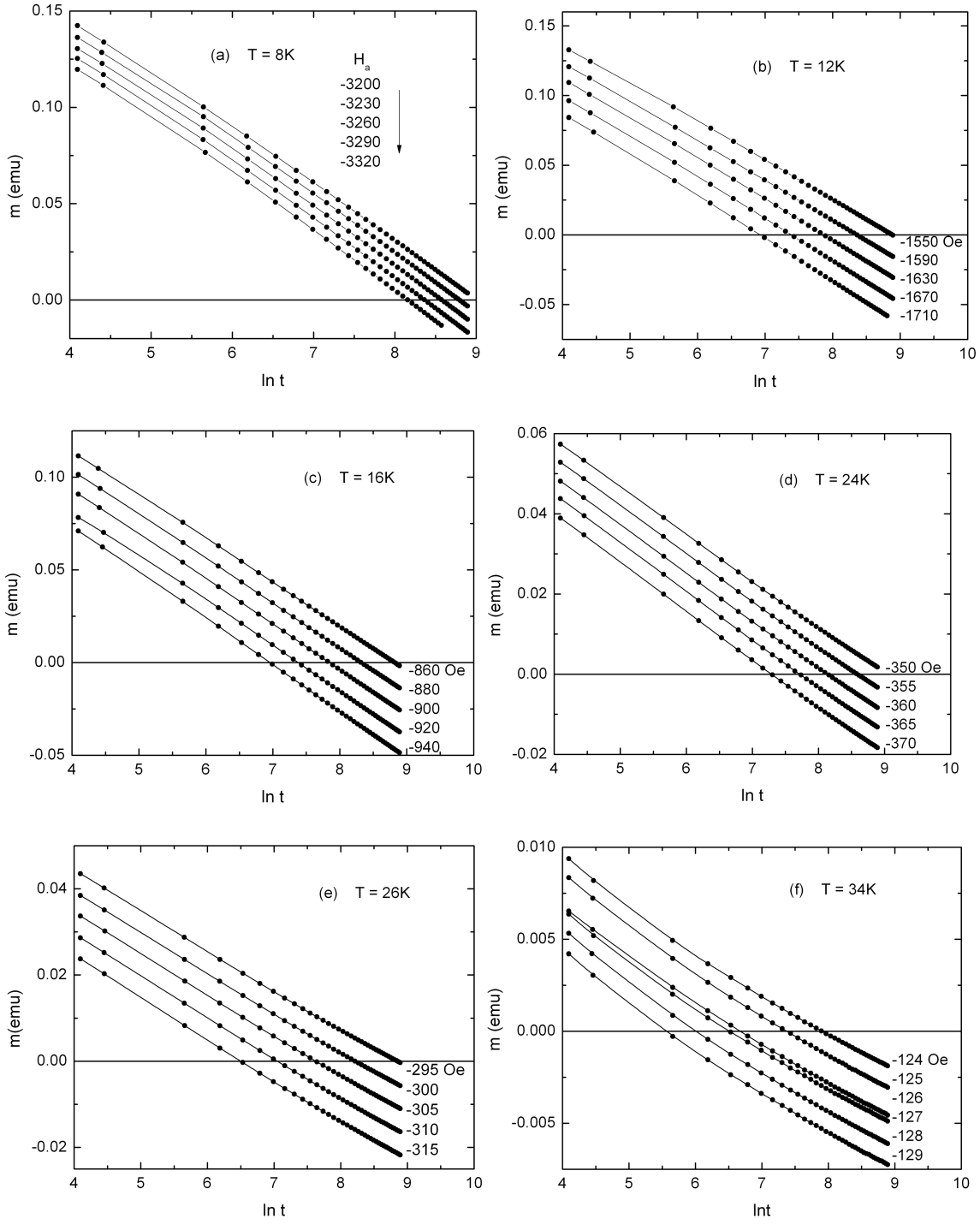

Figure 7.25: Measured viscosity isotherms for $Ca_{0.6}Sr_{0.4}RuO_3$ at temperatures of (a) T = 8K, (b) T = 12K, (c) T = 16K, (d) T = 24K, (e) T = 26K, and (f) T = 34K. The field in which each isotherm is measured is noted to the right of the isotherm. The solid lines are guides to the eye.

The analytical strategy described in Sections 7.3 and 7.4 for the nanoparticulate systems was repeated for the ferromagnetic ruthenate $Ca_{0.6}Sr_{0.4}RuO_3$, and the results are summarized in Figures 7.26 through 7.31 and in Tables 7.9 through 7.12. As before, "reversal time" data obtained from viscosity isotherms like those shown in Figure 7.25 were replotted in the form $T\ln(t_r/\tau_0)$ versus H_a over an extremely wide range of values of the parameter τ_0 between $10^{-40}s \leq \tau_0 \leq 10^{-5}s$, in order to search for evidence of universality. By contrast with the behaviour observed in the nanoparticulates, we were unable to identify any single value of τ_0 which was capable of aligning the *entire* "reversal time" data set, for all measurement temperatures T between $6K \leq T \leq 34K$, onto a common universal curve. The main body of Figure 7.26 shows plots of $T\ln(t_r/\tau_0)$ versus H_a for two values of τ_0, namely, $\tau_0 = 10^{-9}s$ and $\tau_0 = 10^{-12}s$ which, by common consensus [12-14], define approximately the limits of physical acceptability of this parameter. While it may indeed be argued that the data obtained from temperatures below $T \approx 10K$, corresponding to holding fields $H_a \leq -2kOe$, are compatible with a common curve, it is nevertheless transparent from an inspection of this figure that the degree of alignment of neighbouring isothermal segments becomes gradually less satisfactory and the deviations from universality become progressively more severe as the temperature increases above T = 10K. These deviations are illustrated in the inset to Figure 7.26, which shows a magnified view of the behaviour of the two plots for temperatures $T \geq 16K$ and holding fields $H_a \geq -1kOe$. As an illustration of the systematic manner in which the deviations from universality evolve with changes in τ_0, and as further evidence of the absence of convincing universality in this system, Figure 7.27 shows a plot of $T\ln(t_r/\tau_0)$ versus H_a for

an extreme value of $\tau_0 = 10^{-25}$s which lies well outside the nominal range of physical acceptability. In the limit of such extremely short characteristic times, deviations from universal alignment are observed simultaneously at both low temperatures (T < 15K) and high temperatures (T > 25K), as shown by the magnifications in the two insets. (There is some indication that continued decreases to τ_0 may ultimately restore the alignment at high temperatures, but only at the expense of introducing even more severe distortions at low temperatures.)

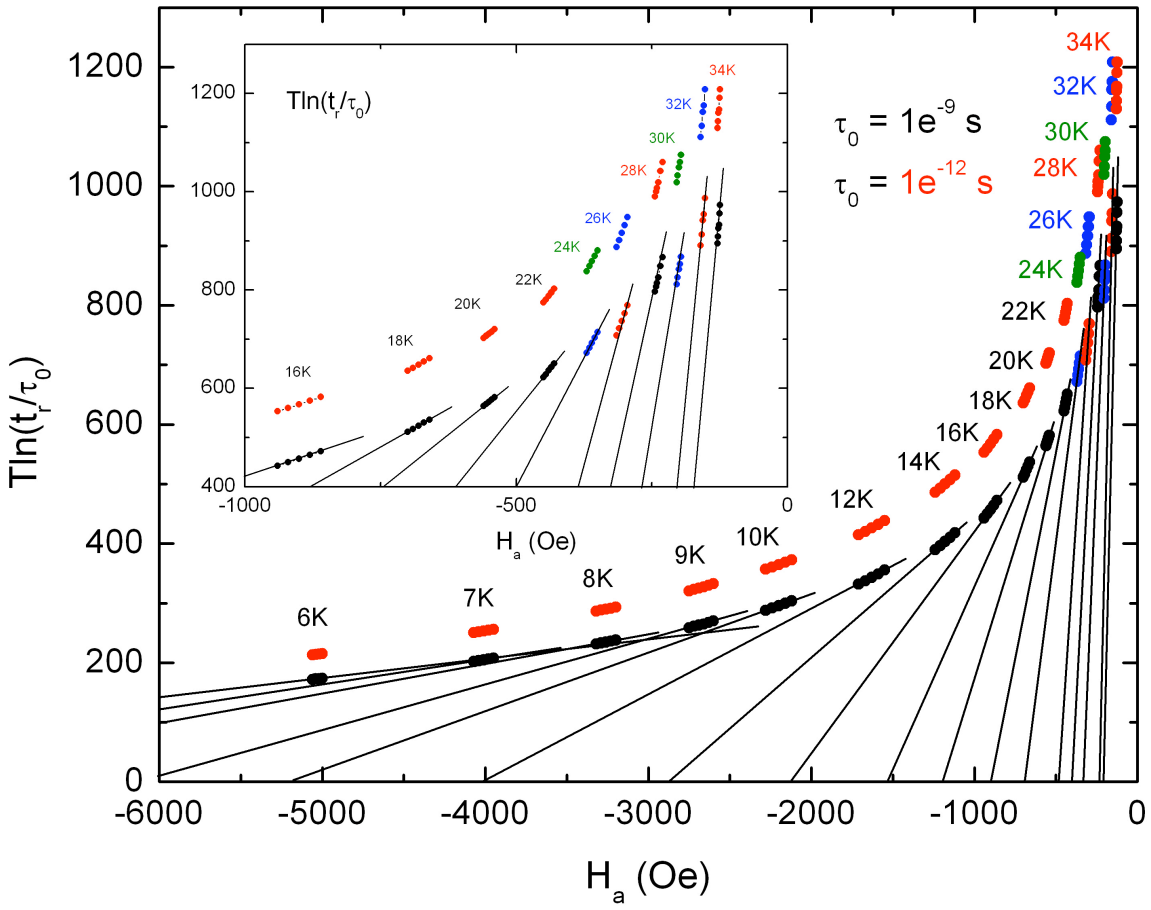

Figure 7.26: Reversal time data $Tln(t_r/\tau_0)$ as a function of applied field H_a of $Ca_{0.6}Sr_{0.4}RuO_3$ for two values of τ_0, listed in the figure, which lie in the physically acceptable range. The straight lines represent the approximation that considers each isothermal segment to belong to the linear regime of its individual isothermal curve. The inset shows a magnification of this plot for temperatures T ≥ 16K.

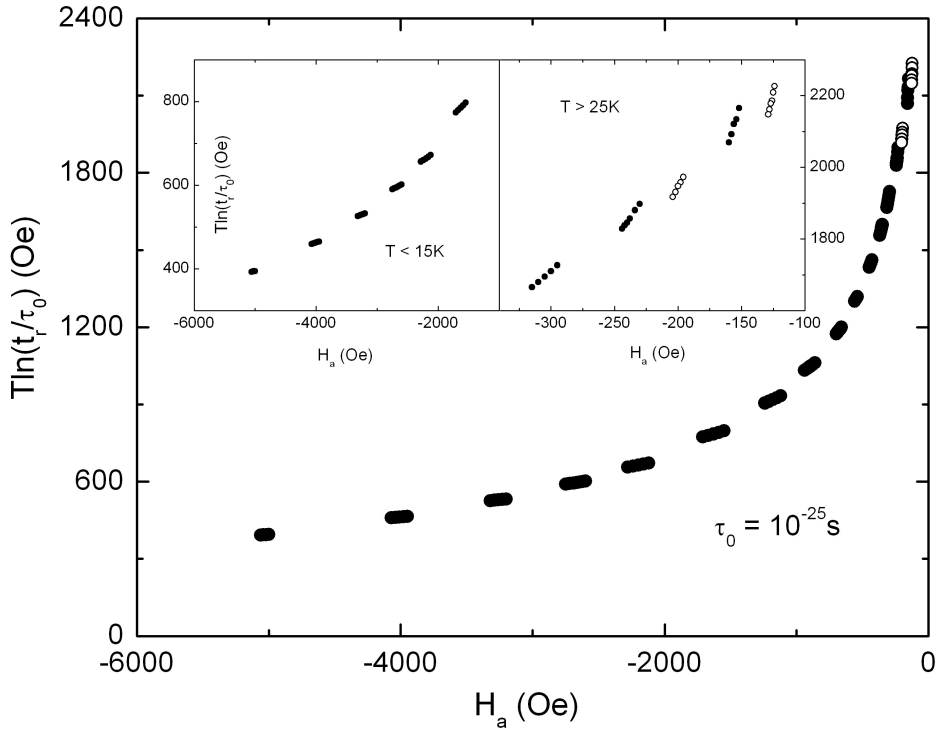

Figure 7.27: A reversal time plot, $T\ln(t_r/\tau_0)$ as a function of applied field H_a, of $Ca_{0.6}Sr_{0.4}RuO_3$ for a value of $\tau_0 = 10^{-25}$ s which is well below the physically acceptable range for τ_0. The insets show magnified views of the plot for "low" temperatures T ≤ 12K and "high" temperatures T ≥ 26K.

Based on this preliminary analysis, we may tentatively conclude that the individual isothermal viscosity segments in Figure 7.26 are each fragments of distinct members of an infinite family of isothermal curves, each of which defines the functional relationship between the holding field H_a and moment reversal time t_r at one fixed temperature T, and that the temperature dependence of the magnetic response observed in the ferromagnetic ruthenate $Ca_{0.6}Sr_{0.4}RuO_3$ is shaped by a coexistence of thermal overbarrier activation events within a free energy landscape which is itself evolving explicitly with temperature. The task of the current analysis is to resolve and quantify the contributions from these two "competing" processes. However, given the fragmentary, non-universal nature of the viscosity data, and hence the absence of any a priori

knowledge regarding the functional forms of the individual isothermal curves, it is necessary, at least in the initial stages of the analysis, to resort to drastic simplifying assumptions. Thus, we may obtain a "zeroth order" estimate for the intrinsic dissipation field $H_{dm}(T)$ and for the elementary characteristic moment reversal $\mu(T)$ by adopting a linear approximation in which each isothermal segment in Figure 7.26 is assumed to belong to the linear regime of its individual isothermal curve. The straight lines in Figure 7.26 represent this linear approximation. The magnitude of the intercepts $H_{int}(T)$ of these straight lines along the H_a-axis then provide an *lower limit* on the true intrinsic dissipation field, $|H_{int}(T)| \leq H_{dm}(T)$, while the slopes of the straight lines provide an *upper limit* on the mean elementary moment reversal $\mu(T)$. Figure 7.28 summarizes the temperature dependence of the two parameters $H_{dm}(T)$ and $\mu(T)$ obtained in this way, as well as the temperature dependence of the thermal fluctuation field $H_f = kT/\mu(T)$. The solid curves in this figure are smooth functional representations of the parameters which were used to generate model simulations of hysteresis loops and FC/ZFC/TRM/IRM response functions.

At this point, it becomes necessary to depart somewhat from the analytical protocol developed for the nanoparticulates in Sections 7.3 and 7.4, since there is insufficient information available from the fragmentary viscosity data in Figure 7.26 to permit an unambiguous identification of the characteristics of the dissipative Preisach density $p_{irrev}(H_d,H_s,T)$ and its evolution with temperature from a comparison with model simulations of universal curves. In particular, further progress demands a heavier reliance on the hysteresis loop data in Figure 7.23 than before. Thus, model simulations of

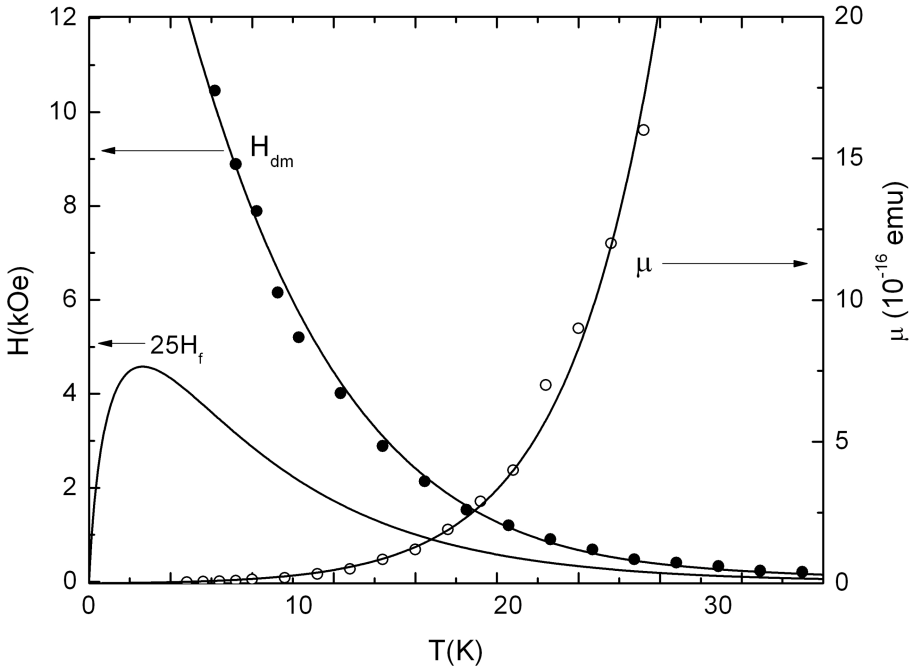

Figure 7.28: The temperature dependence of $H_{dm}(T)$ (solid circles) and $\mu(T)$ (open circles) obtained from the straight lines of Figure 7.26, along with the temperature dependence of the thermal fluctuation field $H_f = kT/\mu(T)$ multiplied by $\ln(t/\tau_0) = 25$. The solid curves are smooth functional representations of the discrete data.

hysteresis loops were generated assuming the superposition Preisach density in Eq(7.7), with the usual lognormal-Gaussian product distribution of dissipative subsystems in Eq(7.5) and the exponential distribution of reversible subsystems in Eq(7.9), as well as the temperature dependences for $H_{dm}(T)$, $\mu(T)$ and $H_f(T)$ shown in Figure 7.28. Fits to the experimental data in Figure 7.23 were used to establish not only the reversible parameters f and λ, but also the dispersions σ_d and σ_s of dissipative fields and bias fields, respectively. The solid curves in Figure 7.29(a) through 7.29(g) show the best model representations of the measured hysteresis loops in Figure 7.23 superposed directly over the data, and Table 7.9 summarizes the parameter values obtained from these fits.

Table 7.9: Hysteresis Loop Simulation Parameters

τ_0 (s)	t_{exp}(s)	σ_d	σ_s (normalized to $H_{dm}(0)$ = 22kOe)	f	λ(10^{-5} Oe^{-1})	M_{sat} (emu)
10^{-9}	10^{2}	0.5 ± 0.1	0.01 ± 0.005	0.66 ±0.05	1.2 ± 0.3	2.0

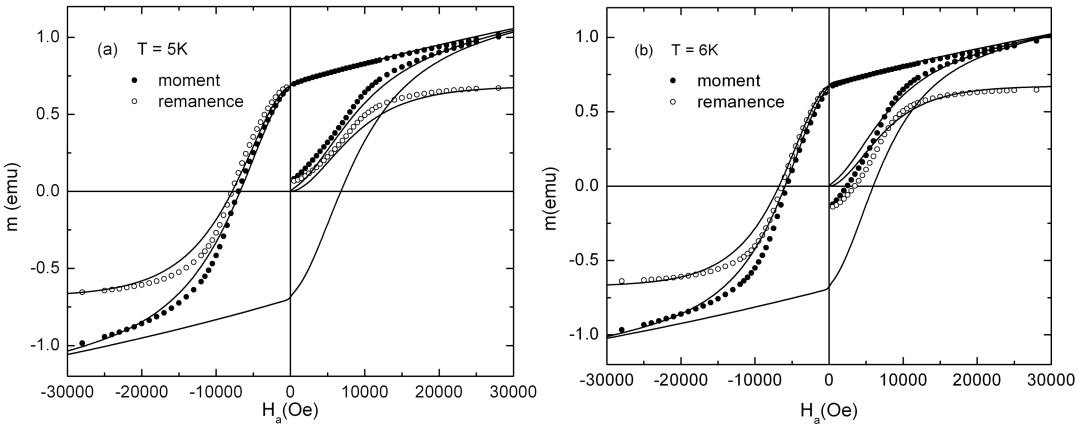

Figure 7.29: Numerical simulations (smooth curves) of hysteresis loops of $Ca_{0.6}Sr_{0.4}RuO_3$, for (a) T = 5K, and (b) T = 6K, superposed on the experimental measurements of the moment (solid circles) and the remanence (open circles) from Figure 7.23.

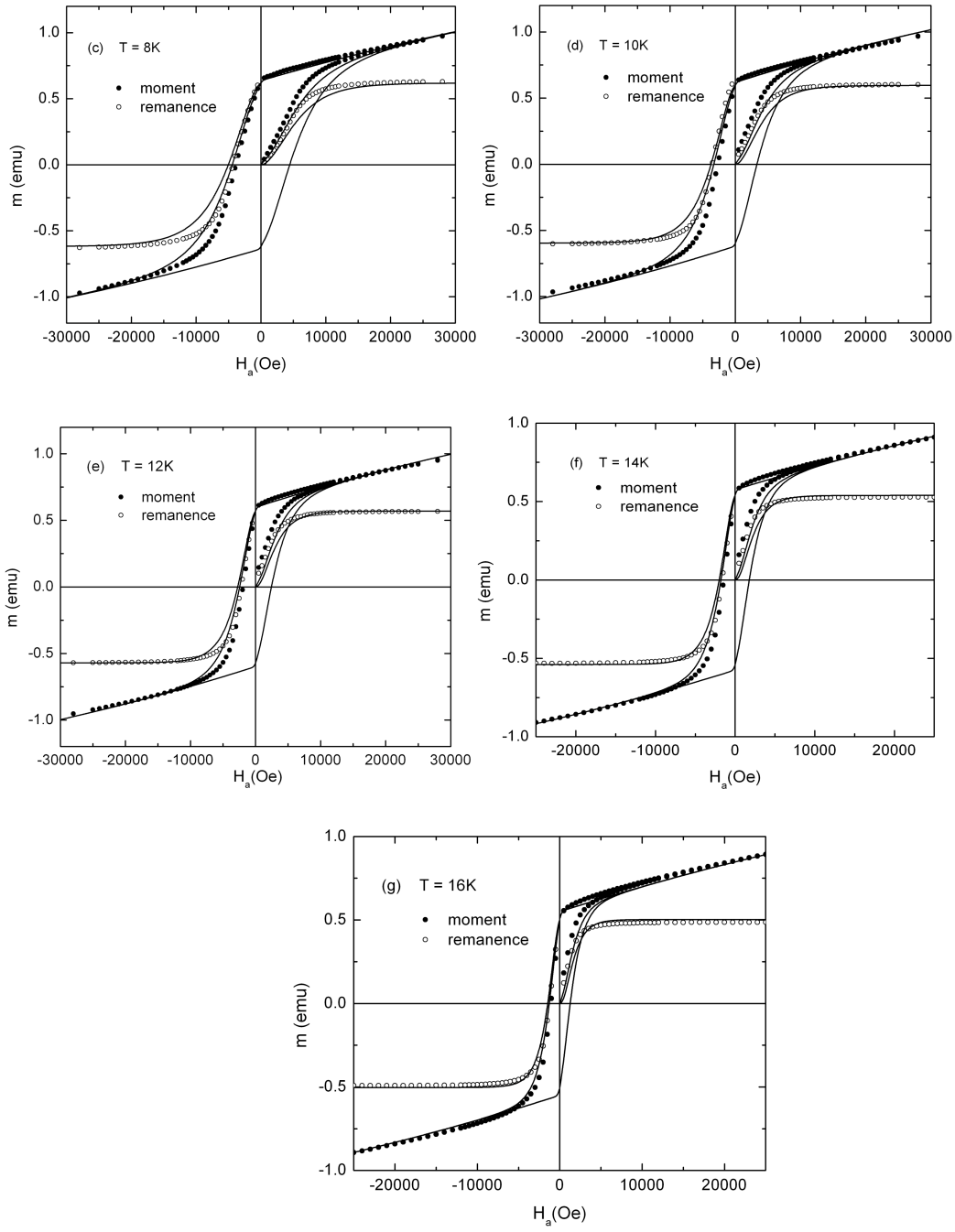

Figure 7.29 cont'd: Numerical simulations (smooth curves) of hysteresis loops of $Ca_{0.6}Sr_{0.4}RuO_3$, for (c) T = 8K, (d) T = 10K, (e) T = 12K, (f) T = 14K, and (g) T = 16K, superposed on the experimental measurements of the moment (solid circles) and the remanence (open circles) from Figure 7.23.

Before we can proceed to exploit the model to predict the results of experimental measurements of the FC/ZFC/TRM/IRM response functions, one further step is necessary. As mentioned earlier, ferromagnetically ordered materials like $Ca_{0.6}Sr_{0.4}RuO_3$ are characterized by a spontaneous moment which decreases systematically with increasing temperature throughout the ferromagnetic phase, from a saturation value at low temperatures $T \rightarrow 0$, where the atomic moments are all perfectly aligned within each domain, to a negligible value in the vicinity of the critical temperature $T \approx T_C$, where thermal fluctuations are sufficient to destroy the cooperative ferromagnetic alignment of the atomic moments [17]. This behaviour is in turn reflected in the temperature dependence of the measured response functions in Figure 7.24, and most directly in the temperature dependence of the FC branch, where the subsystem moments are each permanently frozen into a fixed orientation by a constant cooling field. There is no explicit physical or mathematical provision in the Preisach formalism for describing the critical "melting" of the two-level subsystems, and the associated collapse of the subsystem spontaneous moment $\mu(T)$, as $T \rightarrow T_C$ from below and each bistable subsystem "disintegrates" into a paramagnetic cloud of uncoupled atomic spins (see, however, Souletie [14]). In principle, such effects may be introduced into the formalism phenomenologically through the prefactor $M_{sat}(T) = N(T)\mu(T)$ in Eq(7.8), which represents the **saturation spontaneous moment** of the entire ensemble of two-level subystems in the limit $H_a \rightarrow \infty$ (excluding field-induced growth of the single-subsystem spontaneous moment $\mu(T)$). However, this presents a dilemma since, in the absence of a priori knowledge concerning the total number N(T) of Preisach subsystems, it is

impossible to reconstruct $M_{sat}(T)$ from a knowledge of $\mu(T)$ alone. Furthermore, the magnitude of the elementary activation moment reversal $\mu(T)$ as deduced from the viscosity analysis actually *increases* with increasing temperature, as shown in Figure 7.28, contrary to the behaviour expected of a spontaneous ferromagnetic moment, which implies that the growth of the effective activation volume dominates the critical collapse, at least for all temperatures up to $T \approx 34K$. Reports of activation volumes which increase with increasing temperature are not uncommon in the literature [18, 19], and are not hard to rationalize from a physical perspective. If $\mu(T)$ measures the volume of the material which is swept out when a fragment of domain wall executes a single jump between pinning sites, then it is not unreasonable to expect that the magnitude of this jump will grow on average as warming reduces the height of the pinning barriers, and the walls become increasingly more mobile and freer to translate over longer distances. (From the perspective of the model formalism, this growth in $\mu(T)$ must presumably be counteracted by an even more rapid decrease in $N(T)$, in order that the product $N(T)\mu(T)$ remain well behaved, that is, a monotonically decreasing function of temperature, consistent with the shapes of the FC branches in Figure 7.24.) In light of these conflicting considerations, we have chosen to proceed by adopting the physically reasonable hypothesis that the thermal profile of the FC moment in the limit of low fields (see Figures 7.24(a) and 7.24(b)), where paramagnetic contributions are negligible, provides an essentially undistorted image of $M_{sat}(T) = N(T)\mu(T)$ which summarizes the combined effects of subsystem population changes, activation volume growth and critical collapse. For purposes of model simulations, we have replaced the low field FC data by a smooth

functional representation, as shown in Figure 7.30. With $M_{sat}(T)$ thus established, model simulations of FC/ZFC/TRM/IRM response functions were generated using the parameter values listed in Table 7.9 and the functions plotted in Figure 7.28. The solid curves in Figures 7.31(a) through 7.31(f) show these model simulations overlaid on the measured FC/ZFC/TRM/IRM data. We emphasize that no parameters were allowed to vary during the preparation of these simulations. The model simulations clearly replicate the principal structural features of the data and their systematic variation with field and temperature remarkably well, and offer compelling support, not only for the linear approximation adopted for the interpretation of the viscosity isotherms (straight lines in Figure 7.26) in the thermal fluctuation analysis, but also for our principal conclusion that the temperature dependence of the magnetic response of $Ca_{0.6}Sr_{0.4}RuO_3$ is dominated by field induced transitions over a spectrum of free energy barriers which collapse explicitly with temperature as the system is warmed through the ferromagnetic phase, with thermal overbarrier activation events playing only a comparatively minor role.

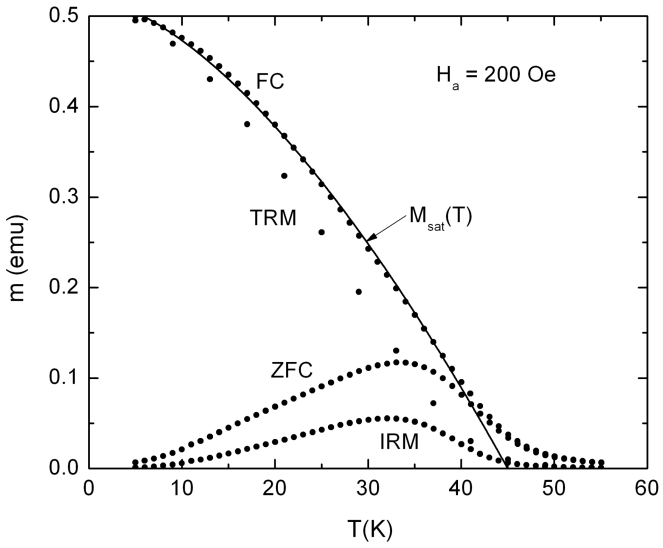

Figure 7.30: A smooth functional representation (solid curve) of the FC moment of low field data in H_a = 200 Oe, used as an approximate description of the saturation moment $M_{sat}(T)$.

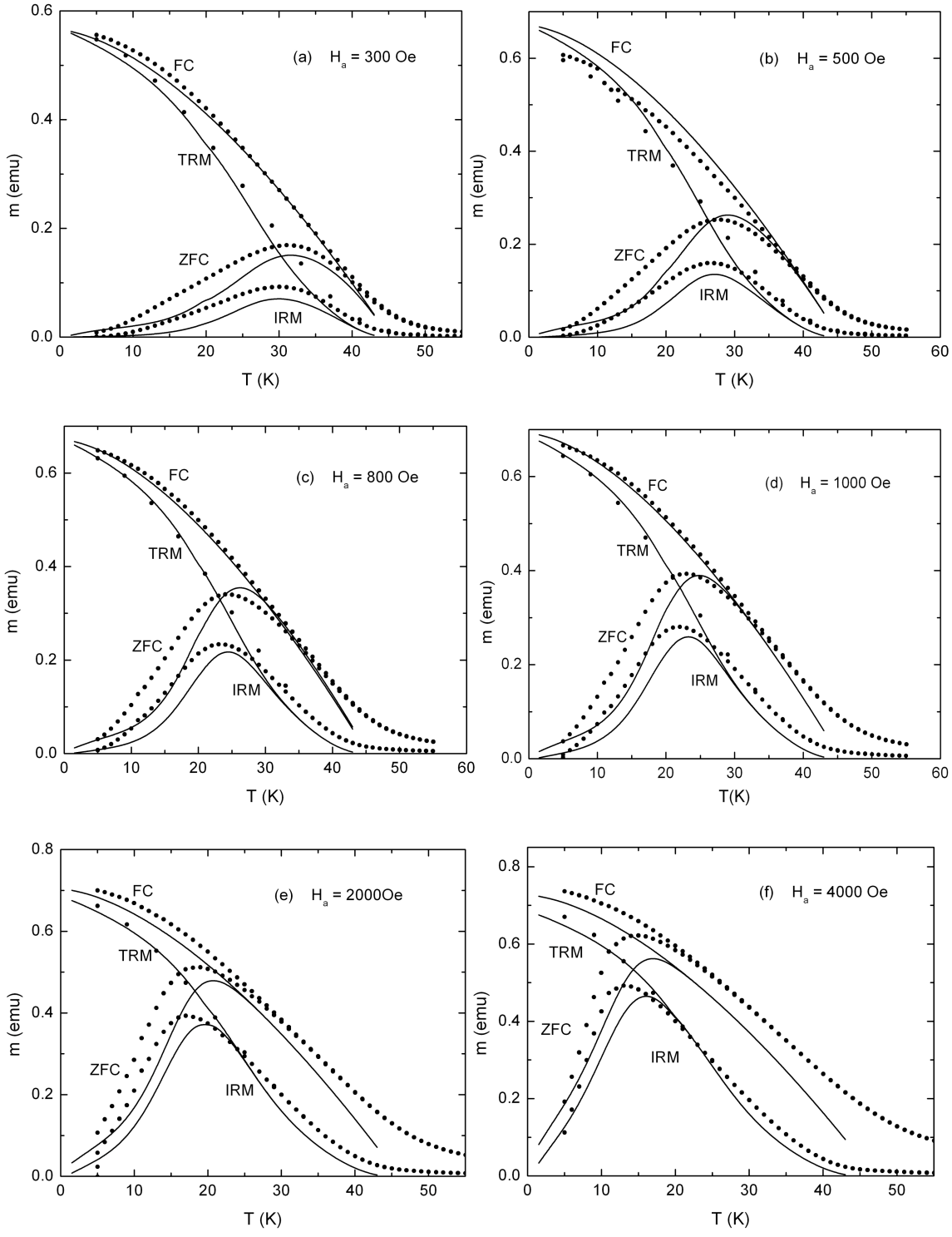

Figure 7.31: Numerical simulations (smooth curves) of the FC moment, ZFC moment, TRM and IRM of $Ca_{0.6}Sr_{0.4}RuO_3$, for (a) H_a = 300 Oe, (b) H_a = 500 Oe, (c) H_a = 800 Oe, (d) H_a = 1000 Oe, (e) H_a = 2000 Oe, and (f) H_a = 4000 Oe, superposed on the experimental measurements (solid dots) originally shown in Figure 7.24.

7.5.2 $Ca_xSr_{1-x}RuO_3$ with x = 0.4

The analysis of the remaining two ruthenates with compositions x = 0.4 and x = 0.2 proceeded in precisely in the same manner as that described above and, consequently, we content ourselves in the next two sections with a brief summary of the highlights only.

Figures 7.32(a) through 7.32(f) show representative measurements of viscosity isotherms performed at six different temperatures T = 7K, 14K, 26K, 34K, 42K and 54K within the ferromagnetic phase $T < T_C \cong 75K$, in a series of negative holding fields $H_a < 0$ (listed in each figure), over an experimental observation time window $10s \le t \le 10^4 s$, and plotted on a logarithmic time scale. The system was saturated in a field $H_{sat} = 40kOe$ prior to recoiling to the holding field H_a and, as before, the functional form of the decay is quasi-logarithmic.

In order to quantify the roles played by thermal overbarrier activation and barrier growth, "reversal time" data obtained from viscosity isotherms like those shown in Figure 7.32 were replotted in the form $T\ln(t_r/\tau_0)$ versus H_a over a wide range of values of the parameter τ_0, and Figure 7.33 shows one such plot for $\tau_0 = 10^{-9}s$. The inset shows a magnified view for temperatures $T \ge 38K$. As before, no single value of τ_0 was capable of aligning the *entire* "reversal time" data set, for all measurement temperatures T between $7K \le T \le 62K$, onto a common universal curve. For values of τ_0 from the physically acceptable range $10^{-12}s \le \tau_0 \le 10^{-9}s$, approximate alignment is observed at low temperatures $T \le 14K$, but deviations from universality are clearly observed for temperatures $T \ge 18K$ and become progressively more severe with increasing temperature, as seen in Figure 7.33.

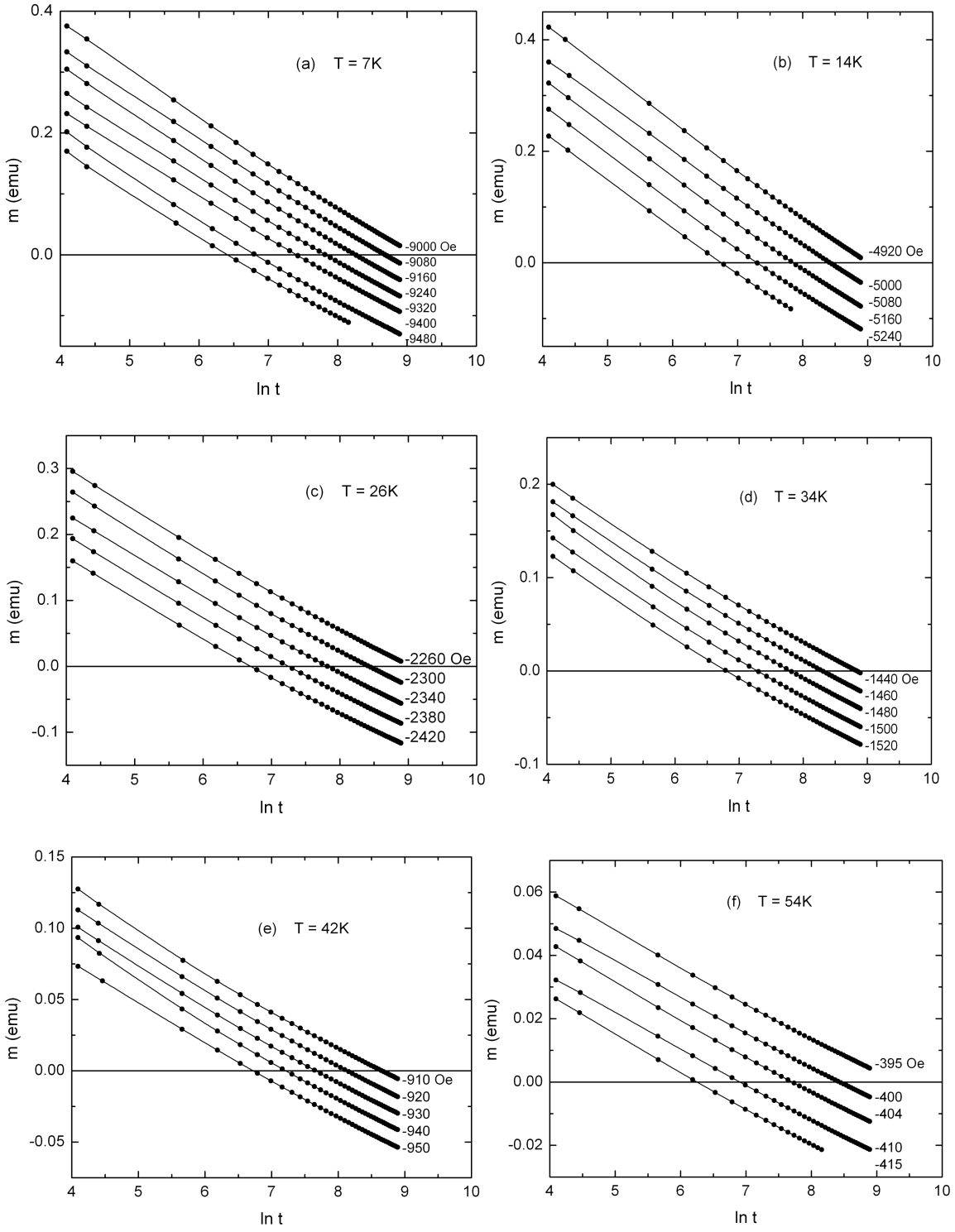

Figure 7.32: Measured viscosity isotherms of $Ca_{0.4}Sr_{0.6}RuO_3$ at temperatures (a) T = 7K, (b) T = 14K, (c) T = 26K, (d) T = 34K, (e) T = 42K, and (f) T = 54K. Each viscosity isotherm was measured is labelled by its holding field H_a. The solid lines are guides to the eye.

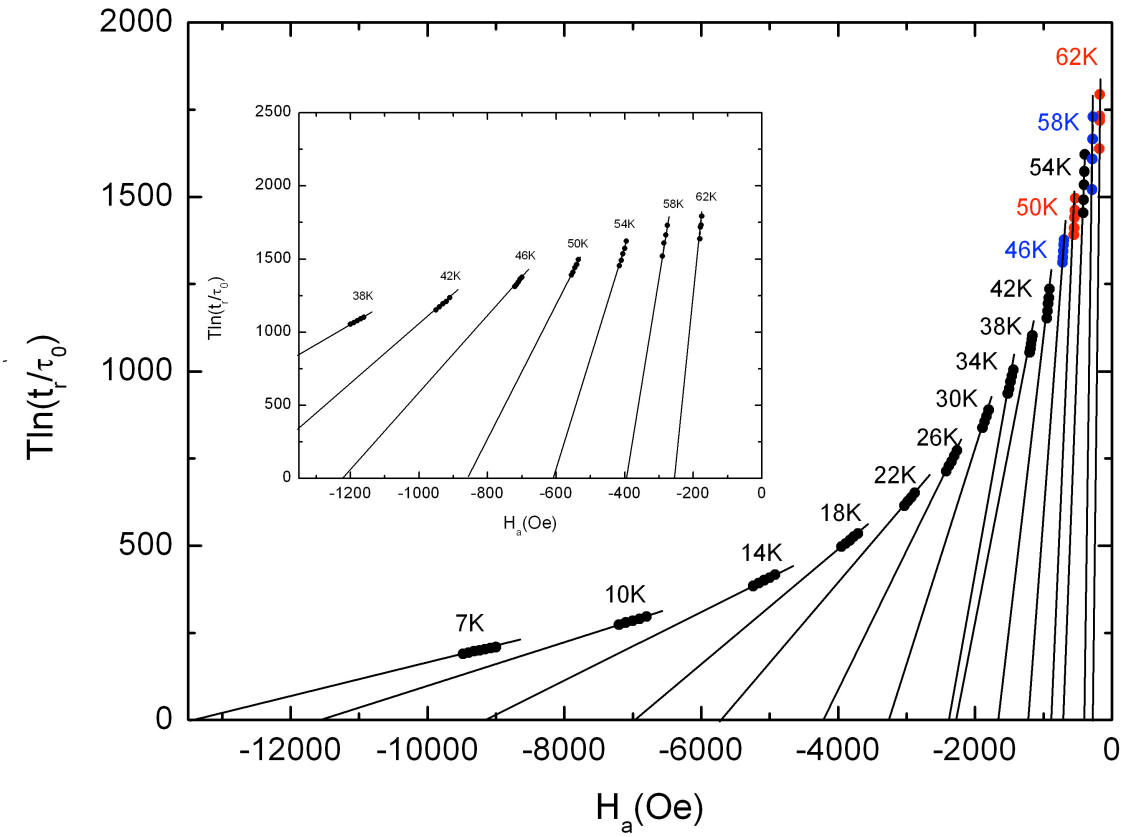

Figure 7.33: Reversal time data $T\ln(t_r/\tau_0)$ as a function of applied field H_a of $Ca_{0.4}Sr_{0.6}RuO_3$ for $\tau_0 = 10^{-9}$s. The straight lines represent the approximation that considers each isothermal segment to belong to the linear regime of its individual isothermal curve. The inset shows a magnification of this plot for those temperatures T ≥ 38K.

The analysis of the viscosity data in Figure 7.33 was conducted by adopting the linear approximation in which each isothermal segment is replaced by a straight line, and Figure 7.34 shows estimates for the median intrinsic dissipation field $H_{dm}(T)$ and the mean elementary moment reversal $\mu(T)$ obtained from the intercept and slope, respectively, of the straight lines in Figure 7.33. The solid curves in Figure 7.34 are smooth functional representations of $H_{dm}(T)$, $\mu(T)$ and the thermal fluctuation field $H_f(T)$

= kT/μ(T). For purposes of comparison, Figure 7.34 also shows the experimental values of the coercive field H_c and the remanent coercive field H_{cr} obtained from measured hysteresis loops. The two coercive fields are virtually identical in magnitude, and lie below the intrinsic dissipation field H_{dm} estimated from the viscosity plots in Figure 7.33.

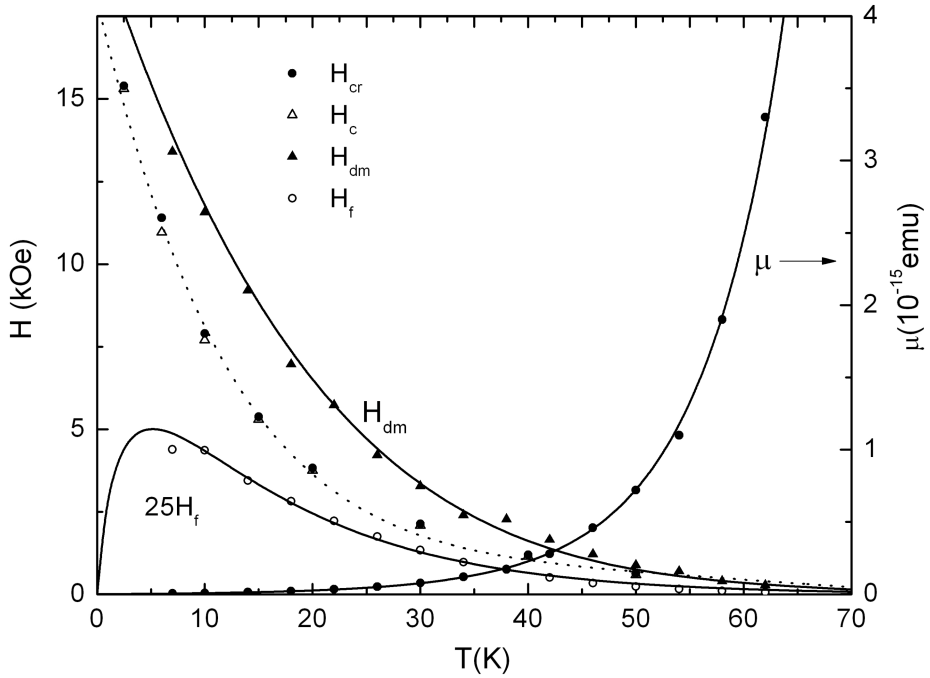

Figure 7.34: The median intrinsic dissipation field $H_{dm}(T)$ and the mean elementary moment reversal μ(T) obtained from the intercept and slope, respectively, of the straight lines in Figure 7.33. The solid curves are smooth functional representations of $H_{dm}(T)$, μ(T) and the thermal fluctuation field $H_f(T) = kT/\mu(T)$, which is multiplied by $\ln(t_r/\tau_0) = 25$.

Model simulations of hysteresis loops were generated assuming the superposition Preisach density in Eq(7.7), with the usual lognormal-Gaussian product distribution of dissipative subsystems in Eq(7.5) and the exponential distribution of reversible subsystems in Eq(7.9), as well as the smooth functional representations for $H_{dm}(T)$, μ(T) and $H_f(T)$ shown in Figure 7.34. Fits to the experimental hysteresis loop data were used

to establish not only the reversible parameters f and λ, but also the dispersions σ_d and σ_s of dissipative fields and bias fields, respectively. The solid curves in Figures 7.35(a) through 7.35(d) show the best model descriptions of four representative hysteresis loops measured at T = 6K, 10K, 15K and 20K, superposed directly over the data, and Table 7.10 summarizes the parameter values obtained from these fits.

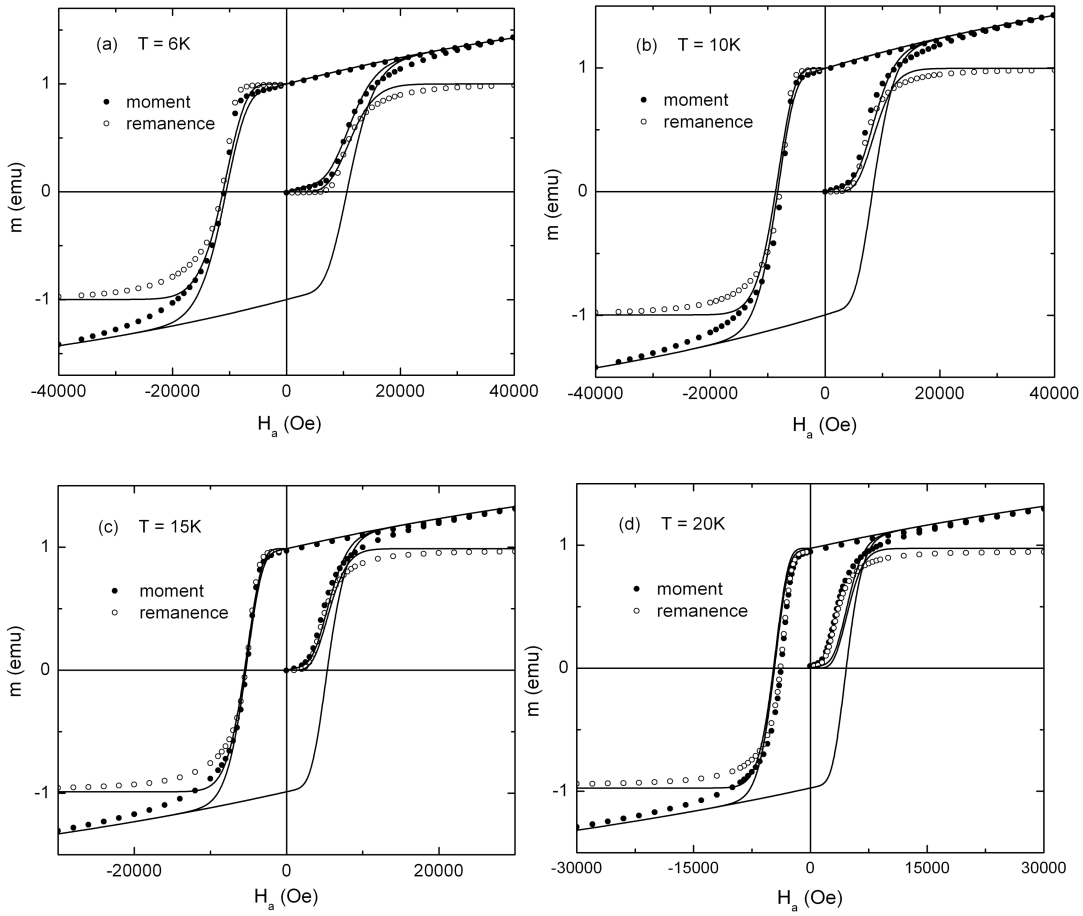

Figure 7.35: Numerical simulations (solid curves) of hysteresis loops of $Ca_{0.4}Sr_{0.6}RuO_3$, for (a) T = 6K, (b) T = 10K, (c) T = 15K, and (d) T = 20K, superposed on the experimental measurements of the moment (solid circles) and the remanence (open circles).

Table 7.10: Hysteresis Loop Simulation Parameters

τ_0 (s)	t_{exp}(s)	σ_d	σ_s (normalized to $H_{dm}(0)$ = 20kOe)	f	λ (10^{-5} Oe^{-1})	M_{sat} (emu)
10^{-9}	10^2	0.2 ±0.05	0.01 ±0.002	0.50 ±0.1	1.4 ±0.5	2.0

Finally, model simulations of FC/ZFC/TRM/IRM response functions were generated using the parameter values listed in Table 7.10 and plotted in Figure 7.34. The solid curves in Figures 7.36(a) through 7.36(g) show these model simulations overlaid on the measured FC/ZFC/TRM/IRM data, and Table 7.11 summarizes the corresponding parameter values, which are identical to those in Table 7.10 with one exception, the dispersion σ_d of dissipation fields, which was increased slightly (but within experimental tolerances) in order to optimize the description.

Table 7.11: FC/ZFC/TRM/IRM Simulation Parameters

τ_0 (s)	t_{exp}(s)	σ_d	σ_s (normalized to $H_{dm}(0)$ = 20kOe)	f	λ (10^{-5} Oe^{-1})	M_{sat} (emu)
10^{-9}	10^2	0.3 ±0.1	0.01 ±0.002	0.50 ±0.1	1.4 ±0.5	2.0

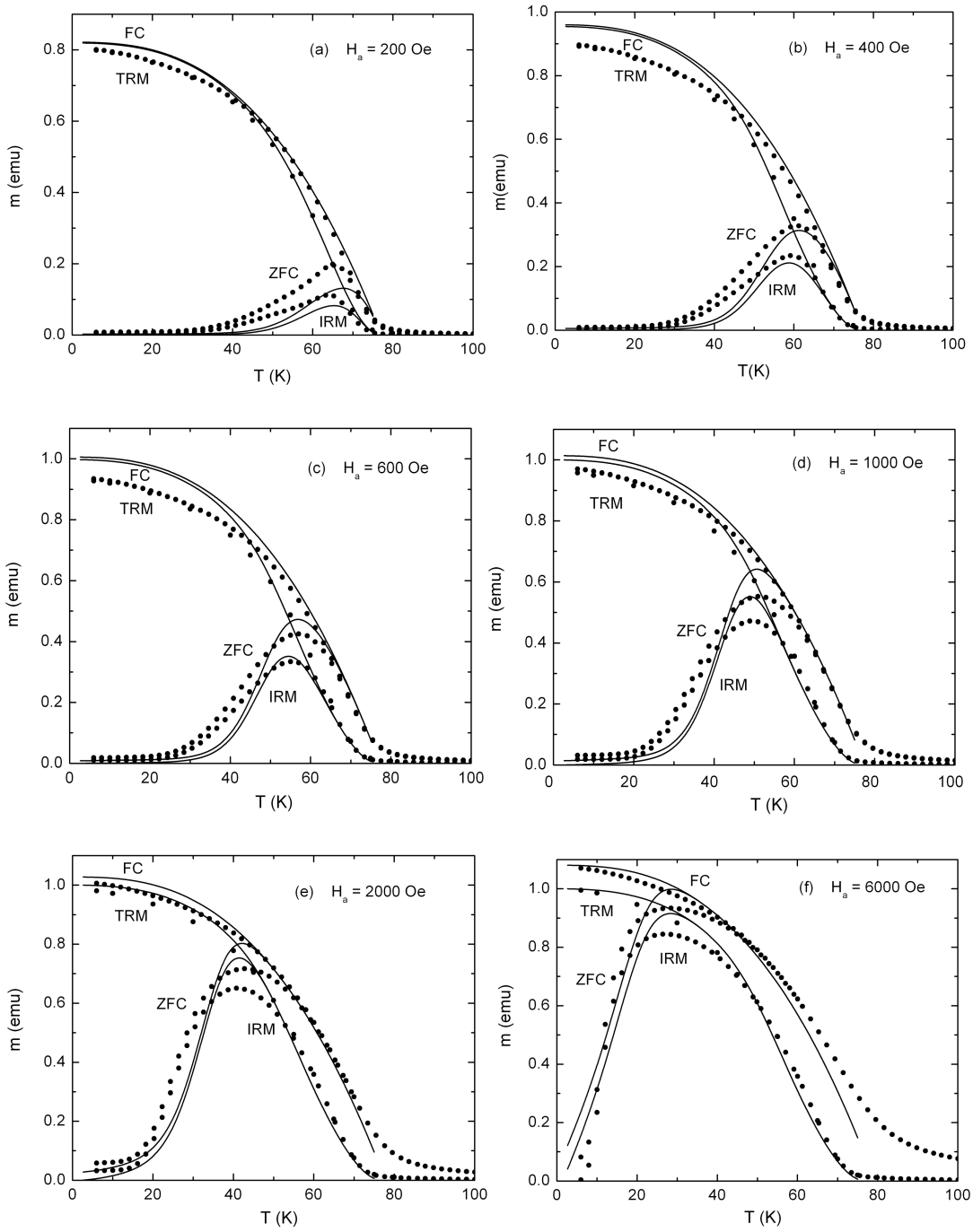

Figure 7.36: Numerical simulations (smooth curves) of the FC moment, ZFC moment, TRM and IRM of $Ca_{0.4}Sr_{0.6}RuO_3$, for (a) H_a = 200 Oe and (b) H_a = 400 Oe (c) H_a = 600 Oe, (d) H_a = 1000 Oe , (e) H_a = 2000 Oe, and (f) H_a = 6000 Oe, superposed on experimental measurements of the FC/ZFC/TRM/IRM (solid circles).

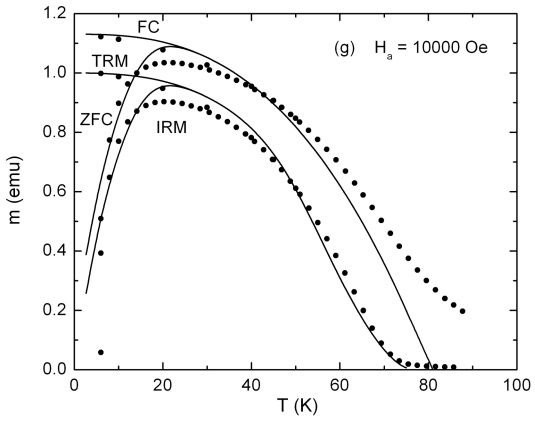

Figure 7.36 cont'd: Numerical simulations (smooth curves) of the FC moment, ZFC moment, TRM and IRM of $Ca_{0.4}Sr_{0.6}RuO_3$ (solid lines), for (g) H_a = 10000 Oe superposed on experimental measurements of the FC/ZFC/TRM/IRM (solid circles).

7.5.3 $Ca_xSr_{1-x}RuO_3$ with x = 0.2

Figures 7.37(a) to 7.37(d) show representative measurements of viscosity isotherms performed at four different temperatures T = 15K, 30K, 60K and 80K within the ferromagnetic phase $T < T_C \cong 120K$, in a series of negative holding fields $H_a < 0$ (listed in each figure), over an experimental observation time window $10s \le t \le 10^4 s$, and plotted on a logarithmic time scale. The system was saturated in a field H_{sat} = 40kOe prior to recoiling to the holding field H_a and, as before, the functional form of the decay is quasi-logarithmic.

In order to quantify the roles played by thermal overbarrier activation and barrier growth, "reversal time" data obtained from viscosity isotherms like those shown in Figure 7.37 were replotted in the form $T\ln(t_r/\tau_0)$ versus H_a over a wide range of values of

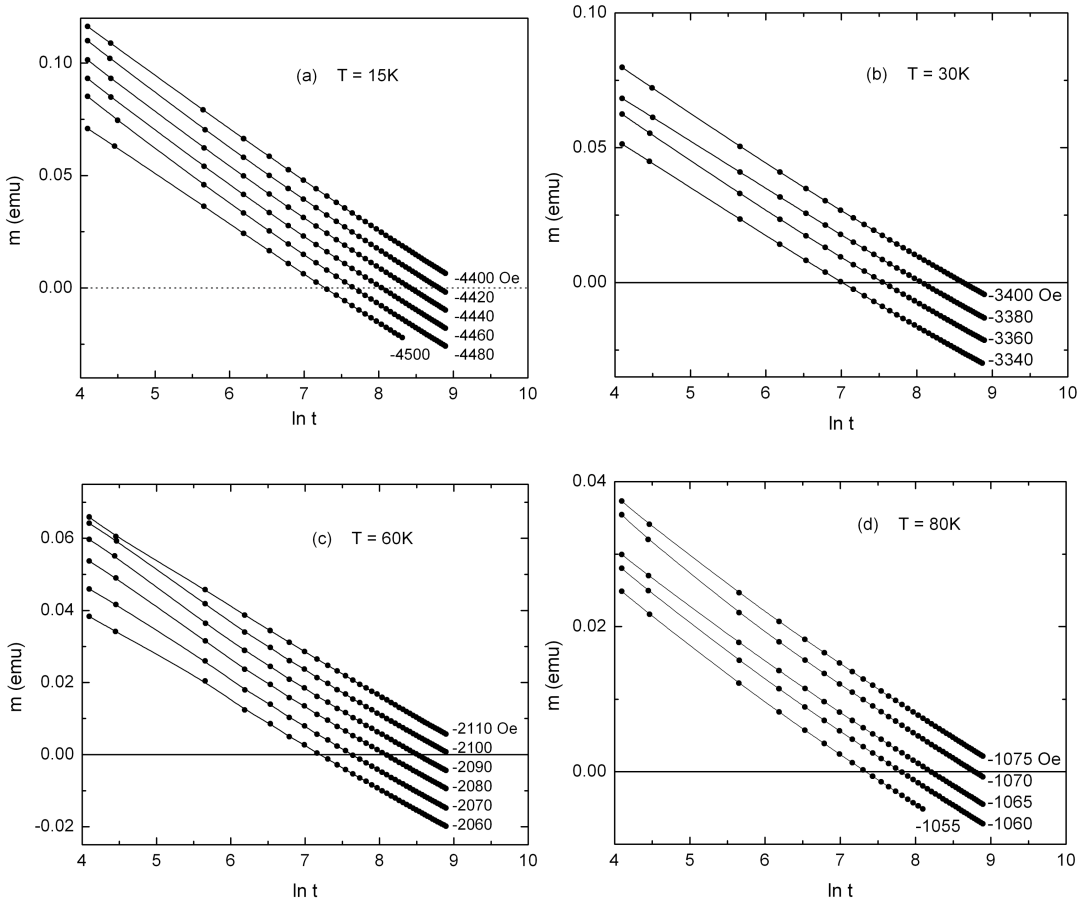

Figure 7.37: Measured viscosity isotherms of $Ca_{0.2}Sr_{0.8}RuO_3$ at temperatures (a) T = 15K, (b) T = 30K, (c) T = 60K, and (d) T = 80K. Each viscosity isotherm is labelled by its holding field H_a. The solid lines are guides to the eye.

the parameter τ_0, and Figure 7.38 shows one such plot for $\tau_0 = 10^{-9}$s. As before, no single value of τ_0 was capable of aligning the *entire* "reversal time" data set, for all measurement temperatures T between $2K \leq T \leq 90K$, onto a common universal curve. For values of τ_0 from the physically acceptable range $10^{-12}s \leq \tau_0 \leq 10^{-9}s$, approximate alignment is observed at low temperatures $T \leq 10K$, but deviations from universality are clearly observed for temperatures $T \geq 15K$ and become progressively more severe with increasing temperature, as seen in Figure 7.38.

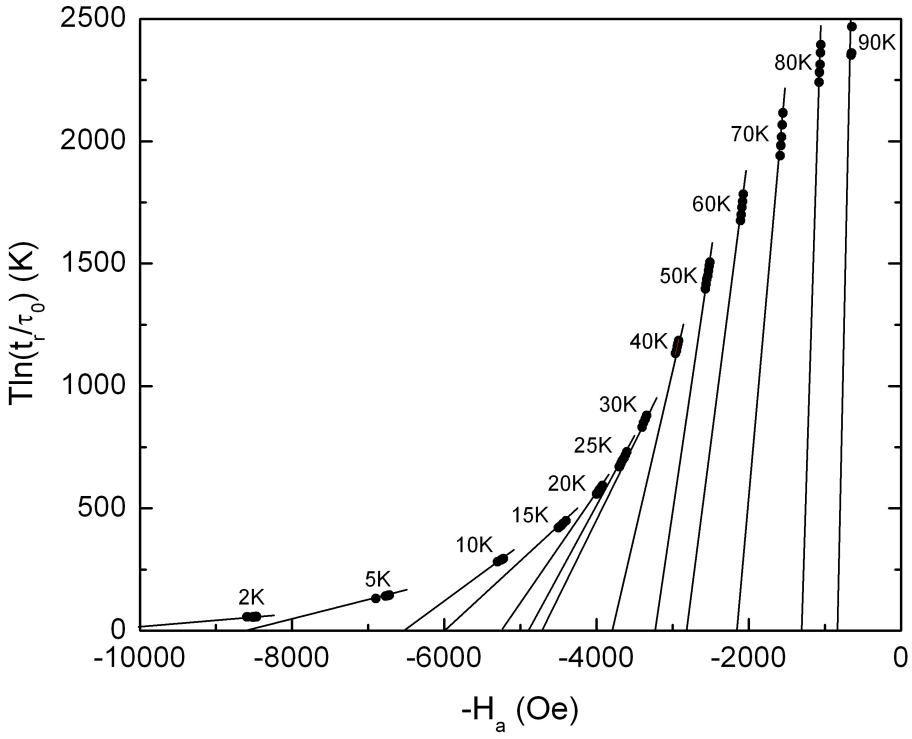

Figure 7.38: Reversal time data $Tln(t_r/\tau_0)$ as a function of applied field H_a of $Ca_{0.2}Sr_{0.8}RuO_3$ for $\tau_0 = 10^{-9}$ s. The straight lines represent the approximation that considers each isothermal segment to belong to the linear regime of its individual isothermal curve.

The analysis of the viscosity data in Figure 7.38 was conducted by adopting the linear approximation in which each isothermal segment is replaced by a straight line, and Figure 7.39 shows estimates for the median intrinsic dissipation field $H_{dm}(T)$ and the mean elementary moment reversal $\mu(T)$ obtained from the intercept and slope, respectively, of the straight lines in Figure 7.38. The solid curves in Figure 7.39 are smooth functional representations of $H_{dm}(T)$, $\mu(T)$ and the thermal fluctuation field $H_f(T) = kT/\mu(T)$.

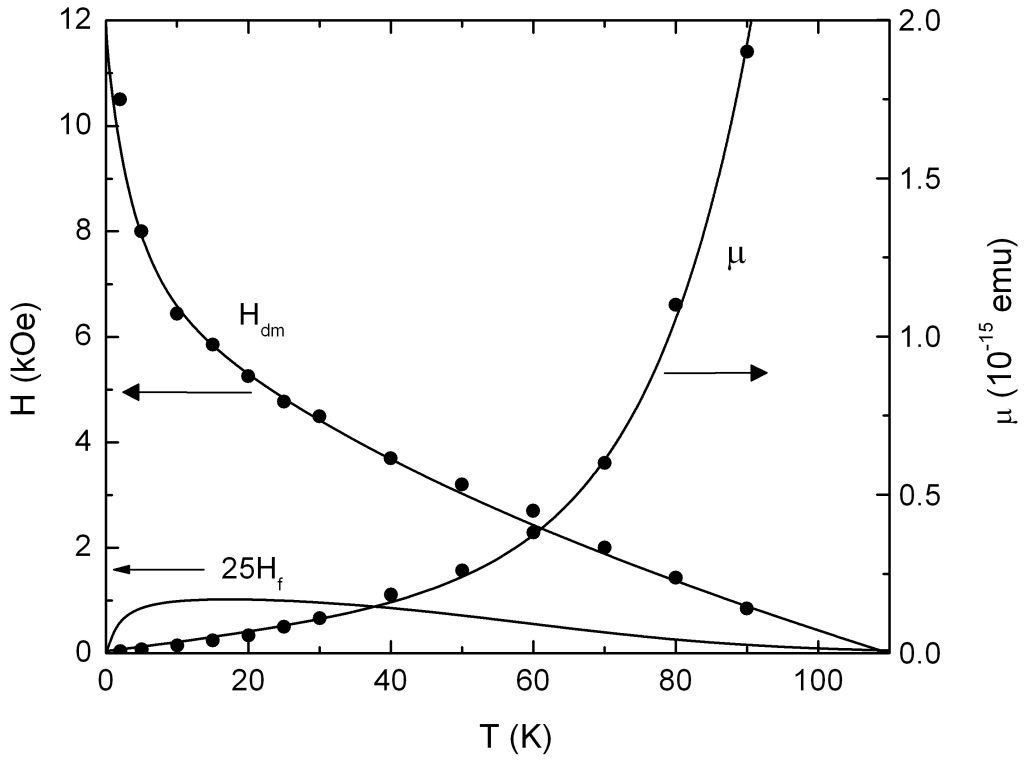

Figure 7.39: The median intrinsic dissipation field $H_{dm}(T)$ and the mean elementary moment reversal $\mu(T)$ obtained from the intercept and slope, respectively, of the straight lines in Figure 7.38 (solid circles). The solid curves in Figure 7.39 are smooth functional representations of $H_{dm}(T)$, $\mu(T)$ and the thermal fluctuation field $H_f(T)$ multiplied by $\ln(t_r/\tau_0) = 25$.

Model simulations of hysteresis loops were generated assuming the superposition Preisach density in Eq(7.7), with the usual lognormal-Gaussian product distribution of dissipative subsystems in Eq(7.5) and the exponential distribution of reversible subsystems in Eq(7.9), as well as the smooth functional representations for $H_{dm}(T)$, $\mu(T)$ and $H_f(T)$ shown in Figure 7.39, and fits to the experimental hysteresis loop data were used to establish not only the reversible parameters f and λ, but also the dispersions σ_d and σ_s of dissipative fields and bias fields, respectively. The solid curves in Figures 7.40(a) through 7.40(d) show the best model descriptions of four representative hysteresis

loops measured at T = 5K, 20K, 40K and 70K, superposed directly over the data, and Table 7.12 summarizes the parameter values obtained from these fits.

Table 7.12: Hysteresis Loop Simulation Parameters

τ_0 (s)	t_{exp}(s)	σ_d	σ_s (normalized to $H_{dm}(0)$ = 12kOe)	f	$\lambda(10^{-5}$ $Oe^{-1})$	M_{sat} (emu)
10^{-9}	10^{2}	0.40 ±0.05	0.03 ±0.01	0.45 ±0.05	2.0 ±0.5	1.5

Finally, model simulations of FC/ZFC/TRM/IRM response functions were generated using the parameter values listed in Table 7.12 and plotted in Figure 7.39. The solid curves in Figures 7.41(a) through 7.41(d) show these model simulations overlaid on the measured FC/ZFC/TRM/IRM data, and Table 7.13 summarizes the corresponding parameter values, which are identical to those in Table 7.12 with one exception, the dispersion σ_d of dissipation fields, which was increased slightly in order to improve the description.

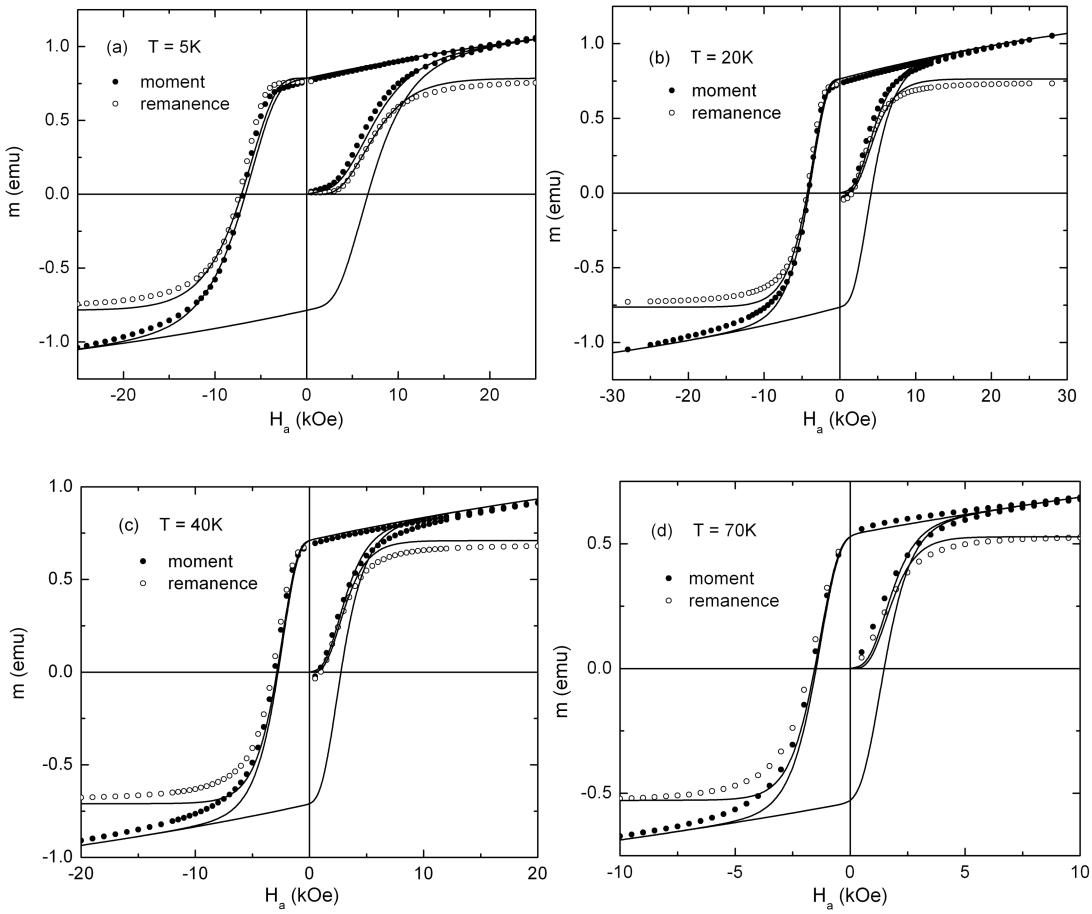

Figure 7.40: Numerical simulations (smooth curves) of hysteresis loops of $Ca_{0.2}Sr_{0.8}RuO_3$, for (a) T = 5K, (b) T = 20K, (c) T = 40K, and (d) T = 70K, superposed on the experimental measurements of the moment (solid circles) and the remanence (open circles).

Table 7.13: FC/ZFC/TRM/IRM Simulation Parameters

τ_0 (s)	t_{exp}(s)	σ_d	σ_s (normalized to $H_{dm}(0)$ = 12kOe)	f	λ (10^{-5} Oe^{-1})	M_{sat} (emu)
10^{-9}	10^2	0.50 ±0.05	0.03 ±0.01	0.45 ±0.05	2.0 ±0.5	1.5

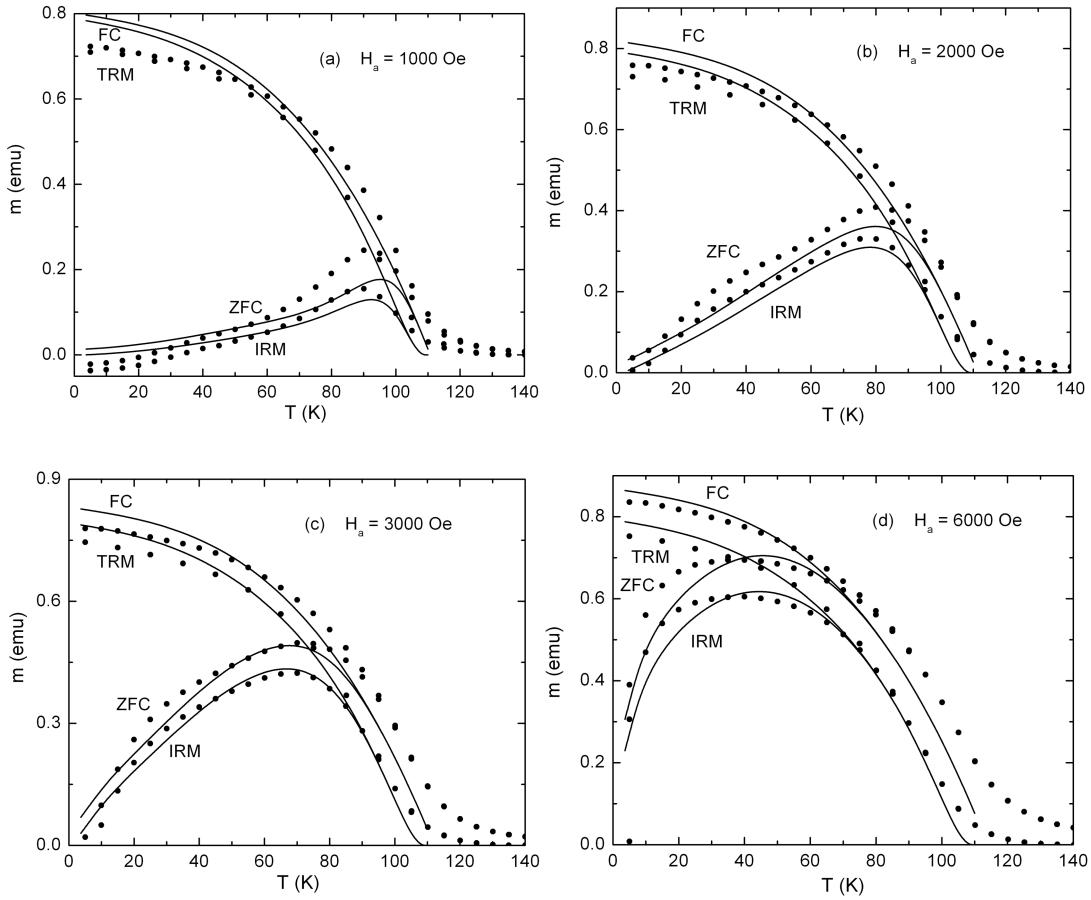

Figure 7.41: Numerical simulations (smooth curves) of the FC moment, ZFC moment, TRM and IRM of $Ca_{0.2}Sr_{0.8}RuO_3$ (solid lines), for (a) H_a = 1000 Oe, (b) H_a = 2000 Oe , (c) H_a = 3000 Oe, and (d) H_a = 6000 Oe , superposed on experimental measurements (solid circles).

7.6 Nanodimensional Fe in Alumina

The final system to be investigated was a nano-structured granular thin film consisting of nanodimensional particles of Fe embedded in an insulating alumina (Al_2O_3) matrix. From a microstructural perspective, this system is closely related to the nanoparticulate titanomagnetite and magnetite systems studied in Sections 7.3 and 7.4. However, from the perspective of its magnetic characteristics, the behaviour of the Fe/Al_2O_3 thin film differs significantly from that of the other two nanoparticulate materials and, in many respects, is more reminiscent of the ferromagnetic ruthenates discussed in Section 7.5.

The field, temperature, and time dependence of the measured magnetic response of the Fe/Al_2O_3 thin film is summarized in Figures 7.42 through 7.45. Figures 7.42(a) through 7.2(d) show four representative hysteresis loops measured at T = 10K, 20K, 30K and 35K, following thermal demagnetization in zero field from a reference temperature T_{ref} = 325K. The loops were generated by repeated application, removal, and reapplication of the magnetic field in increments of ΔH_a = 10 Oe, starting from the demagnetized state and then proceeding to a maximum positive field H_a = 2kOe close to technical saturation, and terminating at a maximum negative field H_a = -2kOe . The measurements in these figures include the initial magnetizing curve, the initial magnetizing remanence (IRM), the descending branch of the major hysteresis loop, and the demagnetizing remanence. The descending branches of the major loops at all temperatures exhibit an anomalous structural feature, in the form of a “knee”, at fields intermediate between the coercive field and the field which defines the onset of the

approach to saturation. As we shall see shortly, similar anomalous structure is observed in measurements of viscosity isotherms. Figure 7.42(e) shows plots of the measured coercive field H_c (solid dots) and the measured remanent coercive field H_{cr} (open circles) as a function of temperature over the entire temperature range investigated here $2K \leq T \leq 220K$. The two coercive fields are almost identical in magnitude, indicating that reversible effects play a relatively minor role in this system.

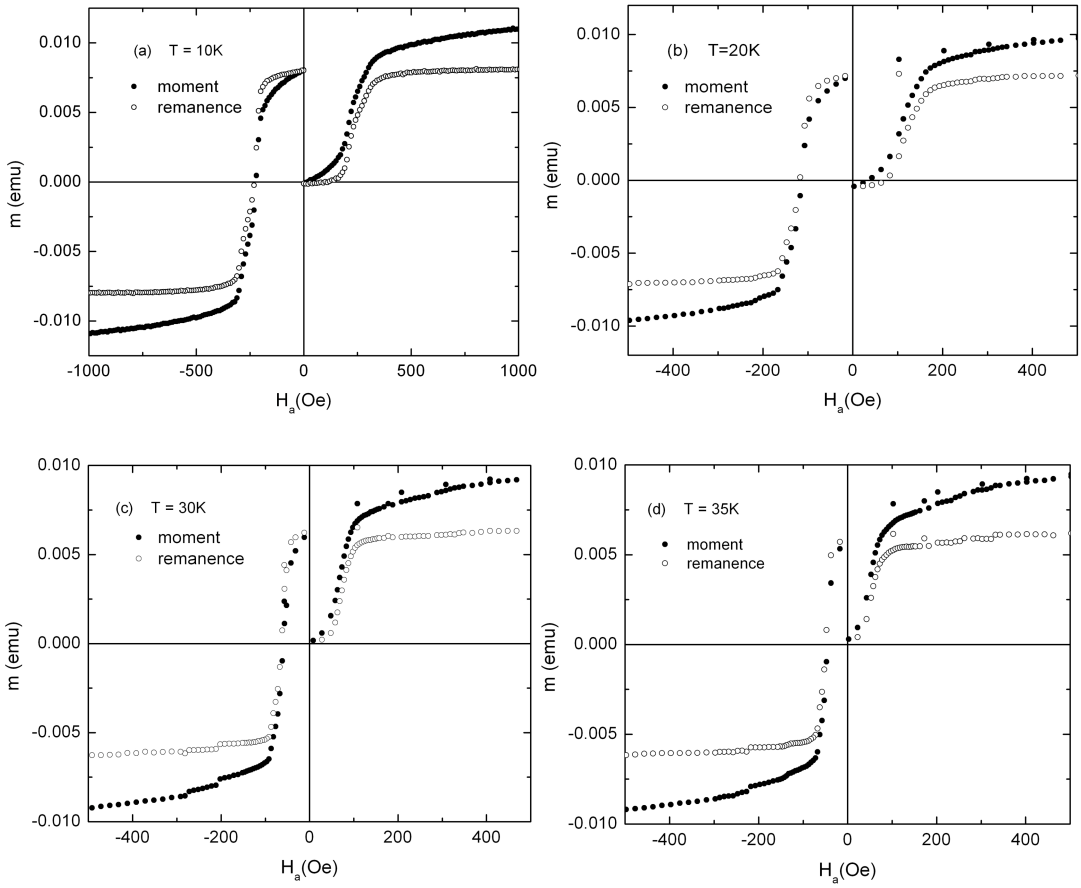

Figure 7.42: Hysteresis loops of Fe/Al_2O_3 measured at (a) T = 10K, (b) T = 20K, (c) T = 30K, and (d) T = 35K.

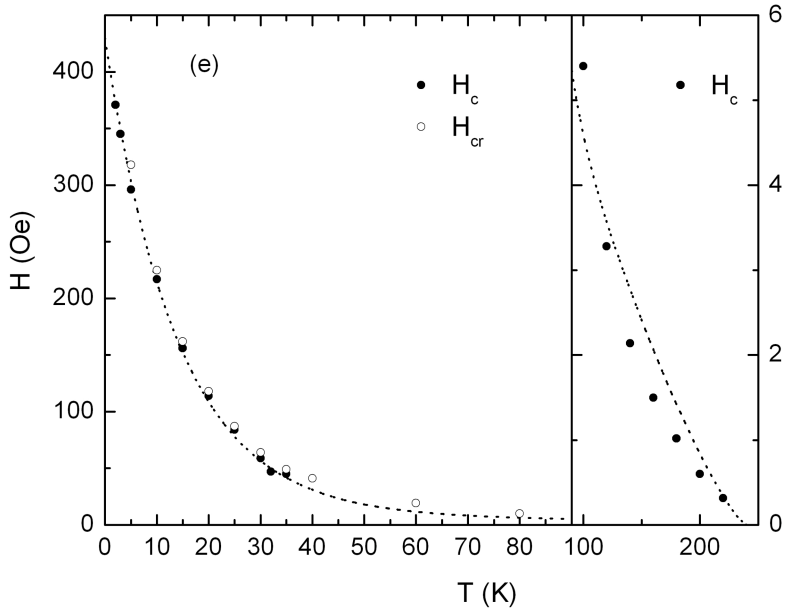

Figure 7.42 cont'd: (e) Measured coercive field H_c (solid circles) and measured remanent coercive field H_{cr} (open circles) for Fe/Al_2O_3. The right hand side is a magnified image of this plot for $90K \leq T \leq 250K$. The dotted lines are guides to the eye.

Figures 7.43(a) through 7.43(c) show representative measurements of the temperature dependence of the field cooled (FC) moment, the zero field cooled (ZFC) moment, the thermoremanent moment (TRM) and the isothermal remanent moment (IRM) between $10K \leq T \leq 300K$ in a series of applied fields H_a listed in the figures. Figure 7.43(a) summarizes the behaviour of the FC and ZFC moments. The ZFC moment is negligible at low temperatures, but then develops rapidly upon warming until it merges with the FC branch, which decreases monotonically with temperature over the entire experimental temperature range. The characteristic temperatures that define the onset of rapid ZFC moment growth, and the bifurcation of the FC and ZFC branches, shift systematically downward with increasing applied field. Figure 7.43(b) shows the temperature dependence of the TRM and the IRM obtained by removing the applied field H_a from the FC and ZFC states, respectively. The systematics are essentially identical to

those just described for the FC and ZFC moments in Figure 7.43(a). A field of H_a = 100Oe is sufficient to saturate the TRM at all measurement temperatures T ≥ 5K. For applied fields H_a < 100Oe, the individual TRM branches deviate progressively further below the saturation branch and merge with the saturation "envelope" at progressively higher temperatures. Although the magnetic response is very soft for all temperatures T > 120K, in the sense that the coercive field H_c becomes vanishingly small (H_c < 5Oe), the remanent moment continues to be a significant fraction of its low temperature saturation value m_{TRM}(T = 5K, H_a = 100Oe) at all temperatures up to T = 200K. Between 200K < T < 250K, the magnitude of the remanence decreases rapidly and vanishes near T ≈ 250K, above which the system response becomes purely reversible. While the behaviour described above is superficially reminiscent of that observed in the two other nanoparticulate systems in Sections 7.3 and 7.4, there are two important distinctions. First, the temperature dependence of the moment of Fe/Al_2O_3 in Figure 7.43(a) above the FC/ZFC bifurcation point exhibits a relatively strong, concave downward curvature, and the moment rapidly approaches vanishingly small values as T → 300K from below, in sharp contrast to the behaviour observed in the superparamagnetic nanoparticulates in Sections 7.3 and 7.4, where the moment decreases very gradually with temperature above the bifurcation point. Second, the magnitude and the thermal profile of both of the remanent moments of Fe/Al_2O_3 in Figure 7.43(b) are very similar to those of the corresponding in-field moment in Figure 7.43(a). In order to emphasize this similarity, the temperature dependence of all four FC/ZFC/TRM/IRM branches have been plotted together in Figure 7.43(c) for a single measurement field H_a = 20Oe. This behaviour is once again quite different from that observed in the superparamagnetic nanoparticulates,

where the IRM is typically a small fraction of the ZFC moment, and where both the TRM and the IRM vanish at much lower temperatures than either the FC or ZFC moments. In fact, the relationship between the four branches shown in Figure 7.43(c) bears a striking resemblance to that observed in the FC/ZFC/TRM/IRM response functions of all three ferromagnetic ruthenates at higher fields (as can be seen by comparing Figure 7.43(c) with, for example, Figures 7.31(e) and (f), Figures 7.36(f) and (g), and Figure 7.41(d)), suggesting that the alumina matrix may well mediate a ferromagnetic coupling between the Fe moments which is strong enough to induce the formation of a collectively frozen state.

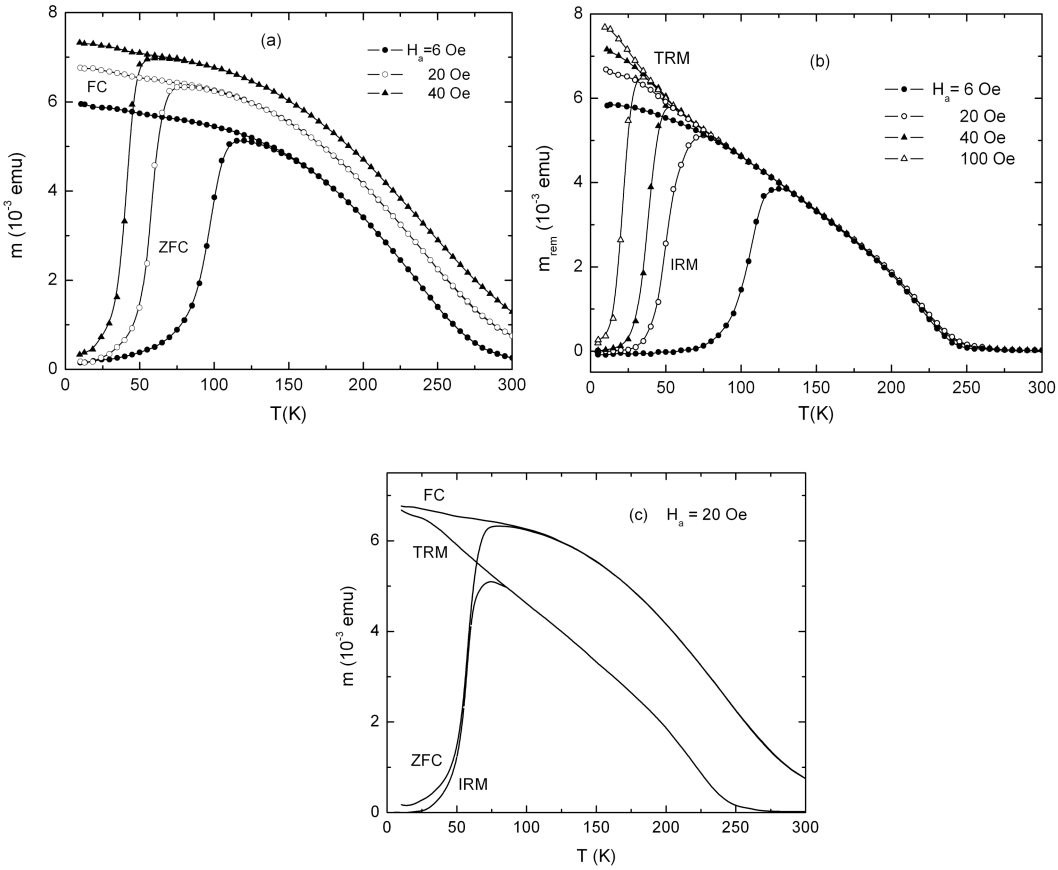

Figure 7.43: Measurements of the FC moment, ZFC moment, TRM, and IRM of Fe/Al_2O_3. (a) The FC and ZFC moments in a series of applied fields listed in the figure. (b) The TRM and IRM in a series of applied fields listed in the figure. (c) The FC moment, ZFC moment, TRM, and IRM in a field H_a = 20 Oe.

Figure 7.44 shows the field dependence of the TRM and the IRM at several selected temperatures within the irreversible phase, with all moments normalized to their respective saturation remanence. These data offer a complementary perspective on the systematics of the temperature dependence summarized in Figure 7.43. Thus, at all measurement temperatures, the TRM is observed to lead the corresponding IRM in the approach to saturation, while cooling delays the approach to saturation for both branches. The distinction between the TRM and IRM branches is particularly pronounced at low temperatures ($T \leq 10K$), where the TRM reaches saturation in applied fields for which the IRM is still a negligible fraction of the saturation remanence.

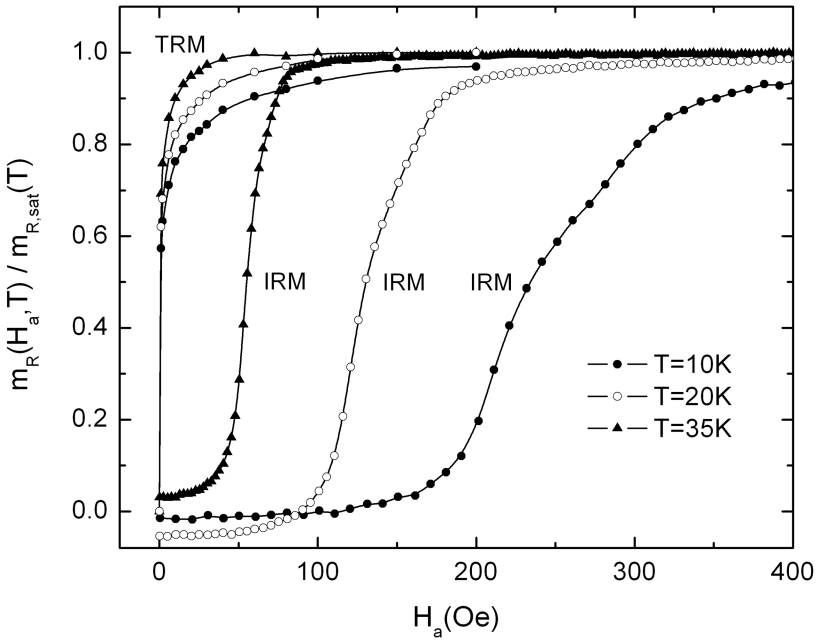

Figure 7.44: The field dependence of the TRM and the IRM of Fe/Al_2O_3 as a function of applied field H_a measured at the three temperatures listed in the figure. The moments have all been normalized to their respective saturation remanence.

Figures 7.45(a) through 7.45(e) show representative viscosity isotherms measured at five different temperatures T = 2K, 5K, 15K, 25K and 32K within the irreversible

regime, after recoiling from a positive saturating field H_a = 3000 Oe to a series of negative holding fields $H_a < 0$ (listed in each figure). The field recoil rate was $|dH_a/dt| \sim$ 100 Oe/s, and the total effective recoil time (from zero field to the holding field) was typically a few seconds, while the time required to stabilize the holding field and lock the magnet in persistent mode was $t_{stab} \sim 60s$. The relaxation of the moment was measured over an experimental observation time window $10s \leq t \leq 10^4 s$, and is plotted in Figure 7.45 on a logarithmic time scale. The most distinctive feature of these relaxation isotherms, and one which sets the Fe/Al_2O_3 system apart from all the systems studied up to this point, is their curvature, which is comparatively weak at the lowest measurement temperatures $T \leq 3K$, but which becomes progressively more pronounced as the temperature is increased. The relaxation response is a highly non-linear function of lnt and is characterized by a well-defined *inflection point* which occurs at a time t_{infl} which is roughly coincident with the time t_r at which the moment reverses sign, and which shifts systematically toward shorter time scales as the magnitude of the holding field increases. Furthermore, relaxation isotherms measured in holding fields with magnitudes in excess of the major loop coercive field ($|H_a| \geq H_c$) exhibit a *secondary inflection point* which lies to the right of the principal inflection point along the lnt-axis, at $lnt_{infl}' > lnt_{infl}$. This secondary structure is clearly visible in Figure 7.45(d) in the relaxation isotherms measured at T = 25K in the two highest holding fields H_a = 90Oe and H_a = 100Oe. As we will show in detail in the following section, this secondary inflection point is the temporal image (equivalent) of the "knee" which is observed in the field dependence of the demagnetizing branch of the major hysteresis loops in Figure 7.42. However, the existence of such a relationship is easy to anticipate from an inspection of the Preisach

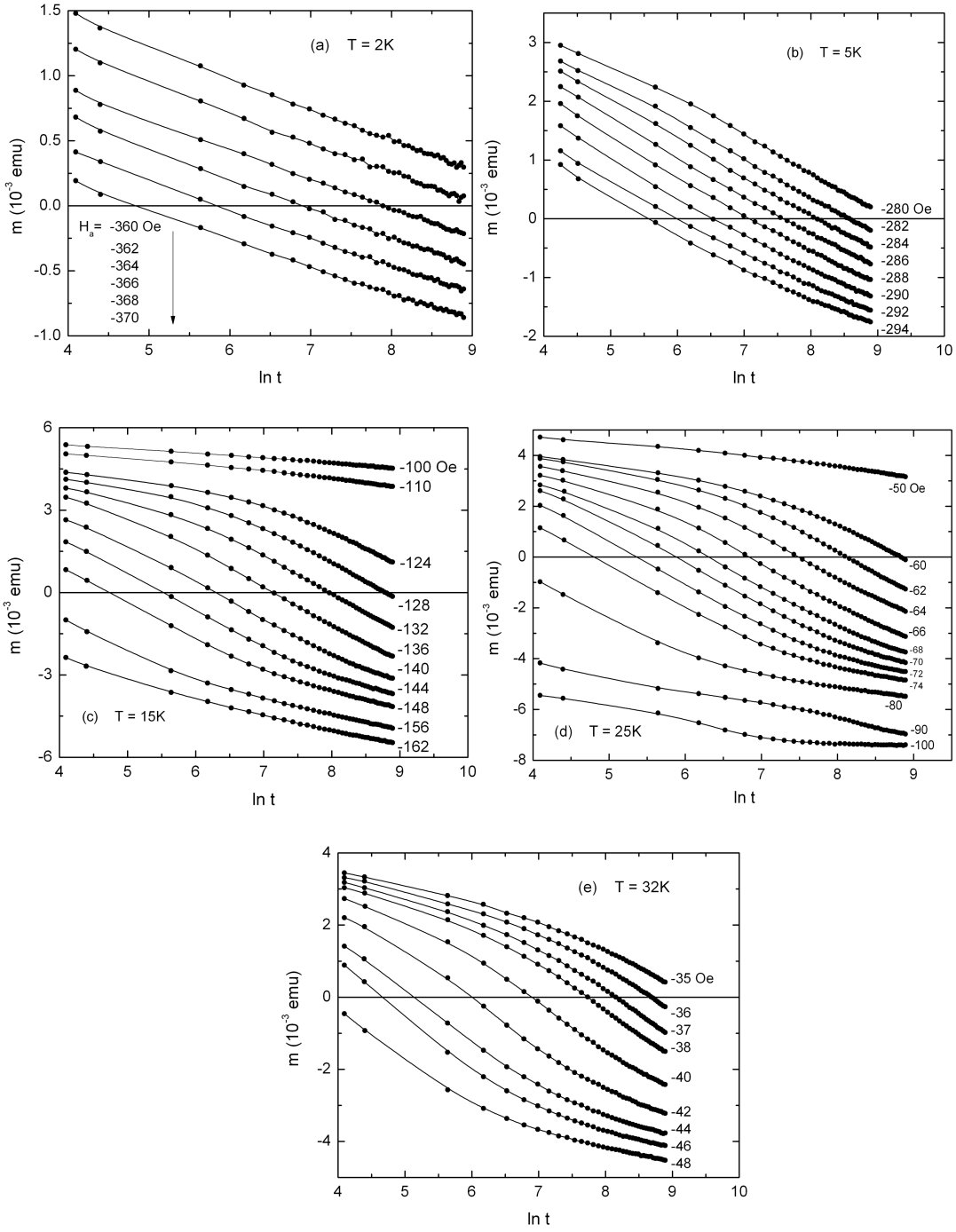

Figure 7.45: Measurements of viscosity isotherms of Fe/Al_2O_3 in a sequence of applied fields (listed in each figure) at temperatures (a) T = 2K, (b) T = 5K, (c) T = 15K, (d) T = 25K, and (e) T = 32K.

diagram in Figure 7.46, which shows that the subset of Preisach elements which experience moment reversal from the +μ state to the –μ state when the frontal boundary moves through the Preisach distribution from position 1 to position 2 (shaded region in Figure 7.46) is the same, whether the motion of the boundary is driven by changes in field H_a at fixed observation time t, or by changes in observation time t at fixed field H_a. As a consequence, the functional form of the relaxation response at a given temperature T is expected to mirror the shape of the demagnetizing branch of the major hysteresis loop at that temperature.

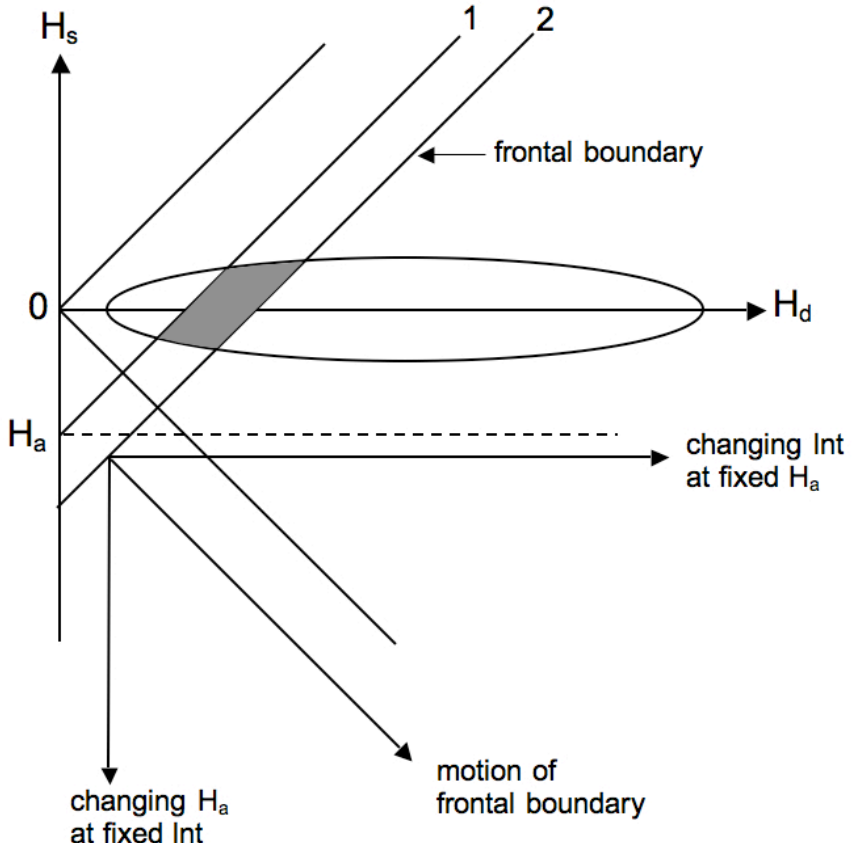

Figure 7.46: The Preisach diagram showing that the subsystems which experience moment reversal from +μ to –μ (shaded region) when the frontal boundary moves from 1 to 2 is the same whether time lapses at a fixed H_a, or the field changes at a constant rate.

The reversal-time-based viscosity analysis was applied to the Fe/Al_2O_3 relaxation isotherms in Figure 7.45, and Figure 7.47 shows a plot of $T\ln(t_r/\tau_0)$ as a function of holding field H_a over the entire temperature range $2K \leq T \leq 40K$ investigated here, for a series of four values of τ_0 lying within the range $10^{-18}s \leq \tau_0 \leq 10^{-6}s$. The inset shows a magnified view of the behaviour of these plots in the limit of low fields $|H_a| \leq 60Oe$ and high temperatures $T \geq 28K$ for $\tau_0 = 10^{-9}s$ and $\tau_0 = 10^{-12}s$. The principal features of these plots and their systematic variation with τ_0 are essentially identical to those of the three ferromagnetic ruthenates in Figures 7.26, 7.33 and 7.38 in Section 7.5. In particular, there is no single value of τ_0 which is capable of simultaneously aligning all of the isothermal viscosity segments to form a single continuous universal curve, although there is some suggestion that, for values of τ_0 in the physically acceptable range $10^{-12}s \leq \tau_0 \leq 10^{-9}s$, the data at low measurement temperatures $T \leq 12K$ may be compatible with a common curve. In the absence of compelling evidence for universality over a significant temperature interval, the linear approximation was adopted for each isothermal segment, and the left panel of Figure 7.48 summarizes the temperature dependence of the median dissipation field $H_{dm}(T)$ obtained from the intercepts, the mean elementary moment reversal $\mu(T)$ obtained from the slopes, and the thermal fluctuation field $H_f = kT/\mu(T)$. The symbols with attached error bars show the individual parameter values, while the solid curves are smooth functional representations which were used to generate model simulations of magnetic response functions. Due to difficulties associated with resolution and excessive data scatter, no reliable viscosity measurements were available for temperatures above T = 50K, and consequently the measured coercive fields were used as

a guide to define the functional representation of $H_{dm}(T)$ in this region. The solid dots in the right hand panel show these measured coercive fields H_c, and the solid curve shows the continuation of the functional representation of $H_{dm}(T)$ from the left hand panel.

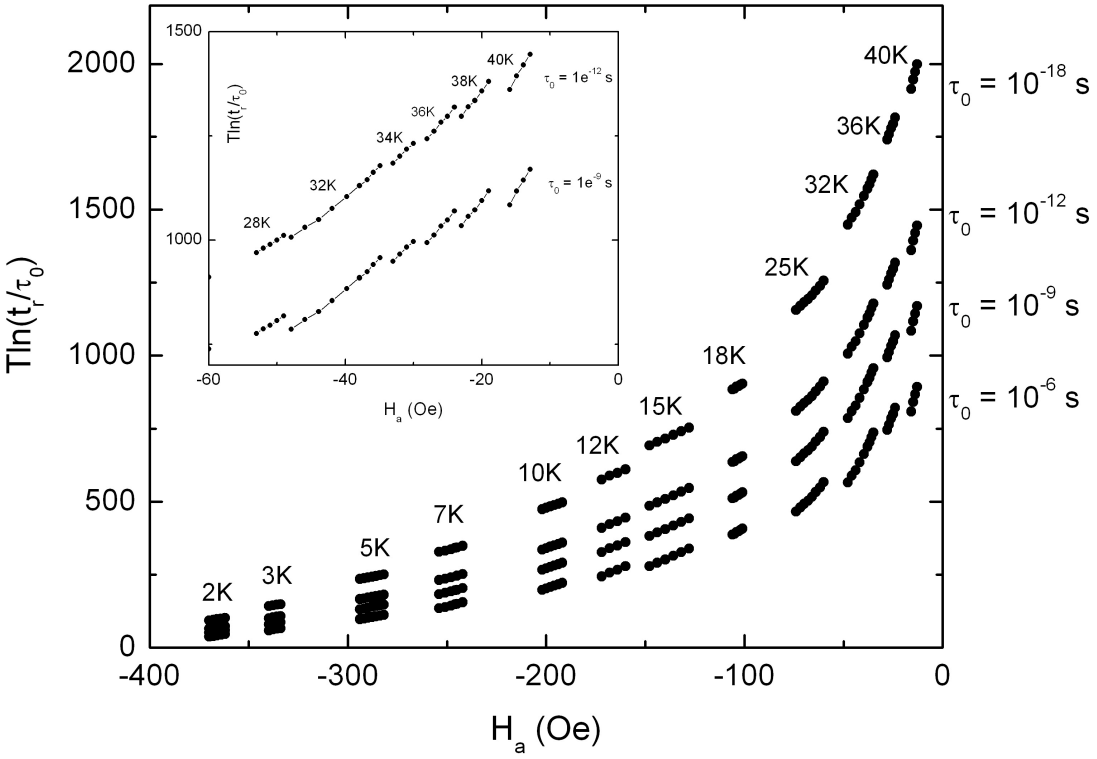

Figure 7.47: Reversal time plots ($Tln(t_r/\tau_0)$ vs. H_a) for four values of τ_0, shown over the entire range of temperatures and holding fields. The inset is a magnified version of the plots for $T \geq 28K$.

As before, model simulations of hysteresis loops were then generated assuming the superposition Preisach density in Eq(7.7), with the usual lognormal-Gaussian product distribution of dissipative subsystems in Eq(7.5) and the exponential distribution of reversible subsystems in Eq(7.9), as well as the temperature dependences for $H_{dm}(T)$, $\mu(T)$ and $H_f(T)$ shown in Figure 7.48, and fits to the experimental data in Figure 7.42 were used to establish not only the reversible parameters f and λ, but also the dispersions σ_d and σ_s of dissipative fields and bias fields, respectively. The solid curves in Figure

7.49(a) through 7.49(d) show the best model representations of the measured hysteresis loops in Figure 7.42 superposed directly over the data, and Table 7.14 summarizes the parameter values obtained from these fits.

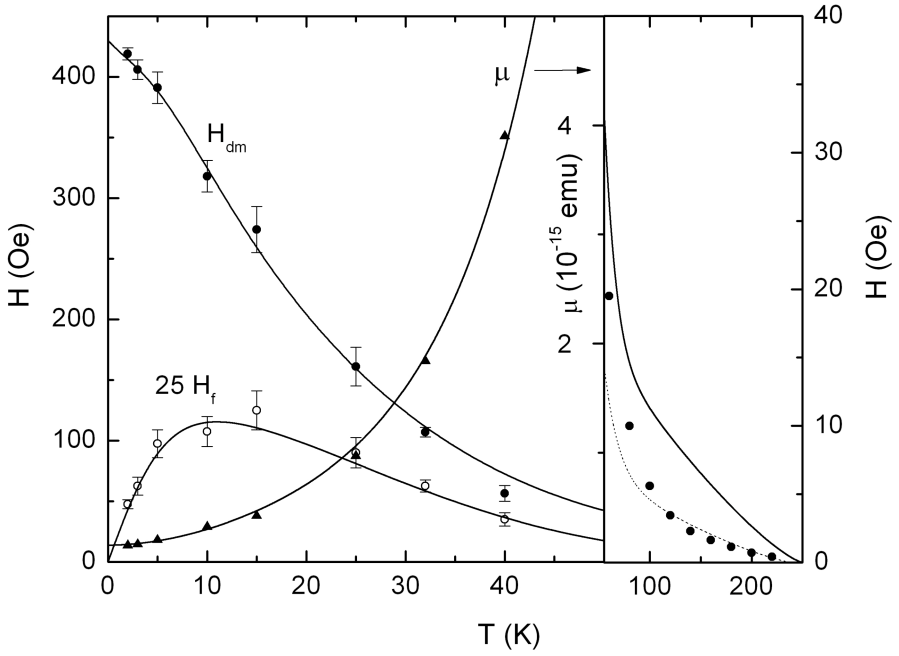

Figure 7.48: The temperature dependence of $H_{dm}(T)$ (solid circles) and $\mu(T)$ (triangles) obtained from the slopes of the individual isotherms in Figure 7.47, along with the temperature dependence of the thermal fluctuation field $H_f = kT/\mu$ (T) (open circles) multiplied by $\ln(t_r/\tau_0) = 25$. The solid curves are smooth functional representations of the point-by-point data.

Table 7.14: Hysteresis Loop Simulation Parameters

τ_0 (s)	t_{exp}(s)	σ_d	σ_s (normalized to $H_{dm}(0) = 430$Oe)	f	λ (10^{-4} Oe^{-1})	M_{sat} (emu)
10^{-9}	10^2	0.1 ±0.02	0.015 ±0.002	0.42 ± 0.03	2.00 ± 0.05	0.012

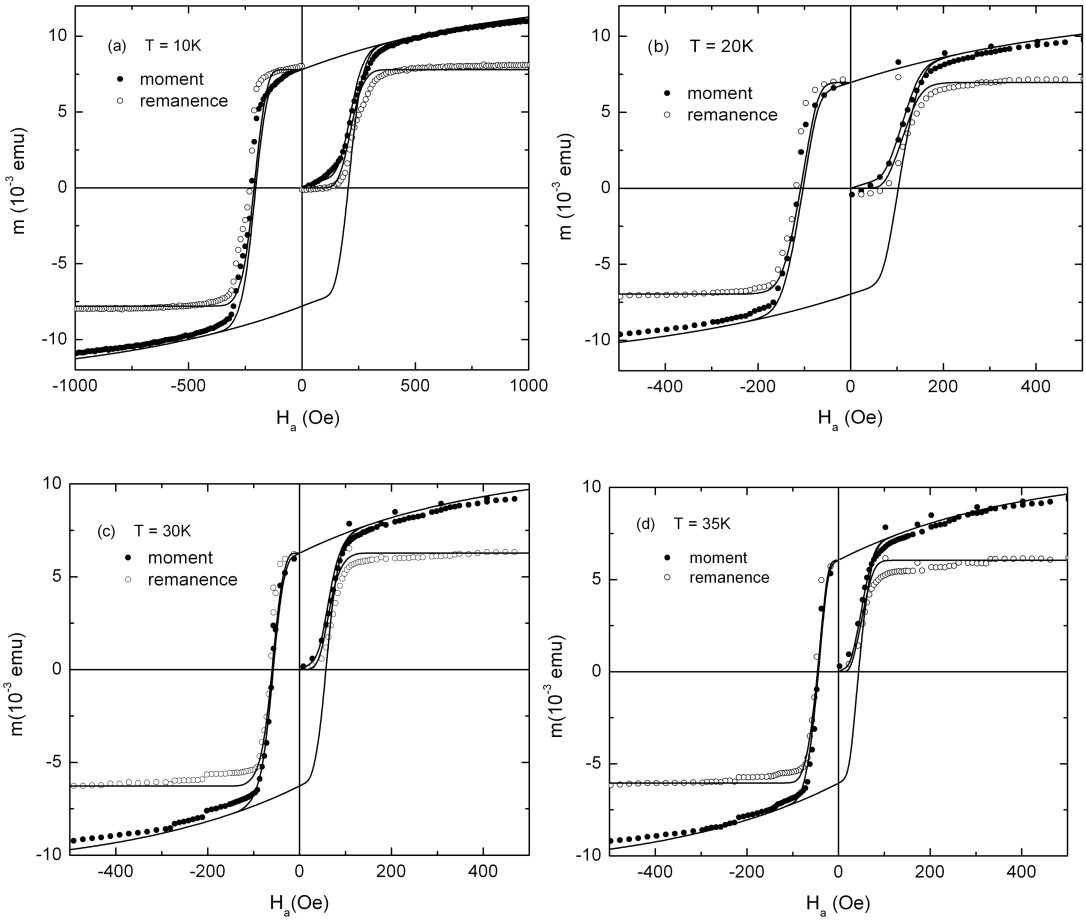

Figure 7.49: Numerical simulations (smooth curves) of hysteresis loops of Fe/Al_2O_3 superposed on the experimental measurements of the moment (solid circles) and the remanence (open circles) from Figure 7.42, at temperatures (a) T = 10K, (b) T = 20K, (c) T = 30K, and (d) T = 35K.

Finally, model simulations of FC/ZFC/TRM/IRM response functions were generated using the parameter values listed in Table 7.14 and plotted in Figure 7.50 and Figure 7.51. The solid curves in Figures 7.50 show model simulations of the remanent moments (TRM and IRM) in five applied fields H_a = 10Oe, 15Oe, 20Oe, 25Oe and 80Oe, assuming a constant, temperature independent saturation moment $M_{sat}(T) = N(T)\mu(T)$, and Figure 7.51 shows model simulations of the entire set of FC/ZFC/TRM/IRM response functions which include a smooth functional representation for the saturation

moment $M_{sat}(T)$ that reproduces the shape of the FC data measured in a field H_a = 6Oe. The model simulations clearly replicate the complex structural characteristics of the experimental data in Figure 7.43, as well as their systematic variation with field and temperature, remarkably well, and offer compelling evidence that the temperature dependence of the magnetic response of Fe/Al_2O_3 is dominated by field induced transitions over a spectrum of free energy barriers which collapse explicitly with temperature as the system is warmed through the irreversible phase. This collapse is illustrated in Figure 7.52, which shows contour plots of the Preisach density of dissipative subsystems $p_{irrev}(H_d,H_s)$ at six temperatures within the irreversible phase. The simulations also lend indirect support to our earlier contention that the system of Fe nanoparticle moments forms a collectively ordered state with ferromagnetic correlations. If this is indeed the case, then it is unlikely that the parameter $\sigma_s = 0.015$ is a direct measure of the actual magnetostatic interaction fields between the Fe nanoparticles (as it is in the superparamagnetic titanomagnetite and magnetite systems), any more than the parameter $\sigma_s \approx 0.02$ in the ferromagnetic ruthenates is a direct measure of the interatomic exchange interactions between the magnetic Ru atoms. We speculate that in magnetically ordered materials, σ_s measures either the strength of the interactions between magnetic domains, or fluctuations in the energies of the metastable states themselves due to spatial variations in the local anisotropy constants (σ_d measures the fluctuations in the metastable state excitation barrier heights).

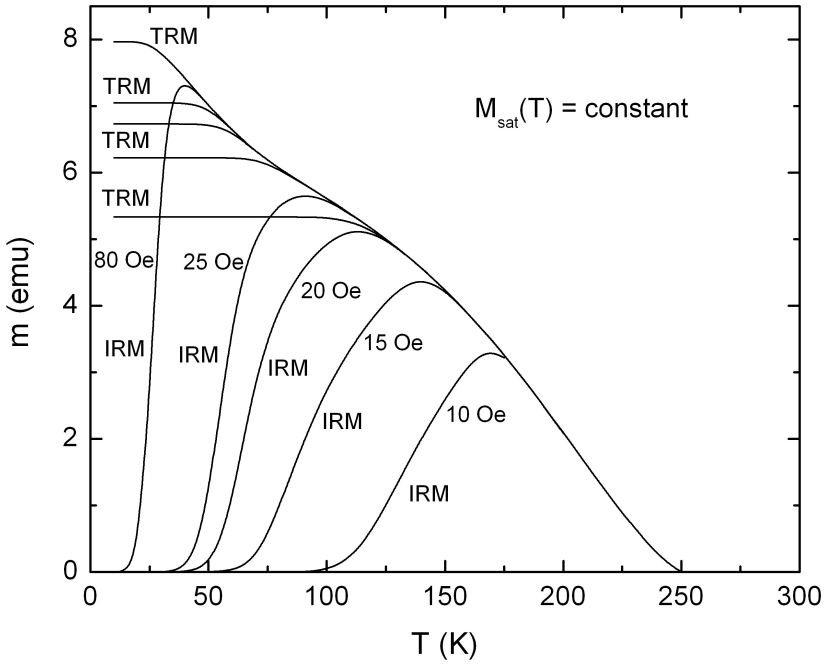

Figure 7.50: Numerical simulations of the TRM and IRM for Fe/Al_2O_3 in the applied fields listed in the figure, assuming a temperature independent saturation moment.

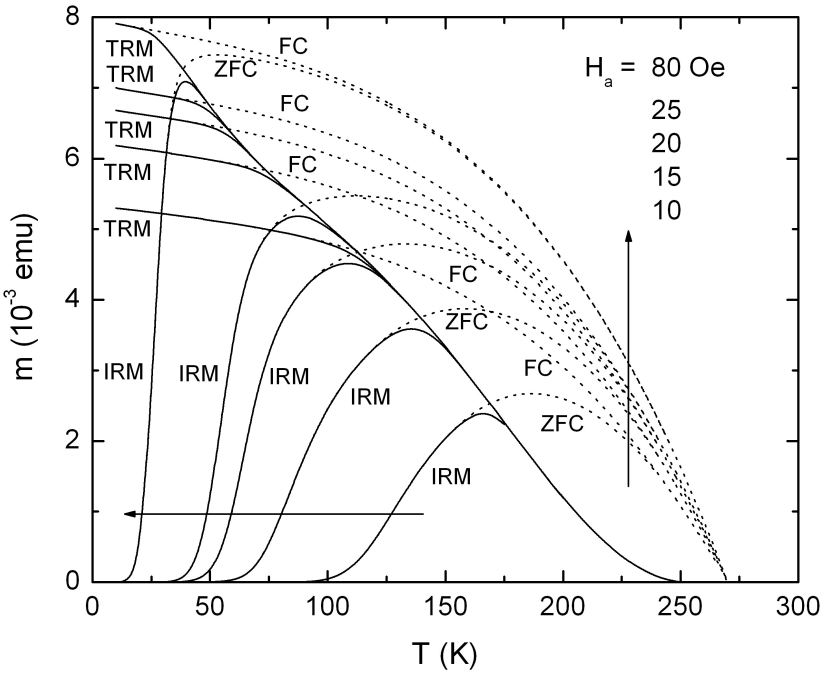

Figure 7.51: Numerical simulations of the FC, ZFC, TRM, and IRM in the applied fields listed in the figure, for comparison with Figure 7.43(a) and 7.43(b). The simulations include a smooth functional representation of the saturation moment $M_{sat}(T)$.

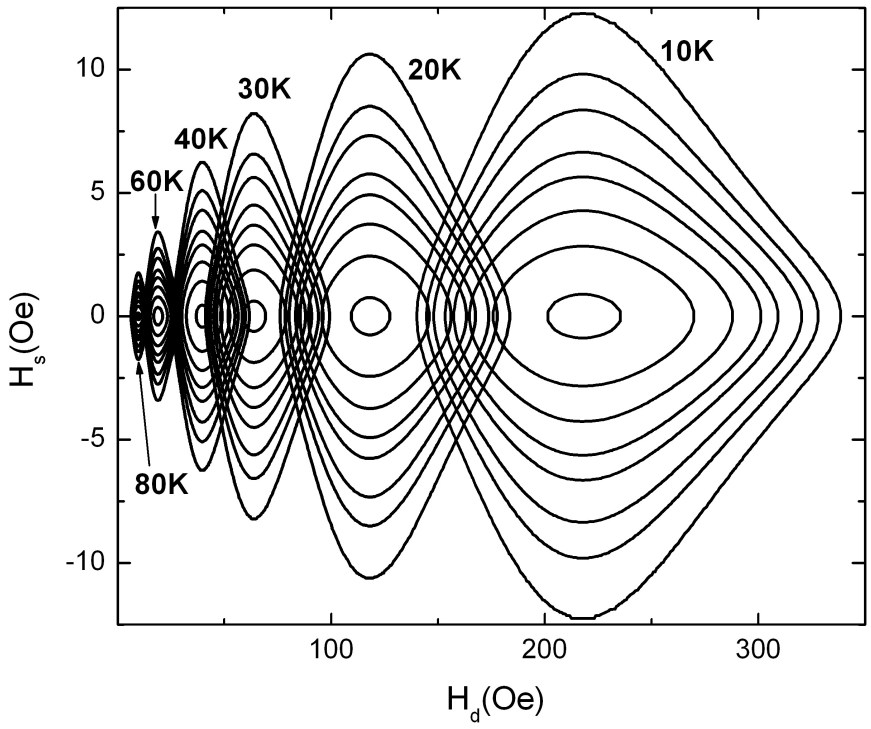

Figure 7.52: Contour plots of the Preisach density of dissipative subsystems $p_{irrev}(H_d,H_s)$ at a series of temperatures within the irreversible phase.

7.7 Comparisons with Other Analytical Strategies

The Preisach two-level subsystem formalism has inspired two other closely related analytical strategies for extracting the thermal fluctuation field H_f from families of viscosity isotherms like those shown in Figure 7.2. Both prescriptions employ a transformation of variables from lnt to an effective field H_{eff}, which is the sum of the applied field and an effective thermal field $H_{eff} = H_a + H_{thermal}$, and which collapses the relaxation isotherms measured at one temperature T in a sequence of different holding fields H_a onto a common "master" relaxation curve which is congruent to the major intrinsic hysteresis loop measured in the limit of infinitely fast sweep rates ($t \rightarrow \tau_0$).

(a) Prescription 1 [20-22]: The first approach applies to a family of relaxation isotherms which have been generated in a series of negative holding fields $H_a < 0$ after recoiling at a prescribed negative rate $dH_a/dt < 0$ from a large positive saturating field. As a consequence of the finite relaxation rate, Preisach subsystems with dissipation fields $H_d < H^* = H_f \ln[H_f/(\tau_0|dH_a/dt|)]$ have already reached their equilibrium ($t \rightarrow \infty$) configuration before the holding field H_0 is stabilized at its final value, and relaxation measurements commence. If the number of Preisach elements with dissipation fields $H_d < H^*$ is vanishingly small, then the Preisach formalism predicts that the measured major loop coercive field H_c will vary linearly with the sweep (or recoil) rate as follows:

$$H_c = H_f \ln(|dH_a/dt|) + C \qquad (7.10)$$

where C is a constant. Furthermore, the entire family of relaxation isotherms $M(t, H_a, dH_a/dt)$ measured in a series of holding fields H_a will collapse onto a single "master" curve $M(H_{athermal})$ under a transformation of variables from lnt to an effective "athermal" field $H_{athermal}$ which summarizes the combined effects of applied field and temperature in the hypothetical limit where thermal effects may be completely eliminated, and which is defined by [20]

$$H_{athermal} = H_a - H_f \ln[(t/\tau_0) + H_f/(\tau_0|dH_a/dt|)] \quad . \tag{7.11}$$

Moreover, this master relaxation curve $M(H_{athermal})$ is identical to the intrinsic $(t \rightarrow \tau_0)$ hysteresis loop obtained by applying the transformation in Eq(7.11) to a series of experimental hysteresis loops measured in a series of different finite sweep rates dH_a/dt [20].

Figure 7.53 shows an application of the transformation in Eq(7.11) to viscosity data obtained from the Fe/Al_2O_3 system studied in Section 7.6. For typical magnetometer sweep rates $dH_a/dt \approx 100$ Oe/s and typical thermal fluctuation fields H_f on the order of a few Oersteds, the second term in Eq(7.11) is negligible in comparison with the first term, and $H_{athermal}$ may be safely approximated by

$$H_{athermal} \cong H_a - H_f \ln(t/\tau_0) \tag{7.12}$$

Figure 7.53 shows the entire set of viscosity isotherms in Figure 7.45(d) measured at T = 25K replotted as a function of the athermal field in Eq(7.12) using the value of the thermal fluctuation field $H_f = 3.6$ Oe obtained from the "linearized" viscosity analysis in Section 7.5, and assuming $\tau_0 = 10^{-9}$ s. For purposes of comparison, the figure also shows the descending branch of the major hysteresis loop measured at T = 25K (solid curve through open circles). The "master" relaxation curve faithfully replicates the shape of the major loop, including the "knee" which is observed near $H_a \cong -200$ Oe close to the approach to saturation.

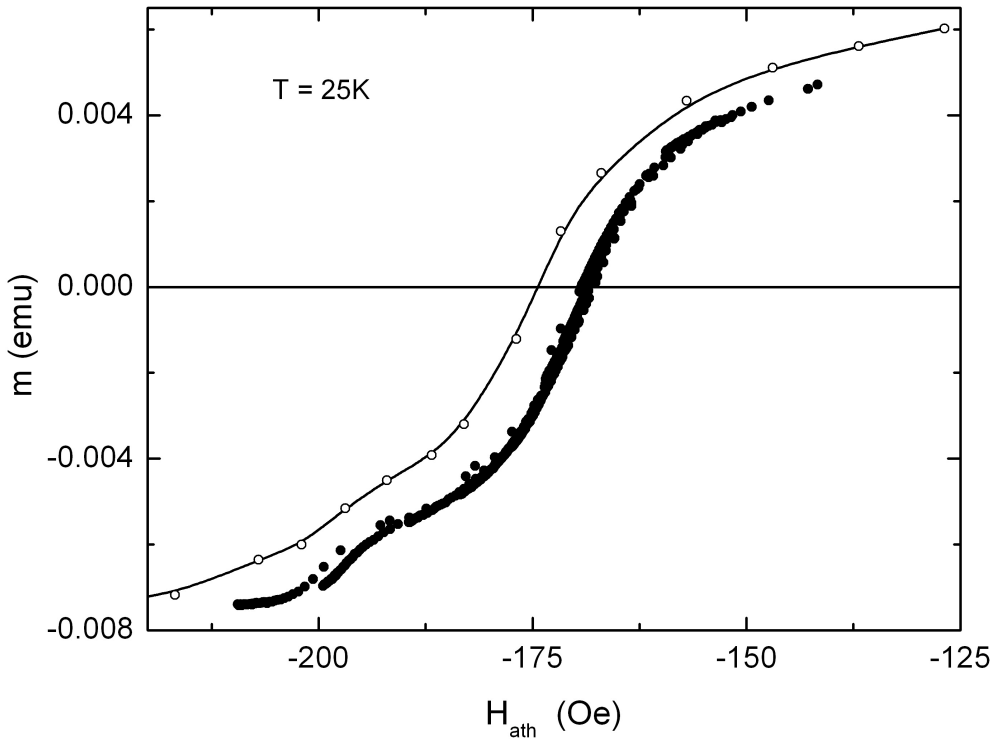

Figure 7.53: Transformation of variables (solid circles) from lnt to an effective field H_{ath} applied to the viscosity data for Fe/Al_2O_3 in Figure 7.45 measured at T = 25K. The solid curve through open circles is the descending branch of the major hysteresis loop measured at T = 25K.

(b) Prescription 2 [23-25]: The second approach is based on the model prediction that viscosity isotherms for a Preisach ensemble of completely non-interacting bistable subsystems with vanishing bias fields $H_s = 0$ are identical in shape and differ only in a horizontal shift along the lnt-axis which varies linearly with the difference in holding field H_a as [23]

$$\Delta \ln t = - \Delta H_a / H_f \quad . \tag{7.13}$$

Thus, by applying suitable time shifts, the entire family of relaxation isotherms in all holding fields may be superposed onto a common curve. Furthermore, this "master" relaxation curve is perfectly congruent with the major hysteresis loop under a transformation of variables from lnt to an effective field given by [23]

$$H_{eff} = H_f \ln t - H_f \ln[\tau_0 \, e^{-(\mu/kT)}] + H_a \tag{7.14}$$

where μ is the chemical potential. Figure 7.54 illustrates this behaviour for a weakly interacting model system with a lognormal-Gaussian Preisach density and with dispersions $\sigma_d = 0.5$ and $\sigma_s = 0.01$. Figure 7.54(a) shows a set of model viscosity isotherms generated in a series of holding fields h_a and plotted as a function of the thermal viscosity field $h_T = h_f \ln(t/\tau_0)$, while Figure 7.54(b) shows the same set of isotherms plotted as a function of the effective field h_{eff} in Eq(7.14), assuming $\mu = 0$. For

all holding fields $|h_a| > 0.2$, the isotherms are perfectly congruent with each other and with the major intrinsic hysteresis loop.

When the Preisach elements are allowed to interact, that is, for non-vanishing values of the dispersion of bias fields σ_s, the relaxation isotherms generated in different holding fields are no longer identical in shape, and each isotherm approaches an asymptotic equilibrium moment $m_{eq}(t \rightarrow \infty)$ which depends on the holding field h_a, as may be clearly seen by an inspection of the four families of model isotherms shown in Figure 7.3. The second prescription claims (without any rigorous, formal justification) that the linear relationship in Eq(7.13) and the field transformation in Eq(7.14) continue to be valid, and continue to produce superposition and congruency, for assemblies of interacting Preisach elements provided that the viscosity isotherms are first *renormalized* to have a common equilibrium moment $m_{eq}(t \rightarrow \infty) = -1$ by implementing the following algorithm[25]:

$$m(t) = [m(0)+1]\left[\frac{m(t)-m(\infty)}{m(0)-m(\infty)}\right] - 1 \quad . \tag{7.15}$$

The successful application of this algorithm clearly depends on accurate estimates for the equilibrium moment $m(\infty)$, which in turn demands that a sufficient portion of the complete relaxation function be accessible within the available experimental time window (typically limited to the interval between $1s \leq t \leq 10^5$ s for commercial magnetometers) to define at least the initial stages of the approach to equilibrium.

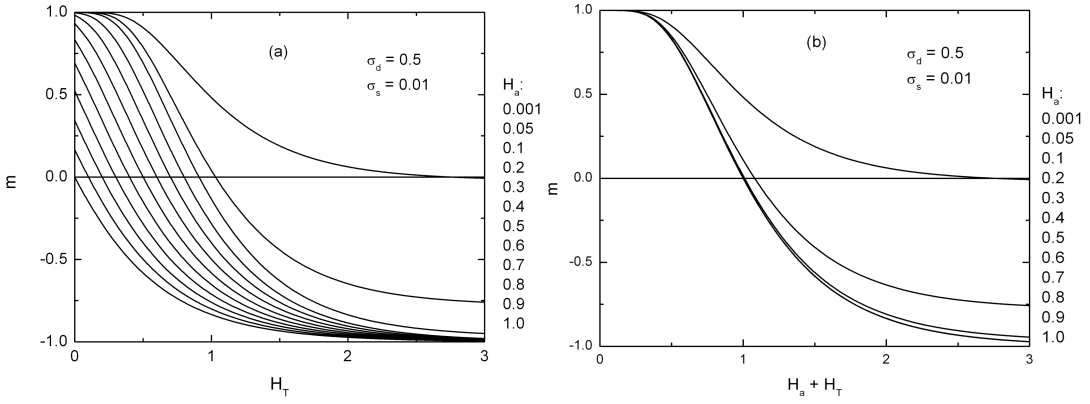

Figure 7.54: Model viscosity isotherms calculated in the fields listed to the right of each plot, for a lognormal-Gaussian Preisach density with $\sigma_d = 0.5$ and $\sigma_s = 0.01$, plotted as a function of (a) H_T, and (b) replotted after the transformation of H_T to $h_{eff} = H_a + H_T$.

The two analytical prescriptions outlined above are very similar in several respects. In both cases, the determination of the thermal fluctuation field H_f depends on the validity of a linear relationship, which is Eq(7.10) for prescription 1 and Eq(7.13) for prescription 2. Both strategies also impose certain conditions on the Preisach distribution of characteristic fields $p(H_d,H_s)$ which effectively demand that the distribution be concentrated in the vicinity of the mean dissipation field H_{dm}. This condition is essentially equivalent to placing limits on the structural disorder which guarantee that the distribution of metastable state excitation barriers is sufficiently narrow that there is a negligible population of Preisach elements with relaxation time constants which lie outside the experimentally accessible time window, at either the long time or short time end of the relaxation spectrum.

However, macroscopic magnetic systems are typically characterized by significant structural disorder (grains and grain boundaries, fluctuations of composition, surface roughness, random variations of particle shape, size, orientation, and position) leading to

an extremely complex free energy landscape with a multitude of local minima and maxima hierarchically distributed over a broad energy scale. As a consequence, the spectrum of system relaxation times extends continuously from microscopic time scales t $= \tau_0 \sim 10^{-9}$ s to geological time scales and beyond, and only a short, quasi-logarithmic fragment of the complete relaxation response curve is observed within the experimental time window. In the absence of both short-time and long-time points of reference and sufficient structural features to define the functional form of the relaxation isotherms, "conventional" scaling prescriptions become highly unreliable, and new strategies must be developed. In particular, we will show that the applicability of "conventional" scaling techniques is severely limited by the temperature at which the isotherms are measured, and that attempts to enforce superposition indiscriminately may lead to spurious behaviour for H_f. The vast majority of magnetic systems studied in our research laboratory possess considerable structural disorder, and one of the principal motivations for the investigations undertaken in this thesis was the need to develop a general strategy for analyzing sets of "fragmentary" relaxation isotherms which is independent of the specific functional form and characteristics of the Preisach distribution.

The presence of structural disorder in a given magnetic material is reflected in the two dispersions of characteristic fields σ_d and σ_s. Vanishing dispersions correspond to the hypothetical limit of negligible disorder. In order to illustrate the relationships between the various strategies as well as the limitations of the individual approaches, we have chosen to present numerical simulations of viscosity isotherms for a model system with a lognormal-Gaussian Preisach density, with dispersions $\sigma_d = 1.0$ and $\sigma_s = 1.0$, corresponding to substantial structural disorder. Figure 7.55 shows the viscosity

isotherms for this model system generated in a sequence of negative holding fields between $0 \leq h_a \leq -8$ and plotted as a function of the reduced thermal viscosity field h_T. The three pairs of vertical lines in this figure show those portions of the isotherms which would be visible experimentally at three different temperatures $h_f = 0.01$, $h_f = 0.03$ and $h_f = 0.1$, if the measurement time window were limited to $10s \leq t \leq 10^4 s$. The presence of significant structural disorder has three principal consequences. (1) The relaxation is very gradual and relatively featureless. (2) Relaxation measurements performed at a single

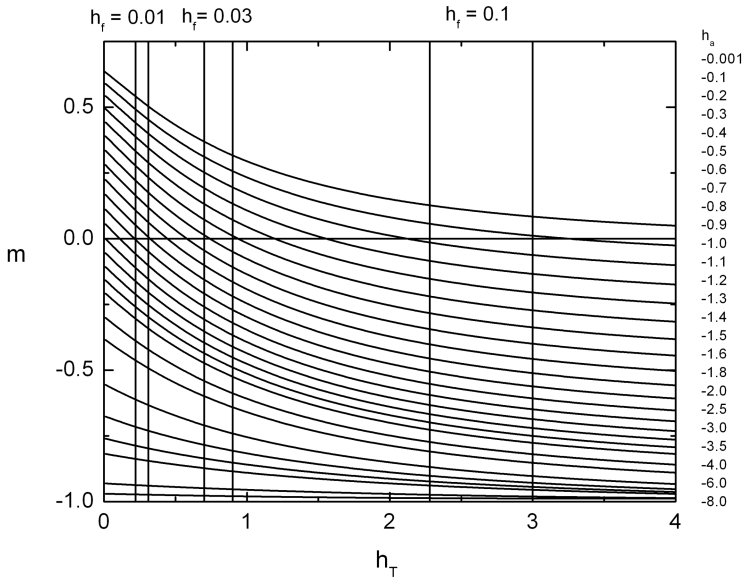

Figure 7.55: Model viscosity isotherms calculated in the fields listed to the right, for a lognormal-Gaussian Preisach density with $\sigma_d = \sigma_s = 1.0$. The vertical lines show those portions of the isotherms which would be visible in an experimental time window $10s \leq t \leq 10^4 s$ at temperatures $h_f = 0.01$, 0.03, and 0.1.

temperature yield only a short quasi-logarithmic fragment of the entire relaxation isotherm. (3) Each isotherm converges to an equilibrium moment in the limit $h_T \rightarrow \infty$ which is dependent on the holding field h_a. This last effect is very specifically related to the finite value of the dispersion of bias fields σ_s. In the limit $\sigma_s \rightarrow 0$, all viscosity isotherms converge to a common equilibrium moment $m_{eq} = \tanh(h_a/h_f) \approx -1$,

independent of σ_d, for $h_a < 0$ and h_f sufficiently small, as illustrated in Figure 7.54(a). In Figures 7.56(a) through 7.56(c), the model relaxation isotherms in Figure 7.55 have been replotted as a function of the effective field $h_{eff} = h_a - h_f \ln(t/\tau_0)$ defined in Eq(7.12), for all three temperatures h_f. For purposes of comparison, these figures also show the descending branch of the intrinsic major hysteresis loop (solid curves) generated in the limit of zero temperature $h_f \rightarrow 0$ and replotted as a function of $|h_a|$. For the lowest

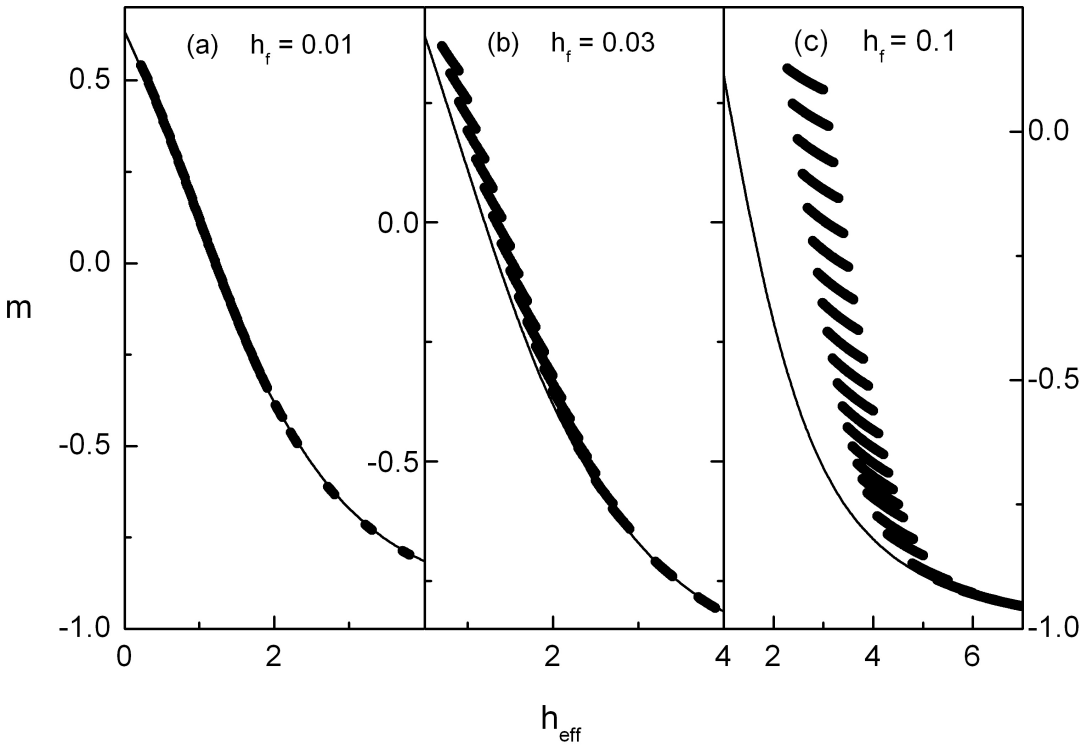

Figure 7.56: The relaxation isotherm segments within the experimental temperature-time windows (solid circles) of Figure 7.55 replotted as a function of h_{eff}: (a) $h_f = 0.01$, (b) $h_f = 0.03$, and (c) $h_f = 0.1$. The solid line in each panel is the descending branch of the intrinsic major hysteresis loop.

temperature data at $h_f = 0.01$, the transformation of variables to h_{eff} does indeed lead to an acceptable (but not perfect) superposition of the original set of isotherms on to a universal curve which is also coincident with the major intrinsic loop. However, the higher

temperature data at $h_f = 0.03$ and $h_f = 0.1$ do not scale onto a universal curve and are far from coincidence with the intrinsic major loop, except perhaps at holding fields approaching negative saturation. It follows that superposition is not, in general, a reliable criterion for establishing the thermal fluctuation field since it presupposes conditions of temperature and disorder that are not a priori verifiable. In fact, any attempt to enforce scaling and congruency with the major loop at these higher temperatures by treating h_f as an adjustable parameter would inevitably lead to a serious underestimate of the fluctuation field, as illustrated in Figure 7.57 for the $h_f = 0.1$ relaxation data, where it is seen that a value of $h_f = 0.01$ yields quite convincing scaling for all fields up to and beyond the coercive field $h_c \approx 1.2$.

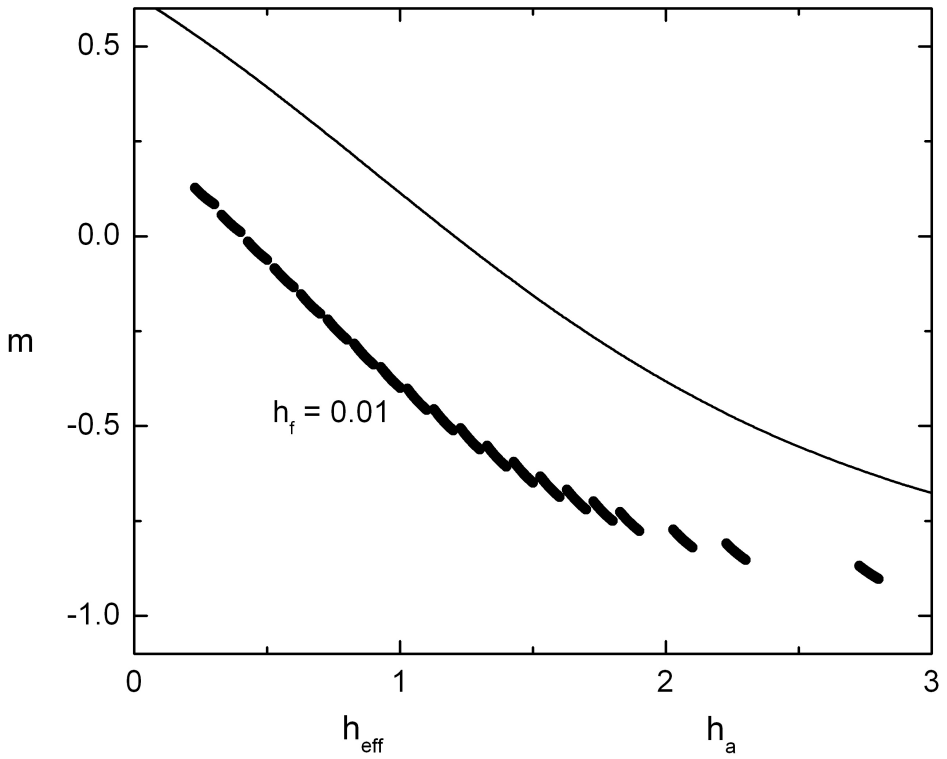

Figure 7.57: Scaling 'attempt' for the $h_f = 0.1$ segments of the viscosity isotherms of Figure 7.55 plotted as a function of h_{ef} (Figure 7.56(c)). The most convincing scaling occurs with $h_f = 0.01$. The solid curve is the descending branch of the hysteresis loop plotted as a function of the applied field h_a.

Furthermore, renormalizing the equilibrium anhysteretic moment to -1, as required by prescription 2, does not significantly improve either the quality of the scaling or the overlap with the intrinsic loop. In Figure 7.58, the model relaxation isotherms in Figure 7.55 have been replotted after renormalizing to a common equilibrium moment $m_{eq} = -1$ using the algorithm in Eq(7.14), and Figures 7.59(a) through 7.59(c) show the effect of replotting the portions of the isotherms which lie within the three temperature windows indicated by the pairs of vertical lines in Figure 7.58 as a function of the effective field $h_{eff} = h_a - h_f \ln(t/\tau_0)$. The deviations from the intrinsic hysteresis loop are in the opposite sense to those in Figure 7.56 obtained from the original isotherms in Figure 7.55, and deviations from isotherm scaling are observed at all temperatures, even at the lowest temperature $h_f = 0.01$, where renormalization actually destroys the "natural" scaling of the original isotherms in Figure 7.56(a).

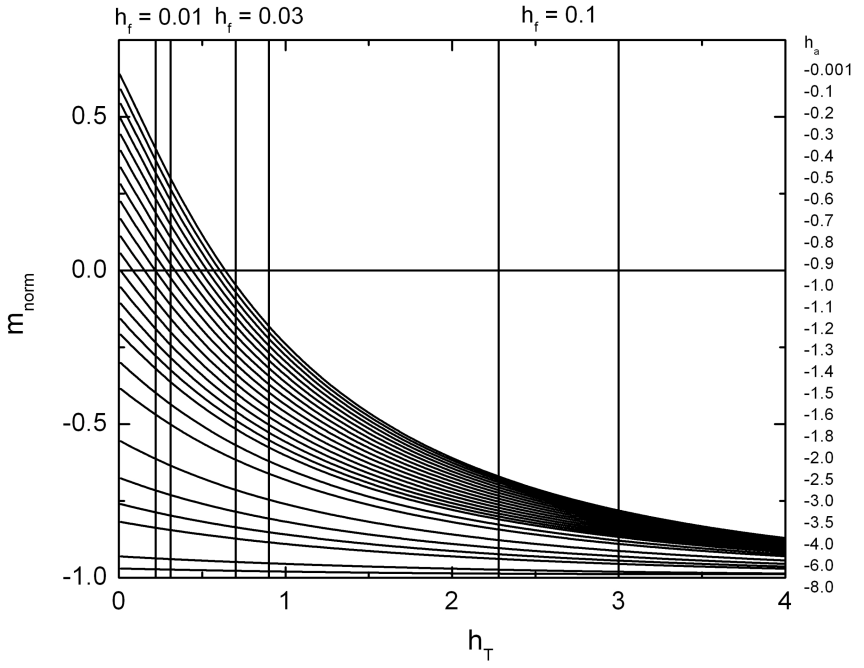

Figure 7.58: The same set of model viscosity isotherms shown in Figure 7.55, replotted with m normalized to a common equilibrium moment $m_{eq} = -1$.

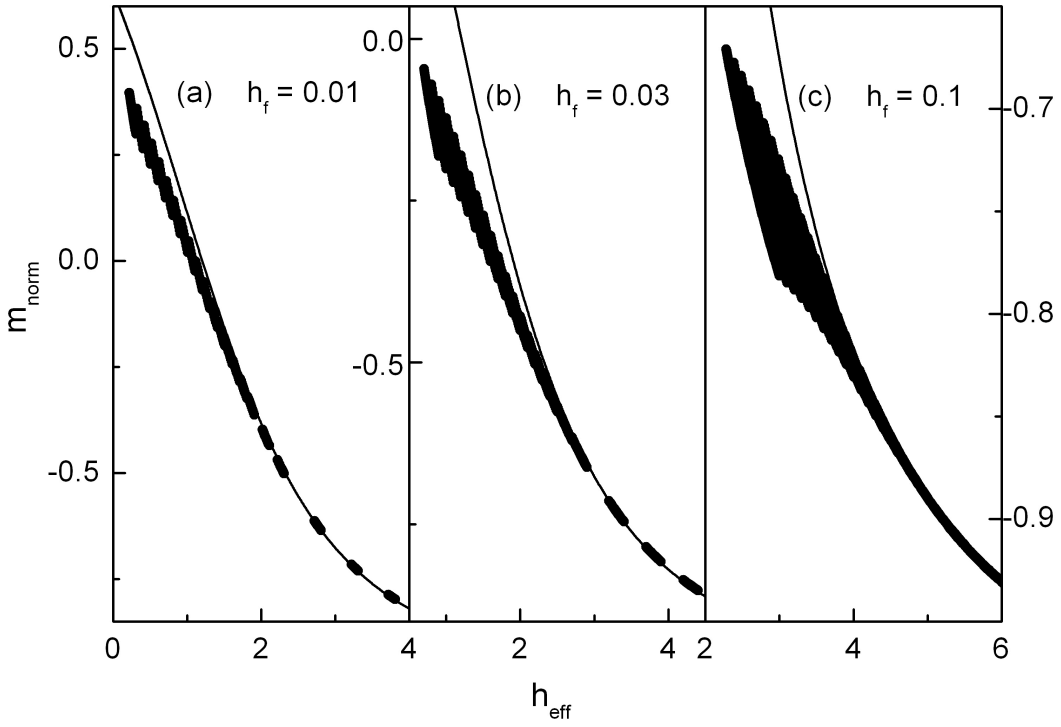

Figure 7.59: The normalized relaxation isotherm segments within the experimental temperature-time windows (solid circles) in Figure 7.58 replotted as a function of h_{eff}: (a) $h_f = 0.01$, (b) $h_f = 0.03$, and (c) $h_f = 0.1$. The solid line in each panel is the descending branch of the instrinsic major hysteresis loop.

Systematics very similar to those shown in the model simulations in Figure 7.56 are observed in experimental measurements of relaxation isotherms. As an example, Figures 7.60(a) through 7.60(c) show the effects of applying the field transformation in Eq(7.12) to the measured viscosity data and major hysteresis loop data of the nanoparticulate magnetite system in Figures 7.18 and 7.16 of Section 7.4. Figure 7.60(a) shows the viscosity data measured at T = 10K (solid dots) after applying the effective field transformation using the value of the elementary moment reversal $\mu = 2.8 \times 10^{-16}$ emu deduced from the viscosity analysis in Figure 7.19, assuming $\tau_0 = 10^{-12}$s, as well as the descending branch of the major hysteresis loop at T = 10K (smooth curve) after

transforming to $H_{eff} = H_f \ln(t_{exp}/\tau_0) + H_a$ assuming an experimental measurement (stabilization) time constant t_{exp} = 100s. The viscosity data scale very convincingly onto a "master" relaxation curve that coincides with the transformed (intrinsic) hysteresis loop. Figures 7.60(b) and 7.60(c) show the result of repeating this procedure at T = 30K and T = 60K, respectively. The deviations from scaling become progressively more pronounced with increasing temperature, and exhibit a systematic evolution with temperature which is strikingly reminiscent of that observed in the model simulations in Figures 7.56(b) and 7.56(c).

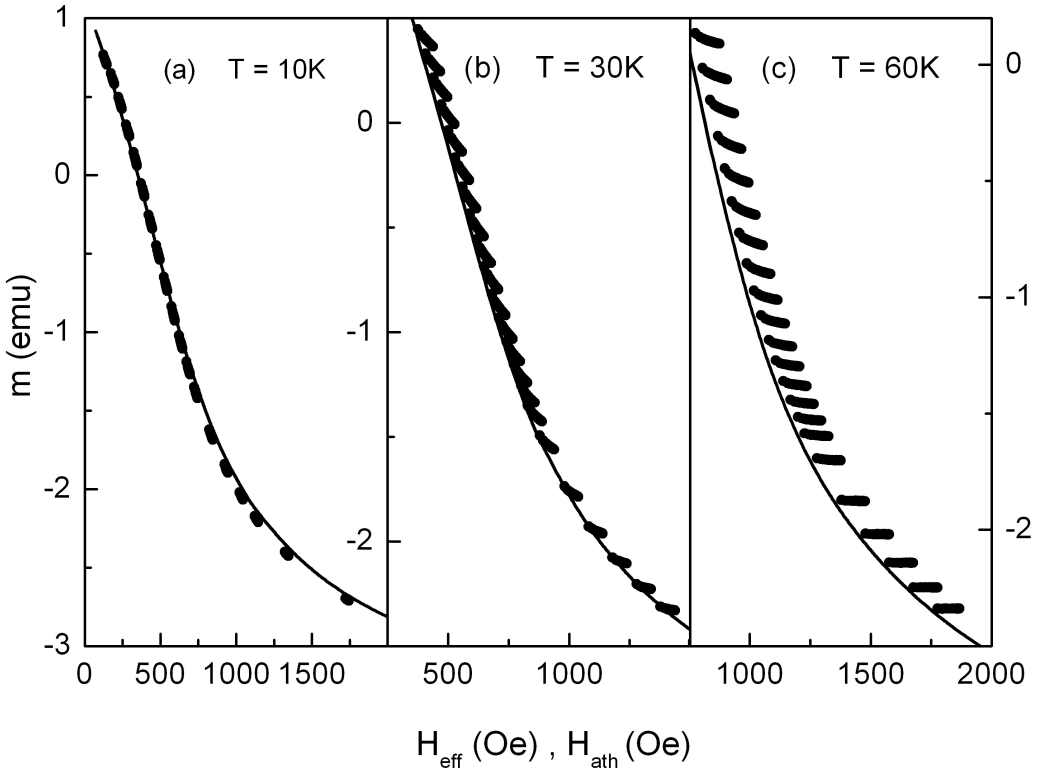

Figure 7.60: Transformation of variables from lnt to an effective field H_{eff} applied to the measured viscosity data for nanoparticulate magnetite from Figure 7.18. The solid curves shown the same transformation applied to and to the measured descending branch of the major hysteresis loop.

The strength of an analytical approach based on "reversal times" rests on the fact that $Tlnt_r$ data collapse onto a universal curve even when the relaxation isotherms do not. The solid curve labeled (a) in Figure 7.61 shows the complete "reversal" curve generated from the model relaxation isotherms in Figure 7.55 for all temperatures $0 \leq h_f \leq \infty$ and all holding fields between $-1.2 \leq h_a \leq 0$. The two pairs of horizontal dotted lines in Figure 7.61 show the portions of the universal curve which would be visible at temperatures $h_f = 0.01$ and $h_f = 0.1$ in a measurement time window $10s \leq t \leq 10^4 s$. With the correct choice of the microscopic time constant τ_0, the segment of curve (a) in Figure 7.61 constructed from reversal times acquired at temperature $h_f = 0.1$ falls on the same curve as the segment acquired at $h_f = 0.01$. However, the corresponding family of relaxation isotherms within the $h_f = 0.1$ window in Figure 7.55 do not collapse onto a common curve, even with the correct choice for h_f and τ_0, as shown in Figure 7.56(c). The solid curve labeled (b) in Figure 7.61 corresponds to the "reversal" curve generated for the renormalized model relaxation isotherms in Figure 7.58. Contrary to the claims of prescription 2, renormalization does not restore the linear relationship between h_T and h_a expected for a non-interacting system (straight line labeled (c) in Figure 7.61), and in fact overcompensates for the curvature of the original plot.

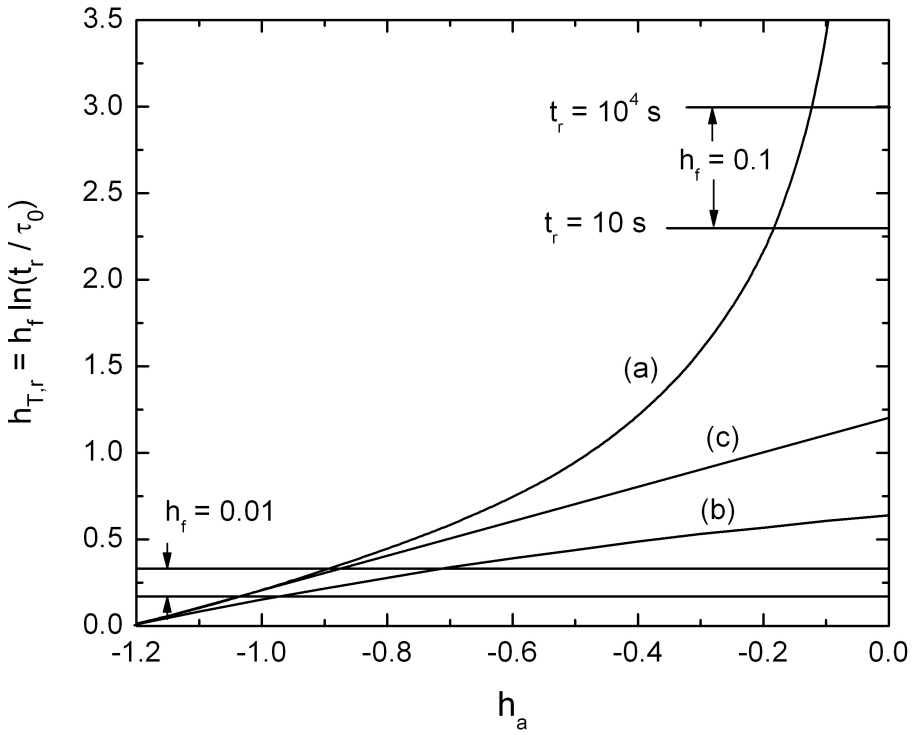

Figure 7.61: (a) Reversal curve generated for the model relaxation isotherms in Figure 7.55. (b) Reversal curve generated for the renormalized model relaxation isotherms in Figure 7.58. (c) Linear relationship between h_{Tr} and h_a expected for a perfectly non-interacting system. The horizontal lines define the limits of the experimental time window $10s \leq t_r \leq 10^4 s$ for $h_f = 0.01$ and $h_f = 0.1$.

7.8 References for Chapter 7

[1] G. Bertotti, Hysteresis in Magnetism (San Diego: Academic Press, 1998).

[2] R.M. Roshko and C.A. Viddal, "Non-Arrhenius relaxation effects in collections of two-level subsystems," Phys. Rev. B **72**, 184422 (2005).

[3] C.A. Viddal and R.M. Roshko, "Interpreting Viscosity Isotherms in Materials with Significant Structural Disorder," J. App. Phys. **103**, 07D922 (2008).

[4] G. Bertotti, V. Basso, C. Beatrice, M. LoBue, A. Magni, and P. Tiberto, "Hysteresis in Magnetic Materials: The Role of Structural Disorder, Thermal Relaxation, and Dynamic Effects," J. Mag. Mag. Mat **226-230**, 1206 (2001).

[5] T. Song, R.M.Roshko, and E. Dan Dahlberg, "Modelling the irreversible response of magnetically ordered materials: a Preisach-based approach," J. Phys. Cond. Matt. **13**, 3443 (2001).

[6] T. Song and R.M. Roshko, "A Preisach model for systems with magnetic order," Physica B **275**, 24 (2000).

[7] L. Néel, "Theorie du traînage magnetique des ferromagnetiques en grains fins avec applications aux terres cuites," Ann. Geophys. **5**, 99 (1949).

[8] J.-L. Dormann, D. Fiorani, and E. Tronc, "Magnetic relaxation in fine-particle systems," Adv. Chem. Phys. **98**, 283 (1987).

[9] P. Prené, E. Tronc, J.-P. Jolivet, J. Livage, R. Cherkaoui, M. Noguès, J.-L. Dormann, and D. Fiorani, "Magnetic properties of isolated γ-Fe_2O_3 particles," IEEE Trans. Mag. **29**, 2658 (1993).

[10] R. Cherkaoui, M. Noguès, J.-L. Dormann, P. Prené, E. Tronc, J.-P. Jolivet, D. Fiorani, and A.M. Testa, "Static magnetic properties at low and medium field of γ-Fe_2O_3 particles with controlled dispersioin," IEEE Trans. Mag. **30**, 1098 (1994).

[11] T. Song and R.M. Roshko, "Preisach Model for Systems of Interacting Superparamagnetic Particles," IEEE Trans. Mag **36**, 223 (2000).

[12] J.J. Préjean and J. Souletie, "Two-level-systems in spin glasses: a dynamical study of the magnetizations below T_G, application to CuMn systems," J. Physique **41**, 1335 (1980).

[13] R. Omari, J.J. Préjean and J. Souletie, "The extra-dimension W = kTLn(t/τ_0) of phase space below the spin glass transition: an experimental study of the relaxation of the magnetization at constant field in CuMn," J. Physique **45**, 1809 (1984).

[14] J. Souletie, "Hysteresis and after-effects in massive substances. From spin-glasses to the sand hill," J. Physique **44**, 1095 (1983).

[15] G. Cao, S. McCall, M. Shepard, J.E. Crow, R.P. Guertin, "Thermal, magnetic, and transport properties of single-crystal $Sr_{1-x}Ca_xRuO_3$ ($0 < \sim x < \sim 1.0$), Phys. Rev. B **56**, 321 (1997).

[16] C. Viddal, R.M. Roshko, H. Kunkel, L. Wei, X.Z. Zhou, and G. Williams, "Critical Behaviour and Irreversibility in a Mixed Perovskite $Ca_{0.6}Sr_{0.4}RuO_3$," J. Mag. Mag. Mat. **272**, 652 (2004).

[17] H.E. Stanley, *Introduction to Phase Transitions and Critical Phenomena* (Oxford: Clarendon Press, 1971).

[18] Hong-wei Zhang, Chuan-bing Rong, Jian Zhang, Shao-ying Zhang, and Bao-gen Shen, "Coercivity of isotropic nanocrystalline $Pr_{12}Fe_{82}B_6$ ribbons," Phys. Rev. B **66**, 184436 (2002).

[19] B.H. Liu, J. Ding, Z.L. Dong, C.B. Boothroyd, J.H. Yin, and J.B. Yi, "Microstructural evolution and its influence on the magnetic properties of $CoFe_2O_4$ powders during mechanical milling," Phys. Rev. B **74**, 184427 (2006).

[20] V. Basso, C. Beatrice, M. LoBue, P. Tiberto, and G. Bertotti, "Connection between hysteresis and thermal relaxation in magnetic materials," Phys. Rev. B **61**, 1278 (2000).

[21] M. LoBue, V. Basso, C. Beatrice, P. Tiberto, and G. Bertotti, "Influence of microstructure on thermal relaxation in nanocrystalline soft magnetic materials," J. Appl. Phys. **89**, 7463 (2001).

[22] M. LoBue, V. Basso, C. Beatrice, P. Tiberto, and G. Bertotti, "Hysteresis and thermal relaxation in random anisotropy systems," J. Mag. Mag. Mat. **242-245**, 1089 (2002).

[23] E. Della Torre, L.H. Bennett, R.A. Fry, and O.A. Ducal, "Preisach-Arrhenius Model for Thermal Aftereffect," IEEE Trans. Mag. **38**, 3409 (2002).

[24] S. Rao, E. Della Torre, L.H. Bennett, H.M. Seyoum, and R.E. Watson, J. Appl. Phys. **97**, 10N113 (2005).

[25] P.J. Chen, S. Rao, E. Della Torre, and L.H. Bennett, "Analysis of the fluctuation field in thermal magnetic aftereffect," J. Appl. Phys. **99**, 08D704 (2006).

Chapter 8

Conclusion and Future Work

One of the characteristic signatures of a material which is not in thermodynamic equilibrium is the dependence of the material properties on the time t for which the material is observed. In magnetic materials, the relaxation of the magnetic properties that accompanies the spontaneous approach to equilibrium, and which is ultimately driven by random energy exchanges with a heat bath, is of considerable fundamental interest for its potential as a sensitive probe of the structure of the free energy landscape, with its multitude of local metastable minima, maxima and saddle points, as well as of considerable practical interest, particularly in connection with the limitations that it imposes on the ultimate bit size of information storage media and on the stability of permanent magnets, both of which depend on the preservation of a stable magnetic state.

The investigation presented here employs model simulations and experimental measurements of the field and temperature and time dependence of a suite of standard macroscopic magnetic response functions, which include viscosity isotherms, hysteresis loop isotherms, the field cooled moment, the zero field cooled moment, the thermoremanent moment and the isothermal remanent moment. Two fundamental aspects of the non-equilibrium relaxation dynamics which characterize the approach to equilibrium were studied: (a) aging, memory, and rejuvenation effects in materials (both

magnetic and nonmagnetic) which are observed to undergo a vitreous transition, either structural or magnetic, into a frozen, disordered glassy ground state configuration, and (b) the intricate relationship between metastability, which is responsible for hysteresis, and thermal fluctuations, which are responsible for relaxing the system toward equilibrum, and their joint evolution with temperature as a material is progressively warmed through the irreversible regime and its hysteretic response to changes in field and temperature gradually and systematically fades toward the ideal equilibrium limit of perfect reversibility. The model simulations are predicated on the "Preisach hypothesis" that the free energy landscape may be decomposed into an ensemble of bistable fragments, each with a double-well free energy profile in a two-state configuration space. The principal emphasis in this thesis is on model systems and real materials which are characterized by substantial structural disorder, which leads to a very broad distribution of energy barriers and a correspondingly broad spectrum of relaxation times stretching from microscopic to geological time scales, as well as to a broad distribution of magnetostatic and exchange interactions of competing magnitude and sign.

8.1. Aging, Memory, and Rejuvenation Effects in Collections of Two-Level Subsystems

The model simulations presented in Chapter 6 offer a systematic and comprehensive theoretical exploration of the relaxation dynamics of a Preisach ensemble of two-level subsystems in response to all of the standard experimental protocols which are employed to study aging, memory and rejuvenation effects in magnetic spin glasses.

The simulations show that these effects are potentially far more ubiquitous than was previously imagined, and that aging, memory and rejuvenation are also fundamental characteristics of Preisach ensembles of interacting bistable elements, although their physical origins are very different from those proposed for spin glasses, which depend on the formation of a cooperatively ordered, highly degenerate, frustrated magnetic ground state, with either a hierarchical tree of metastable configurations which bifurcates with decreasing temperature or with a system consisting of two types of droplet domains which grow by thermal activation. Preisach theory incorporates no such collective critical effects, and Preisach ensembles consist of bistable elements which may indeed interact with each other, but which otherwise relax independently over their own individual energy barriers. In such ensembles, the transition from reversible to irreversible behaviour which occurs as the system is cooled from high temperatures is directly related to the gradual and progressive blocking of the individual Preisach elements as they fall out of thermal equilibrium on the time scale of the experimental measurement. Under these conditions, aging, memory and rejuvenation are all essentially a consequence of trapping a particular group of subsystems into their instantaneous (blocked) equilibrium configurations m_B during cooling, each at a temperature T_B which depends on the properties of that subsystem, and then allowing this group to relax (or age) to thermal equilibrium at a temperature T (lower than all the individual blocking temperatures T_B), thereby replacing their blocked moments $m_B(T_B)$ by equilibrium moments $m_{eq}(T)$ which are all closer to saturation, $|m_{eq}(T)| > |m_B(T_B)|$. When the ensemble is subsequently subjected to a change in field or to a shift in temperature, the relaxation response exhibits characteristic structure which depends on whether this “aging imprint” survives totally

intact, or partially intact, or is completely obliterated by the change (rejuvenation). The effects predicted by the model are similar in magnitude and in their systematic dependence on field and temperature and time to those observed experimentally in spin glasses, although the specific structural details are not all identical. Although the effects described here are all non-collective in origin, they are nevertheless all sensitive to the characteristics of the distribution of bias (or interaction) fields and some, like aging effects under zero field cooled conditions, depend upon the presence of non-vanishing interactions for their existence. It is important to emphasize that the model formalism studied here is in no way intended to replace collective theories of aging and memory based on droplet domain growth or bifurcating hierarchical trees but, rather, we imagine that the behaviour observed in spin glasses is most likely the result of a coexistence of collective and non-collective relaxation dynamics due to some combination of intercluster magnetostatic fields, which are describable by a Preisach-like approach, and genuine interatomic exchange fields, which require cooperative theories of phase transitions.

While the model simulations presented here are certainly compelling, little effort has thus far been expended searching for experimental evidence of aging, memory and rejuvenation in weakly interacting superparamagnetic materials which fall out of equilibrium during cooling via a gradual, progressive blocking process. An age dependence has been observed in the thermoremanent moment of a dilute assembly of Fe_3N nanoparticles, and we have preliminary (but inconsistent) evidence of aging in the TRM of the Fe/Al_2O_3 nanoparticulate thin film. We have also observed memory effects in Fe/Al_2O_3, but only under conditions where temperature cycling is accompanied by a

change in field, which is now a widely accepted and understood memory feature of both superparamagnets and spin glasses. In principle, all of the nanoparticulate assemblies studied in this thesis are potential candidates for observing the types of aging and memory effects described by our numerical simulations, and future work will concentrate primarily on the experimental identification of these effects in these systems.

8.2. Probing the Temperature Dependence of the Free Energy Landscape in Magnetic Materials with Persistent Memory

The magnetic properties of all materials which exhibit persistent memory and a history dependent response to an external field stimulus are functions of temperature, and the joint experimental and theoretical investigation conducted in Chapter 7 was motivated by the need to develop a rigorous analytical framework for the interpretation of this temperature dependence based on physical considerations which are of sufficient generality to embrace all materials with metastable free energy landscapes, independent of the specific details of their microstructure. Surprisingly enough, much of this interpretation is still conducted on a highly qualitative level, and relies on "folklore" recipes and superficial correlations based on flimsy or incomplete evidence. A particularly striking example, which appears with regularity in the scientific literature, is the insistence on treating the bifurcation of the moment as a function of temperature into a field cooled (FC) branch and a zero field cooled (ZFC) branch as a diagnostic signature of spin glass freezing when, in fact, its real physical significance is considerably broader

than this. We have proposed an analytical strategy based on the Preisach two-level subsystem hypothesis which is designed to isolate and quantify the two principal contributions to the temperature dependence of the material properties and response functions: (a) thermal fluctuations which are responsible for relaxing the system toward thermodynamic equilibrium, and (b) the explicit evolution with temperature of the free energy landscape itself, which ultimately originates from the explicit dependence on temperature of intrinsic material parameters, such as anisotropy constants and the spontaneous magnetization. The method was designed specifically for materials that possess substantial structural disorder, where only a short quasi-logarithmic fragment of the entire relaxation function is accessible in an experiment performed over a finite time window, as opposed to "patterned" media that are tailored to have highly regular or periodic microstructures with a narrow distribution of particle volumes and minimal interactions. The strategy is based on the analysis of viscosity isotherms, measured by applying a positive saturating field, recoiling to a negative holding field, and recording the decay of the moment with time at fixed temperature and fixed field, and specifically on a plot of $T\ln(t_r/\tau_0)$ versus H_a, where t_r is the time at which the relaxation isotherm measured at temperature T in a field H_a reverses sign. If the measurements are performed over a sufficiently wide range of closely spaced fields and closely spaced temperatures which ideally span the entire irreversible phase, then this plot will act as a sensitive diagnostic tool to identify which of the two processes listed above is dominant. If thermal overbarrier activation events dominate explicit barrier growth then, for the correct choice of microscopic time constant τ_0, the individual isothermal segments will align to form a continuous universal curve, from which it is possible to obtain the mean elementary

activation moment reversal (or, equivalently, the thermal fluctuation field) and to reconstruct the distribution of metastable state excitation energies. In materials where barrier growth is the dominant source of temperature dependence, the plot will fracture into a sequence of misaligned isothermal segments from which, in principle, it is possible to reconstruct the evolution of the spectrum of metastable state excitation energies with temperature. This strategy has been applied to the interpretation of the magnetic response functions of a series of magnetic systems with a variety of microstructures and magnetically ordered configurations, and these analyses show that a compressed powder of nanodimensional magnetite particles and a system of nanodimensional titanomagnetite particles suspended in a glass matrix are both fluctuation-dominated, while a series of bulk sintered ferromagnetic ruthenates and a thin film of nanodimensional iron particles embedded in alumina are dominated by the explicit evolution of the free energy landscape with temperature.

The analytical strategy proposed here has a number of unsatisfactory features which limit its potential to develop into a rigorous theoretical framework, and which will form the content of future investigations. (a) Principal among these is the fragmentary nature of the reversal time data when landscape evolution becomes an important contributing factor, as it is, for example, in ferromagnetic materials at temperatures close to the critical temperature. Under these circumstances, only a short segment of the entire isothermal reversal time curve which falls within a relatively narrow range of holding fields is visible experimentally at each temperature due to limitations imposed by the finite experimental time window, which is typically only a few orders of magnitude wide (seconds to hours). As a consequence, further analytical progress depends on the

implementation of drastic approximations, which are essentially impossible to justify a priori, although they receive some a posteriori support in the form of comparisons between model predictions and experimental measurements of certain response functions. Further model simulations are currently in progress which may suggest a method to circumvent such limitations. (b) Another is the ad hoc, phenomenological treatment of the "melting" of the spontaneous moment of the two-level subsystems as the ensemble is warmed through the critical magnetic ordering temperature, which infers the temperature dependence of the spontaneous moment from the thermal profile of the field cooled moment. This approach was inspired by the use of "thermomagnetic curves" (the saturation moment as a function of temperature measured in a fixed field during both cooling and warming) in rock magnetism studies to identify magnetic transition temperatures in minerals which consist of a mixture of magnetically distinct phases. We anticipate that the approach developed by J. Souletie to describe the shrinking of the correlation volume in spin glasses to atomic sizes above the glass temperature, based on a crossover from an Arrhenius law to a Fulcher law, may provide some valuable theoretical guidance in this regard.